



HAL
open science

Phase fields for network extraction from images.

Aymen El Ghoul

► **To cite this version:**

Aymen El Ghoul. Phase fields for network extraction from images.. Human-Computer Interaction [cs.HC]. Université Nice Sophia Antipolis, 2010. English. NNT: . tel-00550134

HAL Id: tel-00550134

<https://theses.hal.science/tel-00550134>

Submitted on 23 Dec 2010

HAL is a multi-disciplinary open access archive for the deposit and dissemination of scientific research documents, whether they are published or not. The documents may come from teaching and research institutions in France or abroad, or from public or private research centers.

L'archive ouverte pluridisciplinaire **HAL**, est destinée au dépôt et à la diffusion de documents scientifiques de niveau recherche, publiés ou non, émanant des établissements d'enseignement et de recherche français ou étrangers, des laboratoires publics ou privés.

UNIVERSITY OF NICE - SOPHIA ANTIPOLIS
DOCTORAL SCHOOL STIC
INFORMATION AND COMMUNICATION SCIENCES AND TECHNOLOGIES

THESIS

to fulfill the requirements for the degree of

Doctor of Philosophy in Computer Science

from the University of Nice - Sophia Antipolis

Specialized in CONTROL, SIGNAL AND IMAGE PROCESSING

by

Aymen EL GHOUL

Phase fields for network extraction from images

Supervised by Ian JERMYN and Josiane ZERUBIA

and prepared at INRIA Sophia Antipolis - Méditerranée in the ARIANA research team

Defended on 17 September 2010, in front of the committee composed of

Daniel CREMERS,	Professor, Technical University of Munich	- Reviewer
Amel BENZAZZA-BENYAHIA,	Professor, SUP'COM Tunis	- Reviewer
Horst BISCHOF,	Professor, Graz University of Technology	- Examiner
Jordi INGLADA,	Research-Engineer, CESBIO	- Examiner
Albert BIJAOUI,	Astronomer, 1 st class, OCA	- President
Ian JERMYN,	Senior Researcher, INRIA	- Supervisor
Josiane ZERUBIA,	Research Director, INRIA	- Supervisor

Dedicated to my parents, sisters, wife and daughter.

Acknowledgements

“Seek knowledge from the cradle to the grave.”

— Prophet Mahomet

First, I would like to express my sincere gratitude to my supervisors Ian Jermyn and Josiane Zerubia for giving me the chance to work with them since 2005. I was invited several times as an intern, and then in October 2007 I started my Ph.D. in the ARIANA research group directed by Josiane. Special thanks to Ian for his ad nauseam encouragement and scientific guidance during my thesis, and also for checking the English in all my scientific writing.

I would like to thank Jordi Inglada for his availability for meetings, and for his constructive discussions in the context of a collaboration with the French Space Agency (CNES).

I warmly thank the members of my Ph.D. committee, Professors Albert Bijaoui, Amel Benazza-Benyahia, Daniel Cremers, Horst Bischof, and Doctor Jordi Inglada for evaluating my manuscript.

I would like to thank CNES for providing the satellite images used in this thesis in the context of the ORFEO Accompaniment program.

I would like to thank Marc Spigai and Frédéric Falzon, both working in Thales Alenia Space, for their assistance in making this thesis exist, and the PACA Region which partially funded my research work at INRIA.

Special thanks to my dear friends Praveen and Ahmed for their ad nauseam discussions during the work, lunch and entertainment time. It is nothing but great and unforgettable souvenirs. I would also like to thank them for their support and help during the day of my defense.

I would like to thank my current and former colleagues at INRIA and its neighbourhood: Maria, Saima, Mikael, Athanasios, Sylvain, Aurélie, Vladimir, Giovanni, Marouene, Ihsen, Gregoire, Adrien, Daniele, Csaba, Peter, Avik, Pierre, Alexandre, Olivier, Gabriel, Alexis, Caroline, Raffaele, Ting, Marie, Nabil, Fatih, Ayoub, Guillaume, Dan, Saloua, Vikram, Florent, Virginie, Antoine, Grégory, Nadia, Ameya, Shashank, Carlo, Sotiris, Bayrem, Neismon, Amir, Amine, Mohamad, Imed, Mohamed, Corinne, Claire, Laurie, Christine, Zoltan, Farzad, Gabriele, Adrian, Franz, Véronique, Anuj, Florent, Xavier, Laure.

And now, last but not least, I owe a debt of gratitude to my parents, Najet and Ferjani, and sisters, Imene and Ilhem, whom were always encouraging me to work for better and better grades. I owe a debt of gratitude to my wife, Nadia, as well for her lovely time, lovely advices and lovely observations. By the end of the day, I was able to get my Ph.D. grade successfully, and more importantly we, me and Nadia, have a very lovely daughter, Yomna.

Tunis, December 2010

Contents

Acknowledgements	iii
List of Figures	xiv
List of Tables	xv
Introduction	1
Résumé en français	7
I Phase field HOACs for undirected networks	15
1 State-of-the-art	17
1.1 Introduction	18
1.2 Edge-based deformable contours	18
1.2.1 Parametric deformable models	18
1.2.1.1 Active contours: snakes	18
1.2.1.2 Balloon snakes	20
1.2.1.3 Topology adaptive snakes: T-Snakes	20
1.2.1.4 Gradient vector flow snakes	20
1.2.2 Geometric deformable models	21
1.2.2.1 Curve evolution theory	21
1.2.2.2 Level set method	22
1.2.2.3 Geometric active contours	23
1.2.2.4 Geodesic active contours	23
1.2.2.5 Area and length active contours	24
1.3 Region-based deformable contours	24
1.3.1 Mumford-Shah functional model	24
1.3.2 Region-based Bayesian inference	25
1.4 Shape priors	27
1.4.1 Reference shape-based models	27
1.4.2 Higher-order active contours and phase fields	29
1.4.2.1 Higher-order active contours	30
1.4.2.2 Phase fields	31
1.5 Line network extraction	32
1.5.1 Road network extraction	32
1.5.1.1 Active contours	32
1.5.1.2 Markov random fields and marked point processes	33
1.5.2 Hydrographic network extraction	34
1.5.2.1 Geometry of river networks	34
1.5.2.2 Fractal geometry	34

1.5.2.3	Digital elevation models	34
1.5.2.4	Multiscale and multiresolution analysis	34
1.6	Conclusion	35
2	Phase diagram of a HOAC model	37
2.1	Introduction	38
2.1.1	Higher order active contour (HOAC) model	38
2.1.2	Problem statement	39
2.1.3	Methodology	39
2.1.4	Dimensionless parameters	40
2.2	Stability analysis of a long bar	41
2.2.1	Energy	41
2.2.2	Stability conditions of a long bar	43
2.2.2.1	Analysis of e_0	43
2.2.2.2	Analysis of e_1	44
2.2.2.3	Analysis of e_2	44
2.2.3	Experiments	48
2.3	Stability analysis of a circle	49
2.3.1	Energy	49
2.3.2	Stability conditions of a circle	50
2.3.3	Experiments	54
2.4	Conclusion	55
3	A phase field HOAC model of undirected networks	59
3.1	Introduction	60
3.1.1	Phase fields	60
3.1.2	Phase fields as HOACs	61
3.2	Inflection point long bar model	61
3.2.1	HOAC inflection point long bar model	61
3.2.2	Phase field inflection point long bar model	62
3.3	Likelihood energy and energy minimization	63
3.3.1	Histogram modelling	63
3.3.2	Data energy term	63
3.3.2.1	Multivariate Gaussian model	66
3.3.2.2	Multivariate mixture of two Gaussian model	66
3.4	Experiments and discussion	66
3.4.1	MG model vs. MMG model	66
3.4.2	Inflection point long bar model	67
3.4.3	Robustness of the algorithm to initial conditions	67
3.5	Conclusion	70
II	Phase field HOACs for directed networks	73
4	A phase field HOAC model of directed networks	75
4.1	Introduction	75

4.2	The proposed model	76
4.3	Turing stability analysis	78
4.4	Experiments	81
4.4.1	Geometric evolutions of v for fixed ϕ	81
4.4.2	Geometric evolutions of v and ϕ	83
4.4.3	Segmentation	83
4.5	Conclusion	85
5	Stability analysis of a long bar	91
5.1	Introduction	91
5.2	Stability analysis	92
5.2.1	Energy of the bar	92
5.2.1.1	Local energy of the bar	94
5.2.1.2	Nonlocal energy of the bar	95
5.2.1.3	Total energy of the bar	96
5.2.2	Stability conditions for the bar	96
5.2.2.1	First order stability conditions	96
5.2.2.2	Second order stability conditions	99
5.3	Overall model and parameter settings	99
5.3.1	Overall energy	99
5.3.2	Optimization and parameter settings	99
5.4	Conclusion	102
6	Experimental results	103
6.1	Introduction	103
6.2	Geometric experimental results	104
6.2.1	Geometric evolutions of a long bar	104
6.2.2	Geometric evolutions of a random configuration	105
6.2.3	Geometric evolutions for gap closure	108
6.3	Experimental results on real images	112
6.3.1	ML segmentation	113
6.3.2	MAP segmentation	119
6.4	Conclusion	120
	Conclusion and perspectives	129
A	Stability calculations for a long bar under the undirected network HOAC model	133
A.1	Length of the contour	133
A.2	Area of the contour	134
A.3	The quadratic energy $E_Q(\gamma)$	134
A.3.1	Inner product of tangent vectors	135
A.3.2	Quadratic distance	135
A.3.3	Interaction function	135
A.3.4	Computation of $G(t_\mu, t'_\nu)$	136

B	Variational calculations for the directed network model	145
B.1	First derivatives of phase field terms	145
B.1.1	Derivative of the term weighted by D	145
B.1.2	Derivative of the term weighted by D_v	145
B.1.3	Derivative of the term weighted by L_v	146
B.1.4	Derivative of the nonlocal term	146
B.2	Fourier transform of the linear derivatives	147
C	Turing stability calculations for the directed network model	149
C.1	Stability of the background	151
C.1.1	Particular case: $L_v = 0$ and $\Psi = K_0$	152
C.2	Stability of the foreground	152
C.2.1	Particular case: $L_v = 0$ and $\Psi = K_0$	153
D	Stability calculations for a long bar under the directed network HOAC model	155
D.1	Energy of the long bar	155
D.1.1	Contribution of the local term	155
D.1.2	Contribution of the nonlocal term	158
D.1.3	Total bar energy	158
D.2	Stability constraints	159
D.2.1	First order stability conditions	159
D.2.2	Second order stability conditions	161
D.2.3	Derivatives of the function K_0	163
E	Publications and scientific activities of the author	165
	Bibliography	178

List of Figures

1	Two multi-spectral Quickbird images showing (top) a road network at full resolution (0.61m), and (bottom) a hydrographic network at 1/4 the original resolution (2.44m). (Original images ©DigitalGlobe, CNES processing, images acquired via ORFEO Accompaniment Program.)	1
2	An example of an approximately conserved flow running in a directed network.	2
3	Short-range dependencies (top) and long-range dependencies (bottom) between contour points. The dashed curves and edges define the interaction range and the interaction between two points respectively.	3
4	Deux images Quickbird multi-spectrales montrant (haut) un réseau routier à pleine résolution (0.61m), et (bas) un réseau hydrographique à 1/4 de la résolution originale (2.44 m). (Images originales ©DigitalGlobe, traitement CNES, images acquises via le programme d’Accompagnement ORFEO.)	7
5	Un exemple de flux approximativement conservé dans un réseau directionnel.	8
6	Dépendances courte-portées (haut) et longue-portées (bas). Les courbes et les liaisons en pointillées définissent respectivement la portée d’interaction et l’interaction entre deux points.	9
2.1	Behaviour of the interaction function Ψ	38
2.2	Evolution of an initial contour (rounded square) for different parameter values of the HOAC model given by equation 2.1 using gradient descent algorithm.	39
2.3	Bar parametrization.	41
2.4	Different behaviours of the energy $e_0(w_0)$ for different values of α_C and β_C .	43
2.5	Plot of extrema positions of the energy $e_0(w_0)$ against β_C for $\alpha_C = 1$. The solid and dashed curves correspond to minima and maxima respectively. . .	44
2.6	Perturbation behaviours in eigenvector basis.	45
2.7	(a): bar energy $e_0(w_0)$ plotted against the width w_0 . $\alpha_C = 0.8$, and $\beta_C = 1.39$ computed using equation (2.11) for a desired width $w_0 = 1.2$. (b): eigenvalues λ_{\pm} plotted against the frequency m for the same parameter values in (a). λ_{\pm} are indeed strictly positive for all frequencies $m \in \mathbb{Z}$	46
2.8	Plot of the four possible regions in the plane (w_0, k) corresponding to the sign change of G_+ et G_-	47
2.9	Lower and upper bounds of the parameter α_C in red and blue respectively. .	47
2.10	Phase diagram of a bar ($w_0 \in (0.88, 2)$). Blue and yellow zones refer to positive and negative bar energy per unit length respectively.	48
2.11	Gradient descent evolutions of a long bar for different parameter values given by table 2.1.	50
2.12	Bar energies and their corresponding eigenvalues for the different evolutions given by figure 2.11. The blue and red curves correspond to the in-phase and out-of-phase eigenvalues, λ_+ and λ_- , respectively.	51

2.13	Behaviours of the circle energy, $e_0(r_0)$, for different values of α_C and β_C	53
2.14	Plot of extrema positions of the energy $e_0(r_0)$ against β_C for $\alpha_C = 1$. The solid and dashed curves correspond to minima and maxima respectively.	54
2.15	The blue and red curves shown by figures (a), (b) and (c) correspond to frequencies 0 and 2 respectively. For figure (d), the red and blue curves correspond to lower and upper bounds of α_C respectively.	55
2.16	Phase diagram of a circle ($\hat{r}_0 \in]0.69, \infty[$). The blue and yellow zones correspond to parameter values which give a stable circle with positive and negative energy respectively.	56
2.17	Gradient descent evolutions of a circle for different parameter values given in table 2.1.	57
2.18	Circle energy $e_0(r_0)$ and second order energy $e_2(r_0^*, k)$ corresponding to evolutions given in figure 2.17. r_0^* is the radius of a circle at the energy minimum if it exists.	57
2.19	Phase diagram. Maroon, red, yellow, green, white, blue, pink, grey, magenta correspond respectively to B+, C+, B+ C+, B+ C-, UB UC, B- C+, B- C-, C- and B-; B, C, U, + and - refer respectively to bar, circle, unstable, positive energy and negative energy.	58
3.1	Behaviour of the ultralocal terms ($\lambda = 0.5$ and $\alpha = 0.1$).	60
3.2	3.2(a) and 3.2(b) plot e_0 against bar width w_0 , with $(\alpha_C, \beta_C) = (0.8, 0.53)$ and $(0.7, 0.363)$ respectively, giving a minimum at $w_0^* = 1.2$ and an inflection point at $w_0^* = 0.88$	62
3.3	Top row, from left to right: the R-G-B bands of a multi-spectral satellite image; the G-R-IR bands of the same image; the corresponding manually extracted road network mask. Second row: similar, for a second image. Third row, from, left to right: histograms of the network (red) and background (blue) regions of the R, G, B, and IR bands of the image in the top row; Fourth row: similar, for second image. (Images ©DigitalGlobe, CNES processing, images acquired via ORFEO Accompaniment Program).	64
3.4	From left to right: histograms of R, G, B and IR channels. From top to bottom: histograms of the interior region of the first image, the exterior region of the first image, the interior region of the second image and the exterior region of the second image. Curves in blue, red and black correspond to the histograms, the Gaussian models and the mixture of two Gaussian models respectively.	65
3.5	Segmentations of the two images in figure 3.3, from left to right in each row: ML using MG, ML using MMG, MAP using MG, and MAP using MMG. From 3 rd to 4 th column and from top to bottom: $(w_0, \hat{\alpha}, \lambda_C) = (2, 0.7646, 15)$, $(2, 0.8385, 5)$, $(2, 0.8385, 20)$, and $(2, 0.6169, 10)$	67
3.6	Left: segmentation result using parameter values selected from the maroon zone, $(w_0, \hat{\alpha}, \lambda_C) = (4, 0.2013, 5)$. Right: segmentation result using parameter values leading to an inflection point at the desired bar width, $(w_0, \hat{\alpha}, \lambda_C) = (2, 0.7646, 15)$	70

3.7	Segmentations of the two images in figure 3.3 using different initializations. From top to bottom: NI, -1, +1, UR, ML, -ML, Scaled ML. 1 st image: $(w_0, \hat{\alpha}, \lambda_C) = (3, 1.2578, 30)$ for the 1 st column and $(3, 1.2578, 20)$ for the 2 nd column. Second image: $(2, 0.5924, 15)$ for the 3 rd column and $(2, 0.8385, 20)$ for the 4 th column. The MG data model was used with the inflection point prior model.	71
4.1	Contour plot of the ultralocal term W	79
4.2	3D plot of the ultralocal term W	79
4.3	Geometric evolutions of v keeping ϕ fixed. First column: initial configuration. Second column: intermediate configuration. Third column: final configuration. From top to bottom: result with the divergence term using a vertical initialization; result with the divergence term using a random initialization; result with the smoothing term; result with the smoothing and divergence terms.	82
4.4	Gradient descent evolutions using the undirected network model E_P^s . The initial regions are shown in the leftmost column; time runs from left to right.	84
4.5	Gradient descent evolutions using the new, directed network model E_P . The initial regions are shown in the leftmost column; time runs from left to right.	85
4.6	A zoom on the bottom-left quarter of the final configuration in the fourth experiment with the directed network model, shown in figure 4.5, showing v as well as ϕ (thresholded at ϕ_s).	86
4.7	From left to right, top to bottom: synthetic image with three grey levels and added noise; ground truth; segmentation using undirected network model; segmentation using directed network model. Note how the constraint on branch width in the directed network model avoids including parts of the background that have similar intensity to the ‘river’.	87
4.8	A zoom on the central part of the result in figure 4.7, showing v as well as ϕ (thresholded at ϕ_s).	88
4.9	From left to right, top to bottom: real image; ground truth; segmentation using undirected network model; segmentation using directed network model. Note how the constraint on junction widths in the directed network model guarantees flow conservation. (Images ©DigitalGlobe, CNES processing, images acquired via ORFEO Accompaniment Program).	88
4.10	A zoom on the upper part of the result in figure 4.9, showing v as well as ϕ (thresholded at ϕ_s).	89
4.11	A streamline plot of the result in figure 4.9, showing v as well as ϕ (thresholded at ϕ_s).	89
5.1	First row: a stable network configuration (left) and a zoom on its central part showing ϕ and v (right). Second row: profiles of functions ϕ (left) and $ v $ (right) of the network shown on the right of the first row. Third row: initial (left) and final (right) slices of ϕ and $ v $, given in blue, across a network branch after gradient descent; the proposed approximations of ϕ and $ v $ are shown in black.	93

5.2	Directed bar <i>ansatz</i> , showing the parameterization in terms of the physical parameters w_0 , w , ϕ_m and v_m	94
5.3	Example of solutions of equation (5.5) for some values of ρ^* using Rochery et al. (2005)'s interaction function (left) and K_0 (right). Curves are labeled by the values of ρ^*	97
5.4	Left: behaviour of $\hat{\beta}$ using Rochery et al. (2005)'s interaction function. Right: behaviour of $\hat{\beta}$ using K_0 . The light and dark surfaces show the locations of maxima and minima respectively.	98
5.5	Bar energies against w_0 using Rochery et al. (2005)'s interaction function (left) and K_0 (right).	98
5.6	Bar energy e_P against the bar parameters \hat{w} , \hat{w}_0 , ϕ_m and v_m . Parameter values were chosen such that there is a bar energy minimum at $\pi_B^* = (1.36, 0.67, 1, 1)$	100
6.1	Geometric evolutions of bars using the directed network phase field model E_P . Time runs from left to right. For the first three rows we use Rochery et al. (2005)'s interaction function and K_0 for the last three rows. First column: initial configuration which consists of a set of straight bar of width 10. The function ϕ is -1 in the background and ϕ_s in the foreground, and the initial vector field is $(1, 0)$. 1 st and 4 th rows: when $\hat{\beta} < \hat{\beta}_{\min}$, the initial bars vanish; 2 nd , 3 rd , 5 th and 6 th rows: when $\hat{\beta} > \hat{\beta}_{\min}$, the bars evolve toward bars which have the predicted stable widths $w_0 = 6, 14, 3$ and 6 respectively. The regions are obtained by thresholding the function ϕ at 0.	105
6.2	From top to bottom, the bar energies e_P against the bar parameters \hat{w} , \hat{w}_0 , ϕ_m and v_m ; from left to right, the columns correspond to the last three bar evolutions in figure 6.1 from top to bottom respectively.	106
6.3	Geometric evolutions of a random initial configuration. Time runs from left to right. For the first four rows we use Rochery et al. (2005)'s interaction function while K_0 is used for the last four rows. Parameter values were chosen as a function of the desired stable width. The latter is $w_0 = 5$ for evolutions 1 – 2 and 5 – 6, and $w_0 = 8$ for evolutions 3 – 4 and 7 – 8. All evolutions show that the initial configuration evolves towards a line network-like region where branches have approximately a constant width equal to the desired stable width.	107
6.4	Geometric evolutions starting from a random initial configuration. Time runs from left to right. Parameter values were chosen as a function of the predicted stable width, which was 5 for the first and second rows and 8 for the third row. The regions are obtained by thresholding the function ϕ at 0.	109
6.5	The phase field function ϕ (left) and the magnitude of the vector phase field function $ v $ (right) of the converged configuration of the third experiment in figure 6.4.	109
6.6	The final configuration of v and ϕ (thresholded at 0): (top-left) a zoom on the top-right quadrant, (top-right) a zoom on the central two junctions, and (bottom) a zoom of the converged configurations of the first, second and third evolutions in figure 6.4 respectively.	110

6.7	Geometric evolutions of branches using the prior directed network model E_P . Time runs from top to bottom. ϕ is initialized to be -1 outside the branches and 1 inside, and v is initialized to be 0 outside and of unit magnitude inside, and running along the branches. Parameter values are the same for the three experiments except the divergence weight D_v is 1 , 10 and 100 from left to right. The initial width of branches is 18 and the stable width is fixed to 10 . From left to right: branches shrink until they disappear; branch extremities join each other to form a single branch, and then the latter shrinks until it disappears; branch extremities join each other to form a single branch, and the latter lengthens. Regions are obtained by thresholding ϕ at 0	111
6.8	Configurations of v and ϕ (thresholded at 0) of a zoom on the central gap corresponding to the third experiment in figure 6.7. Time runs from left to right, and from top to bottom.	111
6.9	Three multi-spectral Quickbird images showing road networks, and their reference segmentations extracted manually. The resolution of images 1 and 2 is $1/4$ the original resolution (2.44m); image 3 is at full resolution (0.61m). Images 1, 2 and 3: RGB channels of the images. (Original images ©DigitalGlobe, CNES processing, images acquired via ORFEO Accompaniment Program.)	112
6.10	Five multi-spectral Quickbird images showing hydrographic networks, and their reference segmentations extracted manually. The resolution of images 1 and 3 is $1/4$ the original resolution (2.44m); the resolution of image 2 is $1/16$ the original resolution (9.76m); the resolution of image 4 is $1/2$ the original resolution (1.22m); image 5 is at full resolution (0.61m). Images 2, 3, 4 and 5: RGB channels of the images. Image 1: GBI (mapped to RGB) channels of the image. (Original images ©DigitalGlobe, CNES processing, images acquired via ORFEO Accompaniment Program.)	114
6.11	From top to bottom: original images of road networks; segmentations obtained using NDVI and optimal thresholding; ML segmentations using the MG model; ML segmentations using the MMG model.	115
6.12	From top to bottom: original images of hydrographic networks; segmentations obtained using NDWI and optimal thresholding; ML segmentations using the MG model; ML segmentations using the MMG model.	116
6.13	From top to bottom: original images of hydrographic networks; segmentations obtained using NDWI and optimal thresholding; ML segmentations using the MG model; ML segmentations using the MMG model.	117
6.14	Road network segmentations using the undirected network model (first column) and the directed network model (second column). Regions are obtained by thresholding ϕ at 0	122
6.15	Hydrographic network segmentations using the undirected network model (first column) and the directed network model (second column). Regions are obtained by thresholding ϕ at 0	123
6.16	Hydrographic network segmentations using the undirected network model (first column) and the directed network model (second column). Regions are obtained by thresholding ϕ at 0	124

-
- 6.17 The final configuration of v and ϕ (thresholded at 0) corresponding to the third segmentation in figure 6.14 and first segmentation in figure 6.15. The vector field is indeed zero outside the network and of constant (unit) magnitude inside, smooth, parallel to branch boundaries, and conserved along network branches and at junctions. 125
- 6.18 The final configuration of v and ϕ (thresholded at 0): (top-left) zoom on the left part of the network of the second image and (bottom-left) on the central loop of the network of the third image in figure 6.15; (top-right) zoom on the central loop of the network of the first image and (bottom-right) the second image in figure 6.16. 126
- 6.19 Hydrographic network segmentation from a colour image using the directed network model. Flow conservation is satisfied at junctions, illustrated by a significant change of width, and along branches, as illustrated by a slow change of width. (©2010 Google - Imagery ©2010 TerraMetrics, Map data ©2010 Tele Atlas.) 127

List of Tables

2.1	Parameter values which correspond to the evolutions given by figure 2.11. . .	52
2.2	Parameter values which correspond to the evolutions given by figure 2.17. . .	56
3.1	Quantitative evaluations of the experiments. T, F, P, and N correspond to true, false, positive, and negative respectively.	68
3.2	Similarity measures of the segmentations given by the first column of figure 3.7.	68
3.3	Similarity measures of the segmentations given by the second column of figure 3.7.	69
3.4	Values of energy terms, at the convergence, which correspond to the parameter values of the first column of figure 3.7. ERE refers to Empty Region Energy.	69
3.5	Values of energy terms, at the convergence, which correspond to the parameter values of the second column of figure 3.7. ERE refers to Empty Region Energy.	69
6.1	Quantitative evaluations of the ML segmentations given in figure 6.11. The numbers 1, 2, and 3 correspond to the three images in figure 6.11, from left to right. Completeness= $TP/(TP + FN)$, correctness= $TP/(TP + FP)$ and quality = $TP/(TP + FP + FN)$. T, F, P, and N correspond to true, false, positive, and negative respectively.	118
6.2	Quantitative evaluations of the ML segmentations given in figures 6.12 and 6.13. The numbers 1, 2 and 3 (4 and 5) correspond to the images in figure 6.12 (6.13), from left to right. Completeness= $TP/(TP + FN)$, correctness= $TP/(TP + FP)$ and quality = $TP/(TP + FP + FN)$. T, F, P, and N correspond to true, false, positive, and negative respectively.	118
6.3	Quantitative evaluations of experiments of the three images given in figure 6.14. T, F, P, N, UNM and DNM correspond to true, false, positive, negative, undirected network model and directed network model respectively.	120
6.4	Quantitative evaluations of experiments of the three images given in figure 6.15 (1, 2 and 3) and of the two images given in figure 6.16 (4 and 5). T, F, P, N, UNM and DNM correspond to true, false, positive, negative, undirected network model and directed network model respectively.	120

Introduction

“The true logic of this world is the calculus of probabilities.”

— James Clerk Maxwell

Motivations and goal

Why is real-world visual object recognition hard? An interesting question which [Pinto et al. \(2008\)](#) have tried to answer. At the core of this challenging question is image variation: any given object can cast an infinite number of images, in which it has different sizes, orientations, poses, lighting, etc.

The central challenge we are interested in is the automatic extraction of specific objects from real-world images. By ‘extraction’ is meant: ‘find the region R in the image domain that “contains” the object’, where ‘contains’ means that R is the projection to the image domain of the volume occupied by the object in the real world. Particularly, our central aim is network-like region extraction from very high resolution (VHR) remote sensing images. Figure 4 shows two multi-spectral VHR Quickbird images in which a road network (top) and a hydrographic network (bottom) are present. These images show many difficulties if one is concerned to segment network-like regions. Firstly, the background and the network region have many pixels with very similar radiometry leading to confounding zones which yield misclassification if one uses only local information derived from the image. Secondly, the visual network in the image appears with many gaps and broken edges due to occlusions and the presence of noise (*e.g.* trees, bridges, shadows, cars, etc). Thus, the ‘shape’ of the object in question is mandatory to distinguish between the object and the background. Methods and techniques which do not describe the shape of a network are then completely unsuccessful in segmenting a network from this kind of image.

Directed networks (*e.g.* hydrographic networks in remote sensing imagery and vascular networks in medical imagery) carry ‘flow’ through their branches. This family of networks have characteristic geometric properties which are significantly different to *undirected networks* (*e.g.* road networks). For directed networks, branches tend not to end; different branches may have



Figure 1: Two multi-spectral Quickbird images showing (top) a road network at full resolution (0.61m), and (bottom) a hydrographic network at 1/4 the original resolution (2.44m). (Original images ©DigitalGlobe, CNES processing, images acquired via ORFEO Accompaniment Program.)

very different widths; width changes slowly along each branch; at junctions, total incoming width and total outgoing width tend to be similar. In other words, the flow is approximately *conserved*. See figure 5 for an example of an approximately conserved flow running in a directed network. Of course we can find, but not frequently, road networks which satisfy some of the geometric properties of directed networks *e.g.* the road network in figure 4 satisfies the property of flow conservation at some junctions and along some branches. The specific geometric properties of the region of interest make the problem much harder because they need to be incorporated into the model in order to favour such regions. In addition to that, the *topology* of a network region is a serious difficulty because it is non-trivial and unknown *a priori*. More concretely, network topologies are very diverse depending on the number of connected components and the number of handles (loops) for each of them (see figure 5 for an example of a loop).

To solve the problem of extraction, prior knowledge about network regions need to be incorporated into mathematical models for automated techniques. Grenander et al. (1991) is the pioneer of the idea that a Bayesian approach permits the incorporation of prior knowledge of the object into mathematical models. Mathematically speaking, we seek to construct the *a posteriori* probability distribution $P(R|I, K)$, where I is the image data and K represents prior knowledge about the region of interest R (*e.g.* network region in our case) and the relation between R and I . As usual, this can be written as the product of a likelihood $P(I|R, K)$, and a prior $P(R|K)$ that incorporates knowledge of region ‘shape’. We then infer the region R by maximum *a posteriori* (MAP) estimate. (In practice, we will deal with negative log-probabilities, *i.e.* a total energy $E(R; I, K)$ that is the sum of a likelihood term $E_l(I, R, K)$ and a prior term $E_p(R, K)$.)

In the literature, a huge number of papers propose the incorporation of prior knowledge of the object to be extracted into mathematical models. One of the pioneering models to incorporate prior knowledge is the active contour (snake) model, initially introduced by Kass et al. (1988). The snake model describes generic prior knowledge via short-range dependencies between contour points (see figure 6, top), which guarantees smoothness of the object boundary of the final solution. We also refer to the earlier work in (Geman



Figure 2: An example of an approximately conserved flow running in a directed network.

and Geman, 1984; Ising, 1925) where generic shape knowledge is used. After Kass et al. (1988), many successors were introduced in many application domains. However, they are all almost insufficient for automatic object segmentation because they incorporate generic shape priors, mainly about boundary smoothing which says nothing about the object of interest (e.g. network-like objects in our case). Many recent works have then focused on the incorporation of specific shape priors based on active contours. The key idea for these methods is to seek an optimal region described by perturbation of reference region(s). In other words, the topology of the object of interest is constrained to be the same as the topology of the reference region(s). This is not suitable for our problem, *i.e.* network region extraction, because the topology of a network is non-trivial and unknown *a priori*. So, one has to construct specific shape prior models without constraining the topology.

In Rochery et al. (2006), a higher-order active contour (HOAC) model was introduced to incorporate specific shape priors without constraining the topology. The idea is to introduce long-range dependencies between the boundary points of the region of interest (see figure 6, bottom) which allow to model network regions for some parameter ranges. But, the algorithm used to solve the minimization problem suffers from serious difficulties: not enough ‘automatic’ topological freedom (it is not possible to handle network loops) and is very slow due to the long-range dependencies. A new framework based on phase fields was then introduced by Rochery et al. (2005) to remedy these problems. Moreover, it has been shown that the phase field model is approximately equivalent to the HOAC model for a given region of interest (Rochery et al., 2005).

The undirected network model introduced by Rochery et al. (2005, 2006) works very well for road network extraction from medium resolution optical images of rural and semi-rural areas where road width is approximately constant and relatively small. But, it is not appropriate to satisfy the geometric properties of hydrographic networks because it constrains severely the change of width of network branches. High and very high resolution images bring with them new challenges and difficulties. Peng et al. (2010) extended the earlier model in (Rochery et al., 2005) in order to favour networks where branches prefer to be long and straight. The model was applied successfully for road network extraction from high resolution images of urban areas, but again it is not appropriate for hydrographic networks because the branch rigidity and branch width change are tightly constrained.

The extraction of road and hydrographic networks is crucial in many application domains: cartographic data updating, intelligent navigation, environmental monitoring, disaster management, hydrology, agriculture, planning and management of cultivated territories, water resource management, etc. Recently, the amount of available VHR optical data (QuickBird, Ikonos, and in the near future Pléiades) has become enormous and this brings

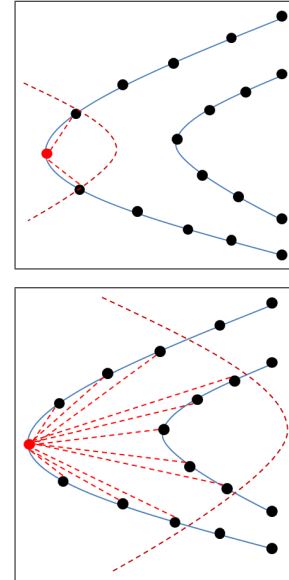


Figure 3: Short-range dependencies (top) and long-range dependencies (bottom) between contour points. The dashed curves and edges define the interaction range and the interaction between two points respectively.

new challenges. VHR images show road and hydrographic networks as 2D regions in the image domain, as opposed to low and medium resolution images where these objects are 1D structures. VHR images provide much more information about network regions and so the extraction accuracy can potentially be much improved by using advanced techniques.

In this thesis, we propose new variational models, based on HOACs and phase fields, for network modelling in general and for hydrographic and road network extraction from VHR remote sensing images in particular.

Firstly, we conduct a stability analysis of an undirected long bar under the phase field HOACs introduced by (Rochery et al., 2005, 2006). This constrains the model parameters to ranges producing stable networks. The result of the stability analysis is illustrated on a ‘phase diagram’ which emphasizes the different stable phases of a long bar. Thus, one can select parameter values from the phase diagram and use them for undirected network extraction from VHR remote sensing images.

Secondly, we propose a new family of phase fields for directed networks. Each directed network branch has a ‘flow direction’, and each junction therefore has ‘incoming’ and ‘outgoing’ branches. The existence of such a flow typically changes the geometry of the network, because often the flow is in some sense *conserved*. Thus branches tend not to end, because this would involve the flow stopping, and junctions often consist of small-width incoming branches joining together to form larger-width outgoing branches or vice-versa. Our goal is hydrographic network extraction from remote sensing images, but the model is probably relevant to other applications involving directed networks (*e.g.* vascular networks in medical imagery). To model such networks, we extend the nonlocal phase field model of undirected networks described by Rochery et al. (2005, 2006). In addition to a scalar phase field representing a region by its smoothed characteristic function and interacting nonlocally so as to favour network configurations, the proposed model contains a vector phase field representing the ‘flow’ through the network branches.

Organization of the manuscript

This manuscript is organized as follows:

Part 1: phase field HOACs for undirected networks

Chapter 1: In the first part, we give a brief state-of-the-art for variational methods for segmentation. We pay particular attention to active contours and shape priors. Two classes of active contours are emphasized: *edge-based* and *region-based* methods. In the second part, we review some of the representative techniques for road and hydrographic network extraction from different types of images.

Chapter 2: Firstly, we briefly recall the HOAC model introduced by Rochery et al. (2006), and we show that this model favours two stable configurations, namely line networks and circular structures, for different parameter values. Secondly, we conduct a stability analysis of a long bar via a Taylor series expansion up to second order of the HOAC model around a long bar. We then are able to constrain the parameter values in order to model networks. Geometric evolutions of a long bar using gradient descent are shown to validate

the theoretical calculations. Finally, we Taylor-expand the prior HOAC model up to second order around a circle in order to find the parameter ranges which lead to stable circular structures. The result of the stability analysis of both long bar and circle is illustrated on a ‘phase diagram’.

Chapter 3: Firstly, we briefly recall the phase field HOAC model of undirected networks introduced by [Rochery et al. \(2005, 2006\)](#), we show the equivalence between phase field modelling and standard active contours, and we show the equivalence of the nonlocal phase field term and the HOAC term. The result is that one can use phase fields instead of active contours. Secondly, we propose an inflection point long bar model to reduce the number of free parameters by 1 and show the improvement produced by this model for network extraction. Finally, we define the data energy term by testing two models, namely a multivariate Gaussian and a multivariate mixture of two Gaussians, and then formulate our primary overall model adapting ‘phase field HOACs’ to the problem of line network extraction from images; we study the robustness of the algorithm to the initialization despite the use of deterministic gradient descent.

Part 2: phase field HOACs for directed networks

Chapter 4: Firstly, we extend the phase field HOAC model of undirected networks introduced by [Rochery et al. \(2005\)](#), and analysed and improved in chapter 2. We incorporate into the model a second phase field function, in addition to the scalar phase field function representing a region by its smoothed characteristic function, which is a vector field representing the ‘flow’ through the network branches. The vector field is strongly encouraged to be zero outside, and of unit magnitude inside the region; to be smooth; and to have zero divergence. This prolongs network branches; controls width variation along a branch; and produces asymmetric junctions for which total incoming branch width approximately equals total outgoing branch width. In conjunction with a new interaction function, it also allows a broad range of stable branch widths. We analyze the Turing stability of both the background and the foreground in order to constrain the parameter values and avoid some undesirable configurations. Secondly, we show geometric evolutions to emphasize the purpose of the vector field and how it behaves in several situations and we apply this new model to the extraction of hydrographic networks from a synthetic image of a river and from a VHR remote sensing image.

Chapter 5: We analyse the stability of a network branch under the directed network model. We focus on zero-frequency perturbations of the region boundary, which correspond to changes in the branch width: we compute the energy of each term of the directed network model on a four-parameter family of *ansatzes* of a directed, straight, long bar. This places constraints on the parameter values of the model so that a network branch be stable to branch width changes.

Chapter 6: Firstly, we confirm the theoretical analysis studied in chapter 5 by numerical experiments. We show geometric evolutions of a long bar and a random configuration that evolve to stable network configurations where the width of their branches is equal to the branch width predicted by theory. We also describe a major advantage of the new directed

network model to solve the problem of occlusions in the network entity to be extracted, by closing the gaps and the broken edges thanks to the flow conservation property. Secondly, we apply the model on the problem of road and hydrographic network extraction from multi-spectral VHR Quickbird images.

Contributions

The main contributions of this thesis are as follows:

1. the analysis of the stability of a long bar under a HOAC model proposed by [Rochery et al. \(2006\)](#) (chapter 2),
2. the introduction of an inflection point long bar energy under a phase field HOAC model for undirected networks (chapter 3),
3. the application of the undirected network model on multi-spectral VHR Quickbird images for rural road network segmentation (chapter 3),
4. the study of the robustness of the algorithm to initialization (chapter 3),
5. the proposal of a new family of local prior phase fields for directed networks, and Turing stability (chapter 4),
6. the analysis of the stability of a directed, straight, long bar using a four-parameter family of *ansatzes* (chapter 5),
7. the application of the directed network model on multi-spectral VHR Quickbird images for road and hydrographic network segmentation (chapter 6).

Résumé en français

“A little knowledge that acts is worth infinitely more than much knowledge that is idle.”

— Gibran Khalil Gibran

Motivations et but

Pourquoi la reconnaissance d’objets visuels dans le monde réel est-elle difficile ? Une question intéressante à laquelle [Pinto et al. \(2008\)](#) avait essayé de répondre. La variation au niveau de l’image est au coeur de cette question difficile : chaque objet donné peut être présent dans un nombre infini d’images, où il apparaît avec différentes tailles, orientations, poses, illuminations, etc.

Le défi principal auquel nous nous sommes intéressés est l’extraction automatique d’objets spécifiques à partir d’images réelles. Dans ce contexte, ‘extraction’ signifie : ‘trouver la région R dans le domaine image qui “contient” l’objet’, où ‘contient’ signifie que R est la projection dans le domaine image du volume occupé par l’objet dans le monde réel. Notre intérêt principal est l’extraction de régions qui forment des réseaux linéiques à partir d’images de télédétection à très haute résolution (THR). La figure 4 montre deux images Quickbird THR multi-spectrales qui contiennent un réseau routier (haut) et un réseau hydrographique (bas). Ces images présentent plusieurs difficultés qui rendent le problème d’extraction très difficile. D’une part, les régions représentant le fond et le réseau ont plusieurs pixels qui ont des radiométries très similaires impliquant des zones de confusion si nous n’utilisons que des informations locales dérivant de l’image. D’autre part, le réseau visuel dans l’image apparaît avec plusieurs sauts dus aux occultations et à la présence de bruit (*e.g.* arbres, ponts, ombres, véhicules, etc). Par conséquent, la ‘forme’ de l’objet en question est nécessaire afin de pouvoir discerner l’objet du fond. Les méthodes et les techniques qui ne décrivent pas la forme d’un réseau sont donc totalement incapables de segmenter automatiquement un réseau à partir de ce type d’images.

Les réseaux directionnels (*e.g.* réseaux hydrographiques en imagerie de télédétection et réseaux vasculaires en imagerie médicale) possèdent un flux dans leurs branches. Cette



Figure 4: Deux images Quickbird multi-spectrales montrant (haut) un réseau routier à pleine résolution (0.61m), et (bas) un réseau hydrographique à 1/4 de la résolution originale (2.44 m). (Images originales ©DigitalGlobe, traitement CNES, images acquises via le programme d’Accompagnement OR-FEO.)

famille de réseaux a des propriétés géométriques caractéristiques qui sont considérablement différentes à celles des réseaux non-directionnels (e.g. réseaux routiers). Pour les réseaux directionnels, les branches tendent à se prolonger ; des branches différentes peuvent avoir des largeurs très différentes ; la largeur change lentement tout au long chaque branche ; aux jonctions, la somme des largeurs entrantes et celle des largeurs sortantes tendent à être similaires. (cf. la figure 5 pour un exemple de flux approximativement conservé dans un réseau directionnel). Bien sûr, nous pouvons trouver, mais pas fréquemment, des réseaux routiers qui satisfassent quelques unes des propriétés géométriques des réseaux directionnels, e.g. le réseau routier dans la figure 4 satisfait la propriété de conservation du flux en quelques jonctions et branches. Les propriétés géométriques spécifiques de la région d'intérêt rendent le problème plus difficile parce qu'elles devront être incorporées dans un modèle afin de favoriser de telles régions. De plus, la topologie d'une région d'un réseau est une difficulté majeure parce qu'elle est non-triviale et inconnue *a priori*. Concrètement, les topologies des réseaux sont très diverses, elles dépendent du nombre de composantes connexes et du nombre de boucles pour chacune d'elles (cf. la figure 5 pour un exemple de boucle).

Afin de résoudre le problème d'extraction automatiquement, des connaissances *a priori* sur les régions des réseaux ont besoin d'être incorporées dans des modèles mathématiques. Grenander et al. (1991) est le pionnier d'une approche bayésienne permettant l'incorporation des connaissances *a priori* de l'objet dans des modèles mathématiques. Mathématiquement parlant, nous cherchons à construire une distribution de probabilité *a posteriori*

$P(R|I, K)$, où I représente les données image et K contient les connaissances *a priori* de la région d'intérêt R (e.g. région d'un réseau dans notre cas) et la relation entre R et I . Cette distribution peut s'écrire, comme toujours, comme un produit d'une vraisemblance $P(I|R, K)$, et d'un *a priori* $P(R|K)$ qui incorpore des connaissances sur la forme de la région. Nous inférons donc la région R par estimation au sens du maximum *a posteriori* (MAP). (En pratique, nous manipulerons des log-probabilités négatives, i.e. une énergie totale $E(R; I, K)$ qui est la somme d'un terme de vraisemblance $E_I(I, R, K)$ et d'un terme *a priori* $E_P(R, K)$.)

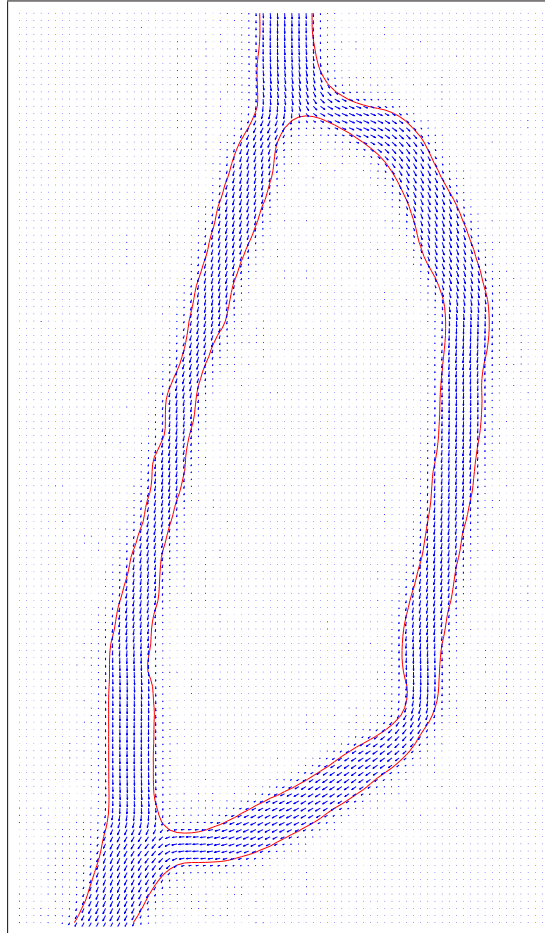


Figure 5: Un exemple de flux approximativement conservé dans un réseau directionnel.

Dans la littérature, beaucoup d'articles proposent l'incorporation des connaissances *a priori* de l'objet à extraire dans des modèles mathématiques. Un des modèles pionniers incorporant des connaissances *a priori* est le modèle des contours actifs (ou "snakes"), initialement introduit par Kass et al. (1988). Le modèle de snakes décrit des connaissances *a priori* génériques via des dépendances à courte-portée (locales) (voir figure 6, haut), qui assurent le lissage du contour de l'objet de la solution finale. Citons aussi les travaux antérieurs publiés dans (Geman and Geman, 1984; Ising, 1925) qui utilisent des connaissances de forme génériques. Après Kass et al. (1988), plusieurs travaux ont été introduits dans plusieurs domaines applicatifs. Cependant, presque tous sont insuffisants pour la segmentation automatique d'objets parce qu'ils incorporent des *a priori* de forme génériques, essentiellement sur le lissage du contour de l'objet qui nous renseigne en rien sur l'objet d'intérêt (e.g. objets de forme linéique dans notre cas). Beaucoup de travaux récents se sont donc focalisés sur l'incorporation d'*a priori* de formes spécifiques fondés sur les contours actifs. L'idée-clé de ces méthodes est de déterminer une région optimale décrite par des perturbations d'une ou plusieurs région(s) de référence. Autrement dit, la topologie de l'objet d'intérêt est contrainte d'être la même que celle des régions de référence. Cela ne convient pas à notre problématique, i.e. l'extraction de régions de réseaux linéiques, parce que la topologie d'un réseau est non-triviale et inconnue *a priori*. En conséquence, nous nous intéressons à la construction de modèles d'*a priori* de forme sans contraindre la topologie.

Dans (Rochery et al., 2006), un modèle des contours actifs d'ordre supérieur (CAOS) a été introduit afin d'incorporer des *a priori* de forme spécifiques sans contraindre la topologie. L'idée est d'introduire des dépendances à longue-portée entre les points du contour de la région d'intérêt (voir figure 6, bas) qui permettent de modéliser des régions de forme linéiques pour quelques valeurs des paramètres. Mais, l'algorithme utilisé pour résoudre le problème de minimisation souffre des difficultés majeures suivantes : liberté topologique 'automatique' insuffisante (il n'est pas possible de créer et contrôler les boucles d'un réseau), et l'algorithme est très lent du fait des dépendances à longue-portée. Une nouvelle formulation fondée sur les champs de phase a été donc introduite par Rochery et al. (2005) pour surmonter ces problèmes. De plus, il a été montré que le modèle de champ de phase est approximativement équivalent au modèle des CAOSs pour une région d'intérêt donnée (Rochery et al., 2005).

Le modèle de réseaux non-directionnels introduit par Rochery et al. (2005, 2006) permet une bonne extraction des réseaux routiers à partir d'images optiques à moyenne résolution, de zones rurales et semi-rurales où la largeur des routes est approximativement constante et relativement petite. Mais, il n'est pas adapté pour satisfaire les propriétés géométriques des réseaux hydrographiques parce qu'il contraint fortement le changement de largeur des branches du réseau. Les images à haute et très haute résolutions appor-

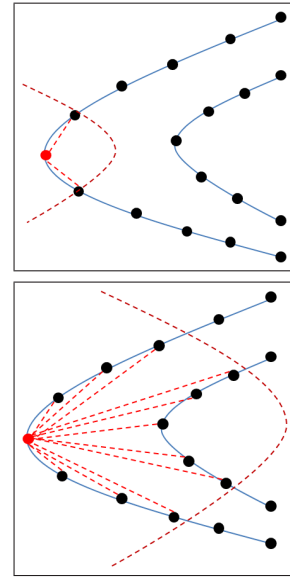


Figure 6: Dépendances courte-portées (haut) et longue-portées (bas). Les courbes et les liaisons en pointillées définissent respectivement la portée d'interaction et l'interaction entre deux points.

tent de nouveaux défis et de nouvelles difficultés. Peng et al. (2010) ont étendu le modèle de (Rochery et al., 2005, 2006) afin de favoriser les réseaux dont les branches tendent à être longues et droites. Le modèle a été appliqué avec succès à l'extraction de réseaux routiers à partir d'images haute résolution de zones urbaines, mais ce modèle n'est pas adapté aux réseaux hydrographiques parce que la rigidité des branches et le changement de largeur des branches sont fortement pénalisés.

L'extraction de réseaux routiers et hydrographiques est cruciale dans plusieurs domaines d'applications : mise à jour cartographique, navigation intelligente, gestion environnementale, gestion des désastres, hydrologie, agriculture, planification et gestion des territoires cultivés, gestion des ressources en eau, etc. Récemment, la quantité de données optiques THR disponibles (Quickbird, Ikonos, et dans le futur proche Pléiades) est devenu énorme et cela apporte de nouveaux défis. Les images THR montrent des réseaux routiers et hydrographiques sous forme de régions 2D dans le domaine image, contrairement aux images à basse et moyenne résolution où ces objets apparaissent comme des structures 1D. Les images THR fournissent beaucoup plus d'information sur les régions des réseaux et donc la précision d'extraction peut être nettement améliorée, en utilisant des techniques avancées.

Dans cette thèse, nous proposons de nouveaux modèles variationnels, fondés sur les CAOSs et les champs de phase, pour la modélisation de réseaux linéiques en général, et pour l'extraction de réseaux routiers et hydrographiques à partir d'images de télédétection THR en particulier.

En premier lieu, nous étudions l'analyse de la stabilité d'une barre longue non-directionnelle pour le modèle des CAOSs des champs de phase introduit par Rochery et al. (2005, 2006). Cela contraint les paramètres du modèle à des gammes de valeurs produisant des réseaux stables. Le résultat de l'analyse de stabilité est illustré par un 'diagramme de phase' qui met en évidence les différentes phases stables d'une longue barre. Par conséquent, nous pouvons choisir les valeurs des paramètres à partir du diagramme de phase et nous les utilisons pour l'extraction de réseaux non-directionnels à partir d'images de télédétection THR.

En second lieu, nous proposons une nouvelle famille de champs de phase pour des réseaux directionnels. Chaque branche d'un réseau directionnel possède une 'direction du flux', et en conséquence, chaque jonction possède des branches entrantes et des branches sortantes. L'existence d'un tel flux change, typiquement, la géométrie du réseau, parce que le flux est souvent *conservé* en quelques sortes. Ainsi, les branches tendent à se prolonger, parce que sinon cela impliquerait une perte brusque du flux, et les jonctions se composent souvent de branches entrantes ayant de faibles largeurs qui se joignent ensemble pour former des branches sortantes ayant des largeurs plus importantes, ou bien vice-versa. Notre but est l'extraction de réseaux hydrographiques à partir d'images de télédétection THR, mais le modèle est probablement pertinent pour d'autres applications impliquant des réseaux directionnels (e.g. réseaux vasculaires en imagerie médicale). Pour modéliser de tels réseaux, nous étendons le modèle de champ de phase non-local de réseaux non-directionnels de Rochery et al. (2005, 2006). En plus d'un champ de phase scalaire représentant une région par une version lisse de sa fonction caractéristique et interagissant non-localement pour favoriser des configurations de réseau, le modèle proposé contient un champ de phase vectoriel représentant le 'flux' dans les branches du réseau.

Organisation du manuscrit

Ce manuscrit est organisé comme suit :

Partie 1 : CAOSs des champs de phase pour des réseaux non-directionnels

Chapitre 1 : En premier lieu, nous décrivons un bref état-de-l'art des méthodes variationnelles pour la segmentation d'images. Nous nous focalisons sur les contours actifs et les *a priori* de formes. Deux classes des contours actifs sont mises en évidence : les méthodes basées contours et basées régions. En second lieu, nous rappelons les techniques les plus représentatives pour l'extraction de réseaux routiers et hydrographiques à partir d'images de différents types.

Chapitre 2 : Premièrement, nous rappelons brièvement le modèle des CAOSs introduit par [Rochery et al. \(2006\)](#), et nous montrons que ce modèle favorise deux configurations stables, à savoir des réseaux linéiques et des structures circulaires, pour différentes valeurs des paramètres. Deuxièmement, nous établissons une analyse de stabilité d'une barre longue via un développement en séries de Taylor jusqu'au second ordre du modèle des CAOSs au voisinage d'une barre longue. Ainsi, nous pouvons contraindre les valeurs des paramètres afin de modéliser des réseaux. Nous montrons des évolutions géométriques d'une barre longue en utilisant l'algorithme de descente de gradient pour valider l'analyse théorique. Finalement, nous développons en séries de Taylor le modèle des CAOSs jusqu'au second ordre au voisinage d'un cercle afin de trouver les gammes des valeurs de paramètres qui garantissent la stabilité des structures circulaires. Le résultat de l'analyse de stabilité aussi bien d'une barre longue que d'un cercle est illustré par un 'diagramme de phase'.

Chapitre 3 : Tout d'abord, nous rappelons brièvement le modèle des CAOSs des champs de phase pour des réseaux non-directionnels introduit par [Rochery et al. \(2005, 2006\)](#), nous montrons l'équivalence entre les contours actifs classiques et les champs de phase locaux, et nous montrons l'équivalence entre le terme des CAOSs et le terme non-local des champs de phase. Le résultat est que nous pouvons utiliser les champs de phase au lieu des contours actifs. Puis, nous proposons un modèle de point d'inflexion d'une barre longue pour réduire le nombre de paramètres libres par 1 et nous montrons l'amélioration de l'extraction de réseaux assurée par ce modèle. Enfin, nous définissons le terme d'énergie d'attache aux données en testant deux modèles, à savoir une gaussienne multivaluée et un mélange de deux gaussiennes multivaluées, ensuite, nous formulons le modèle total primaire en adaptant les 'champs de phase des CAOSs' au problème d'extraction de réseaux linéiques à partir d'images ; nous étudions la robustesse de l'algorithme à l'initialisation bien que nous utilisons une descente de gradient.

Partie 2 : CAOSs des champs de phase pour des réseaux directionnels

Chapitre 4 : En premier lieu, nous étendons le modèle des CAOSs des champs de phase pour des réseaux non-directionnels introduit par [Rochery et al. \(2005\)](#), et analysé et amélioré dans le chapitre 2. Nous incorporons dans le modèle une seconde fonction de champ de phase, en plus d'un champ de phase scalaire représentant une région par

une version lisse de sa fonction caractéristique, qui est un champ vectoriel représentant le ‘flux’ dans les branches du réseau. Le champ vectoriel est fortement favorisé afin d’être zéro à l’extérieur et de magnitude unitaire à l’intérieur de la région ; d’être lisse ; et à avoir une divergence nulle. Cela prolonge les branches du réseau ; contrôle les variations de largeur tout au long d’une branche ; et forme des jonctions non-symétriques dont la largeur entrante totale est approximativement égale à la largeur totale sortante. En conjonction avec une nouvelle fonction d’interaction, le modèle assure aussi une vaste gamme de largeurs de branches stables. Nous analysons la stabilité de Turing de l’extérieur et de l’intérieur afin de contraindre les valeurs des paramètres et d’éviter quelques configurations indésirables. En second lieu, nous montrons des évolutions géométriques pour mettre en évidence l’apport du champ vectoriel et son comportement pour différentes situations et nous appliquons ce nouveau modèle à l’extraction de réseaux hydrographiques à partir d’une image synthétique d’une rivière et d’une image de télédétection THR.

Chapitre 5 : Nous analysons la stabilité d’une branche d’un réseau dans le cas du modèle de réseaux directionnels. Nous nous focalisons sur les perturbations de fréquence zéro du contour d’une région, ce qui correspond aux variations de la largeur d’une branche : nous calculons l’énergie pour chaque terme du modèle de réseaux directionnels en utilisant une famille d’*ansatz* définie par quatre paramètres d’une barre longue, droite et directionnelle. Cela génère des contraintes sur les valeurs des paramètres du modèle pour qu’une branche d’un réseau soit stable aux changements de largeur de celle-ci.

Chapitre 6 : Tout d’abord, nous validons l’analyse théorique étudiée au chapitre 5 par des expériences numériques. Nous montrons les évolutions géométriques d’une barre longue et d’une configuration aléatoire vers des configurations de réseaux linéiques stables dont la largeur moyenne des branches est égale à la largeur prédite par la théorie. Nous décrivons aussi un avantage majeur du nouveau modèle de réseaux directionnels pour résoudre le problème d’occultations dans l’entité du réseau à extraire, en fermant les sauts grâce à la propriété de conservation du flux. Puis, nous appliquons le modèle au problème d’extraction de réseaux routiers et hydrographiques à partir d’images Quickbird THR multi-spectrales.

Contributions

Les contributions principales de cette thèse sont les suivantes :

1. l’analyse de stabilité d’une barre longue pour un modèle de type CAOSs proposé par [Rochery et al. \(2006\)](#) (chapitre 2),
2. l’introduction d’une énergie d’une barre longue de point d’inflexion pour un modèle des CAOSs des champs de phase pour des réseaux non-directionnels (chapitre 3),
3. l’application du modèle des réseaux non-directionnels sur des images Quickbird THR multi-spectrales pour la segmentation des réseaux routiers ruraux (chapitre 3),
4. l’étude de la robustesse de l’algorithme à l’initialisation (chapitre 3),

5. la proposition d'une nouvelle famille de champs de phase ayant un *a priori* local pour des réseaux directionnels, et l'analyse de Turing (chapitre 4),
6. l'analyse de stabilité d'une barre longue, droite et directionnelle en utilisant une famille d'*ansatz* à quatre paramètres (chapitre 5),
7. l'application du modèle des réseaux directionnels sur des images Quickbird THR multi-spectrales pour la segmentation des réseaux routiers et hydrographiques (chapitre 6).

Part I

Phase field HOACs for undirected networks

State-of-the-art

“Losers live in the past. Winners learn from the past and enjoy working in the present toward the future.”

— Denis Waitley

Contents

1.1	Introduction	18
1.2	Edge-based deformable contours	18
1.2.1	Parametric deformable models	18
1.2.1.1	Active contours: snakes	18
1.2.1.2	Balloon snakes	20
1.2.1.3	Topology adaptive snakes: T-Snakes	20
1.2.1.4	Gradient vector flow snakes	20
1.2.2	Geometric deformable models	21
1.2.2.1	Curve evolution theory	21
1.2.2.2	Level set method	22
1.2.2.3	Geometric active contours	23
1.2.2.4	Geodesic active contours	23
1.2.2.5	Area and length active contours	24
1.3	Region-based deformable contours	24
1.3.1	Mumford-Shah functional model	24
1.3.2	Region-based Bayesian inference	25
1.4	Shape priors	27
1.4.1	Reference shape-based models	27
1.4.2	Higher-order active contours and phase fields	29
1.4.2.1	Higher-order active contours	30
1.4.2.2	Phase fields	31
1.5	Line network extraction	32
1.5.1	Road network extraction	32
1.5.1.1	Active contours	32
1.5.1.2	Markov random fields and marked point processes	33
1.5.2	Hydrographic network extraction	34
1.5.2.1	Geometry of river networks	34
1.5.2.2	Fractal geometry	34
1.5.2.3	Digital elevation models	34
1.5.2.4	Multiscale and multiresolution analysis	34
1.6	Conclusion	35

This chapter gives a brief state-of-the-art for active contours, shape priors, and road and hydrographic network extraction from images. These three fields have a long history in the literature and a huge number of papers were published dealing with these issues. Here, we emphasize the most pioneering methods and techniques.

1.1 Introduction

Due to the insufficiency of low-level information, which uses only available features in the image, to solve problems in the real-world applications, high level information must be provided by users or experts in one way or another. High-level information abstracts the global behaviour of the system as opposed to low-level information which describes only local (individual) behaviour. Active contour-based methods are a way to describe high-level information and knowledge about the segmentation.

The framework of active contours aims to construct energy functionals which combine different energy terms, where each describes specific high-level information about the system and taken together they interact so as to satisfy global desiderata for the system. A solution of the system minimizes, globally or locally, the energy functionals. Active contours allow to segment an object from an image, and high-level information corresponds to the knowledge we have about the object in question.

According to the literature, active contour methods can be categorized into two families: *edge-based* and *region-based* approaches. These two approaches consider two families of methods: one which describes *generic* high-level information (without shape priors) and the other which describes *specific* high-level information (with shape priors).

In our work, we focus on road and hydrographic network extraction from remote sensing images. We highlight very briefly some of the most representative techniques in the literature which deal with these issues.

1.2 Edge-based deformable contours

Active contours are originally edge-based methods: the contour is pushed toward edges or boundaries of the object. Two classes of methods are involved: *parametric deformable* models and *geometric deformable* models. The former constructs energy functionals which depend on contour parametrization and while for the latter the functionals are not dependent (*i.e.* are invariant to re-parametrization). Geometric deformable methods have the advantage that they can be described implicitly via higher dimensional representations which we detail later on.

1.2.1 Parametric deformable models

1.2.1.1 Active contours: snakes

The original active contour (or snake) model was initially introduced by [Kass et al. \(1988\)](#). A region of interest $R \subset \Omega$, where Ω is the image domain, is described by its boundary ∂R . The region boundary ∂R is described by an embedding $\gamma : S^1 \rightarrow \Omega$ where S^1 is a

circle. The key idea consists of constructing an energy functional to be minimized over the set of curves parameterized by γ . The total energy incorporates a prior (internal) energy of the curve and a data (external) energy linking the curve to the image data: $E(\gamma) = E_P(\gamma) + E_I(\gamma)$. The internal energy is

$$E_P(\gamma) = \int_{S^1} ds \alpha |\dot{\gamma}(s)|^2 + \beta |\ddot{\gamma}(s)|^2, \quad (1.1)$$

where $\dot{\gamma}$ and $\ddot{\gamma}$ are the first and second derivatives of γ ; α and β are the weights of the first and second order terms respectively. The first order term controls the stretching (elasticity) of the curve making it acting like a membrane; the second order term controls the bending (rigidity) of the curve making it acting like a thin plate. The prior energy E_P ensures the smoothness of the region boundary ∂R during the minimization process.

The role of the external energy E_I is to attract the curve toward the desired object boundaries as well as other features of interest. It is computed by integrating a potential energy function P along the contour γ :

$$E_I(\gamma) = \int_{S^1} ds P(\gamma(s)).$$

To find edges within an image, the external force is taken to be $P(\gamma) = -\lambda |\partial I(\gamma)|^2$ where I is the image and λ is a positive parameter. So, if $E = E_P + E_I$ is minimized then the smoothed curve γ is pushed toward object edges where the magnitude of the gradient of the image, $|\partial I|$, is high. One can also choose $P(\gamma) = \lambda I(\gamma)$ which permits to push the curve toward dark locations.

To find the minimizing curve of the energy E , the deformable contour is made dynamic by treating γ as a function of time and we follow a Euler-Lagrange scheme (gradient descent algorithm):

$$\begin{aligned} \gamma_t(s, t) &= \frac{\delta E(\gamma(s))}{\delta \gamma(s)} \\ &= \alpha \ddot{\gamma}(s) - \beta \frac{\partial^2 \ddot{\gamma}(s)}{\partial s^2} + F(\gamma(s)). \end{aligned} \quad (1.2)$$

where $\gamma_t = \partial \gamma / \partial t$ and $F(\gamma) = -\partial P(\gamma(s))$ is the external force. The energy E is then minimized by placing an initial contour on the image domain and then deforming it by equation (1.2). The snake model has several advantages: the segmentation procedure unifies the image data, smoothing priors and initial estimation; the snakes converge to an energy minimum if initialized properly; and the capture range around features of interest can be relatively enlarged by the use of an external force incorporating a blurring effect of the original image.

On the other hand, the snake model suffers mainly of three limitations. Firstly, the external force vanishes rapidly around the features of interest which implies a very short capture range of the original snake: the initial contour must be carefully initialized by the user. Secondly, complex and noisy images produce features of interest (edges for example) leading to attract the contour to a local minimum which does not corresponds to the object of interest. Thirdly, the parametric (explicit) representation of the snake does not allow an automatic change of topology which is mandatory if the object of interest has, *a priori*, an unknown topology.

1.2.1.2 Balloon snakes

The internal force in the snake model tends to shrink the initial contour until it reaches the features of interest. Without the presence of the external force, the curve disappears. To remedy these problems, [Cohen \(1991\)](#) introduced the so-called ‘balloon’ model. The key idea is to add an inflation force which makes the curve behaves like a balloon. The curve is stopped when it meets a strong edge and it passes through if the edge is weak enough compared to the inflation force. The balloon model defines a modified external force $F(\gamma) = k_1 \hat{n} - k \frac{\partial P}{|\partial P|}$ where \hat{n} is the normal unit vector and weighted by the positive parameter k_1 . The parameter k_1 controls the inflation/deflation of the snake during the deformation process: it plays the same role as constraining of the area force of the snake interior. An extra energy term can be then constructed as $E_{\text{area}} = -k_1 \text{Area}(\gamma) = -k_1 \int dA$, measuring the area inside the region delimited by the contour γ . The balloon model enlarges the capture range due to inflation/deflation force which implies less sensitivity to initialization and less user guidance.

[Cohen and Cohen \(1993\)](#) improves the balloon model by defining an external force as a distance function from each point to its closest edge points in the image. In this case, the external force has large values everywhere in the image domain yielding to an enlarged capture range. A 3D generalization of the balloon model was introduced by [Cohen and Cohen \(1993\)](#), and solved the model by the use of the finite element method which speeds up the convergence and gives better stability.

1.2.1.3 Topology adaptive snakes: T-Snakes

The snake model does not allow automatic change of topology during the optimization process due to the explicit (parametric) representation of the contour. [McInerney and Terzopoulos \(1995, 2000\)](#) constructed a set of rules for topology changes to be used during balloon model deformation. The snakes are defined in terms of an affine cell image decomposition (ACID). During the contour deformation under the influence of external and internal forces, the model is reparametrized by a new set of nodes and elements by efficiently computing the intersection points of the contour with the ACID lattice. This method allows to distinguish between the interior and exterior regions. By doing this, the snake may merge and split by connecting and disconnecting the contour.

1.2.1.4 Gradient vector flow snakes

The pressure (balloon) force ([Cohen, 1991](#); [Cohen and Cohen, 1993](#)) permits to remedy the problem of contour initialization by the enlarged capture range. However, the pressure force is constrained to not be neither very strong nor very low as described so far. This makes the balloon model not able to push the contour toward concave boundaries. [Xu and Prince \(1997\)](#) introduced a new external force, called Gradient Vector Flow (GVF), to solve relatively the issues of contour initialization and concave boundaries. The GVF is computed as a diffusion of the gradient vectors of a gray-level or binary edge map derived from the image. The external force F in (1.2) is replaced by the GVF. The GVF field is defined to be the vector field $\mathbf{v}(x, y) = (u(x, y), v(x, y))$, where x and y are the Cartesian

coordinates, that minimizes the energy functional

$$E(\mathbf{v}) = \iint dx dy \mu(u_x^2 + u_y^2 + v_x^2 + v_y^2) + |\partial f|^2 |\mathbf{v} - \partial f|^2, \quad (1.3)$$

where u_x, u_y, v_x and v_y are the first derivatives of the vector field \mathbf{v} which is constrained to be smooth. If $|\partial f|$ is small, the energy is dominated by partial derivatives of the vector field, yielding a smooth field. On the other hand, when $|\partial f|$ is large, the second term dominates the integrand, and is minimized by setting $\mathbf{v} = \partial f$. Equation (1.3) is minimized following Euler-Lagrange scheme:

$$\begin{aligned} u_t &= \mu \partial^2 u - (u - f_x) |\partial f|^2, \\ v_t &= \mu \partial^2 v - (v - f_y) |\partial f|^2, \end{aligned}$$

where f_x and f_y are the first derivatives of f . The converged GVF field \mathbf{v} replaces then the external force F in equation (1.2). Other attempts based on GVF snakes were proposed by (Cheng and Foo, 2006; Tang et al., 2004; Wei et al., 2004; Xu and Prince, 1998) to enlarge the capture range for better object boundary detection.

Independently, Li and Acton (2008) provided a new method to automatically initialize the active contour model by estimating the underlying external energy field using the solution of Poisson's equation. The proposed method selects an initial model with an associated energy that approaches the minimum energy. This novel method accelerates active contour model convergence and improves performance by initializing the active contour model close to features of interest.

Bauer et al. (2009) proposed an automated approach for the segmentation of airways in Computed Tomography (CT) datasets. The approach is based on GVF and consists of two main processing steps. Initially, airway-like structures are identified and their centerlines are extracted. These centerlines are used in a second step to initialize the actual segmentation of the corresponding airways.

1.2.2 Geometric deformable models

Parametric deformable methods have a major limitation, due to the explicit representation of contours, which is the automatic change of topology in an efficient and fast manner. To overcome this problem, geometric deformable models are initially introduced by (Caselles et al., 1993; Malladi et al., 1995) and provide an automatic method to handle topological changes using the curve evolution theory (Alvarez et al., 1993; Sapiro, 2001; Sapiro and Tannenbaum, 1993) and level set method (Osher and Sethian, 1988; Sethian, 1996, 1999).

1.2.2.1 Curve evolution theory

Parametric deformable methods describe curves by quantities which depend on parameters such as the derivatives of an arbitrary parametrized curve. Curve evolution theory aims to study curve deformations using only geometric quantities like the unit normal vector and curvature. An example of such a deformation process is provided by the following system:

$$\gamma_t = F(\kappa) \hat{\mathbf{n}}, \quad (1.4)$$

where $F(\kappa)$ is the speed of curve evolution; κ is the curvature computed at each contour point; and \hat{n} is the inward unit normal of the curve. We give two examples of the speed function F , which are the most used in many application domains.

Firstly, the curvature deformation which is described by the so-called geometric heat equation obtained by using $F = \alpha\kappa$ where α is a positive parameter. The evolution system smooths the curve and shrinks it (Grayson, 1989). The curvature deformation has a similar effect to the elastic internal force in the parametric deformable model. Secondly, the constant deformation which is given by the use of a constant speed function $F = F_0$. The constant deformation plays the same role as the pressure force in the balloon model.

The implementation of geometric deformable models is made using level set methods and a great amount of work has investigated the construction of the speed function in order to solve a particular problem.

1.2.2.2 Level set method

Evolving curves using level sets was initially introduced by Osher and Sethian (1988). The curve ∂R (*i.e.* the region boundary) is described implicitly as a level set of a 2D scalar function, ϕ , (*i.e.* the level set function) defined in the image domain Ω : $\phi : \Omega \rightarrow \mathbb{R}$. The curve is then defined by the set of points in Ω which have a zero level set: $\partial R = \{x \in \Omega | \phi(x) = 0\}$. The curve deformation is controlled by the deformation of the level set function $\phi(x, t)$ during the time t .

Level set methods have many advantages: natural handling of topology changes (splitting and merging of contours), cusps, and corners as ϕ evolves; using fast narrow band adaptive techniques, the computational complexity is the same as other methods, with the advantages of increased accuracy and robust modelling; higher-dimension level set functions are reasonably easily treated.

On the other hand, level set methods have also some drawbacks: increasing the dimensionality of the original curve induces greater computational complexity; the algorithm is very slow because the level set function needs to be initialized and updated to be a distance function during the evolution process.

Now we represent, in the level set framework, the curve evolution equation (1.4) of the curve ∂R . Let $\phi(x, t)$ being the zero-level set function of the contour $\gamma(s, t)$: $\phi(\gamma(s, t), t) = 0$. Differentiating the latter equation and using the chain rule, one can get

$$\phi_t + \partial\phi \cdot \gamma_t = 0, \quad (1.5)$$

where ∂ is the gradient of a scalar 2D function. Assuming that $\phi < 0$ inside the zero-level set and $\phi > 0$ outside, the inward unit normal vector to the level set curve is $\hat{n} = -\frac{\partial\phi}{|\partial\phi|}$. Using equation (1.4), we can rewrite equation (1.5) as

$$\phi_t = F(\kappa)|\partial\phi|, \quad (1.6)$$

where the curvature is given by

$$\kappa = \operatorname{div} \left(\frac{\partial\phi}{|\partial\phi|} \right) = \partial \cdot \frac{\partial\phi}{|\partial\phi|} = \frac{\phi_{11}\phi_2^2 - 2\phi_1\phi_2\phi_{12} + \phi_{22}\phi_1^2}{(\phi_1^2 + \phi_2^2)^{3/2}},$$

where ϕ_i and ϕ_{ij} are the first and second derivatives with respect to Cartesian coordinates labeled by $i, j \in \{1, 2\}$. A common choice of the level set function ϕ is the signed distance

function from each point of the grid to the zero level set: $\phi(x) = d(x, \partial R)$. That constraint must be checked and satisfied for the initial curve, and at every few iterations during the evolution process because it can be violated (Adalsteinsson and Sethian, 1999; Sethian, 1999).

1.2.2.3 Geometric active contours

Caselles et al. (1993) introduced a geometric active contour model based on the curve evolution theory and level set method. The model takes the following form:

$$\phi_t = g(|\partial I|)(\kappa + F_0)|\partial\phi| ,$$

where g is a general edge detector, $g : \mathbb{R}^+ \rightarrow \mathbb{R}^+$ such that g being a strictly decreasing function and $g(r) \rightarrow 0$ as $r \rightarrow \infty$, which can take the form

$$g(|\partial I|) = \frac{1}{1 + |\partial(G * I)|} ,$$

where $G * I$ is the convolution of the image I with the Gaussian G . If $F_0 > 0$ then the curve shrinks and if $F_0 < 0$ then the curve expands. The multiplicative term $g(|\partial I|)$ permits to stop the curve evolution when edges, *i.e.* high gradients, are met. This model can work well if g is very close to 0, *i.e.* when objects have good contrast, which is not the case in practice if one is dealing with complex images.

Kichenassamy et al. (1995) analyzed the geometric active contour model from a curve evolution point of view and proposed some modifications based on gradient flows relative to certain new feature-based Riemannian metrics. The feature of interest is considered to lie at the bottom of a potential well which leads to a more efficient attraction of the curve to the desired feature.

1.2.2.4 Geodesic active contours

To remedy the problem of the geometric active contour model, Caselles et al. (1997) proposed an extension of it called geodesic active contour model. The proposed approach is based on the relation between active contours and the computation of geodesics or minimal distance curves which lay in a Riemannian space whose metric is defined by the image content. It has been proved that the minimization of a simplified snake model without the second order term is equivalent to the minimization of the length of the contour multiplied by an edge detector. Previous models of geometric active contours are improved, allowing stable boundary detection when their gradients suffer from large variations, including gaps. The contour evolution equation is

$$\gamma_t = g(|\partial I|)(\kappa + F_0) \hat{n} - (\partial g \cdot \hat{n}) \hat{n} ,$$

and the level set implementation is

$$\phi_t = g(|\partial I|)(\kappa + F_0)|\partial\phi| + \partial g \cdot \partial\phi ,$$

The constant velocity F_0 pushes the curve inwards (or outward) and it is crucial in the above model in order to allow convex initial curves to capture non-convex shapes. Often

in real images, the function g has different, non-zero values at different locations along the boundaries. The second term allows to stop the curve to the boundaries of the objects specially when gradient values include gaps. Other attempts to solve a similar problem were studied by (Kichenassamy et al., 1996; Yezzi et al., 1997).

Paragios et al. (2004) combined the geodesic active contour flow and the gradient vector flow external force for snakes. The resulting motion equation is considered within a level set formulation. The flow implementation exhibits robust behaviour and has fast convergence rate.

Reinbacher et al. (2010) proposed an anisotropic weighted total variation energy with an additional global volume constraint to segment thin and elongated structures like articular cartilage directly in 3D. This approach is an extension of the geodesic active contour model. The volume constraint defines a minimum size for the resulting segmentation. The segmentation model works interactively, allowing the user to incorporate prior knowledge into the segmentation process and correct the segmentation results. The model is solved in a globally optimal manner, and the algorithm is faster compared to manual segmentation methods.

1.2.2.5 Area and length active contours

Siddiqi et al. (1998) used the geodesic active contour model and added to it a new area term weighted by the edge detection function. The new weighted contour length and contour interior area framework enforces and improves the attraction of the contour toward the desired object boundary. The convergence of the new model is faster than the geodesic active contour model. The level set implementation is (Siddiqi et al. (1998))

$$\phi_t = \alpha \{g(|\partial I|)\kappa|\partial\phi| + \partial g \cdot \partial\phi\} + \frac{1}{2} (\partial \cdot (x\phi)) |\partial\phi| ,$$

where α is a positive factor in order to make the units compatible; $x\phi = (x_1\phi, x_2\phi)$ and $x = (x_1, x_2) \in \Omega$.

1.3 Region-based deformable contours

Edge-based deformable models described so far use local edge information to attract the active contour toward the object boundaries. This approach describes the data near the region boundary; and it fails to distinguish between the interior and the exterior of regions, and thus spatial information about pixel is lost except when the pixels are close to an edge or a boundary. Region-based models overcome these limitations by identifying each region of interest by the use of certain global region features to guide the motion of the active contour. The regions are described by statistical features such as the intensity, color, histogram, texture, or motion.

1.3.1 Mumford-Shah functional model

Mumford and Shah (1985, 1989) introduced an optimal approximation of an image as a partition of regions of piecewise smooth intensities in order to solve the segmentation problem. In a variational formulation, for a given image I , the sought solution $(u, \partial R)$ is

defined such that u is a piecewise smooth approximation of the image I and the boundary ∂R is a 1D subset of edges. The energy functional takes the following form

$$E(u, \partial R) = \int_{\Omega} (u(x) - I(x))^2 dx + \lambda \int_{\Omega \setminus \partial R} |\partial u|^2 dx + \mu L(\partial R),$$

where $L(\partial R)$ is the length of the region boundary ∂R . The first term encourages u to be an approximation of the image I ; the second term makes u smooth within each disjoint region; and the third term enforces the boundary ∂R to have minimal length. Thus, the minimizing function u is a piecewise smooth approximation of the image I . Two problems are then combined within the same functional: image denoising and segmentation. In the case of the latter, the boundary ∂R defines a partition of the image domain Ω into disjoint regions Ω_i , *i.e.* $\Omega = \bigcup_i \Omega_i$, where each is approximated by a smooth function $u_i : \Omega_i \rightarrow \mathbb{R}$.

A cartoon model can be derived from the above functional by considering $\lambda \rightarrow \infty$ which leads to the function u being a piecewise constant function (Mumford and Shah, 1989). The cartoon model takes the form

$$E(u, \partial R) = \sum_i \int_{\Omega_i} (u_i - I(x))^2 dx + \mu L(\partial R),$$

where in this case u_i is a constant value. The spatially discrete form is related to Potts model (Potts, 1952). In the case of a binary segmentation ($i \in \{1, 2\}$), the discrete version was introduced by (Ising, 1925; Lenz, 1920) for modelling ferromagnetism.

Chan and Vese (2001a) proposed a binary segmentation deriving from the Mumford-Shah model. In this case, the approximation u is reduced to two values measuring the average of I in the interior and exterior of the segmented region. The level set derivation of the energy functional has this form

$$E(\phi, c_{\text{in}}, c_{\text{out}}) = \int_{\Omega} dx \left\{ \mu |\partial H \phi(x)| + \lambda_{\text{in}} (I(x) - c_{\text{in}}(\phi(x)))^2 H(\phi(x)) \right. \\ \left. + \lambda_{\text{out}} (I(x) - c_{\text{out}}(\phi(x)))^2 (1 - H(\phi(x))) \right\},$$

where H is the Heaviside function; c_{in} and c_{out} are the averages of I inside and outside the evolving contour. This formulation does not constrain the initial curve to be close to object boundaries or edges as opposed to edge-based approaches because the evolution of the curve depends on the statistics of the interior and exterior of the regions and not just on the object boundaries.

Chan and Vese (2001b) generalized the active contour model without edges in (Chan and Vese, 2001a) by considering a piecewise smooth function instead of a constant function, allowing to model the intensity inside each region. Vese and Chan (2002) extended the work in (Chan and Vese, 2001b) to a multiphase level set framework for image segmentation. The key idea is to define different level set functions to represent the region boundaries. This formulation overcomes the problems of vacuum and overlap; it needs only $\log_2 n$ level set functions for n phases in the piecewise constant case; complex topologies are easily represented; and two level set functions are sufficient to describe any partition using the Four-Color Theorem (Appel and Haken, 1996).

1.3.2 Region-based Bayesian inference

The segmentation problem is in general very hard. Prior knowledge K about the region of interest R is then provided in one way or another to efficiently segment a given image I . A probabilistic approach can be adopted to deal with this problem.

Let \mathcal{R} , \mathcal{J} and \mathcal{K} being the set of all possible regions, images and knowledge respectively. Using the Bayes' theorem, we can construct a posterior probability $P(R|I, K)$ as

$$P(R|I, K) = \frac{P(I|R, K)P(R|K)}{P(I|K)},$$

where $P(I|R, K)$ is the likelihood probability of the image data I given R and K , and $P(R|K)$ is the *a priori* probability of the region of interest R given the knowledge K . The former links the region to the image data. To solve the problem of segmentation, a *loss function* $L : \mathcal{R} \times \mathcal{R} \rightarrow \mathbb{R}$ is then needed. In general we want to find the region \hat{R} that minimizes the value

$$\langle L(\hat{R}) \rangle = \int_{\mathcal{R}} dR L(\hat{R}, R)P(R|I, K).$$

Apart from some special cases, where one can use special loss functions (Jermyn, 2000), in general in the absence of any information except the preconditions for probability theory, the delta function is the only

obvious loss function, $L(\hat{R}, R) = -\delta(\hat{R}, R)$. So, the above equation becomes $\langle L(\hat{R}) \rangle = -P(\hat{R}|I, K)$, and minimizing the mean loss function L is then equivalent to maximizing the *a posteriori* probability:

$$\hat{R} = \arg \max_{R \in \mathcal{R}} P(R|I, K).$$

This is the so-called maximum *a posteriori* (MAP) estimate. In practice, we will deal with negative log-probabilities, *i.e.* a total energy $E(R; I, K)$ that is the sum of a likelihood term $E_I(I, R, K)$ and a prior term $E_P(R, K)$. We then end up with an energy minimization problem:

$$\begin{aligned} \hat{R} &= \arg \min_{R \in \mathcal{R}} E(R; I, K) \\ &= \arg \min_{R \in \mathcal{R}} E_I(I, R, K) + E_P(R, K). \end{aligned}$$

This probabilistic formulation of the region-based segmentation problem was adopted in many papers (Ben Ayed et al., 2006; Besag, 1986; Geman and Geman, 1984; Ising, 1925; Jehan-Besson et al., 2003; Leclerc, 1989; Paragios and Deriche, 2002a; Tsai et al., 2001). We refer to Cremers et al. (2007) for a more complete review of statistical approaches to level set segmentation.

Zhu and Yuille (1996) described an equivalence between the Mumford-Shah functional in the case of cartoon model and the Bayesian MAP estimate. Brox and Cremers (2009) completed the study in (Zhu and Yuille, 1996) to the case of piecewise smooth approximations and showed that the Mumford-Shah functional can be interpreted as a first order approximation of a specific MAP estimate, where pixel intensities are not, as usual, identically distributed but where the distribution varies with the position in the image.

(Paragios and Deriche, 2002a, b) introduced a new framework to deal with frame partition problems in computer vision: geodesic active region model. The idea is to combine an edge-based functional deriving from the geodesic active contour model (Caselles et al., 1997) and a region-based Bayesian inference deriving from a MAP estimate. The minimizing curves are constrained: to be regular and smooth; to be attracted by the boundary points (edge-based information); and to create a partition that is optimal according to the expected region properties of the different hypotheses (region-based information). Paragios and Deriche (2002a) made two assumptions to simplify the problem: the contours are equiprobable; and there is no correlation between the regions labeling, and all the pixels within each region are identically and independently distributed. The geodesic active region functional, to be minimized, is

$$E(\partial R) = - \int_{\Omega_{\text{in}}} \ln(P_{\text{in}}(I(x))) dx - \int_{\Omega_{\text{out}}} \ln(P_{\text{out}}(I(x))) dx + \mu L(\partial R) ,$$

where P_{in} and P_{out} are the likelihood probabilities of the interior and exterior of the contour ∂R . The level set representation of the evolution equation takes the form

$$\phi_t = \left\{ \ln \frac{P_{\text{out}}(I)}{P_{\text{in}}(I)} + \mu\kappa \right\} |\partial\phi| .$$

In (Paragios and Deriche, 2002a), the likelihood probabilities follow the normal distribution and their parameters are learnt in advance in a supervised way. Rousson (2004) also used normal distributions to model the likelihoods, but the parameters are dynamically calculated during contour evolution. Using the form of the Heaviside function in the Chan-Vese model, the level set representation of the evolution equation is

$$\phi_t = \left\{ - \frac{(I - c_{\text{in}}(\phi))^2}{2\sigma_{\text{in}}^2(\phi)} + \frac{(I - c_{\text{out}}(\phi))^2}{2\sigma_{\text{out}}^2(\phi)} + \frac{1}{2} \ln \frac{\sigma_{\text{out}}^2(\phi)}{\sigma_{\text{in}}^2(\phi)} + \mu\kappa \right\} \delta(\phi) ,$$

where the parameters c_{in} , c_{out} , σ_{in}^2 and σ_{out}^2 are updated at each iteration using their explicit expressions given in (Chan and Vese, 2001a; Rousson, 2004).

1.4 Shape priors

So far, we have reviewed the pioneering active contour methods, whether edge-based or region-based, which drive curve evolution based on information (*e.g.* intensity, color, texture, motion) from the image, and having some regularization terms to ensure the smoothness of the region boundary during the evolution process. In real-world applications, the image quality is often degraded by noise or partial occlusion; or the contrast between the object and the background is low. This makes these methods unsuccessful because of the lack of prior information they contain about the object to be segmented. Grenander et al. (1991) is the pioneer of the idea that a Bayesian approach allows the incorporation of sophisticated and specific shape priors of the object into the model. As a result, there has been a great deal of work on models incorporating more sophisticated shape knowledge or information.

1.4.1 Reference shape-based models

One category of shape priors is based on reference shapes. The key idea is to seek a region which has a ‘similar’ shape to the reference region(s). Most of this work models an ensemble of regions as perturbations of one or more reference region(s) (Chen et al., 2001, 2002; Cohen and Cohen, 1996; Cootes and Taylor, 1992; Cremers, 2007, 2008; Cremers and Soatto, 2003; Cremers et al., 2001, 2002, 2003, 2006; Foulonneau et al., 2003; Gastaud et al., 2004; Klassen et al., 2004; Leventon et al., 2000; Riklin Raviv et al., 2004, 2007; Rousson and Paragios, 2002; Srivastava et al., 2003; Staib and Duncan, 1992; Székely et al., 1996; Tagare, 1997; Taron et al., 2009; Vaillant et al., 2004; Vinson et al., 2001; Yuille et al., 1992). This is a very flexible approach, and it works well for many applications. We will recall some of this work in the following.

Cohen and Cohen (1996) introduced a hybrid hyperquadric model by describing implicitly some local features in a global shape model. It incorporates global and local properties of the shape by means of its parameters, independently of the resolution of the data.

Leventon et al. (2000) extended geodesic active contours (Caselles et al., 1997; Kichenassamy et al., 1995) by incorporating shape information into the evolution process. A statistical shape model over a training set of curves is firstly constructed by the use of principal component analysis (PCA). PCA is applied to a set of shapes described by signed distance functions. The result is then the derivation of the most significant modes of shape deformations. The segmentation procedure is performed in two steps: the active contour is evolved both locally, based on image gradients and curvature, and globally to a MAP estimate of shape and pose. The latter contains the influence of the shape information.

Chen et al. (2001, 2002) introduced a model which incorporates shape priors in geometric active contour models. Their model differs from the model introduced by Leventon et al. (2000) because they use a non-probabilistic approach. The key idea is to deform a geometric active contour with a vector field that it derives from the shape prior. The shape prior takes the form

$$E_P(\gamma, T) = \int_{S^1} d^2(T(\gamma(s))) |\dot{\gamma}(s)| ds$$

where $d(x) = d(\gamma^*, x)$ measures the distance of the point x to the shape template γ^* and T is scale, translation and rotation transform. The model incorporates an edge-based data term which makes it sensitive to initialization.

Cremers et al. (2001) introduced a model which incorporates statistical shape knowledge based on the Mumford-Shah functional. The contour is described explicitly as a closed spline curve. A set of training shapes is used to construct a prior shape model by describing the spline control point vectors by a Gaussian probability distribution. This shape energy term is then added to the Mumford-Shah energy functional. The spline representation describes a shape efficiently but topology change is constrained.

Rousson and Paragios (2002) proposed a model that incorporates global/local shape properties of the object of interest. Firstly, the model is constructed directly in the level set representation using a set of samples. The shape prior energy is defined, in the level set formulation, as

$$E_P(\phi, T, s) = \int_{\Omega} \left\{ \frac{(s\phi(x) - \phi_M(T(x)))^2}{2\sigma_M^2(T(x))} + \ln(\sigma_M(T(x))) \right\} H(\phi(x)) dx ,$$

$\phi_M(x)$ and $\sigma_M^2(x)$ are a representative shape and a confidence map respectively; T and s are a transformation and a scalar factor. The first term minimizes the distance between the evolving surface and the shape model, and the second term penalizes parts of the shape with low confidence.

The work in (Rousson and Paragios, 2002) has the following drawbacks. Firstly, the energy integral is restricted to the positive part of the level set function yielding a bias toward small shapes. Secondly, the dissimilarity distance incorporated into the model is not symmetric. A symmetric distance was proposed by Cremers and Soatto (2003) to overcome these limitations:

$$E_P(\phi, T) = \int_{\Omega} (\phi(x) - \Psi_0(T(x)))^2 \left[\frac{h(\phi(x)) + h(\psi_0(T(x)))}{2} \right] dx ,$$

where h is the normalized Heaviside function. This symmetric pseudo-distance measures dissimilarities and averages the squared deviation of shapes over both areas $\phi(x)$ and $\Psi_0(T(x))$; Ψ_0 is the reference shape. The proposed distance measure has two advantages: first it is symmetric and second it does not depend on object area due to the normalization.

Riklin Raviv et al. (2004) proposed a new model which incorporates a single prior image and developed a variational segmentation framework which is pose invariant. The key idea is the special form of the shape prior and the integration of the projective transformations via unlevelled sections. Prior knowledge is represented by a generalized cone, which is constructed based on the known instance of the object contour. The level set function and the projective transformation parameters are estimated in alternation by minimization of the energy functional. The proposed shape prior measures a distance between a planar section of the generalized cone and the zero-crossing of the evolving level set function. Riklin Raviv et al. (2007) introduced an algorithm to generalize the previous work to an eight-parameter projectivity model.

Rousson and Paragios (2007) introduced a 3D-wise probabilistic level set formulation to account for prior knowledge and to address the problem of similarity invariant shape constraint. The major difference between this work and (Rousson and Paragios, 2002) is that the latter measures similarity between the evolving level set and the shape model, and the former between the evolving level set and the image. The pose parameters are derived guided only by the image data, which makes the algorithm much faster and allows robust estimation of parameters.

The methods listed so far are static in time. Cremers (2006) introduced temporal statistical shape models. The authors constructed a shape probability, at a given time, which depends on the shapes observed in the past. The dynamical shape model is based on a Bayesian formulation using level set representation. The governing equation deforms the interface by utilizing both the radiometric information of the current image as well as a dynamical shape prior which uses the segmentations obtained by the preceding frames. The image energy term is taken to be

$$E_I(\alpha_t, \theta_t) = \int \left\{ \left(\frac{(I_t - \mu_1)^2}{2\sigma_1^2} + \ln \sigma_1 \right) H\phi_{\alpha_t, \theta_t} + \left(\frac{(I_t - \mu_2)^2}{2\sigma_2^2} + \ln \sigma_2 \right) (1 - H\phi_{\alpha_t, \theta_t}) \right\} dx ,$$

where $\phi_{\alpha_t, \theta_t} \triangleq \phi_0(T_{\theta_t}x) + \alpha_t^t \psi(T_{\theta_t}x)$; T is a transformation; ϕ_0 denote the mean shape of a temporal sequence of training shapes (ϕ_1, \dots, ϕ_n) ; $\psi = (\psi_1, \dots, \psi_n)$ is the set of the first n eigenmodes obtained by PCA; and θ_t is the transformation parameters. The dynamical shape model takes the form

$$E_P(\alpha_t, \theta_t) = \frac{1}{2} \mathbf{v}^t \Sigma^{-1} \mathbf{v} ,$$

where $\mathbf{v} = \alpha_t - \boldsymbol{\mu} - A_1 \hat{\alpha}_{t-1} - A_2 \hat{\alpha}_{t-2}$: the shape vectors α_t of a sequence of level set functions are approximated by a Markov chain of second order. $\boldsymbol{\mu}$ is the mean vector of the noise and A_i are the transition coefficients. (Cremers, 2007, 2008) extended the work in (Cremers, 2006) and constructed a nonlinear dynamical shape prior. A mixture of autoregressive models was used to approximate the temporal evolution of the eigenmodes of the level set function.

1.4.2 Higher-order active contours and phase fields

The family of reference shape-based prior models referred in the previous section has shown its success in efficiently segmenting objects from images and sequences of images in many real-world application domains. Multi-component shapes are handled naturally by level set representations where splitting and merging are allowed during the evolution process. This family of models constrains the topology of the region sought to be similar to that of the reference region(s).

However, in many real-world application domains, the region sought can have arbitrary topology (*e.g.* if the entity consists of an unknown number of similar objects). In this case, the sought region (or shape) cannot be described by perturbations around a finite number of points in the space of regions. So, reference shape-based prior models are not appropriate for this problem because they assume that the topology is known *a priori*.

One particular problem that falls into this new category of objects (*i.e.* that have unknown topology) is the extraction of ‘network’-shaped regions (*i.e.* regions composed of branches that join together at junctions), *e.g.* road or hydrographic networks in remote sensing images, or vascular networks in medical images. Such network regions may have several connected components and may be multiply connected, *i.e.* may have many loops. A second problem is tree crown extraction from images where the number of trees is unknown *a priori*, which makes the topology of the region unknown too.

As a result, a new generation of active contours incorporating specific and sophisticated shape priors is introduced: higher-order active contours (HOACs) embedded in a phase field framework.

1.4.2.1 Higher-order active contours

HOACs were introduced by Rochery et al. (2006) in order to incorporate sophisticated and specific shape priors without constraining topology, as opposed to reference shape-based models. This new generation of active contours incorporates non-trivial shape information about the region being modelled via explicit long-range interactions between region boundary points, thereby removing the need for reference regions. In addition to boundary

smoothing terms, a long-range interaction term is added:

$$E_P(R) = \lambda L(R) + \alpha A(R) - \frac{\beta}{2} \iint_{(S^1)^2} ds ds' \dot{\gamma}(s) \cdot \dot{\gamma}(s') \Psi \left(\frac{|\gamma(s) - \gamma(s')|}{d} \right),$$

where R is a region (*i.e.* shape) in the image domain; L is region boundary length; A is region area; γ is an arbitrary parametrization of the boundary of R ; $\dot{\gamma}$ is its derivative, *i.e.* the tangent vector field; $\Psi(z)$ defines the interaction between two boundary points separated by a distance zd where d is the interaction range. The long-range interactions described by the quadratic term (*i.e.* the third term) are responsible for the prior shape information: they favour parallel (anti-parallel) tangent vectors when the inner product is positive (negative). The presence of HOAC term penalizes a large number of false contour configurations, and eliminates many local energy minima, thanks to the incorporation of more sophisticated prior knowledge. HOACs are more robust to noise than conventional active contours, do not require estimation of the pose of the shape, and permit a generic initialization.

The HOAC prior energy defined by [Rochery et al. \(2006\)](#) was used to model network-shaped regions. However, it was soon discovered that it could be used to model other families of regions too, notably a ‘gas of circles’ (regions composed of an arbitrary number of approximate circles) introduced by [Horvath et al. \(2009\)](#), simply by varying the model parameters.

The contour representation suffers from a number of drawbacks, both for classical active contours in general, and for HOACs in particular:

- an initial region, as with other active contour approaches, is needed for the gradient descent algorithm. Although the inclusion of more specific prior knowledge means that a generic, hence automatic initialization can be used, the final result still depends on this choice;
- a level set representation is used to perform the gradient descent evolution, and this does not enable the formation of handles (loops). Road networks, for instance, can have a complex topology with many handles, and the choice of initialization affects which of these are detected. This is a serious drawback in our work because we focus on road and hydrographic network extraction from images;
- the quadratic term produces nonlocal forces, whose evaluation requires boundary extraction and integration followed by velocity extension at each iteration of the algorithm, and this is very time consuming.

To overcome these drawbacks, [Rochery et al. \(2005\)](#) reformulated HOACs as nonlocal ‘phase fields’ for network modelling. In chapter 3, we will recall this model.

1.4.2.2 Phase fields

The phase field framework has a long history in physics for modelling many phenomena. We refer to ([Chen, 2002](#); [Gonzalez-Cinca et al., 2003](#); [Thornton et al., 2003](#)) for reviews of some of the phase field methods existing in the state-of-the-art. Suppose the following physical phenomenon: an interface moving with a velocity proportional to the gradient

of some field (*e.g.* temperature, pressure...). This leads to a problem of non-equilibrium pattern formation during the deformation. The interface evolves in time and space, making the problem hard to solve analytically. Phase field models are an alternative solution. They describe a moving boundary problem as a set of partial differential equations which are significantly easier to manipulate.

The interface is then described by the different phases of the system: the boundaries of the phases are the interface. A phase field function is built to describe the regions (*i.e.* phases). It is a continuous function in space which maps each phase to a distinct value. So the transition from one phase to another is represented by a change in the value of the phase field function. An interface between phases is then produced, and the range of value changes corresponds to the interface width. The whole domain is treated simultaneously, and an implicit representation of regions, and so the interface, is described by the phase field function. Describing the interface implicitly allows more topological freedom during the evolution. During the last decade, the image processing and computer vision communities have been interested in the topic of phase fields in order to describe efficiently phase transitions within the image domain.

[Samson et al. \(2000\)](#) introduced a model based on phase field models derived from the phase transition theory in mechanics. The variational-based model was applied successfully on both synthetic and satellite images to segment images into homogeneous regions, where each is described by a distinct value of the phase field function.

[Grossauer and Scherzer \(2003\)](#) introduced a phase field model for ‘restoration-inpainting’. The authors used the complex Ginzburg-Landau equation which enables, in a straightforward way, the efficient restoration of higher dimensional data, to improve sparsely sampled volumetric data and to fill in fragmentary surfaces.

[Beneš et al. \(2004\)](#) proposed an algorithm for image segmentation based on the solution of the Allen-Cahn equation. The model is seen as a regularization of the level set motion by mean curvature, where a force is defined so that the initial level set is close to the object of interest.

[Aubert et al. \(2005\)](#) introduced a novel model for detecting in an image singularities of co-dimension greater than or equal to two. This is equivalent to detecting isolated points in a 2D image or points and curves in a 3D image. The proposed model is based on Ginzburg-Landau functionals, and it uses a diffusion coefficient depending on the image data in addition to a data term.

Here, we list the important advantages offered by the phase field framework:

- the space of phase field functions is linear, thus facilitating model building, learning, and analysis;
- gradient descent uses only the partial differential equation resulting from an energy functional, with no need for ad hoc regularization or reinitialization; numerical implementation is simple;
- a completely neutral initialization for gradient descent is possible;
- components of a region can be created or destroyed anywhere in the image domain; handles (*i.e.* loops) can be created and destroyed in the interior of existing regions (this is mandatory for ‘complex’ network modelling);

- HOAC terms require no boundary extraction, integration, or velocity extension; indeed prior terms are local (*i.e.* diagonalized) in the Fourier domain; the algorithm is fast.

1.5 Line network extraction

Due to the continuous increase in the number and size of remote sensing images, the problem of road and hydrographic network extraction from images is continuously challenging. The main reason new tools have to be developed to solve this problem is the resolution of images. Each range of resolution needs different tools for efficient extraction. The second difficulty is the huge number and size of images which, requires automatic, fast, robust and efficient methods for network extraction.

(Fortier et al., 1999; Mena, 2003; Quackenbush, 2004) proposed an almost complete review of the existing methods for road network extractions. They consider different image resolutions (low, medium and high resolutions), and different image complexities (rural area, semi-urban area, and urban area). Many types of sensors have also been considered: the image data includes panchromatic imagery, infra-red band, color imagery (RGB), multi-spectral imagery, hyper-spectral imagery (Hyperspectral Digital Imagery Collection Experiment, HYDICE), synthetic aperture radar imagery (SAR), light detection and ranging imagery (LIDAR), and so on. In the following, we will briefly review some of the existing representative works for road and hydrographic network extraction from images.

1.5.1 Road network extraction

1.5.1.1 Active contours

Line networks have characteristic geometric properties which need strong and high-level knowledge provided by a human being. Active contour-based models provide a very flexible way to incorporate either generic or specific prior knowledge about the object in question.

(Laptev et al., 2000; Mayer et al., 1998) proposed a method which takes advantage of the scale-space behaviour of roads in combination with geometrically constrained edge extraction by the use of snakes. Firstly, the method starts by extracting lines in coarse scale which are less precise but also less disturbed by cars, shadows, etc., than features in fine scale. Secondly, these extracted lines initialize ribbon snakes in fine scale which describe the roads as bright, more or less homogeneous elongated areas. The ribbons which minimize the energy are with constant width and considered as salient roads. The model closes gaps between adjacent ends of salient roads. However, this method is restricted to the case of line networks where branch widths are approximately the same.

Peteri et al. (2003) introduced an algorithm for road extraction from high resolution satellite images. A topologically correct graph of the road network is first extracted, and roads are then extracted as surface elements. The extraction algorithm makes use of specific active contours (snakes) combined with a multiresolution analysis for reducing geometric noise. The extraction of roads is made by firstly extracting the road segments and then the road intersections. However, this method fails to extract sharp edges of intersections partly

due to their poor image definition, and the topology of the correct graph is critical to the extraction.

[Youn and Bethel \(2004\)](#) assumed that the road network and block pattern in a city have a semi-regular grid pattern. The image is then segmented according to dominant road directions. The road lines are detected to construct initial approximations for the snake refinement. Finally, road edges are refined by applying adaptive snakes.

[Rochery et al. \(2006\)](#) introduced a higher-order active contour (HOAC) model to extract road networks from medium resolution optical images. The model is described in section 1.4.2. Based on the HOAC family, [Peng et al. \(2008a, b, 2010\)](#) proposed new shape priors for road network extraction from very high resolution (VHR) satellite images. The model incorporates first a nonlinear nonlocal HOAC term, and then an additional linear nonlocal HOAC term to improve the computational speed. Both terms allow separate control of branch width and branch curvature, and encourage network branches to elongate. The linear term has several advantages: it is more efficient, and it is able to model multiple widths simultaneously. This work solves the problem of urban road networks, but the solution involves favouring long straight branches, which is not well adapted to non-urban road and hydrographic networks.

1.5.1.2 Markov random fields and marked point processes

Markov random fields provide an appropriate way to model contextual dependencies between entities. MRF based models have been widely used to solve the problem of extraction of line (road) networks.

[Stoica et al. \(2004\)](#) assumed that roads form a thin network in the image leading to approximate a network by connected line segments. The authors proposed a model based on a point process able to simulate and detect thin networks. The model favours aligned segments and penalizes superposition. The image data term is based on statistical hypothesis tests. A simulated annealing algorithm, based on a Monte Carlo dynamics for finite point processes, is used to avoid local minima.

[Lacoste et al. \(2005\)](#) extended the work in ([Stoica et al., 2004](#)), and used an initial segmentation by Markov random field as a seed from which to build a hierarchical model of the network using a marked point process. This works well when the image is sufficiently clean for the MRF segmentation to capture most of the network, and when the network has a tree structure.

([Lacoste et al., 2004, 2010](#)) models the network region using a marked point process of polylines. The polylines can better fit sinuous line networks than models based on segments through a relevant construction of the data term derived from the image. This model works well when the network has constant width over significant distances, since each polyline has a fixed width.

1.5.2 Hydrographic network extraction

1.5.2.1 Geometry of river networks

([Dodds and Rothman, 2000a, b, c](#)) proposed a geometric representation for modelling hydrographic networks. The idea is to study geometric properties of a hydrographic network such as scaling laws which describe the self-similarities between different sub-basins, the

fluctuations and deviations of main and secondary streams of the basin, and finally the connectivity between different network channels. The authors defined different geometric measures of the basin such as the length and the area of a drainage region. These measures are modelled by empirical probability densities obtained by statistical measures from a training set of river networks.

1.5.2.2 Fractal geometry

(Cieplak et al., 1998; Rodríguez-Iturbe and Rinaldo, 1997; Tarboton, 1996) introduced models of river networks based on fractal geometry. The structure and scaling of river networks characterized using fractal dimensions related to Horton's laws (Horton, 1932, 1945) is assessed. These papers have shown the importance of the fractal aspect of river networks. Dimension estimates using the Hortonian scaling system are biased and do not admit space filling. Tarboton (1996) solved this problem by characterizing the scaling and fractal properties of river networks.

1.5.2.3 Digital elevation models

(Coppola et al., 2007; Mantilla and Gupta, 2005; O'Callaghan and Mark, 1984) introduced models based on the digital elevation model (DEM) for hydrographic network extraction from remote sensing images. The key idea is to use the elevation information at each point in the region occupied by the hydrographic network: the depth information allows the determination of the direction of the flow running along the network branches. This family of techniques is complementary to that based on radiometric information.

1.5.2.4 Multiscale and multiresolution analysis

Dillabaugh et al. (2002) introduced a method for semi-automatic extraction of rivers from high-resolution images. A two stage, multi-resolution approach is employed. Firstly, a line detector technique developed by Fischler et al. (1981) is used to track rivers in lower resolution data. Secondly, these initial river estimates are refined using the active contour model (Kass et al., 1988). This work uses an interesting multiscale approach, but relies on user input to specify network endpoints, and is limited in the network topologies that it can find.

Mason et al. (2006) described a semi-automatic technique developed to extract networks from high-resolution LiDAR data. The method is performed in a multi-level knowledge-based approach. Firstly, low-level algorithms extract channel fragments based mainly on image features. Secondly, a high-level processing step improves the network using domain knowledge. The approach adopted at low level uses multi-scale edge detection to detect channel edges, then associates adjacent anti-parallel edges together to form channels. The segmentation algorithm works well on high-resolution LiDAR data. This method is not appropriate for aerial photographs because they are not clean enough compared to the LiDAR data. Lohani et al. (2006) extended this work to the extraction of channels from aerial photographs. These methods failed to extract some of the minor channels because the spectral characteristics of channel and non-channel areas are similar.

1.6 Conclusion

In this chapter, we have given a brief survey of active contours in segmentation as well as techniques for road and hydrographic network extraction from images. Active contour methods are categorized into two different classes: edge-based and region-based. The former has many limitations because it considers local information around the boundary of the object in question. Between the two types of edge-based active contours, geometric active contours have many advantages over parametric active contours, such as computational simplicity and the ability to change curve topology during evolution. The introduction of region-based methods tends to give better segmentation results because they use global information about the object. The corresponding energy functionals tends to have fewer local minima which makes reasonable the use of local optimization algorithms. Moreover, we have mentioned a family of active contour methods which incorporates specific knowledge about the shape of the object: the so-called shape priors. Our interest fits this family of methods because we aim to model network-like regions which have complex shapes and need specific and sophisticated shape priors for automatic (or semi-automatic) solution of the problem of extraction.

We also made a brief survey of techniques for the particular problem of road and hydrographic network extraction from images. Due to the variety of the available data (particularly VHR images) and the complexity they contain, the problem of line network extraction is still very challenging and continues to attract the attention of computer vision community and the remote sensing community.

None of the existing methods or techniques solve the particular problem we are dealing with: extraction of hydrographic networks from VHR satellite images. The main difficulties are as follows: the network has an arbitrary topology unknown *a priori*; significant change of branch widths at network junctions; different network branches may have significantly different widths; the background and the object may have many pixels with similar local properties leading to many pixels from the background being classified as network and vice-versa; the visual hydrographic network in the image appears with many gaps due to the presence of noise (*e.g.* trees, bridges...). Our main aim is then the construction of new shape priors which incorporate specific knowledge so that characteristic geometric properties of hydrographic networks are favoured.

Phase diagram of a HOAC model

“You can tell whether a man is clever by his answers. You can tell whether a man is wise by his questions.”

— Naguib Mahfouz

Contents

2.1	Introduction	38
2.1.1	Higher order active contour (HOAC) model	38
2.1.2	Problem statement	39
2.1.3	Methodology	39
2.1.4	Dimensionless parameters	40
2.2	Stability analysis of a long bar	41
2.2.1	Energy	41
2.2.2	Stability conditions of a long bar	43
2.2.2.1	Analysis of e_0	43
2.2.2.2	Analysis of e_1	44
2.2.2.3	Analysis of e_2	44
2.2.3	Experiments	48
2.3	Stability analysis of a circle	49
2.3.1	Energy	49
2.3.2	Stability conditions of a circle	50
2.3.3	Experiments	54
2.4	Conclusion	55

In this chapter, we briefly recall the HOAC model introduced by [Rochery et al. \(2006\)](#), and show that this model favours two stable configurations, namely line network and circular structures, for some parameter values. Firstly, we conduct a stability analysis of a long bar via a Taylor series expansion up to second order of the HOAC model around a long bar. Secondly, we recall the stability calculations for a circle performed by ([Horvath et al., 2006a, b, 2009](#)). The result of the stability analysis is illustrated on a ‘phase diagram’ leading to a good selection of parameter values giving stable circles and stable bars.

2.1 Introduction

2.1.1 Higher order active contour (HOAC) model

The prior HOAC energy introduced by [Rochery et al. \(2006\)](#) is

$$E_{C,P}(R) = \lambda_C L(R) + \alpha_C A(R) - \frac{\beta_C}{2} \iint_{(S^1)^2} dt dt' \dot{\gamma}(t) \cdot \dot{\gamma}(t') \Psi \left(\frac{|\gamma(t) - \gamma(t')|}{d} \right), \quad (2.1)$$

where R is a region in the image domain; L is region boundary length; A is region area; γ is an embedding, and an element of the equivalence class $[\gamma] = \{\gamma\epsilon : \epsilon \in \text{Diff}(S^1)\}$ where $\text{Diff}(S^1)$ is the set of diffeomorphisms of S^1 , representing the region boundary and parameterized by $t \in S^1$ where S^1 is a circle; $\dot{\gamma}$ is its derivative, *i.e.* the tangent vector field; $\Psi(z)$ defines the interaction between two boundary points separated by a distance zd ; and λ_C , α_C , β_C , and d are real parameters. The long-range interactions described by the quadratic term (*i.e.* the third term in equation (2.1)) are responsible for the prior shape information: they favour parallel (anti-parallel) tangent vectors when the inner product is positive (negative). We notice that the energy functional is invariant to Euclidean transformations (*i.e.* translation and rotation). The length and the area are given by

$$L(R) = \int_{S^1} \dot{\gamma}(t) dt, \\ A(R) = \frac{1}{2} \int_{S^1} \dot{\gamma}(t) \wedge \gamma(t) dt,$$

where \wedge is the cross product and the interaction function $\Psi(z)$ is (*cf.* [Rochery et al. \(2006\)](#))

$$\Psi(z) = \begin{cases} \frac{1}{2} \left(2 - z + \frac{1}{\pi} \sin \pi z \right) & \text{if } 0 \leq z < 2 \\ 0 & \text{if } z \geq 2. \end{cases} \quad (2.2)$$

Figure 2.1 shows the profile of Ψ given by equation (2.2).

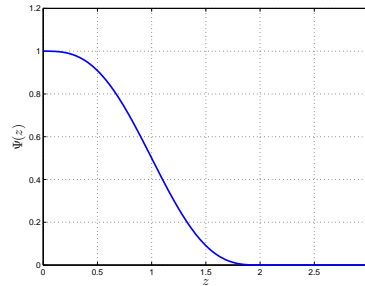


Figure 2.1: Behaviour of the interaction function Ψ .

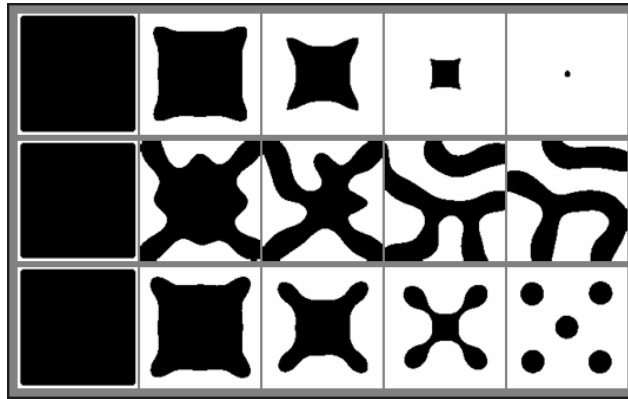


Figure 2.2: Evolution of an initial contour (rounded square) for different parameter values of the HOAC model given by equation 2.1 using gradient descent algorithm.

2.1.2 Problem statement

We use gradient descent algorithm to seek minima of the energy given by equation (2.1). Figure 2.2 shows different behaviours observed during gradient descent. For the three experiments, we use the same initial configuration: a rounded square. Each row corresponds to different parameter values and time runs from left to right. The first row shows that the initial contour vanishes as in the case of a classical active contour model, (*i.e.* $\beta_C = 0$), because the quadratic term is weak enough compared to the length and area terms. For the second row, the stable configuration is made up of a set of arms, of approximately constant width, joined at junctions. The third row shows that the stable configuration is a set of circles of approximately constant radius.

Our goal in this chapter is to find the values of the parameters λ_C , α_C , β_C and d which give a stable region (*i.e.* a preferred region which minimizes the energy) of the desired type. As can be seen, at least two geometric configurations can be made energy minima by manually tuning the parameter values, namely network shapes and regions composed of circles, which are interesting for line network and tree crown extraction from remote sensing images.

The problem now is how to find the model parameter values that give the desired stable region. To do so, we introduce a stability analysis of the desired energy minima to constrain the parameter values for network and circle modelling.

2.1.3 Methodology

The proposed methodology is to analyse the stability of a desired region which is described by its boundary, and the latter is described by γ_0 . In this work, we focus on two desired regions: a network and a circle. A circle is obviously parametrized in polar coordinate system. Ideally, the stability of an arbitrary network shape should be analysed, but this is an extremely complex problem. However, network shapes are essentially composed of basic components: ‘arms’, which are relatively long and have low curvature on the scale of their width, and ‘junctions’. The most important type of stability concerns the arms, since

without arms there can be no network. A tractable and reasonable approximation therefore seems to be to analyse the stability of a long, straight bar.

We first Taylor-expand the HOAC energy around a desired configuration, γ_0 , to second order. We then impose stability conditions: the first functional derivative should be zero (γ_0 is an energy extremum) and the second functional derivative should be positive definite (the extremum is a minimum). These conditions constrain the model parameter values. The results can be summarized in a ‘phase diagram’ illustrating the zones in parameter space leading to stable configurations which can be either bars or circles. The Taylor series expansion of the energy to second order around γ_0 is given by

$$E_P^{(2)}(\gamma) = E_P^{(2)}(\gamma_0 + \delta\gamma) \\ \triangleq E_{C,P}(\gamma_0) + \langle \delta\gamma | \frac{\delta E_{C,P}}{\delta\gamma} \Big|_{\gamma_0} \rangle + \frac{1}{2} \langle \delta\gamma | \frac{\delta^2 E_{C,P}}{\delta\gamma^2} \Big|_{\gamma_0} | \delta\gamma \rangle, \quad (2.3)$$

where $\langle \cdot | \cdot \rangle$ is a metric defined over the space of embeddings, and $\delta\gamma$ is a small perturbation of γ_0 . The configuration γ_0 is stable if and only if $\frac{\delta E_{C,P}}{\delta\gamma} \Big|_{\gamma_0} = 0$, *i.e.* if γ_0 is an extremum of $E_{C,P}$, and the Hessian matrix $\frac{\delta^2 E_{C,P}}{\delta\gamma^2} \Big|_{\gamma_0}$ is positive definite, *i.e.* the extremum is a minimum.

Such stability analysis will become more important as region models become more sophisticated, which is inevitable if automatic solutions to segmentation problems are to be found. The interest of the calculation is thus not limited to the current model, or even to HOAC models in general.

2.1.4 Dimensionless parameters

The geometric energy $E_{C,P}$ of the contour depends on 4 parameters: λ_C , α_C , β_C and d . To simplify the stability analysis, we notice that

$$E_{C,P}(\gamma, \lambda_C, \alpha_C, \beta_C, d) = \tilde{E}_{C,P}(\tilde{\gamma}, \tilde{\lambda}, \tilde{\alpha}, \tilde{\beta}, 1),$$

where $\tilde{\lambda} = \lambda_C d$, $\tilde{\alpha} = \alpha_C d^2$, $\tilde{\beta} = \beta_C d^2$ and $\tilde{\gamma} = \frac{\gamma}{d}$. Since we can multiply the energy $E_{C,P}$ by a constant while preserving the stability properties, it is sufficient to analyse the functional

$$\hat{E}_{C,P}(\hat{\gamma}) = L(\hat{\gamma}) + \hat{\alpha} A(\hat{\gamma}) - \frac{\hat{\beta}}{2} \iint dt dt' \dot{\hat{\gamma}}(t) \cdot \dot{\hat{\gamma}}(t') \Psi(|\hat{\gamma}(t) - \hat{\gamma}(t')|), \quad (2.4)$$

where $\hat{\alpha} = \tilde{\alpha}/\tilde{\lambda}$, $\hat{\beta} = \tilde{\beta}/\tilde{\lambda}$, $\hat{E}_{C,P} = \tilde{E}_{C,P}/\tilde{\lambda}$ and $\tilde{\gamma} = \frac{\gamma}{d}$. The parameters $\hat{\alpha}$ and $\hat{\beta}$ are dimensionless. The stability analysis of the geometric HOAC model given by equation (2.1) is then equivalent to analysing the energy $\hat{E}_{C,P}$ given by equation (2.4). We can also think of this as putting $\lambda_C = d = 1$ which is equivalent to using the parameter d as a unit length and $1/(\lambda_C d)$ as an energy unit. Hereafter, this point is implicit: for example, the width of the bar means the width divided by d and the radius of a circle means the radius divided by d . If it is necessary, all the quantities can be multiplied by powers of d and by λ_C to restore the standard units. So, our aim is reduced to determining the phase diagram which represents the regions of the plane (α_C, β_C) which satisfy the stability conditions, given in section 2.1.3, of the desired contour γ_0 .

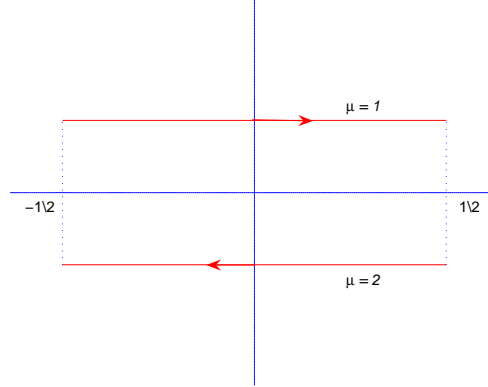


Figure 2.3: Bar parametrization.

2.2 Stability analysis of a long bar

In this section, the contour γ_0 is a bar of length l and width $w_0 \ll l$. Figure 2.3 shows the *ansatz* for the bar model. The bar parametrization γ_0 is

$$\gamma_{0,\mu}(t_\mu) = \begin{cases} x_{0,\mu}(t_\mu) = \pm_\mu l t_\mu & t_\mu \in [-0.5, 0.5] \\ y_{0,\mu}(t_\mu) = \pm_\mu \frac{w_0}{2} \end{cases}, \quad (2.5)$$

where $\pm_\mu = 1$ if $\mu = 1$ and -1 if $\mu = 2$. Both bar sides are parameterized separately by two variables t_1 and t_2 and labeled by the parameter μ as shown in figure 2.3. Perturbations of the bar are defined by tangential and normal changes: $\delta\gamma_\mu(t_\mu) = (\delta x_\mu(t_\mu), \delta y_\mu(t_\mu))$. A perturbation δx does not change the equivalence class of γ_0 , and so it can be ignored: $\delta x_\mu = 0$. So, we focus only on normal perturbations of the bar.

2.2.1 Energy

The Taylor series expansion of the energy $E_{C,P}$ to second order is given by equation (2.3). The second order term $\delta^2 E_{C,P}/\delta^2 \gamma$ can be simplified if we can find a basis which diagonalizes it. This is possible due to the symmetry of the circle S^1 . Each term of the energy $E_{C,P}$ is either a simple integral of a derivative of γ or a double integrals of a function of $s - s'$ where s is the curvilinear coordinate of the circle. Therefore, the operator $\delta^2 E_{C,P}/\delta^2 \gamma$ is a function of $s - s'$, and not of $s + s'$. So, this term can be diagonalized in the Fourier basis of the tangent space at the point γ_0 of the contour space. Thus, the perturbations can be expressed in terms of Fourier coefficients: $\delta y_\mu(t_\mu) = \sum_{k_\mu} a_{\mu,k_\mu} e^{i k_\mu t_\mu}$ where a_{μ,k_μ} is the Fourier component of frequency k_μ relative to the side bar labeled by μ . The spatial wavelength is defined as $\lambda_\mu = \frac{l}{m_\mu}$ where $m_\mu \in \mathbb{Z}$ and then the frequency becomes

$k_\mu = \frac{2\pi}{\lambda_\mu} = \frac{2\pi m_\mu}{l}$. The perturbed contour γ is then defined as

$$\begin{aligned}\gamma_\mu(t_\mu) &= \gamma_{0,\mu}(t_\mu) + \delta\gamma_\mu(t_\mu) \\ &= \begin{cases} x_\mu(t_\mu) &= \pm_\mu l t_\mu \\ y_\mu(t_\mu) &= \pm_\mu \frac{w_0}{2} + \sum_{k_\mu} a_{\mu,k_\mu} e^{ik_\mu l t_\mu} \end{cases},\end{aligned}\quad (2.6)$$

and the Taylor series expansion to second order around the bar γ_0 , given by equation (2.3), can be expressed in terms of the Fourier coefficients as follows:

$$\begin{aligned}E_P^{(2)}(\gamma) &= E_P^{(2)}(\gamma_0 + \delta\gamma) \\ &= E_{C,P}(\gamma_0) + \sum_\mu \sum_{k_\mu} a_{\mu,k_\mu} \frac{\delta E_{C,P}}{\delta a_{\mu,k_\mu}} + \frac{1}{2} \sum_{\mu,\nu} \sum_{k_\mu,k_\nu} a_{\mu,k_\mu} a_{\nu,k_\nu} \frac{\delta^2 E_{C,P}}{\delta a_{\mu,k_\mu} \delta a_{\nu,k_\nu}}.\end{aligned}\quad (2.7)$$

We will show explicitly that the matrix $\frac{\delta^2 E_{C,P}}{\delta a_{\mu,k_\mu} \delta a_{\nu,k_\nu}}$ is diagonal in the Fourier basis and the vector $\frac{\delta E_{C,P}}{\delta a_{\mu,k_\mu}}$ is equal to zero except for $k_\mu = 0$.

The length and the area of the contour are given to second order in terms of the Fourier coefficients by (cf. appendix A)

$$\begin{aligned}L(\gamma) &= \sum_\mu \int_{\square\gamma_\mu} |\dot{\gamma}_\mu(t_\mu)| dt_\mu \\ &\simeq l \left\{ 2 + \frac{1}{2} \sum_k k^2 (|a_{1,k}|^2 + |a_{2,k}|^2) \right\},\end{aligned}\quad (2.8)$$

$$\begin{aligned}A(\gamma) &= \int_{\square\gamma_1} l(y_1(t_1) - y_2(-t_1)) dt_1 \\ &= l[w_0 + (a_{1,0} - a_{2,0})],\end{aligned}\quad (2.9)$$

where $\square\gamma_\mu$ is the domain of the parametrization γ_μ . Computing the quadratic term and defining the quantities G_{ij} , the geometric energy per unit length of the contour γ , $e_P^{(2)} = E_P^{(2)}/l$, is given by (cf. appendix A)

$$\begin{aligned}e_P^{(2)}(\gamma) &= \underbrace{2\lambda_C + \alpha_C w_0 - \beta_C G_{00}(w_0)}_{e_0} \\ &\quad + [a_{1,0} - a_{2,0}] \underbrace{[\alpha_C - \beta_C G_{10}(w_0)]}_{e_1} \\ &\quad + \frac{1}{2} \sum_k [|a_{1,k}|^2 + |a_{2,k}|^2] \underbrace{[k^2 + \beta_C G_{20}(w_0, k)]}_{e_{20}} \\ &\quad + (a_{1,k} a_{2,k} + a_{1,-k} a_{2,-k}) \underbrace{\beta_C G_{21}(w_0, k)}_{e_{21}} \\ &= e_0 + e_1 (a_{1,0} - a_{2,0}) + \frac{1}{2} \sum_k a_k^\dagger e_2 a_k,\end{aligned}\quad (2.10)$$

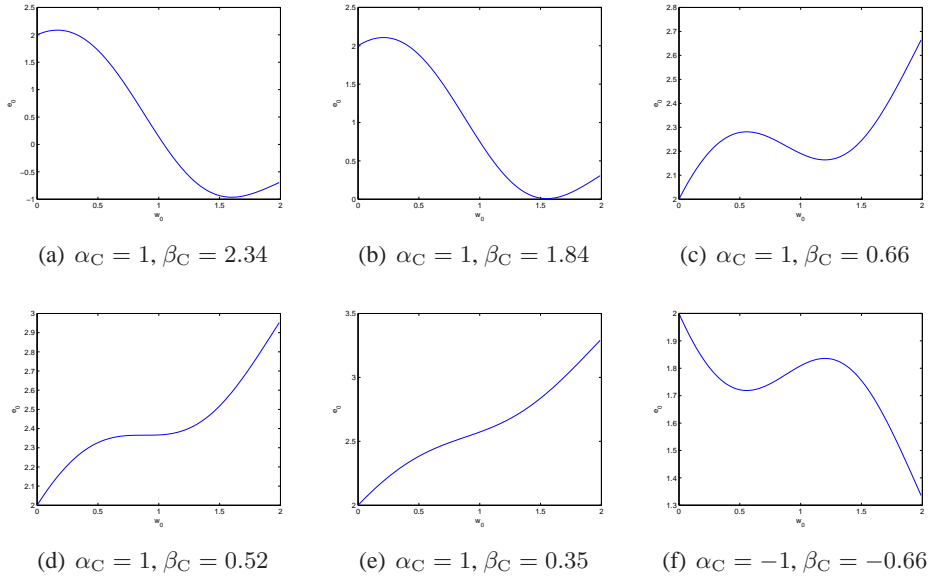


Figure 2.4: Different behaviours of the energy $e_0(w_0)$ for different values of α_C and β_C .

where $a_k = (a_{1,k}^*, a_{2,k})$; \dagger and $*$ indicate respectively Hermitian and complex conjugates. $e_0(w_0)$ is the energy per unit length of a long bar of width w_0 , while $e_1(w_0) = \partial e_0(w_0)/\partial w_0$ is the change in energy due to a change in width (to first order, non-zero Fourier frequencies do not contribute). $e_2(w_0, k)$ is, for each frequency k , a symmetric 2×2 matrix whose diagonal and off-diagonal terms, e_{20} and e_{21} , express the self-energy of perturbations of one side, and the interaction between perturbations of opposite sides of the bar respectively. We notice that if $l \rightarrow \infty$, the sum in the equation (2.10) becomes an integral over k . We keep the sum (*i.e.* l big but not infinity) because the positivity verification of e_2 requires a discretization of the Fourier domain.

2.2.2 Stability conditions of a long bar

Equation (2.10) gives the Taylor series expansion to second order of the geometric energy per unit length of the contour γ around a long bar of width w_0 . We aim to find the width w_0 which minimizes this energy: the width w_0 which satisfies the two stability conditions (*i.e.* $e_1(w_0) = 0$ and $e_2(k, w_0)$ is positive definite $\forall k$).

2.2.2.1 Analysis of e_0

Figure 2.4 shows different behaviours of the bar energy $e_0(w_0)$ against the bar width w_0 for different parameter values of α_C and β_C . Figures 2.4(d) and 2.4(e) show an inflection point with zero and non-zero first derivatives, respectively, and then in these cases the bar vanishes. Figure 2.4(f) shows that, when $\alpha_C < 0$, the energy $e_0(w_0)$ diverges if w_0 increases. We then constrain $\alpha_C > 0$.

For the parameter values corresponding to figures 2.4(a), 2.4(b) and 2.4(c), the energy

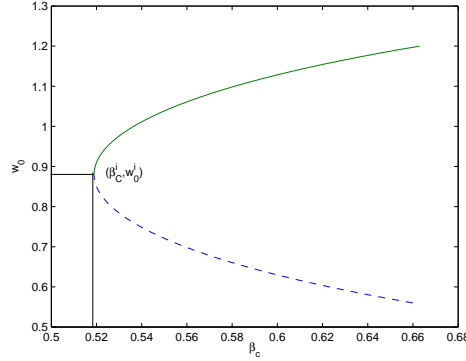


Figure 2.5: Plot of extrema positions of the energy $e_0(w_0)$ against β_C for $\alpha_C = 1$. The solid and dashed curves correspond to minima and maxima respectively.

$e_0(w_0)$ has two extrema: a minimum and a maximum. The second order term of equation (2.10), the Hessian matrix e_2 , separates these two extrema: if e_2 is positive definite then the extremum corresponds to a minimum, and if e_2 is negative definite then the extremum corresponds to a maximum.

The parameter values corresponding to figure 2.4(c) give a positive minimum energy per unit length of the bar. In this case, the minimizer shrinks the bar until the approximation of a long bar fails. As the bar becomes shorter, the contributions of both extremities become important compared to the contributions of the straight part of the bar, and then both extremities interact with each other. At this point, the bar may evolve towards a stable circle or vanish. In the case of figure 2.4(a), the minimum energy of the bar is negative. So, the minimizer lengthens the bar. This situation is not preferred.

2.2.2.2 Analysis of e_1

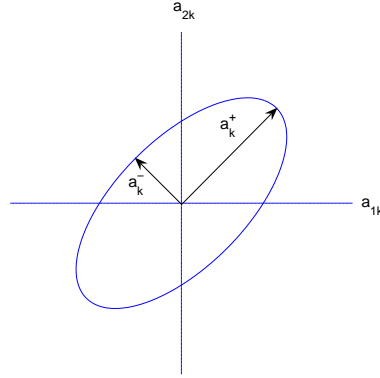
The first stability condition of a long bar (*i.e.* $e_1(w_0) = 0$) constrains the parameters of the HOAC model. This condition ensures that the geometric energy of the bar have an extremum. We then obtain the parameter constraint

$$\beta_C(\alpha_C, w_0) = \frac{\alpha_C}{G_{10}(w_0)}. \quad (2.11)$$

Equation (2.11) shows that, for a fixed value of the bar width w_0 , the curve of the function $\beta_C(\alpha_C)$ is a straight line with gradient $1/G_{10}(w_0)$. Figure 2.5 shows w_0 against the parameter β_C for a fixed value of α_C . This curve has a particular point (β_C^I, w_0^I) which corresponds to an inflection point of e_0 . For $\beta_C < \beta_C^I$, the energy $e_0(w_0)$ does not have an extremum. The minimum cannot be located below the value $w_0 = w_0^I$ since the solid curve corresponds to the minimum while the dashed curve corresponds to the maximum.

2.2.2.3 Analysis of e_2

The second order stability condition of a long bar, *i.e.* that the Hessian matrix e_2 be positive definite, is ensured by constraining the eigenvalues of e_2 to be strictly positive so that the



(a) Representation of the perturbations in eigenvector basis.

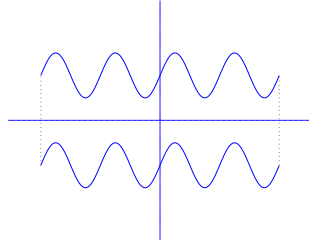
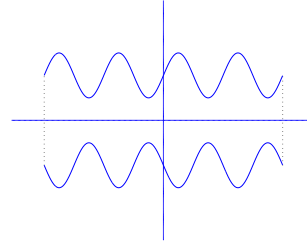
(b) Contribution of λ_+ .(c) Contribution of λ_- .

Figure 2.6: Perturbation behaviours in eigenvector basis.

extremum of the energy corresponds to a minimum. The eigenvalues of e_2 are $\lambda_{\pm} = e_{20} \pm e_{21}$ and the eigenvectors are $v_{\pm} = (1, \pm 1)$ respectively. So, equation (2.10) can be written as a function of the eigenvalues as

$$e_P^{(2)}(\gamma) = e_0 + e_1(a_{1,0} - a_{2,0}) + \frac{1}{4} \sum_k \lambda_+ |a_k^+|^2 + \lambda_- |a_k^-|^2, \quad (2.12)$$

where $a_k^{\pm} = a_{1,k} \pm a_{2,k}^*$. Figure 2.6(a) shows the representation of the perturbations $a_{1,k}$ and $a_{2,k}$ corresponding to each side of the bar in the eigenvector basis v_+ and v_- . These eigenmodes are illustrated in figure 2.6: a_+ describes in-phase perturbations of the two sides, while a_- describes out-of-phase perturbations. For low frequencies, the former cost less energy, as locally the sides of the shape are still parallel. For higher frequencies, the difference is negligible.

Figure 2.7 shows that for fixed parameter values which give a minimum of the energy e_0 , both eigenvalues λ_+ and λ_- are strictly positive for all frequencies. This positivity condition allows us to constrain the parameter values to be bounded by upper and lower limits.

To find these bounds, we express explicitly the eigenvalues λ_{\pm} and we then constrain them to be strictly positive. Substituting e_{20} and e_{21} by their expressions given by equa-

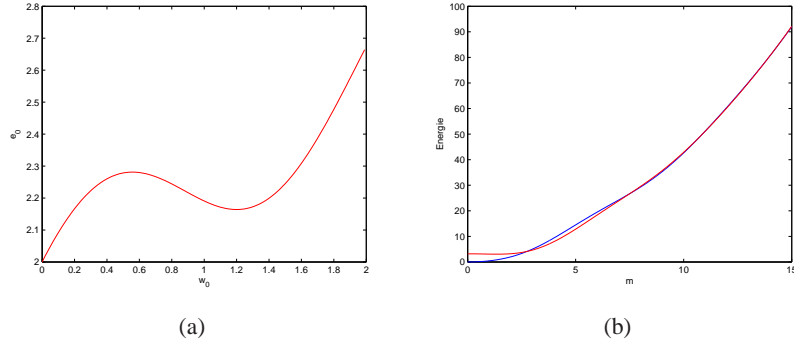


Figure 2.7: (a): bar energy $e_0(w_0)$ plotted against the width w_0 . $\alpha_C = 0.8$, and $\beta_C = 1.39$ computed using equation (2.11) for a desired width $w_0 = 1.2$. (b): eigenvalues λ_{\pm} plotted against the frequency m for the same parameter values in (a). λ_{\pm} are indeed strictly positive for all frequencies $m \in \mathbb{Z}$.

tion (2.10), λ_{\pm} become

$$\lambda_{\pm}(\alpha_C, \beta_C, w_0, k) = k^2 + \beta_C G_{\pm}(w_0, k) ,$$

where $G_{\pm}(w_0, k) = G_{20}(w_0, k) \pm G_{21}(w_0, k)$; the parameters λ_C and d are fixed to 1 without loss of generality. Replacing β_C by its expression given by the first stability condition in equation (2.11), we obtain

$$\lambda_{\pm}(\alpha_C, w_0, k) = k^2 + \frac{\alpha_C}{G_{10}(w_0)} G_{\pm}(w_0, k) ,$$

and so the second order stability condition of a long bar becomes

$$k^2 + \frac{\alpha_C}{G_{10}(w_0)} G_{\pm}(w_0, k) > 0 , \forall k ,$$

which is equivalent to

$$\alpha_C G_{\pm}(w_0, k) > -k^2 G_{10}(w_0) , \forall k , \quad (2.13)$$

since $G_{10}(w_0) > 0$ because the interaction function Ψ is a decreasing function (*cf.* Appendix A). This inequality gives a lower bound on the parameter α_C if $G_{\pm}(w_0, k) > 0$, so the bound is always negative, and yet $\alpha_C > 0$: the lower bound of α_C equals 0.

Figure 2.8 shows the regions of the (w_0, k) plane corresponding to the sign change of G_{\pm} . The white, red, blue and black regions correspond to $G_+(w_0, k) > 0$ and $G_-(w_0, k) > 0$, $G_+(w_0, k) > 0$ and $G_-(w_0, k) < 0$, $G_+(w_0, k) < 0$ and $G_-(w_0, k) > 0$, and $G_+(w_0, k) < 0$ and $G_-(w_0, k) < 0$ respectively.

The bounds on the parameter α_C are given by figure 2.9. A long bar with a width $w_0 \in (0, 2)$ is stable if the value of α_C is bounded by a lower bound (the red curve), which is equal to 0, and by an upper bound (the blue curve). The three vertical lines correspond to the singularity points of the functions $G_{\pm}(w_0, k)$ where $k \in K$, K is the frequency

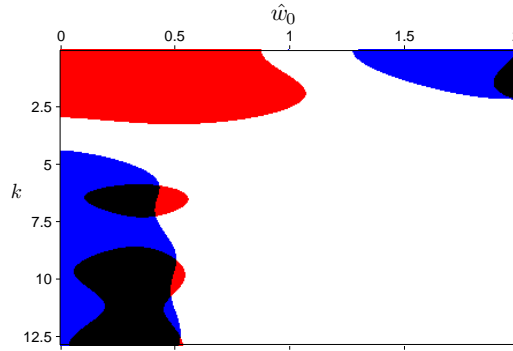


Figure 2.8: Plot of the four possible regions in the plane (w_0, k) corresponding to the sign change of G_+ et G_- .

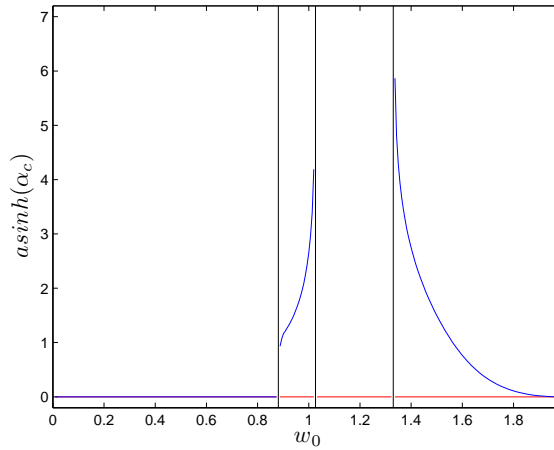


Figure 2.9: Lower and upper bounds of the parameter α_C in red and blue respectively.

set which contributes to the bounds on the parameter α_C . For $w_0 \in (0, 0.8802)$, where $\alpha_{min} = \alpha_{max} = 0$, no stable bar exists. If $w_0 \in (1.33, 2)$, then a bar of width w_0 is stable if the value of α_C is below the blue curve given by figure 2.9. For $w_0 \in (1.03, 1.33)$, a bar with width w_0 is stable if $\alpha_C > 0$ (the upper bound of α_C is $+\infty$ in this interval).

The goal of the stability analysis is to delineate the region(s) of the plane (α_C, β_C) which give(s) a stable bar of width w_0 . By analogy with a physical system, we call it ‘phase diagram’. The stability conditions of first and second order studied previously, allow us to find the phase diagram of a bar. Equation (2.11) shows that for each value w_0 , the plot of the function $\beta_C(\alpha_C, w_0)$ is a line with slope $1/G_{10}(w_0)$ and since α_C is bounded, the set of (α_C, β_C) becomes a segment for each value w_0 . Plotting the set of lines with variable slopes as a function of $w_0 \in (0.88, 2)$, we obtain the phase diagram given in figure 2.10. The colored regions correspond to the set of points (α_C, β_C) which give stable bars. The sign of the minimum energy plays an important role for contour evolutions using gradient

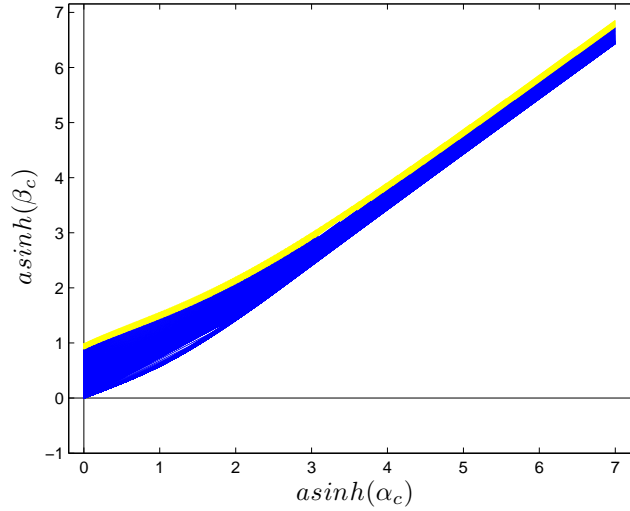


Figure 2.10: Phase diagram of a bar ($w_0 \in (0.88, 2)$). Blue and yellow zones refer to positive and negative bar energy per unit length respectively.

descent. The regions colored in blue and yellow in figure 2.10 give positive and negative minimum energy respectively. The parameter values which belong to the yellow region lengthen the bar whereas the values from the blue region shorten the bar until it vanishes or a stable circle is created. The white region corresponds to the set of parameter values for which no stable bar exists.

2.2.3 Experiments

The stability analysis which we have done previously, allows us to select good values of the parameters from the phase diagram. The phase diagram given by figure 2.10 gives the ranges of the dimensionless parameters (*cf.* section 2.1.4): $\hat{\alpha}$, $\hat{\beta}$ and \hat{w}_0 . We then compute the values of the real parameters for a given width w_0 as follows: $\alpha_C = \hat{\alpha}\lambda_C/d$, $\beta_C = \hat{\beta}\lambda_C/d$ and $d = w_0/\hat{w}_0$. λ_C is fixed to 1 because it just scales the energy while minima remain the same. Figure 2.11 shows different evolutions of a long bar using a gradient descent algorithm to minimize the HOAC energy given by equation (2.1). Each pair of rows corresponds to the same point $(\hat{\alpha}, \hat{\beta}, \hat{w}_0)$ selected from the phase diagram given by figure 2.10, and changing the value of w_0 we obtain the values given in table 2.1 for each experiment.

For experiments 1–4, we choose 2 points of the phase diagram, given in figure 2.10, which belong to the lower white region. These parameter values produce an inflection point in the bar energy: the quadratic term is weak compared to the length and area terms. So for these values, the bar is unstable and it disappears: the bar width decreases to 0. Figure 2.12 shows, for the parameter values corresponding to evolutions 1–4, that the bar energy has an inflection point and the minimum is then located at $w_0 = 0$.

For experiments 5–10, the selected parameter values show also that the bar shrinks.

For these experiments, the parameter values were selected from the blue zone, of the phase diagram, which gives a stable bar with a positive energy as shown in figure 2.12 (5–10) and their corresponding eigenvalues are strictly positive at the minimum. So the energy of the long bar, *i.e.* $E_0 \approx le_0$, is positive and the gradient descent algorithm decreases the bar length l to 0 while the width remains at its stable value.

For experiments 11–14, we choose parameter values which give a stable bar with positive energy but these same values give a stable circle. The corresponding plots 11–14 given in figure 2.12 show that the bar energy has a minimum at w_0 and then the radius of the stable circle will be $r_0 = w_0/2$.

For experiments 15–16, the parameter values are selected from the yellow region of the phase diagram which give a stable bar with a negative energy as shown in figure 2.12 (15–16). So the bar energy, *i.e.* $E_0 \approx le_0$, is negative and it then lengthens making a “snake” shape while the width remains at its stable value.

For experiments 17–22, we choose three points of the upper white region of the phase diagram which gives an unstable bar. Figure 2.12 shows that, for evolutions 17–22, the bar energy has a minimum and then the out-of-phase eigenvalue, λ_- , is strictly positive for zero frequency. For these evolutions, the bar is unstable to some non-zero frequencies which give negative eigenvalues. These unstable frequencies split the bar into stripes with widths approximated to the corresponding wavelengths.

2.3 Stability analysis of a circle

In this section, we focus on the stability analysis of a circle for circular structure modelling. The result will be illustrated in the so-called ‘phase diagram’ of a circle. The stability calculations for a circle were performed by Horvath et al. (2006a, b, 2009). Since γ_0 parameterizes a circle, it is easier to express it in terms of polar coordinates (r, θ) on Ω . For a suitable choice of coordinate on S^1 , a circle of radius r_0 centred on the origin is then given by $\gamma_0(t) = (r_0(t), \theta_0(t))$, where $r_0(t) = r_0$, $\theta(t) = t$, and $t \in [-\pi, \pi)$.

2.3.1 Energy

As we mentioned in section 2.1.2, we first Taylor-expand the energy $E_{C,P}$ around a circle γ_0 of radius r_0 . We are interested in the behaviour of small perturbations $\delta\gamma = (\delta r, \delta\theta)$. The first thing to notice is that the energy $E_{C,P}$ is defined on 1-chains so tangential changes in γ do not affect its value. We then set $\delta\theta = 0$, and concentrate on δr . The terms of the energy $E_{C,P}$ are either a simple integral over t or a double integral of a function of $t - t'$ so it is easier to express the perturbations δr in terms of Fourier coefficients because they diagonalize the second order operator: $\delta r(t) = \sum_k a_k e^{ir_0 kt}$. The expansion of the energy $E_{C,P}$ given by equation (2.1) in Taylor series to second order around a circle γ_0 is given by (*cf.* Horvath et al. (2006a, b, 2009))

$$e_P^{(2)}(\gamma) = e_P^{(2)}(\gamma_0 + \delta\gamma) = e_0(r_0) + a_0 e_1(r_0) + \frac{1}{2} \sum_k |a_k|^2 e_2(k, r_0), \quad (2.14)$$

	Initial contour	Evolution 1	Evolution 2	Evolution 3	Evolution 4
1					
2					
3					
4					
5					
6					
7					
8					
9					
10					
11					
12					
13					
14					
15					
16					
17					
18					
19					
20					
21					
22					

Figure 2.11: Gradient descent evolutions of a long bar for different parameter values given by table 2.1.

where

$$e_0(r_0) = 2\pi\lambda_C r_0 + \pi\alpha_C r_0^2 - \pi\beta_C G_{00}(r_0), \quad (2.15)$$

$$e_1(r_0) = 2\pi\lambda_C + 2\pi\alpha_C r_0 - 2\pi\beta_C G_{10}(r_0), \quad (2.16)$$

$$e_2(k, r_0) = 2\pi\lambda_C r_0 k^2 + 2\pi\alpha_C - 2\pi\beta_C G_2(k, r_0), \quad (2.17)$$

$$G_2(k, r_0) = 2G_{20}(r_0) + G_{21}(k, r_0) - 2ir_0 k G_{23}(k, r_0) + r_0^2 k^2 G_{24}(k, r_0), \quad (2.18)$$

and $G_{ij} = \int_{-\pi}^{\pi} dp e^{-ir_0(1-\delta(j))kp} F_{ij}(p)$.

2.3.2 Stability conditions of a circle

Figure 2.13 shows the energy of a circle of radius r_0 against r_0 for different values of the parameters α_C and β_C . Figures 2.13(a), 2.13(b) and 2.13(c) show that $e_0(r_0)$ has a minimum and adjusting the values of α_C and β_C , the minimum energy can be positive or

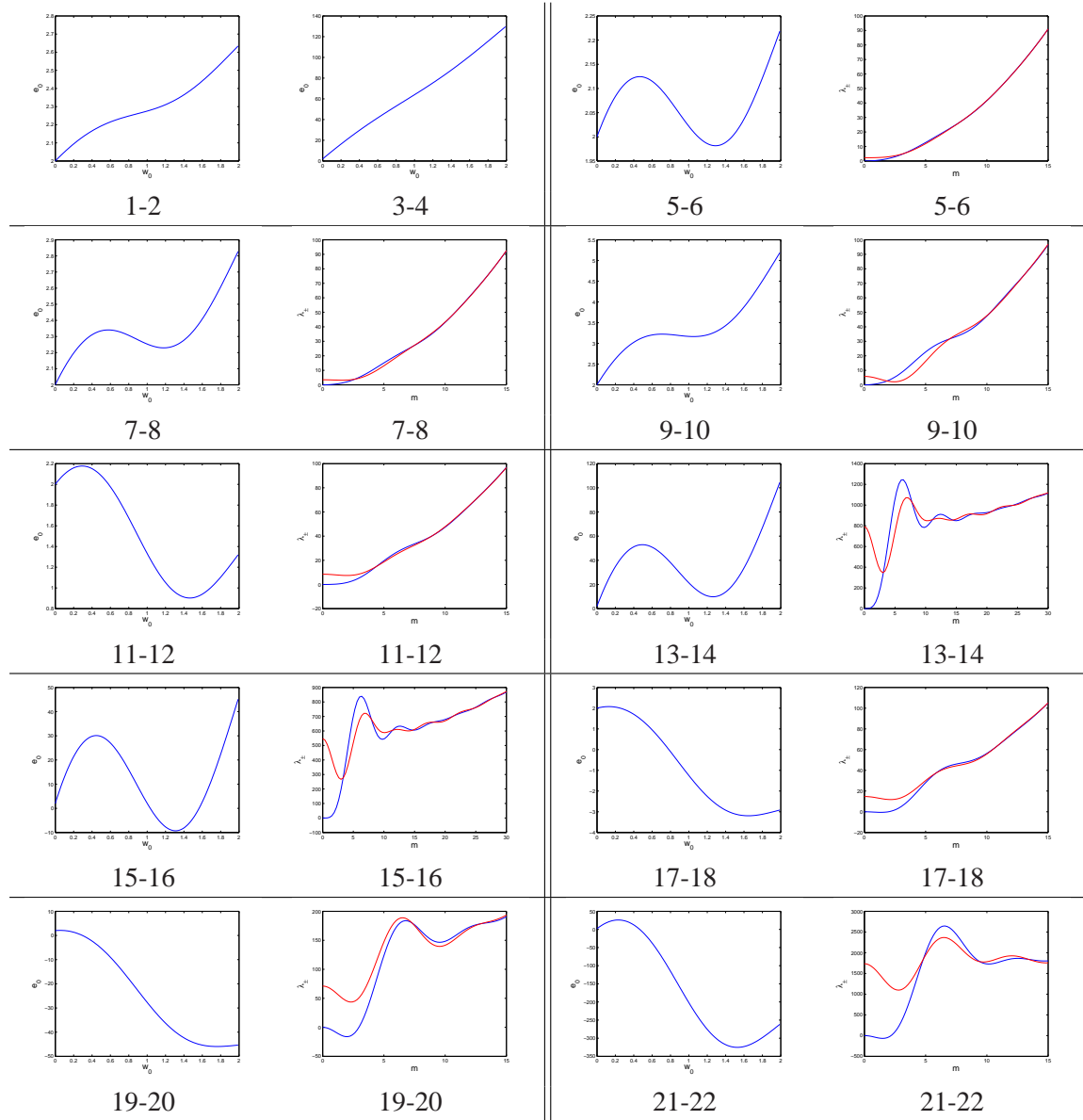


Figure 2.12: Bar energies and their corresponding eigenvalues for the different evolutions given by figure 2.11. The blue and red curves correspond to the in-phase and out-of-phase eigenvalues, λ_+ and λ_- , respectively.

	$asinh(\hat{\alpha})$	$asinh(\hat{\beta})$	\hat{w}_0	$e_0(\hat{w}_0)$	w_0	α_C	β_C	d
1	0.5	0.2	0	2	0	0.052	0.02	10
2	0.5	0.2	0	2	0	0.035	0.013	15
3	5	3	0	2	0	7.42	1	10
4	5	3	0	2	0	3.7	0.5	20
5	0.5	0.4	1.29	1.98	10	0.067	0.053	7.75
6	0.5	0.4	1.29	1.98	20	0.034	0.027	15.5
7	1	0.7	1.18	2.22	10	0.139	0.09	8.44
8	1	0.7	1.18	2.22	20	0.069	0.045	16.94
9	2	1.45	1.05	3.17	10	0.38	0.21	9.52
10	2	1.45	1.05	3.17	20	0.19	0.11	19
11	1	1.2	1.465	0.903	10	0.172	0.221	6.82
12	1	1.2	1.465	0.903	20	0.086	0.111	13.65
13	6	5.7	1.26	9.84	20	12.71	9.42	15.87
14	6	5.7	1.26	9.84	30	8.48	6.28	23.8
15	5.5	5.3	1.301	-9.28	10	16.32	13.13	7.63
16	5.5	5.3	1.301	-9.28	20	8.02	6.56	15.26
17	1	2	1.645	-3.19	10	0.193	0.597	6.08
18	2	2	1.645	-3.19	20	0.097	0.298	12.16
19	2	4	1.76	-45.9	10	0.638	4.8	5.68
20	2	4	1.76	-45.9	15	0.319	2.4	11.36
21	6	6.5	1.525	-325.3	20	15.38	25.37	13.11
22	6	6.5	1.525	-325.3	25	12.3	20.3	16.4

Table 2.1: Parameter values which correspond to the evolutions given by figure 2.11.

negative. The number of stable circles decreases if $e_0(r_0) > 0$ and increases if $e_0(r_0) < 0$. Figures 2.13(d), 2.13(e) and 2.13(f) do not show energy minima for the corresponding parameter values.

A circle of radius r_0 is a minimum of the energy $e_0(r_0)$ if and only if it satisfies the stability conditions: $e_1(r_0) = 0$ and $e_2(r_0, k) > 0, \forall k$. The first order stability condition implies the parameter constraint

$$\beta_C(\lambda_C, \alpha_C, r_0, d) = \frac{\lambda_C + \alpha_C r_0}{G_{10}(r_0, d)}. \quad (2.19)$$

Figure 2.14 shows the positions of energy extrema against β_C for a chosen value $\alpha_C = 1$ satisfying the parameter constraint (2.19). If $\beta_C < \beta_C^I$ then the energy e_0 does not have extrema. If $\beta_C > \beta_C^I$ then e_0 has both a maximum (dashed curve) and minimum (solid curve). The second order stability condition is then necessary to find an energy minimum. The expression for e_2 is given by equation (2.17):

$$e_2(\lambda_C, \alpha_C, \beta_C, d, r_0, k) = 2\pi\lambda_C r_0 k^2 + 2\pi\alpha_C - 2\pi\beta_C G_2(d, r_0, k).$$

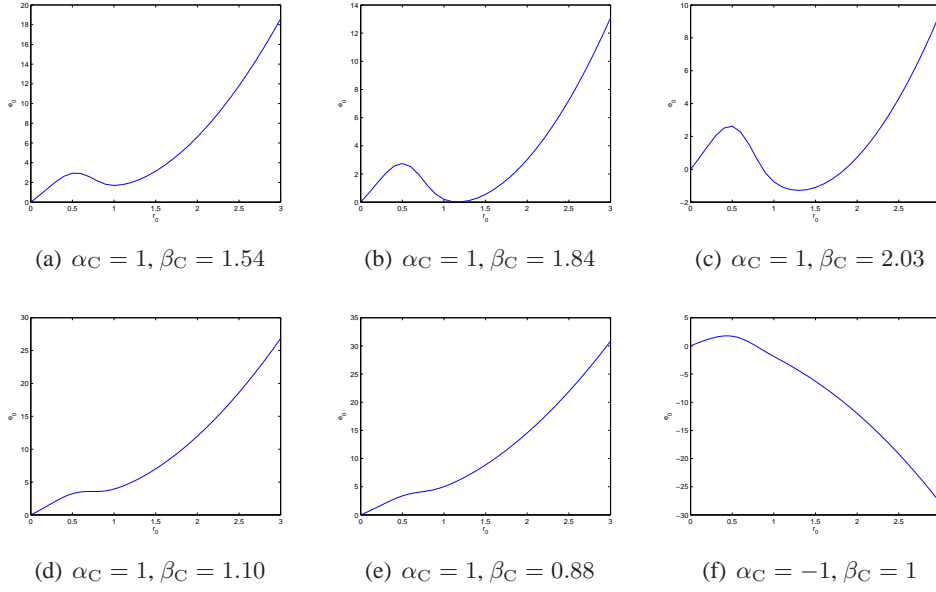


Figure 2.13: Behaviours of the circle energy, $e_0(r_0)$, for different values of α_C and β_C .

A perturbation of frequency $m = 1$ ($k = \frac{m}{r_0} = \frac{1}{r_0}$) of a circle corresponds to a translation of it. $E_{C,P}$ is translation invariant, we then ignore the perturbation of frequency 1 because it does not have any effect in the energy. Then, the second stability condition becomes

$$e_2(\lambda_C, \alpha_C, \beta_C, d, r_0, k) > 0, \forall k \neq \frac{1}{r_0}.$$

Without loss of generality we set $\lambda_C = d = 1$ (cf. section 2.1.4):

$$e_2(\alpha_C, \beta_C, r_0, k) > 0, \forall k \neq \frac{1}{r_0},$$

and substituting β_C by its expression given by equation (2.19), we then have

$$r_0 k^2 + \alpha_C - \frac{1 + \alpha_C r_0}{G_{10}(r_0)} G_2(r_0, k) > 0, \forall k \neq \frac{1}{r_0},$$

which can be rewritten, by defining the functions $a(r_0, k) = 1 - r_0 \frac{G_2(r_0, k)}{G_{10}(r_0, k)}$ and $f(r_0, k) = \frac{G_2(r_0, k)}{G_{10}(r_0, k)} - r_0 k^2$, as

$$\alpha_C a(r_0, k) > f(r_0, k), \forall k \neq \frac{1}{r_0}.$$

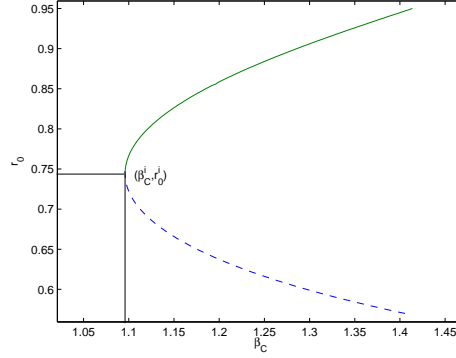


Figure 2.14: Plot of extrema positions of the energy $e_0(r_0)$ against β_C for $\alpha_C = 1$. The solid and dashed curves correspond to minima and maxima respectively.

Depending on the sign of $a(r_0, k)$, we obtain these two conditions:

$$\begin{aligned} \text{if } a(r_0, k) > 0 \text{ then } \alpha_C > \frac{f(r_0, k)}{a(r_0, k)}, \forall k \neq \frac{1}{r_0} \text{ so } \alpha_C > \alpha_C^{\min} = \max_k \frac{f(r_0, k)}{a(r_0, k)}, \\ \text{if } a(r_0, k) < 0 \text{ then } \alpha_C < \frac{f(r_0, k)}{a(r_0, k)}, \forall k \neq \frac{1}{r_0} \text{ so } \alpha_C < \alpha_C^{\max} = \min_k \frac{f(r_0, k)}{a(r_0, k)}. \end{aligned}$$

Figures 2.15(a), 2.15(b) and 2.15(c) show the behaviours of the functions $a(r_0, k)$, $f(r_0, k)$ and $fa = \frac{f(r_0, k)}{a(r_0, k)}$, respectively, for the frequencies 0 (blue curves) and 2 (red curves) which contribute to determine the lower and upper bounds of the parameter α_C . Figure 2.15(d) shows the bounds of the parameter α_C obtained by taking the maximum or the minimum of the functions given by figure 2.15(c) with respect to the sign of $a(r_0, k)$. The condition $\alpha_C > 0$ implies that there is no stable circle of radius $r_0 < 0.69$. If $0.69 < r_0 < 1.1$ then the upper value of α_C is $+\infty$ and the lower bound is given by the red curve. If $r_0 > 1.1$ then the energy has a stable circle of radius r_0 for each value of α_C which lies between the red curve and the blue curve.

The parameter constraint given by equation (2.19) shows that for each radius r_0 of a stable circle (*i.e.* $r_0 \in (0.69, +\infty)$), the parameter β_C is expressed linearly as a function of α_C . The curve representing β_C against α_C for a given value r_0 is then a line of slope $\frac{r_0}{G_{10}(r_0)}$. Figure (2.16) shows the phase diagram of a circle obtained by plotting the different lines representing β_C against α_C for different values of $r_0 \in (0.69, +\infty)$. The blue and yellow zones correspond to parameter values which give a stable circle with positive and negative energy respectively.

2.3.3 Experiments

In this section, we show geometric evolutions of a circle using gradient descent, given in figure 2.17, for different model parameter values given in table 2.2. These parameter values were selected from different zones of the circle's phase diagram given in figure 2.16. Figure 2.18 shows the energy behaviours of a circle and the second order energies corresponding to the evolutions given in figure 2.17.

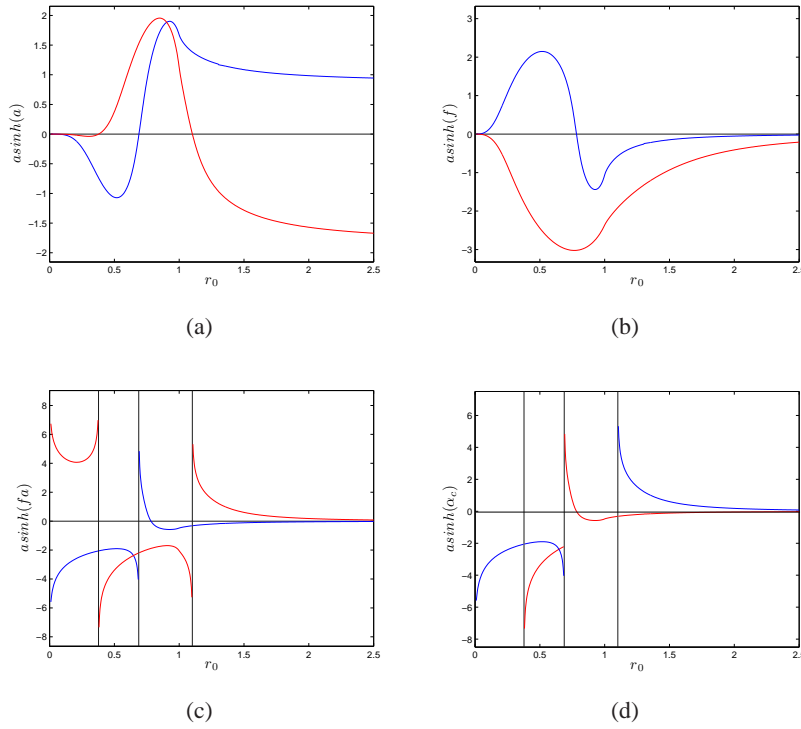


Figure 2.15: The blue and red curves shown by figures (a), (b) and (c) correspond to frequencies 0 and 2 respectively. For figure (d), the red and blue curves correspond to lower and upper bounds of α_C respectively.

Evolutions 1 and 2 show that the initial circle shrinks until it disappears for the parameter values selected from the lower white zone of the phase diagram. The circle is then unstable. At that zone the quadratic term is weak compared to the other terms, *i.e.* the length and the area terms which constitute the classical active contour model.

Evolutions 3 and 4 show that the circle is stable for the selected parameter values from the blue zone. Figure 2.18 shows that for these parameter values the circle energy has a minimum and the second order energy is strictly positive for all frequencies k .

Evolutions 5 and 6 show that the parameter values selected from the upper white zone evolve the circle toward a complex shape due to some unstable frequencies. Figure 2.18 shows that for these parameter values, the second order energy evaluated at the desired radius has some unstable frequencies which give negative second order energy.

2.4 Conclusion

In this chapter, we have analysed the stability of both a long bar and a circle under a HOAC energy in order to produce stable line and circular structures. The latter were the aim of other works for tree crown extraction from remote sensing images (*cf.* Horvath et al. (2006a, b, 2009)). The former, *i.e.* line network modelling, is our focus.

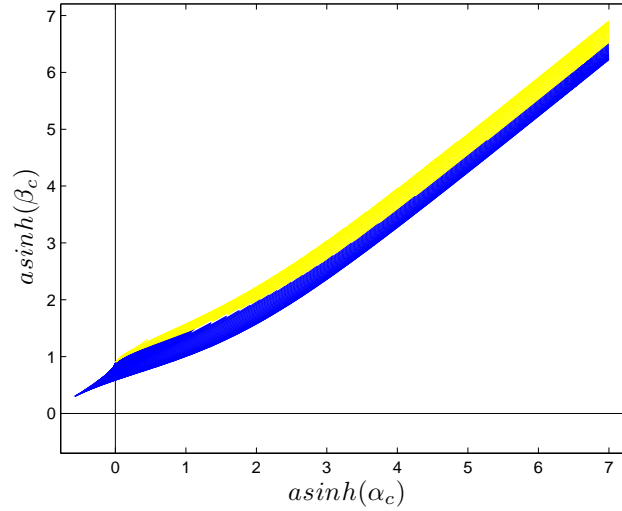


Figure 2.16: Phase diagram of a circle ($\hat{r}_0 \in]0.69, \infty[$). The blue and yellow zones correspond to parameter values which give a stable circle with positive and negative energy respectively.

	$asinh(\hat{\alpha})$	$asinh(\hat{\beta})$	\hat{r}_0	$e_0(\hat{r}_0)$	r_0	α_C	β_C	d
1	0.5	0.2	-	-	-	0.104	0.04	5
2	0.5	0.2	-	-	-	0.052	0.02	10
3	1	1.2	0.94	2.371	5	0.221	0.284	5.319
4	1	1.2	0.94	2.371	15	0.074	0.095	15.96
5	1	2	2.34	-16.67	10	0.275	0.849	4.274
6	1	2	2.34	-16.67	15	0.183	0.566	6.41

Table 2.2: Parameter values which correspond to the evolutions given by figure 2.17.

The stability analysis of both structures generates constraints and bounds on the model parameters which have led to the diagrams given in figures 2.10 and 2.16. Combining both studies, one can superimpose both diagrams to get a full phase diagram which is shown in figure 2.19. The phase diagram enables parameter values to be chosen to model a particular situation. The sign of e_0 is important for both structures as we have mentioned.

In the case of a bar, if $e_0 < 0$ then the bar lengthens to minimize the total energy, while if $e_0 > 0$ then the bar shrinks until it disappears. The first situation is undesirable because gradient descent tends to create arbitrary network branches to minimize the total energy. Suitable parameter values therefore lie in the maroon region of the phase diagram, which gives a stable bar with positive energy per unit length and no stable circles.

	Initial contour	Evolution 1	Evolution 2	Evolution 3	Evolution 4
1					
2					
3					
4					
5					
6					

Figure 2.17: Gradient descent evolutions of a circle for different parameter values given in table 2.1.

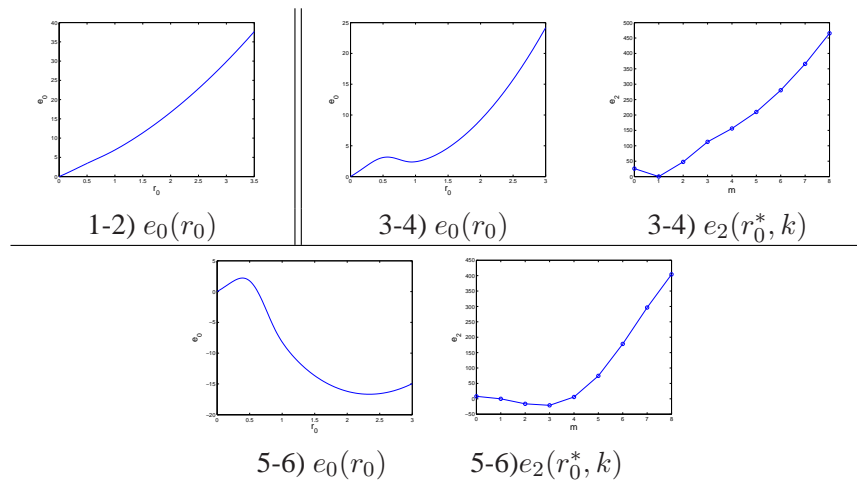


Figure 2.18: Circle energy $e_0(r_0)$ and second order energy $e_2(r_0^*, k)$ corresponding to evolutions given in figure 2.17. r_0^* is the radius of a circle at the energy minimum if it exists.

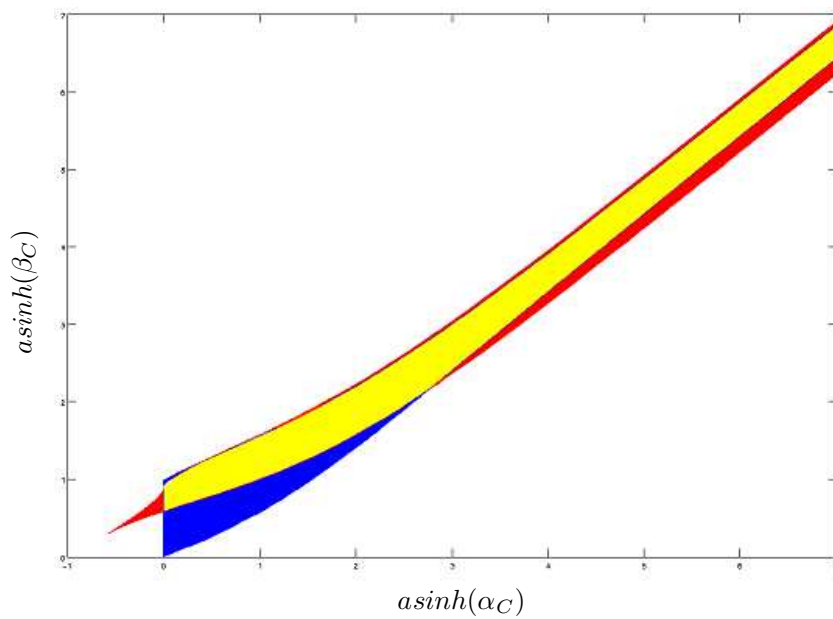


Figure 2.19: Phase diagram. Maroon, red, yellow, green, white, blue, pink, grey, magenta correspond respectively to B+, C+, B+ C+, B+ C-, UB UC, B- C+, B- C-, C- and B-; B, C, U, + and - refer respectively to bar, circle, unstable, positive energy and negative energy.

A phase field HOAC model of undirected networks

“All the sciences came to exist in Arabic. The systematic works on them were written in Arabic writing.”

— Ibn Khaldun

Contents

3.1	Introduction	60
3.1.1	Phase fields	60
3.1.2	Phase fields as HOACs	61
3.2	Inflection point long bar model	61
3.2.1	HOAC inflection point long bar model	61
3.2.2	Phase field inflection point long bar model	62
3.3	Likelihood energy and energy minimization	63
3.3.1	Histogram modelling	63
3.3.2	Data energy term	63
3.3.2.1	Multivariate Gaussian model	66
3.3.2.2	Multivariate mixture of two Gaussian model	66
3.4	Experiments and discussion	66
3.4.1	MG model vs. MMG model	66
3.4.2	Inflection point long bar model	67
3.4.3	Robustness of the algorithm to initial conditions	67
3.5	Conclusion	70

In the previous chapter, we performed a stability analysis of a network branch which led the determination of the phase diagram of the HOAC model, allowing a good selection of parameter values for network modelling. Based on that, we describe, in this chapter, a phase field HOAC inflection point long bar model and apply it to road network extraction from VHR remote sensing images of rural areas. We use the phase field framework to reduce computational complexity.

3.1 Introduction

3.1.1 Phase fields

In this section, we recall briefly the phase field HOAC model introduced by [Rochery et al. \(2005\)](#). A phase field ϕ is a real-valued function on the image domain Ω . A phase field determines a region by the map $\zeta_z(\phi) = \{x \in \Omega : \phi(x) > z\}$ where z is a given threshold. The basic, local phase field energy is

$$E_0^s(\phi) = \int_{\Omega} d^2x \left\{ \frac{D}{2} \partial\phi \cdot \partial\phi + \lambda \left(\frac{\phi^4}{4} - \frac{\phi^2}{2} \right) + \alpha \left(\phi - \frac{\phi^3}{3} \right) \right\}. \quad (3.1)$$

If (3.1) is minimized subject to $\zeta_z(\phi) = R$, *i.e.* for a fixed region, then away from the boundary, the minimizing function ϕ_R assumes the value 1 inside, and -1 outside R thanks to the ultralocal terms. Figure 3.1 shows the behaviour of the ultralocal terms, *i.e.* the terms weighted by λ and α . To guarantee 2 stable phases at -1 and 1 of the system, the inequality $\lambda > |\alpha|$ must be satisfied. We choose $\alpha > 0$ so that the energy at -1 is less than at 1 . This will favor pixels belonging to the outside of R rather than to the interior. The derivative term ensures the smoothness of ϕ_R , producing a narrow interface around the boundary ∂R interpolating between -1 and $+1$. We denote w the interface width.

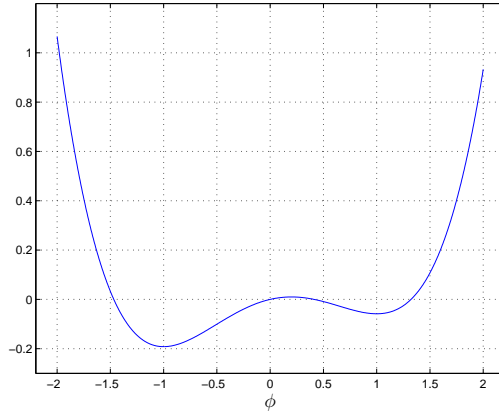


Figure 3.1: Behaviour of the ultralocal terms ($\lambda = 0.5$ and $\alpha = 0.1$).

To introduce prior shape information, a nonlocal term is then added to give a total energy $E_P^s = E_0^s + E_{NL}$, where ([Rochery et al., 2005](#))

$$E_{NL}(\phi) = -\frac{\beta}{2} \iint_{\Omega^2} d^2x d^2x' \partial\phi(x) \cdot \partial\phi(x') \Psi \left(\frac{|x - x'|}{d} \right), \quad (3.2)$$

where d is the interaction range. This term creates long-range interactions between points of ∂R (because $\partial\phi_R$ is zero elsewhere) using an interaction function, Ψ , which decreases as a function of the distance between the points. The interaction function Ψ is given by equation (2.2).

The first functional derivative of the local term E_0^s , with respect to ϕ , is

$$\frac{\delta E_0^s(\phi)}{\delta \phi} = -D\partial^2\phi + \lambda(\phi^3 - \phi) + \alpha(1 - \phi^2), \quad (3.3)$$

while the first functional derivative of the nonlocal term E_{NL} , with respect to ϕ , is (cf. Appendix B.1.4)

$$\frac{\delta E_{\text{NL}}(\phi)}{\delta \phi} = \beta \int_{\Omega} d^2x' \partial\phi(x') \cdot \partial\Psi\left(\frac{|x - x'|}{d}\right). \quad (3.4)$$

3.1.2 Phase fields as HOACs

The phase field local energy, E_0^s , of ϕ_R is given approximately by a linear combination of the length of ∂R and the area of R , and the nonlocal phase field term, E_{NL} , is proportional to the HOAC term (cf. Rochery et al. (2005)):

$$\begin{aligned} E_0(\phi_R) &\approx \lambda_C L(R) + \alpha_C A(R) \triangleq E_{C,0}(R), \\ E_{\text{NL}}(\phi_R) &\propto E_{C,Q}(R). \end{aligned}$$

where $E_{C,Q}(R)$ is the quadratic term in equation (2.1). The result is that one can use phase fields instead of HOACs. The equations relating the phase field model parameters and the HOAC model parameters are (cf. Rochery et al. (2005))

$$\begin{cases} \alpha = \frac{3}{4}\alpha_C, \\ \beta = \frac{1}{4}\beta_C, \\ D = \frac{w}{4}\lambda_C, \\ \lambda = \lambda_C \frac{15}{8w} \left\{ 1 + \sqrt{1 - \frac{4}{5}w^2 \left(\frac{\alpha_C}{\lambda_C}\right)^2} \right\}. \end{cases} \quad (3.5)$$

3.2 Inflection point long bar model

In chapter 2, we described the stability analysis of a network branch abstracted as a long bar under a HOAC model given by equation (2.1). The result is the phase diagram given in figure 2.19. We then are able to select parameter values which produce stable networks. In Conclusion 2.4, we argued that the maroon zone of the phase diagram gives suitable parameter values for network modelling and will be our primary preferred zone.

3.2.1 HOAC inflection point long bar model

Figure 3.2(a) shows the energy per unit length $e_0(w_0)$ plotted against bar width w_0 for a particular parameter setting from the maroon region with a stable width $\hat{w}_0^* = 1.2$. Parameter settings that produce energy curves like figure 3.2(a) have a disadvantage when minimized using gradient descent. Imagine an area of background in the image, and a network branch formed there by the vagaries of gradient descent. Because it lies in the background, and assuming the data model is reasonable, there will be a force inwards on the branch, tending to make it shrink and disappear. This is as it should be. However, if

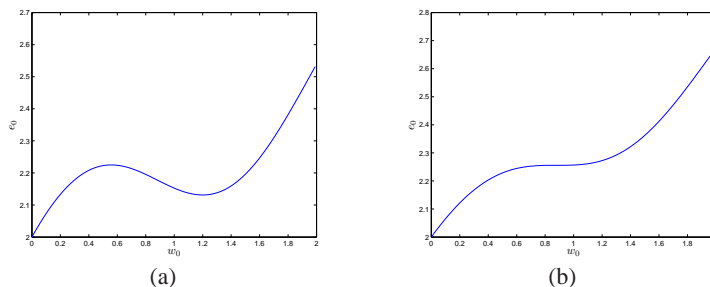


Figure 3.2: 3.2(a) and 3.2(b) plot e_0 against bar width w_0 , with $(\alpha_C, \beta_C) = (0.8, 0.53)$ and $(0.7, 0.363)$ respectively, giving a minimum at $w_0^* = 1.2$ and an inflection point at $w_0^* = 0.88$.

the width of the branch lies in the basin of attraction of the stable width, there is a threshold that the force has to surmount if it is to push the branch over the maximum shown in figure 3.2(a), and down to zero width. The result is the formation of ‘phantom roads’, false positives that cannot disappear due to the stability of the network branch.

Global optimization algorithms are one way to avoid local minima, but unfortunately our problem is NP-hard. We choose a slightly less ambitious approach: we change the energy functional to avoid the creation of these local minima while preserving as much prior knowledge as possible. This problem can be solved by constraining the parameters so that the energy function has an inflection point at a desired width w_0 (*i.e.* $\lambda_-(w_0, 0) = 0$) rather than a minimum. Figure 3.2(b) shows a plot of energy per unit length versus width for a parameter setting that gives an inflection point. Such inflection points lie on the lower edge of the coloured area of the phase diagram, with $\hat{\alpha}$ values in the range $[0, 0.9083]$. The value of $\hat{w}_0 = 0.88$ all along this line, and this is the only value that allows an inflection point.

3.2.2 Phase field inflection point long bar model

To model networks with the phase field model, we first select parameter values for the contour using the phase diagram. In practice, this means fixing w_0 (which is an application-determined physical parameter), and then selecting values of $\hat{\alpha}$ and $\hat{\beta}$ from the maroon region of the phase diagram. These give \hat{w}_0 , which gives the required d , and hence α_C/λ_C , which is upper-bounded so that λ is real. A choice of λ_C then gives the actual values of the parameters in $E_{C,P}$. These are then converted using equations given by (3.5). we choose¹ $w = 3$.

Once we impose the inflection point condition, \hat{w}_0 is fixed, and $\hat{\alpha}$ is sufficient to determine $\hat{\beta}$ and hence all the other parameters except λ_C . However, the inflection point condition constrains the parameters to a co-dimension 1 set in parameter space, so that a generic change in the parameters, however small, will violate the condition. One can then wonder

¹It cannot be too small, or a subpixel discretization will be needed for gradient descent, and it cannot be too large or the phase field model will not be a good approximation to the HOAC model (*cf.* Rochery et al. (2005)).

how well this condition is preserved when the parameters are converted from contour to phase field, especially since this conversion is based on a relatively crude approximation to ϕ_R . In practice, numerical experiments show that the inflection point condition is well preserved, with configurations at the inflection point remaining stationary to subpixel accuracy over thousands of iterations of gradient descent.

3.3 Likelihood energy and energy minimization

So far we have spoken only of the prior energy E_P^s . In this section, we focus on the likelihood energy E_I . Figure 3.3 shows two, 120cm resolution, multi-spectral test images (red, green, blue and infrared channels), together with manually extracted road network masks, and the histograms of the network and the background for each band.

3.3.1 Histogram modelling

We test two models: the multivariate Gaussian model (MG) (*cf.* Horvath (2007)) and the mixture of two multivariate Gaussian model (MMG). The multivariate model describes vectorial statistics, such as the mean and the covariance of the 4 channels, combining all channels. Multimodal statistics are well modeled using a mixture of two Gaussians.

Figure 3.4 shows the histograms of the four channels, the monovariate Gaussian model and the mixture of two Gaussian models in blue, red and black respectively. The statistics are computed for each channel independently of the others (the models are monovariate in this case). It is clear that the monovariate mixture of two Gaussian model fits better the histograms than the monovariate Gaussian model, for both monomodal and bimodal histograms.

3.3.2 Data energy term

We assume that $P(I|R, K) = P(I_R|R, \theta_R, K)P(I_{\bar{R}}|\bar{R}, \theta_{\bar{R}}, K)$, where I_R and $I_{\bar{R}}$ are the restrictions of the image to the network R and the background \bar{R} respectively, and θ_R and $\theta_{\bar{R}}$ are the corresponding model parameters (which previously were included in the generic K). We further assume that the image values at different pixels are independent given these parameters. Taking negative logarithms, and using $\phi_{\pm} = (1 \pm \phi)/2$ to restrict integrations to the network or background respectively, gives the following likelihood energy:

$$\begin{aligned} E_I(\phi) &= - \int_{\Omega} dx \left\{ \ln(\pi_{\theta_R}(I(x))) \phi_+(x) + \ln(\pi_{\theta_{\bar{R}}}(I(x))) \phi_-(x) \right\} \\ &= - \int_{\Omega} dx \frac{\phi(x)}{2} \left\{ \ln(\pi_{\theta_R}(I(x))) - \ln(\pi_{\theta_{\bar{R}}}(I(x))) \right\} + k, \end{aligned} \quad (3.6)$$

where $\pi_{\theta_R} = P(I_R|R, \theta_R, K)$ and $\pi_{\theta_{\bar{R}}} = P(I_{\bar{R}}|\bar{R}, \theta_{\bar{R}}, K)$ and k is a ϕ -independent constant, which we drop. The functional derivative of the data energy term with respect to ϕ is

$$\frac{\delta E_I(\phi)}{\delta \phi} = - \frac{1}{2} \left\{ \ln(\pi_{\theta_R}(I(x))) - \ln(\pi_{\theta_{\bar{R}}}(I(x))) \right\}. \quad (3.7)$$

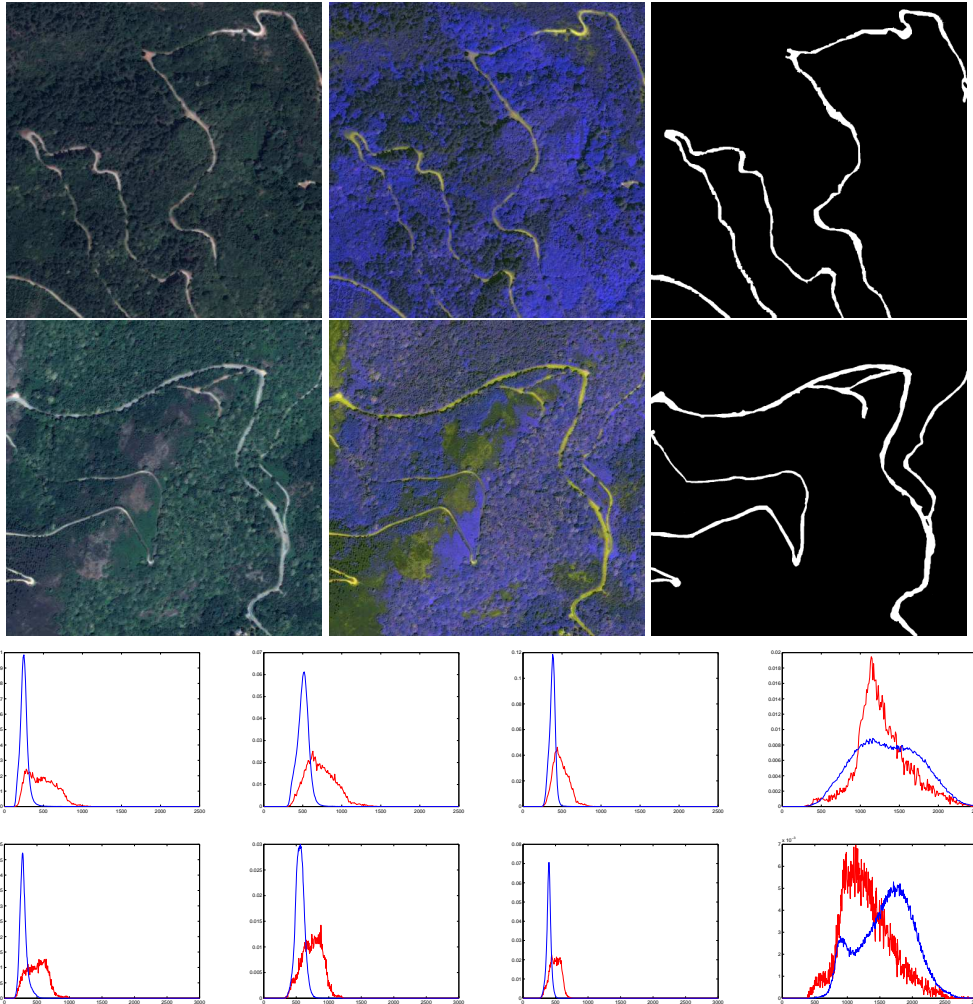


Figure 3.3: Top row, from left to right: the R-G-B bands of a multi-spectral satellite image; the G-R-IR bands of the same image; the corresponding manually extracted road network mask. Second row: similar, for a second image. Third row, from, left to right: histograms of the network (red) and background (blue) regions of the R, G, B, and IR bands of the image in the top row; Fourth row: similar, for second image. (Images ©DigitalGlobe, CNES processing, images acquired via ORFEO Accompaniment Program).

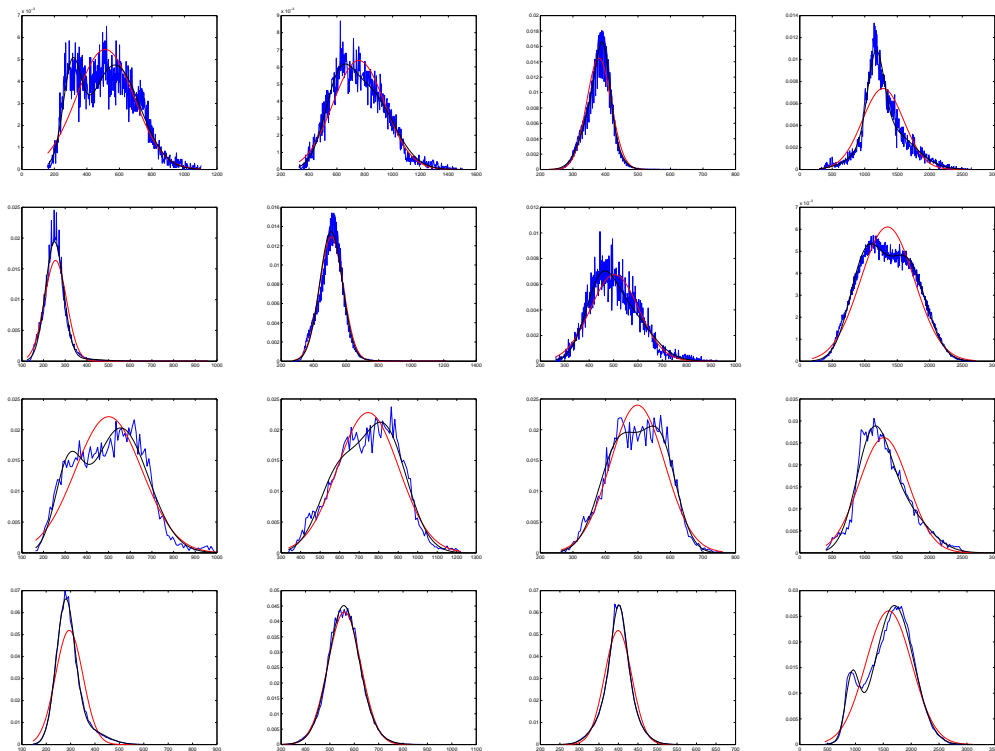


Figure 3.4: From left to right: histograms of R, G, B and IR channels. From top to bottom: histograms of the interior region of the first image, the exterior region of the first image, the interior region of the second image and the exterior region of the second image. Curves in blue, red and black correspond to the histograms, the Gaussian models and the mixture of two Gaussian models respectively.

3.3.2.1 Multivariate Gaussian model

After simple calculations, the MG model can be written as

$$E_1(\phi) = \frac{1}{4} \int_{\Omega} dx \left\{ (I(x) - \mu)^T \Sigma^{-1} (I(x) - \mu) - (I(x) - \bar{\mu})^T \bar{\Sigma}^{-1} (I(x) - \bar{\mu}) + \ln \frac{|\Sigma|}{|\bar{\Sigma}|} \right\} \phi(x), \quad (3.8)$$

where μ and $\bar{\mu}$ are the mean vectors of the bands of I_R and $I_{\bar{R}}$ respectively; Σ and $\bar{\Sigma}$ are the covariance matrices of I_R and $I_{\bar{R}}$ respectively; t indicates transpose. $\theta = (\mu, \bar{\mu}, \Sigma, \bar{\Sigma})$ is learnt from the original images and their masks using maximum likelihood.

3.3.2.2 Multivariate mixture of two Gaussian model

The MMG model is designed to take into account the heterogeneity in the appearance of the network produced by occlusions. It takes the form

$$E_1(\phi) = -\frac{1}{2} \int_{\Omega} dx \left\{ \ln \sum_{i=1}^2 p_i |2\pi \Sigma_i|^{-1/2} e^{-\frac{1}{2} (I(x) - \mu_i)^t \Sigma_i^{-1} (I(x) - \mu_i)} - \ln \sum_{i=1}^2 \bar{p}_i |2\pi \bar{\Sigma}_i|^{-1/2} e^{-\frac{1}{2} (I(x) - \bar{\mu}_i)^t \bar{\Sigma}_i^{-1} (I(x) - \bar{\mu}_i)} \right\} \phi(x). \quad (3.9)$$

where p_i and \bar{p}_i weight the two Gaussian components for I_R and $I_{\bar{R}}$ respectively; t indicates transpose. $\theta = (p_1, p_2, \bar{p}_1, \bar{p}_2, \mu_1, \mu_2, \bar{\mu}_1, \bar{\mu}_2, \Sigma_1, \Sigma_2, \bar{\Sigma}_1, \bar{\Sigma}_2)$ is learnt from the original images and their masks using maximum likelihood combined with the EM algorithm (cf. Dempster et al. (1977); Ingrassia and Rocci (2007); Moon (1996)).

3.4 Experiments and discussion

The total phase field energy to minimize is $E(\phi; I) = E_P^s(\phi) + E_I(I, \phi)$. We use gradient descent to seek energy minima (cf. Rochery et al. (2005)).

3.4.1 MG model vs. MMG model

We compare the segmentation performance of the MG and MMG data models. We begin by looking at the performance of the two models using maximum likelihood classification, *i.e.* with E_P^s set to zero. Results on the two images in figure 3.3 are shown in the first two columns of figure 3.5. In this case, the MMG model performs worse than the MG model, since it allows some parts of the background to be classified as network. With the addition of the prior, however, the results using the MMG model are better than those of the MG model on both images, as shown in the last two columns of figure 3.5. See table 3.1 for quantitative evaluations.

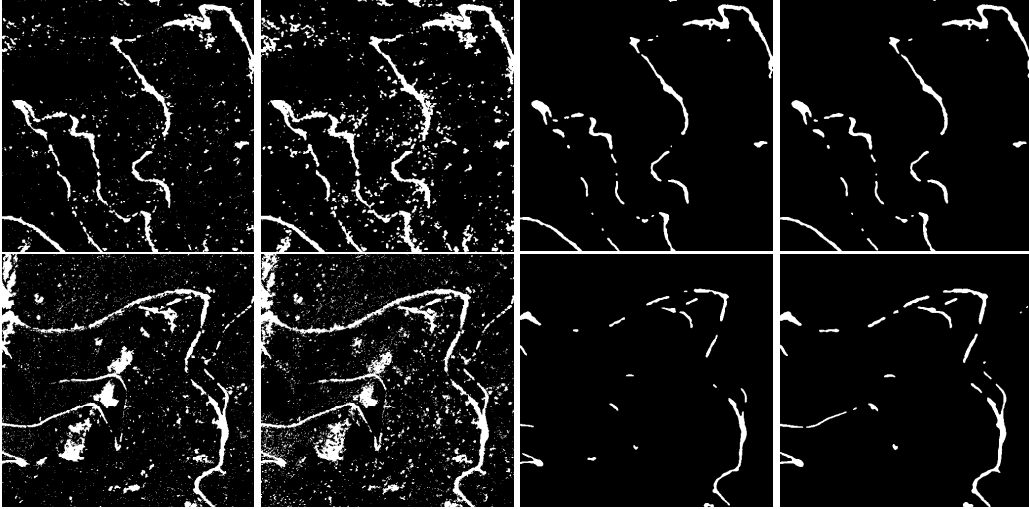


Figure 3.5: Segmentations of the two images in figure 3.3, from left to right in each row: ML using MG, ML using MMG, MAP using MG, and MAP using MMG. From 3rd to 4th column and from top to bottom: $(w_0, \hat{\alpha}, \lambda_C) = (2, 0.7646, 15)$, $(2, 0.8385, 5)$, $(2, 0.8385, 20)$, and $(2, 0.6169, 10)$.

3.4.2 Inflection point long bar model

We compare the segmentation performance of the previous, energy minimum model (EMM) and the new energy inflection point model (EIPM). The first is obtained using parameter values from the maroon region of the phase diagram given by figure 2.19, and gives an energy per unit length as a function of width as shown in figure 3.2(a), while the second uses the parameter constraints detailed in section 3.2.2 to create an inflection point model, with an energy per unit length as a function of width as shown in figure 3.2(b). The idea is to avoid false positives in the background by rendering a network configuration only marginally stable in the absence of supporting image data. The results are shown in figure 3.6: the false positives are indeed eliminated without creating false negatives. See table 3.1 for quantitative evaluations.

3.4.3 Robustness of the algorithm to initial conditions

Initialization dependence of the final result, *i.e.* becoming trapped in a local minimum, is a drawback of deterministic descent algorithms. However, it might be hoped that with sufficient prior knowledge built into the model, the entropy of the probability distribution would be reduced enough to eliminate most, if not all local minima, and thereby reduce or remove initialization dependence. To test this, we examine the convergence of the algorithm using different initializations for the phase field ϕ :

- to the constant value $\phi_0 = \alpha/\lambda$, which corresponds to the maximum of the ultralocal terms shown by figure 3.1, which is the threshold z , and hence to all of Ω being boundary (the neutral initialization, NI);

		Completeness = TP / (TP+FN)	Correctness = TP / (TP+FP)	Quality = TP / (TP+FP+FN)
ML	MG	0.7343	0.4923	0.4179
	MGM	0.8152	0.3467	0.3214
MAP	MG	0.5962	0.7955	0.5170
	MGM	0.5982	0.8028	0.5216
ML	MG	0.6839	0.3754	0.3199
	MGM	0.7370	0.3338	0.2983
MAP	MG	0.3275	0.9405	0.3208
	MGM	0.4730	0.9282	0.4563
EMM	MMG	0.7591	0.5798	0.4897
EIPM	MMG	0.5982	0.8028	0.5216

Table 3.1: Quantitative evaluations of the experiments. T, F, P, and N correspond to true, false, positive, and negative respectively.

- to the constant value -1 , corresponding to all of Ω being background;
- to the constant value $+1$, corresponding to all of Ω being foreground;
- when values of ϕ are sampled independently from a uniform distribution on $[-1, 1]$ (UR);
- to the ML result;
- to $1 -$ the ML result;
- to the ML result scaled linearly towards ϕ_0 .

	NI	-1	+1	UR	ML	-ML	ScML
NI	1	0.994	0.035	0.997	1	0.994	1
-1	0.994	1	0.029	0.996	0.994	1	0.994
+1	0.035	0.029	1	0.031	0.035	0.029	0.035
UR	0.997	0.996	0.031	1	0.997	0.996	0.997
ML	1	0.994	0.035	0.997	1	0.994	1
-ML	0.994	1	0.029	0.996	0.994	1	0.994
ScML	1	0.994	0.035	0.997	1	0.994	1

Table 3.2: Similarity measures of the segmentations given by the first column of figure 3.7.

Figure 3.7 shows segmentations of the two images in figure 3.3, each with two different parameter settings, and using the above initializations. We observe that for the first and fourth parameter settings, which correspond to the first and fourth columns of figure 3.7, only the initialization of ϕ at 1 does not converge toward ϕ_R which characterizes the region

	NI	-1	+1	UR	ML	-ML	ScML
NI	1	0.998	0.997	0.999	0.999	0.998	0.999
-1	0.998	1	0.994	0.999	0.998	1	0.999
+1	0.997	0.994	1	0.996	0.997	0.994	0.997
UR	0.999	0.999	0.996	1	0.999	0.999	0.999
ML	0.999	0.998	0.997	0.999	1	0.998	1
-ML	0.998	1	0.994	0.999	0.998	1	0.999
ScML	0.999	0.998	0.997	0.999	1	0.999	1

Table 3.3: Similarity measures of the segmentations given by the second column of figure 3.7.

$\times 10^6$	NI	-1	+1	UR	ML	-ML	ScML
ERE	0.8267	0.8267	0.8267	0.8267	0.8267	0.8267	0.8267
E_P^s	0.3283	0.3061	3.1089	0.3212	0.3284	0.3062	0.3283
E_1	0.4234	0.4479	0.6081	0.4303	0.4233	0.4479	0.4234
E	0.7517	0.7540	3.7169	0.7514	0.7517	0.7541	0.7517

Table 3.4: Values of energy terms, at the convergence, which correspond to the parameter values of the first column of figure 3.7. ERE refers to Empty Region Energy.

$\times 10^5$	NI	-1	+1	UR	ML	-ML	ScML
ERE	8.2675	8.2675	8.2675	8.2675	8.2675	8.2675	8.2675
E_P^s	1.3098	1.2540	1.3718	1.2910	1.3095	1.2535	1.3092
E_1	3.8859	3.9447	3.8850	3.9029	3.8860	3.9447	3.8862
E	5.1957	5.1987	5.2568	5.1938	5.1954	5.1982	5.1953

Table 3.5: Values of energy terms, at the convergence, which correspond to the parameter values of the second column of figure 3.7. ERE refers to Empty Region Energy.



Figure 3.6: Left: segmentation result using parameter values selected from the maroon zone, $(w_0, \hat{\alpha}, \lambda_C) = (4, 0.2013, 5)$. Right: segmentation result using parameter values leading to an inflection point at the desired bar width, $(w_0, \hat{\alpha}, \lambda_C) = (2, 0.7646, 15)$.

of interest R which is the region occupied by the network, and the rest of segmentations agreed within 0.99 pixel similarity for both images. Tables 3.2 and 3.3 show quantitative similarity measures of segmentations given by the first and second columns of figure 3.7 respectively.

Tables 3.4 and 3.5 give the values of the prior energy, the data energy, the total energy, and the total energy of the empty region (*i.e.* $\phi(x) = -1 \forall x \in \Omega$) at the converged solution. In the case of $\phi(x) = 1 \forall x \in \Omega$, table 3.4 shows that the prior energy (3.1089×10^6) dominates with comparison to the data energy (0.6081×10^6). This explains why the solution gets stuck at $\phi(x) = 1 \forall x \in \Omega$ and does not evolve toward -1 because the latter phase costs energy. The rest of the experiments show that the total energy of the solution is always less than that of the empty region, which proves that a network branch is produced if the total energy is decreased.

The neutral initialization is located at the maximum of the ultralocal terms everywhere in Ω for which the prior gradient term disappears. At the maximum, the force of the ultralocal terms is 0 and so the prior force is 0 at this starting point ϕ_0 . So only the data term allows the evolution of ϕ_0 at the first iteration. ϕ_0 then evolves to the ML segmentation and thus the gain will be only one iteration, if the starting point is the ML segmentation itself. This is negligible with respect to the number of iterations at convergence, which is of order of 5000 iterations. Later on, we use the neutral initialization because the prior does not favor, at the first iteration, either the interior ($\phi = 1$) or the exterior ($\phi = -1$) of the region R .

3.5 Conclusion

We have described a phase field HOAC model for road network extraction from VHR satellite images of rural areas. The contributions of this model are: the use of inflection point

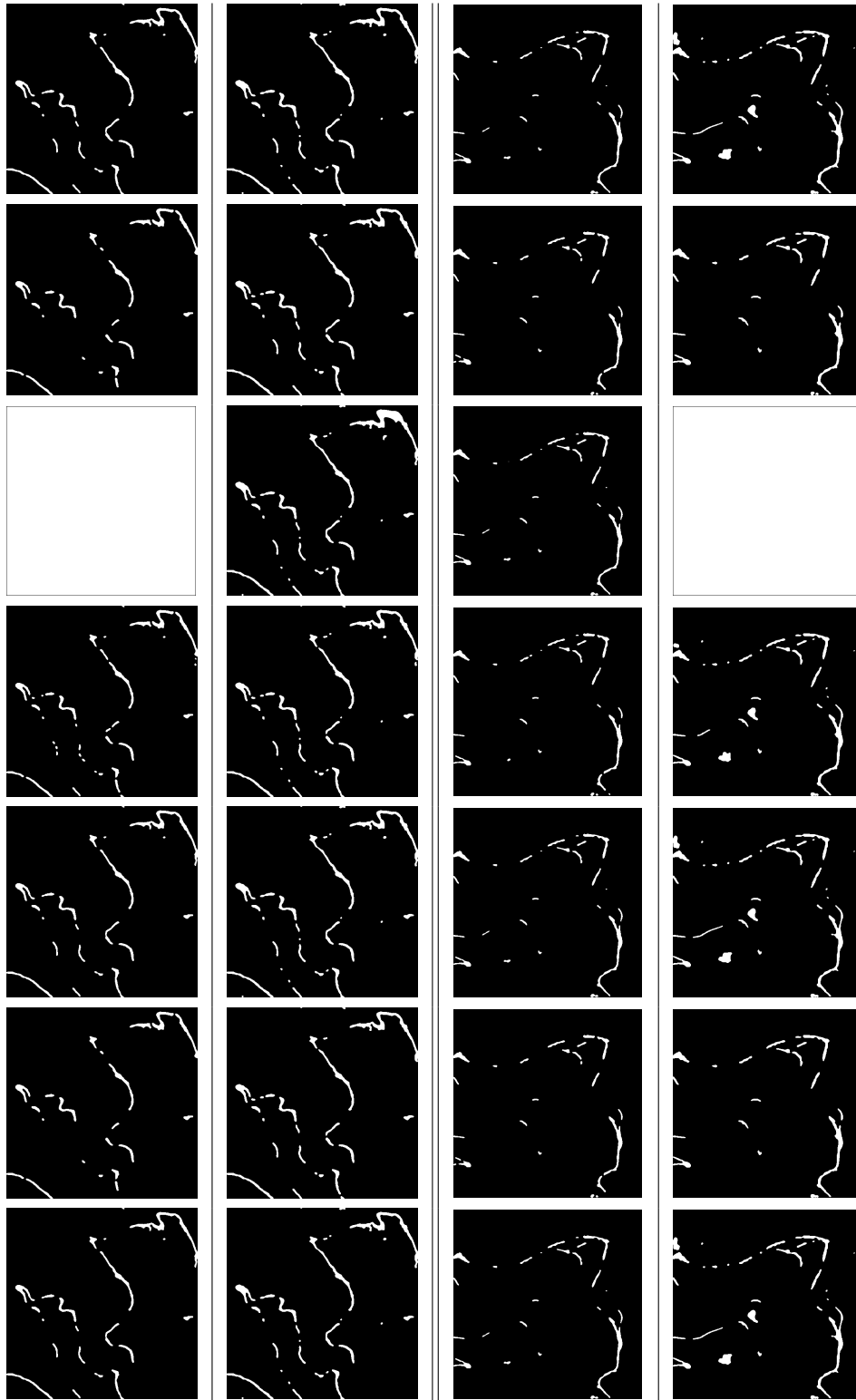


Figure 3.7: Segmentations of the two images in figure 3.3 using different initializations. From top to bottom: NI, -1, +1, UR, ML, -ML, Scaled ML. 1st image: $(w_0, \hat{\alpha}, \lambda_C) = (3, 1.2578, 30)$ for the 1st column and $(3, 1.2578, 20)$ for the 2nd column. Second image: $(2, 0.5924, 15)$ for the 3rd column and $(2, 0.8385, 20)$ for the 4th column. The MG data model was used with the inflection point prior model.

parameter values, which we show both reduces the number of free prior parameters and eliminates false positives; the use of multivariate mixture of two Gaussian models for foreground and background, which we show outperforms the maximum-likelihood-preferred multivariate Gaussian models when coupled with our prior model; and initialization independence despite the use of deterministic gradient descent, as shown by experiments.

In contrast, the proposed undirected network model has two main limitations. Firstly, the model favours network regions where branches have approximately the same width. Secondly, the model does not close gaps in the network as shown in the segmentation results. In the second part of this thesis, we will introduce a new family of phase field models of directed networks to remedy these two problems.

Part II

Phase field HOACs for directed networks

A phase field HOAC model of directed networks

“A new idea comes suddenly and in a rather intuitive way. But intuition is nothing but the outcome of earlier intellectual experience.”

— Albert Einstein

Contents

4.1	Introduction	75
4.2	The proposed model	76
4.3	Turing stability analysis	78
4.4	Experiments	81
4.4.1	Geometric evolutions of v for fixed ϕ	81
4.4.2	Geometric evolutions of v and ϕ	83
4.4.3	Segmentation	83
4.5	Conclusion	85

In the first part of this thesis, we studied the phase field higher-order active contour (HOAC) model introduced by (Rochery et al., 2005, 2006) and conducted a stability analysis of a network branch leading to a phase diagram which enables us to select good parameter values to model undirected networks (*i.e.* the flow in them proceeds in both directions like road networks). Many of the networks that appear in applications (e.g. hydrographic networks in remote sensing, vascular networks in medical imaging) are, however, directed. In this chapter, we introduce a phase field HOAC model of directed networks for hydrographic network extraction from very high resolution (VHR) remote sensing images.

4.1 Introduction

Unlike the road networks previously modelled, hydrographic networks are directed: each network branch has a ‘flow direction’, and each junction therefore has ‘incoming’ and ‘outgoing’ branches. The existence of such a flow typically changes the geometry of the network, because often the flow is in some sense conserved, and suggests that different models are needed. Mathematically speaking, the problem is formulated probabilistically by constructing densities incorporating prior knowledge K about the region R occupied by the entity in the image domain Ω , *i.e.* geometrical, or shape, information. More specifically, we would like a prior model $P(R|K)$ that incorporates typical directed network properties by satisfying the following desiderata:

1. network shapes, in a general sense, should be favoured, *i.e.* high probability regions should take the form of a ‘fattened graph’;
2. a large range of branch widths should be possible, but
3. changes of width should be slow, except
4. at junctions, where the branch widths should be (softly) constrained so that $\sum_i w_i = 0$, where the widths w_i are negative for incoming flow and positive for outgoing flow. Note that this includes the fact that branches should not end, *i.e.* they should be prolonged, since these can be viewed as junctions with only incoming flow.¹

To construct such a model, we start from the phase field higher-order active contour model used by Rochery et al. (2005) and described in section 3.1.1, and extend it. The phase field function ϕ still represents the region R corresponding to the network, and still interacts nonlocally so as to favour network configurations. In addition there is a vector field v representing the ‘flow’ through the network branches. The vector field is coupled to ϕ in such a way that it is strongly encouraged: to be zero outside R ; to have unit magnitude inside R ; to have zero divergence; to be smooth; and to be parallel to the region boundary ∂R (*i.e.* to run ‘along’ the network, not ‘across’ it). The idea is that smoothness and parallelism, coupled with the constraint on the magnitude, will aid prolongation of network branches, and allow a larger range of stable widths, while stabilizing rate of change of width; while divergencelessness will produce asymmetric junctions for which total incoming branch width equals total outgoing branch width.

We describe a stability analysis of the background (*i.e.* exterior of R) and the foreground (*i.e.* interior of R) under the model that provides some constraints on the model parameters (more will appear when we examine stability of a network branch in the next chapter), and then the results of preliminary geometric experiments that show the utility of the above constraints.

4.2 The proposed model

Directed networks by definition possess a sense of direction in each branch, usually due to a unidirectional flow through a channel represented by the branch. Conservation of flow then leads to geometric constraints on the network, particularly at junctions, meaning that directed networks possess different characteristic geometric properties to undirected networks. To model such networks, we introduce a phase field prior, $E_P(\phi, v)$, that in addition to ϕ , is a functional of a tangent vector phase field v which ‘represents’ the flow through the network. We note immediately that v is not supposed to be equal to the physical flow through the network. This would require a much more complicated model than the one we are proposing. Rather, v is an auxiliary quantity (probabilistically speaking, a hidden

¹Such a linear constraint arises if ‘flow volume’ is proportional to branch width in the image. This will be true if flow speed is roughly constant, and if ‘channel volume’ is proportional to branch width in the image, which is true for river networks if channel depth is roughly constant. On the other hand, for tubular networks in three dimensions, one would rather expect the sum of the (appropriately signed) squares of the widths to be zero. In any case, our aim is not to model the detailed physics of each situation, but to model networks that possess certain qualitative geometric properties.

variable) that introduces interactions that constrain the geometry of the network. We will see, however, that in many ways it does behave like a physical flow.

Since v is zero outside the network, we design the ultralocal term of the model to have only two local minima: the background, where $(\phi(x), |v(x)|) = (-1, 0)$; and the foreground where $(\phi(x), |v(x)|) = (1, 1)$. This control of the magnitude of v is in one sense unphysical: for example, the channel may widen while the flow speed decreases, thereby conserving the flow. However, in another sense, it represents real physical effects. Often rigidity in the physical nature of the channel (*e.g.* stiffness of the channel wall, resistance to widening in the substrate in which the channel is embedded) means that such widening is not possible. Some rigidity is already built into the model via ϕ , but control of the magnitude of v , coupled with the divergence term to be described in a moment, reinforces this: it will control the rapidity of width variations. Control of the magnitude of v also represents the fact that in directed networks there is a force that pushes the flow through the network (*e.g.* gravity, pressure), which, in conjunction with viscosity and frictional forces, produces a preferred speed. Again, we do not pretend to be modelling the physics in detail: the constraint on the magnitude of v is a stand-in for these effects, designed to realize certain constraints on the geometry.

In addition to the ultralocal term, we introduce a term that penalizes the divergence of v . This represents a soft version of flow conservation, but the parameter multiplying this term will be large so that in general the divergence will be small. We also add a small overall smoothing term on v , since constraining the divergence is not sufficient to ensure smoothness. Because of the transition from $|v| = 1$ to $|v| = 0$ across the boundary of the region, the divergence term tends to make v parallel to the boundary, *i.e.* the flow is along the channel. Coupled with the constraint on $|v|$ inside the channel, this means that width variations are constrained to be slow along a channel, while at junctions, it tends to produce configurations where total incoming flow is approximately equal to total outgoing flow, which translates to the sum of the incoming widths being approximately equal to the sum of the outgoing widths.

The total prior energy, $E_P(\phi, v)$, is then the sum of a local term E_0 and the nonlocal term E_{NL} given by equation (3.2). E_0 is

$$E_0(\phi, v) = \int_{\Omega} d^2x \left\{ \frac{D}{2} \partial\phi \cdot \partial\phi + \frac{D_v}{2} (\partial \cdot v)^2 + \frac{L_v}{2} \partial v : \partial v + W(\phi, v) \right\}. \quad (4.1)$$

The third term is the smoothing term: $\partial v : \partial v = \sum_{m,n} (\partial_m v^n)^2$, where $m, n \in \{1, 2\}$ label the two Euclidean coordinates. $W(\phi, v)$ is an ultralocal term which defines the stable phases $(\phi, |v|) = (-1, 0)$ and $(\phi, |v|) = (1, 1)$. The generic form of W we use is a fourth order polynomial in ϕ and $|v|$, constrained to be differentiable:

$$W(\phi, v) = \frac{|v|^4}{4} + (\lambda_{22} \frac{\phi^2}{2} + \lambda_{21} \phi + \lambda_{20}) \frac{|v|^2}{2} + \lambda_{04} \frac{\phi^4}{4} + \lambda_{03} \frac{\phi^3}{3} + \lambda_{02} \frac{\phi^2}{2} + \lambda_{01} \phi. \quad (4.2)$$

Just as in the case of the undirected network model, we expect that E_P has local minima corresponding to network shapes. This was directly verified for the undirected network model via a stability analysis of a long bar in chapter 2. In the next chapters, we perform

such an analysis for the current model. In addition, numerical experiments show that such an expectation is indeed correct.

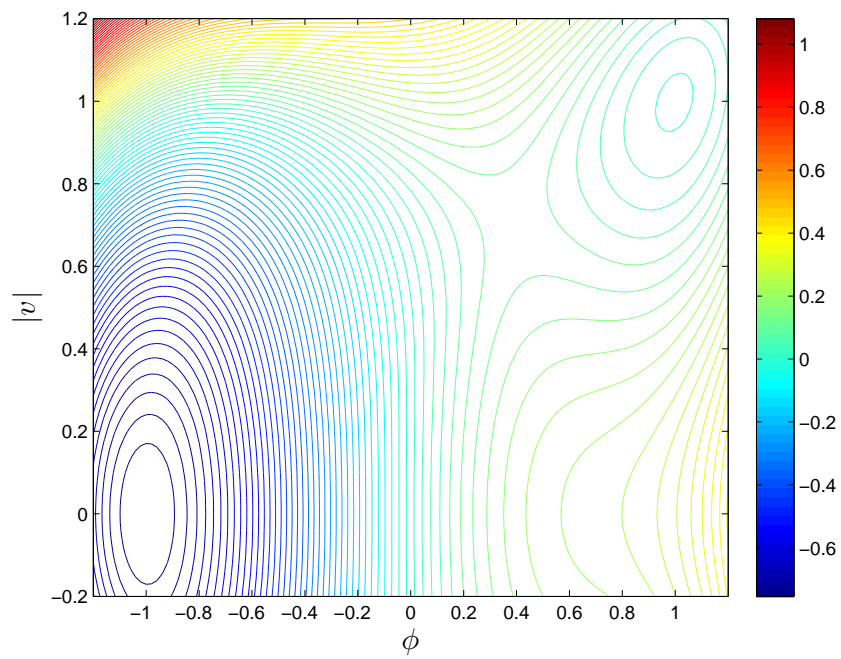
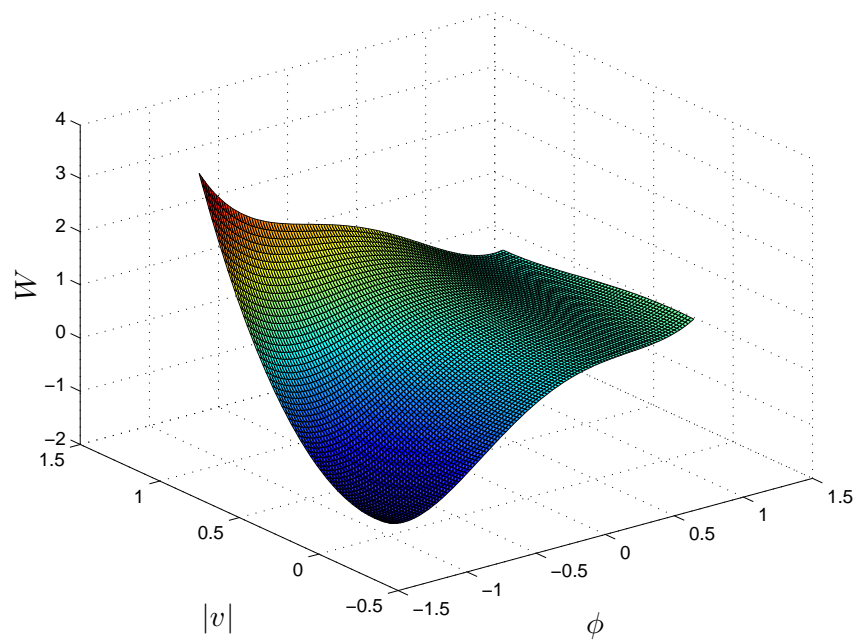
4.3 Turing stability analysis

In this section, we detail the Turing stability analysis (*cf.* Turing (1952)) for the model $E_P = E_0 + E_{NL}$. In the case of the reaction-diffusion system incorporating at least two scalar phase field functions, it has been shown that the presence of diffusion terms, which play the role of smoothing and stabilizing, may form spatial patterns from a uniform phase which is a solution of the reaction terms of the system. So, there are conditions under which a spatially uniform phase is stable in the absence of diffusion but can become unstable to non-uniform perturbations. Here, we study this phenomenon in the case of our model E_P . In our case, the reaction part of the model is the part where all gradient terms are suppressed (*i.e.* their weight are set to 0) and only W remains. Let $(\phi(x), v(x)) = (\phi_0, v_0) \forall x \in \Omega$ be a uniform phase of the system. We assume that the uniform phase is stable which sets the first order variations of W evaluated at (ϕ_0, v_0) to 0 and the Hessian matrix of W to be positive definite at (ϕ_0, v_0) . Now, we study the overall model by analysing the effect of the gradient terms (*i.e.* terms which are weighted by the parameters D, β, L_v and D_v) to the stable uniform solution (ϕ_0, v_0) . The question is then if the uniform phase (ϕ_0, v_0) remains stable by adding an arbitrary infinitesimal perturbation $(\delta\phi, \delta v)$ to it, or it evolves toward other phases showing spatial patterns which we want to avoid. Mathematically, a uniform phase (ϕ_0, v_0) is stable to small changes $\delta\phi$ and δv if the Hessian matrix of $E_P(\phi, v)$ evaluated at (ϕ_0, v_0) is positive definite. As mentioned before, we would like the model E_P to have two stable uniform phases: the background (*i.e.* the exterior of R) and the foreground (*i.e.* the interior of R) described by $(\phi_0, v_0) = (-1, 0)$ and $(1, 1)$ respectively.² So, we require that the phases $(-1, 0)$ and $(1, 1)$ be stable to small changes.

In the first stage, we ensure the uniform phases $(-1, 0)$ and $(1, 1)$ are minima of W . This sets the first order variations of W evaluated at $(-1, 0)$ and $(1, 1)$ equal to zero; and constrains the Hessian matrix of W evaluated at $(-1, 0)$ and $(1, 1)$ to be positive definite. This allows us to express some of the parameters of W as a function of the others: $\lambda_{20} = -1 - \lambda_{22}/2 - \lambda_{21}$, $\lambda_{01} = -\lambda_{22}/4 - \lambda_{21}/4 - \lambda_{03}$ and $\lambda_{02} = -\lambda_{22}/4 - \lambda_{21}/4 - \lambda_{04}$; and lower and upper bounds on parameter values of W are generated to satisfy the positive definiteness condition. We also constrain the free parameters $(\lambda_{04}, \lambda_{03}, \lambda_{22}, \lambda_{21})$ of W so that the phases $(-1, 0)$ and $(1, 1)$ are the only two minima of W by requiring that W be bounded below, and require that the energy of the foreground is greater than of the background, *i.e.* $W(1, 1) > W(-1, 0)$. Figures 4.1 and 4.2 show a contour plot and a 3D plot, respectively, of W satisfying these requirements, and showing local minima at the desired points $(-1, 0)$ and $(1, 1)$. The saddle point (ϕ_s, v_s) between the two minima plays an important role in initializing the gradient descent algorithm: the ‘neutral’ initialization is given by $(\phi, |v|) = (\phi_s, v_s)$, the direction of v being random.

In the second stage, Turing analysis leads to a study of the second order variations of the model E_P in order to constrain the effect of the gradient terms. The components of the Hessian matrix H of $E_P(\phi, v)$ are (see Appendix B.1 for more details about the first partial

²The notation $(\phi_0, v_0) = (1, 1)$ means that the vector field v_0 is of unit magnitude.

Figure 4.1: Contour plot of the ultralocal term W .Figure 4.2: 3D plot of the ultralocal term W .

derivatives)

$$\begin{aligned}
H_{11} &= \frac{\delta^2 E_P(\phi, v)}{\delta\phi'\delta\phi} \\
&= \left[D\Box + \lambda_{22}\frac{|v|^2}{2} + 3\lambda_{04}\phi^2 + 2\lambda_{03}\phi + \lambda_{02} \right] \delta(x, x') - \beta\Box\Psi(x, x') , \\
H_{22} &= \frac{\delta^2 W(\phi, v)}{\delta v'\delta v} \\
&= \left[L_v\delta_{ij}\Box - D_v\partial_i\partial_j + (|v|^2 + \lambda_{22}\frac{\phi^2}{2} + \lambda_{21}\phi + \lambda_{20})\delta_{ij} + 2v^i v^j \right] \delta(x, x') , \\
H_{12} &= \frac{\delta^2 E_P(\phi, v)}{\delta v'\delta\phi} = \frac{\delta^2 E_P(\phi, v)}{\delta\phi'\delta v} \\
&= (\lambda_{22}\phi + \lambda_{21})v\delta(x, x') ,
\end{aligned}$$

where primed and unprimed quantities are evaluated at x and x' respectively; δ_{ij} is the Kronecker delta and $i, j \in \{1, 2\}$ label the Cartesian coordinates; \Box is the negative Laplacian operator *i.e.* $\Box = -\partial^2$; $\delta(x, x')$ is the Dirac delta; $\partial_i\partial_j$ is the second-order tensor operator defined as

$$\begin{pmatrix} \partial_1^2 & \partial_1\partial_2 \\ \partial_2\partial_1 & \partial_2^2 \end{pmatrix} ,$$

and we then notice that: H_{11} is a scalar, H_{12} is a vector and H_{22} is a 2×2 matrix. The Hessian matrix H can then be written as

$$H = \begin{pmatrix} H_{11} & H_{12}^1 & H_{12}^2 \\ H_{12}^1 & H_{22}^{11} & H_{22}^{12} \\ H_{12}^2 & H_{22}^{12} & H_{22}^{22} \end{pmatrix} .$$

As we mentioned, our aim is to analyse the stability of a given configuration (ϕ_0, v_0) corresponding to uniform phase field functions: $(\phi(x), v(x)) = (\phi_0, v_0), \forall x \in \Omega$. We then need to evaluate the Hessian matrix at the uniform fields (ϕ_0, v_0) . The components of H depend on: 1) the Dirac delta function which is diagonal in the space domain and in the Fourier domain as well and 2) the shift invariant function Ψ which can be diagonalized in the Fourier domain. Hence, the Fourier domain diagonalizes the matrix H in the sense of reducing the two spatial variables x and x' to one Fourier variable k instead of k and k' . This is due to the shift invariance of the operators in the spatial domain. The functions H_{ij} evaluated at (ϕ_0, v_0) in the Fourier domain can then be written as (see Appendix B.2 for some examples of Fourier transform calculations)

$$\begin{aligned}
\hat{H}_{11} &= [D - \beta\hat{\Psi}(k)]k^2 + \underbrace{\lambda_{22}\frac{|v_0|^2}{2} + 3\lambda_{04}\phi_0^2 + 2\lambda_{03}\phi_0 + \lambda_{02}}_{F_{11}} , \\
\hat{H}_{22} &= D_v k_i k_j + 2v_0^i v_0^j + L_v k^2 \delta_{ij} + \underbrace{(|v_0|^2 + \lambda_{22}\frac{\phi_0^2}{2} + \lambda_{21}\phi_0 + \lambda_{20})\delta_{ij}}_{F_{22}} , \\
\hat{H}_{12} = \hat{H}_{21} &= \underbrace{(\lambda_{22}\phi_0 + \lambda_{21})v_0}_{F_{12}} ,
\end{aligned}$$

and then \hat{H} becomes

$$\hat{H} = \begin{pmatrix} \hat{H}_{11} & F_{12}v_0^1 & F_{12}v_0^2 \\ F_{12}v_0^1 & L_v k^2 + D_v k_1^2 + 2(v_0^1)^2 + F_{22} & D_v k_1 k_2 + 2v_0^1 v_0^2 \\ F_{12}v_0^2 & D_v k_1 k_2 + 2v_0^1 v_0^2 & L_v k^2 + D_v k_2^2 + 2(v_0^2)^2 + F_{22} \end{pmatrix}. \quad (4.3)$$

We then constrain \hat{H} to be positive definite, for all frequencies k , at $(\phi_0, v_0) = (-1, 0)$, *i.e.* the background, and $(\phi_0, v_0) = (1, 1)$, *i.e.* the foreground. This is equivalent to constraining the 3 eigenvalues of \hat{H} to be strictly positive $\forall k$. In other words, a configuration (ϕ_0, v_0) is stable if it is stable to every k -frequency small change. For example, the 0-frequency perturbation corresponds to adding a small constant value to (ϕ_0, v_0) .

Replacing (ϕ_0, v_0) in \hat{H} and simplifying the positivity conditions of its eigenvalues, we constrain the parameter values by lower and upper bounds in addition to the parameter constraints obtained by putting the first order variations equal to zero. Thus, we select parameter values which ensure the positivity of the eigenvalues for all frequencies k . This guarantees Turing stability. Appendix C details the stability calculations for the background and the foreground.

4.4 Experiments

In section 4.4.1, we study gradient descent evolutions using E_P for fixed ϕ . In section 4.4.2, we study gradient descent evolutions using E_P^s and E_P . In section 4.4.3, we show a segmentation result on a synthetic image of a ‘river configuration’ and on a real satellite image. The interaction function Ψ will be taken to be either the interaction function described by Rochery et al. (2005, 2006), and given by equation (2.2), or the modified Bessel function of the second kind of order 0, K_0 .

We employ a forward Euler scheme for gradient descent evolutions. In the next chapter, we detail the governing equations for gradient descent algorithm and how parameter values are selected in practice.

4.4.1 Geometric evolutions of v for fixed ϕ

Figure 4.3 shows gradient descent evolutions of v with ϕ fixed to a ‘junction’ configuration.³ The first experiment uses the divergence term but no smoothing. Initialized with constant $v = (0, -v_s)$, it shows the effects of the divergence term and the potential, which align the field with the network while conserving the flow. In the second experiment, the initial v was given a random direction at each point. In this case, the divergence of v is small and v is parallel to the boundary near the boundary, but it is not smooth. The condition of small divergence still allows a great deal of freedom: we can add to v any u with $\partial \cdot u = 0$ that preserves the magnitude. The third experiment uses the smoothing term instead of the divergence term. The result is a smooth field, but the field does not run along the network. The fourth experiment uses both divergence and smoothing terms. The vector field evolves from an initially random configuration towards a smooth and divergence-free configuration that runs along the network.

³The parameter values were $(\lambda_{04}, \lambda_{03}, \lambda_{22}, \lambda_{21}) = (2.275, -0.467, 1.34, -3)$ for all evolutions, while from top to bottom: $(L_v, D_v) = (0, 0.1); (0, 0.1); (0.1, 0)$ and $(0.1, 0.1)$.

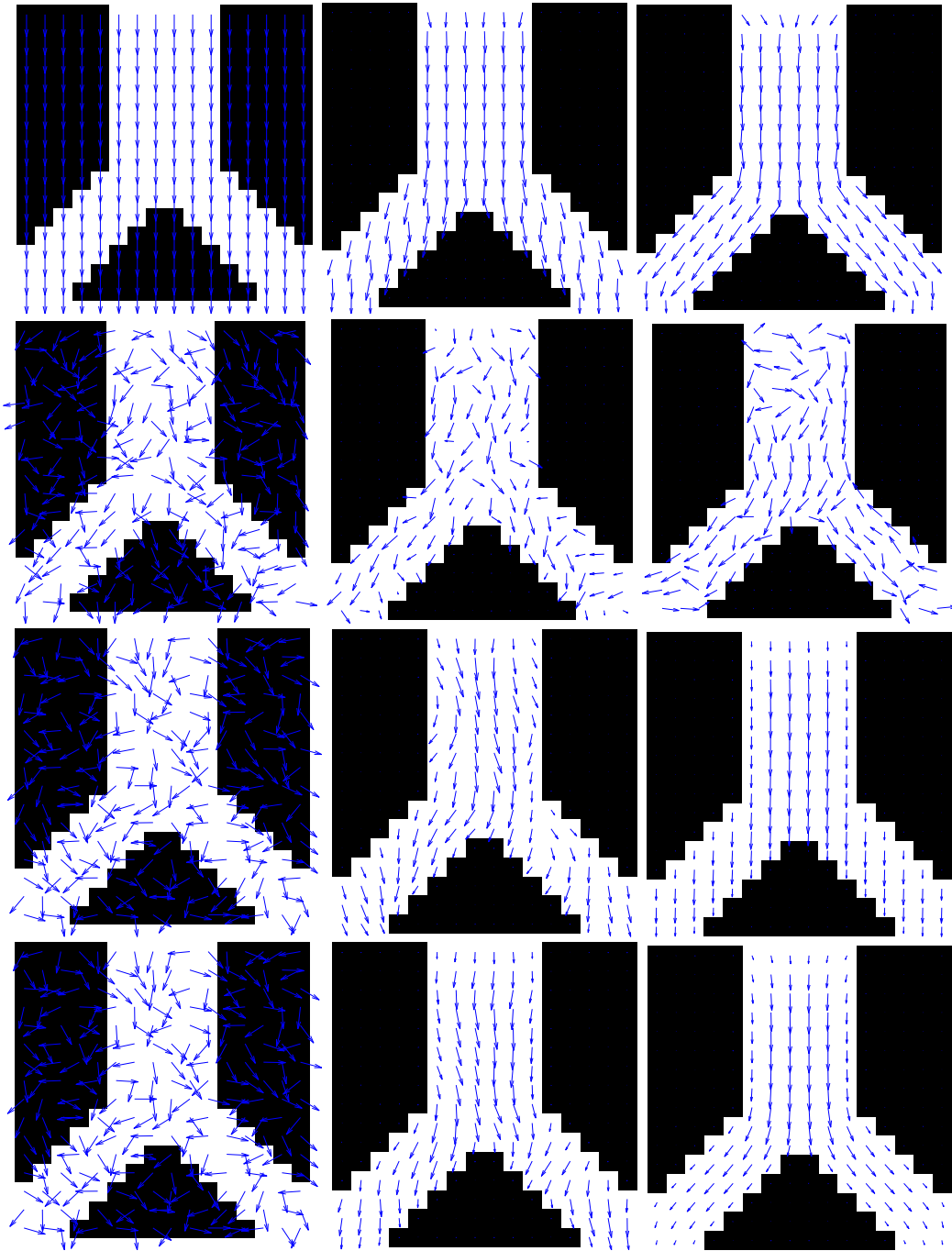


Figure 4.3: Geometric evolutions of v keeping ϕ fixed. First column: initial configuration. Second column: intermediate configuration. Third column: final configuration. From top to bottom: result with the divergence term using a vertical initialization; result with the divergence term using a random initialization; result with the smoothing term; result with the smoothing and divergence terms.

4.4.2 Geometric evolutions of v and ϕ

Figure 4.5 shows gradient descent evolutions using the new energy E_P .⁴ For comparison, figure 4.4 shows gradient descent evolutions using the undirected network phase field model E_P^s .⁵ The initial regions are shown in the leftmost column; time runs from left to right. The binary images are obtained by thresholding ϕ at ϕ_s . The initial configuration for v had $(0, -v_s)$ everywhere, while ϕ had the value -1 outside the region and ϕ_s inside.

Both models produce stable network configurations, but it is illuminating to examine the differences in detail. The first two experiments in each set used the interaction function introduced by Rochery et al. (2005, 2006). This interaction function constrains the possible stable widths quite severely. This renders moot desiderata 2 and 4 described in the introduction of this chapter, and as a result, in these four experiments, the widths of the branches are all more or less the same. The directed network model, though, tends to produce straighter branches with even less width variation than those in the undirected case. This corresponds to desideratum 3.

The last two experiments in each group use K_0 as the interaction function. This constrains the stable width far less severely, and as a result we see a large range of widths in both groups. We have thus satisfied desideratum 2 for our directed network model. However, the spatial distribution of this range is very different in the undirected and the directed cases. In the undirected case, each branch varies in width along its length, tending to ‘bulge out’ away from junctions. In the directed case, in contrast, each branch tends to preserve the same width, although the extent to which it does this depends on the value of the divergence term. This can be seen by comparing the last two experiments in the directed case. The parameter D_v was 20 in the third experiment and 240 in the fourth. As a result, there are some width variations along each branch in the third experiment, whereas in the fourth, they are absent. This satisfies desideratum 3. In addition, the fourth experiment produces long straight branches, while at junctions the sum of incoming and outgoing widths tend to be similar. This can be seen in figure 4.5, but it is more clearly illustrated in figure 4.6, which shows a zoom on the bottom-left quarter of the final configuration in the fourth experiment with the directed network model.⁶ Thus desideratum 4 is satisfied too.

4.4.3 Segmentation

Figure 4.7 shows an experiment using a synthetic image of a ‘river’, consisting of three regions each with a different (constant) intensity value, plus added Gaussian noise. The highest intensity I_1 corresponds to the ‘river’, while the lowest I_{-1} and intermediate $I_0 = (I_{-1} + I_1)/2$ intensities correspond to the background. The zone with intensity I_0 is designed to resemble a network, but one that does not respect ‘flow’ conservation.

⁴From top to bottom, parameter values were: $(\lambda_{04}, \lambda_{03}, \lambda_{22}, \lambda_{21}, D, \beta, d, L_v, D_v) = (3.13, -0.99, 0.131, -2, 0.7, 0.4, 4, 7, 240)$; $(3.13, -0.99, 0.131, -2, 1, 2, 4, 7, 240)$; $(1, 0.072, 0.207, -1, 1, 2, 3, 2, 20)$ and $(1.25, -0.325, 0.368, -1, 1, 2, 3, 7, 240)$.

⁵From top to bottom, parameter values were: $(\lambda, \alpha, D, \beta, d) = (1.24, 0.038, 0.75, 0.137, 4)$; $(1.24, 0.056, 0.75, 0.125, 4)$; $(1.23, 0.076, 0.75, 0.83, 5.65)$ and $(1.23, 0.076, 0.75, 0.917, 5.65)$.

⁶Although not shown here, the evolution of the vector field in this experiment showed an interesting behaviour. At a certain point, it ran from right to left across the short, narrow, horizontal branch (call it B) in figure 4.6. The branch joining B from the lower left widened during the gradient descent, and the flow in B gradually reversed to accommodate the extra flow. This in turn increased the width of the wide, vertical branch flowing down from the right-hand end of B.

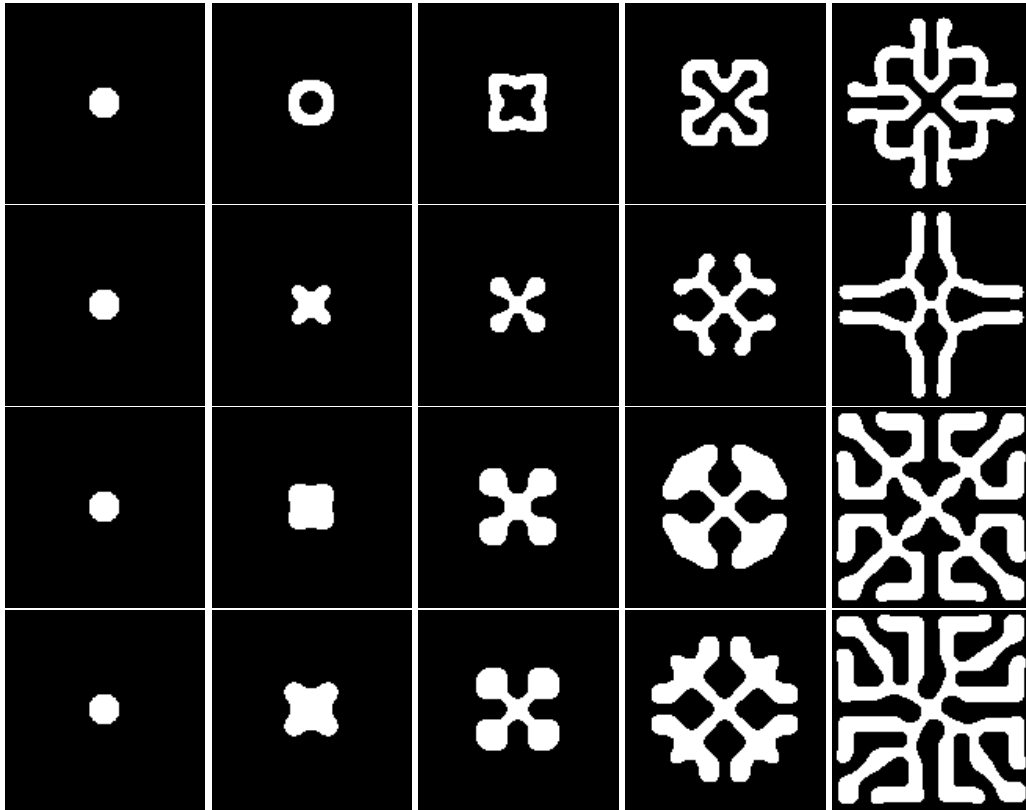


Figure 4.4: Gradient descent evolutions using the undirected network model E_p^s . The initial regions are shown in the leftmost column; time runs from left to right.

The likelihood $P(I|R, K)$ is a product of Gaussian distributions for the intensity at each pixel, with means I_1 for points in R and I_{-1} for points in its complement \bar{R} . The variances for R and \bar{R} are the same. Maximum likelihood classification is thus unable to classify points with intensity I_0 ; the prior that decides whether such points are part of the estimated river region or not.

As can be seen in the bottom row of figure 4.7, the undirected network model, although it finds a network-shaped region, includes a significant amount of the confounding region with intensity I_0 . The directed network model on the other hand, is considerably more accurate because of the geometric constraints arising from ‘flow’ conservation.⁷ Figure 4.8 shows a zoom on the central part of the bottom-right result in figure 4.7, showing v as well as ϕ .

Figure 4.9 shows a segmentation result on a real image of rivers. It shows that the directed network model improves the segmentation result. This is particularly true at network junctions where the divergence-free property of the vector field constrains the geometry in such a way that the flow through them is conserved. Figure 4.10 and 4.11 show clearly how

⁷The parameters used for the undirected and directed network models were: $(\lambda, \alpha, D, \beta, d) = (25, 0.053, 15, 0.01)$ and $(\lambda_{04}, \lambda_{03}, \lambda_{22}, \lambda_{21}, D, \beta, d, L_v, D_v) = (1.025, -0.211, 0.564, -1.5, 0.2, 0.2, 5, 8, 1000)$.

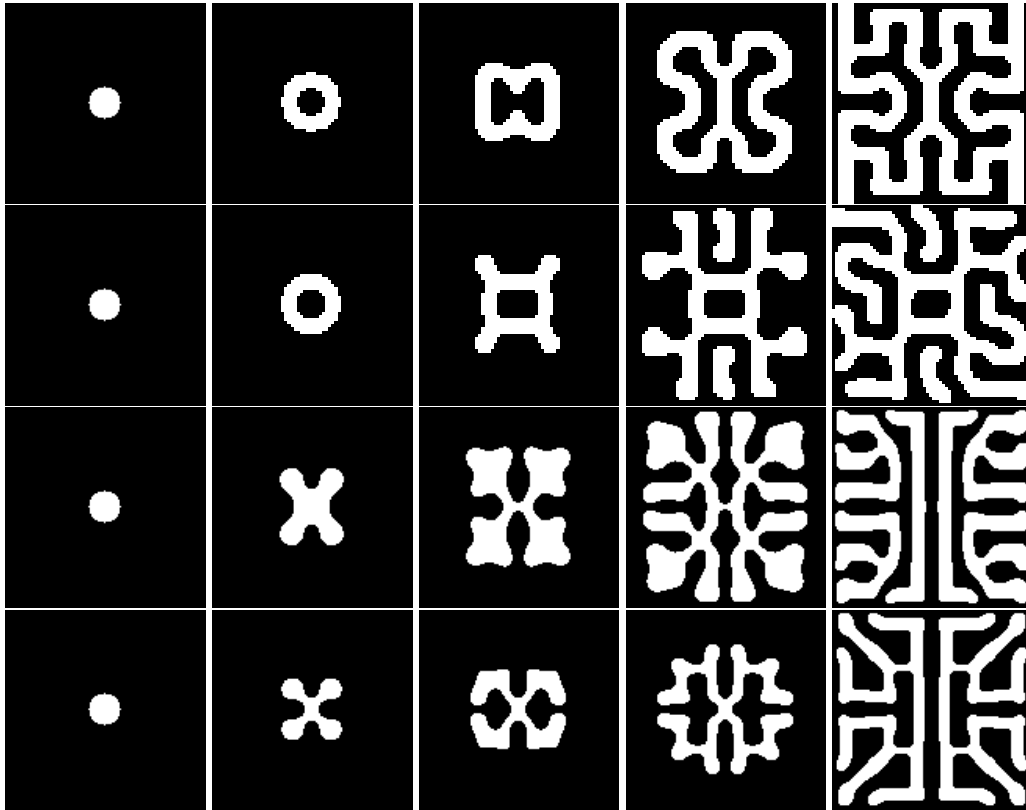


Figure 4.5: Gradient descent evolutions using the new, directed network model E_P . The initial regions are shown in the leftmost column; time runs from left to right.

the vector field behaves along network branches.

4.5 Conclusion

We have introduced a nonlocal phase field model for directed network-shaped regions. The model contains two field variables: a scalar field that describes the region by its smoothed characteristic function, with a long-range interaction that tends to produce network-shaped regions, and a vector field that represents the ‘flow’ through the network. The vector field is strongly encouraged to be divergence-free, and of unit magnitude inside and zero magnitude outside the region. This forces the field in the region to be parallel to the region boundary, and to conserve flow. This results in slow width variations along a network branch, except at junctions, where total incoming flow/width is encouraged to be equal to total outgoing flow/width. We have confirmed the expected behaviour of the model via gradient descent evolutions, and via an extraction experiment on a synthetic image representing part of a hydrographic network and on a real image as well, showing that the new model can avoid errors that arise if the undirected network model is used.

The proposed directed network model has some difficulties involving parameter tuning. The prior model E_P has many free unphysical parameters, which are the weights of

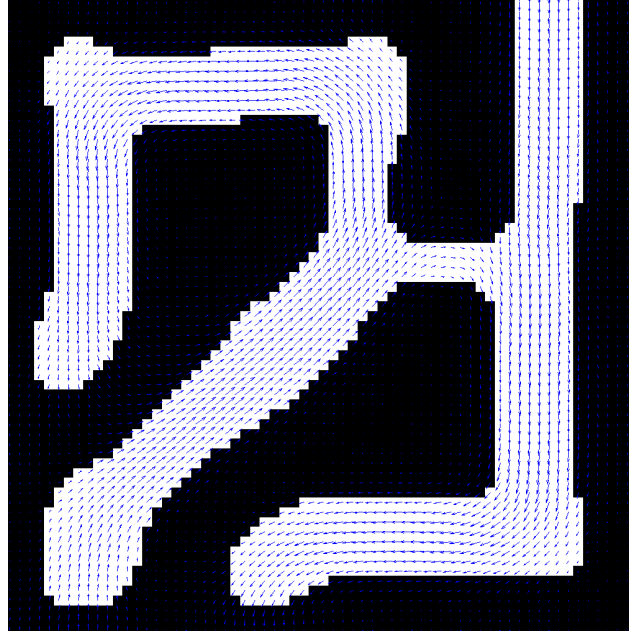


Figure 4.6: A zoom on the bottom-left quarter of the final configuration in the fourth experiment with the directed network model, shown in figure 4.5, showing v as well as ϕ (thresholded at ϕ_s).

energy terms, making parameter setting very difficult. In the next chapter, we will focus on constraining the parameter values for network modelling. A second issue is that the weight of the divergence term must be very large to obtain very low divergence of the vector field. This enforces the gradient descent step to be very small so that the algorithm does not diverge, and consequently the execution time is very large. So, we apply the model on relatively small real images (about 256×256).

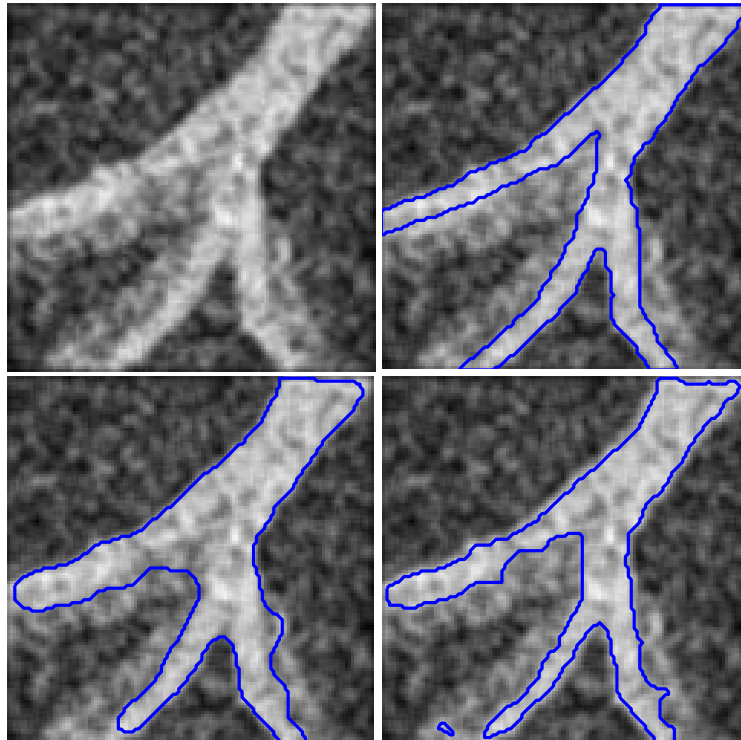


Figure 4.7: From left to right, top to bottom: synthetic image with three grey levels and added noise; ground truth; segmentation using undirected network model; segmentation using directed network model. Note how the constraint on branch width in the directed network model avoids including parts of the background that have similar intensity to the ‘river’.

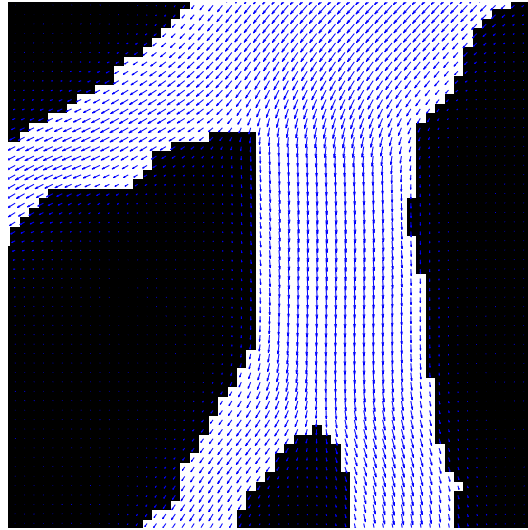


Figure 4.8: A zoom on the central part of the result in figure 4.7, showing v as well as ϕ (thresholded at ϕ_s).

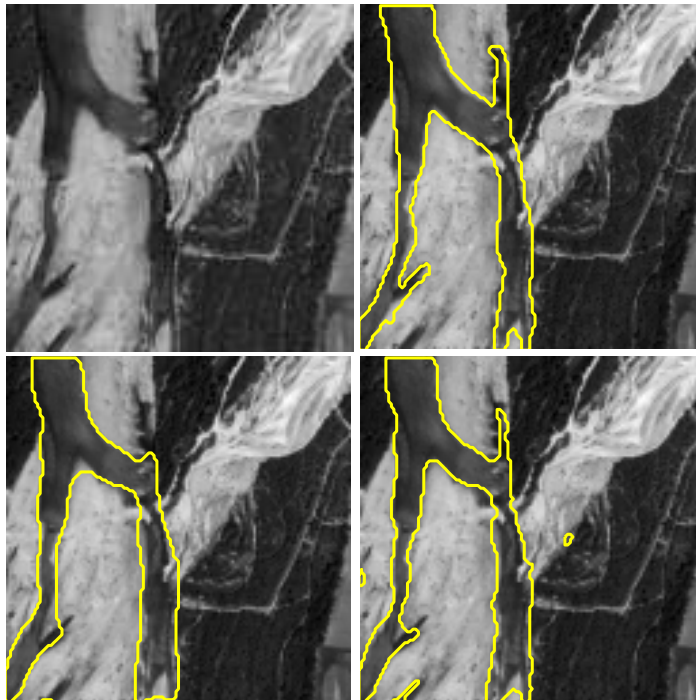


Figure 4.9: From left to right, top to bottom: real image; ground truth; segmentation using undirected network model; segmentation using directed network model. Note how the constraint on junction widths in the directed network model guarantees flow conservation. (Images ©DigitalGlobe, CNES processing, images acquired via ORFEO Accompaniment Program).

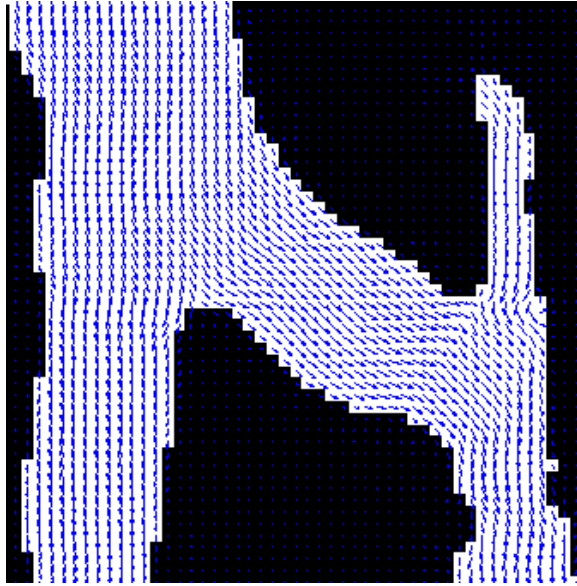


Figure 4.10: A zoom on the upper part of the result in figure 4.9, showing v as well as ϕ (thresholded at ϕ_s).

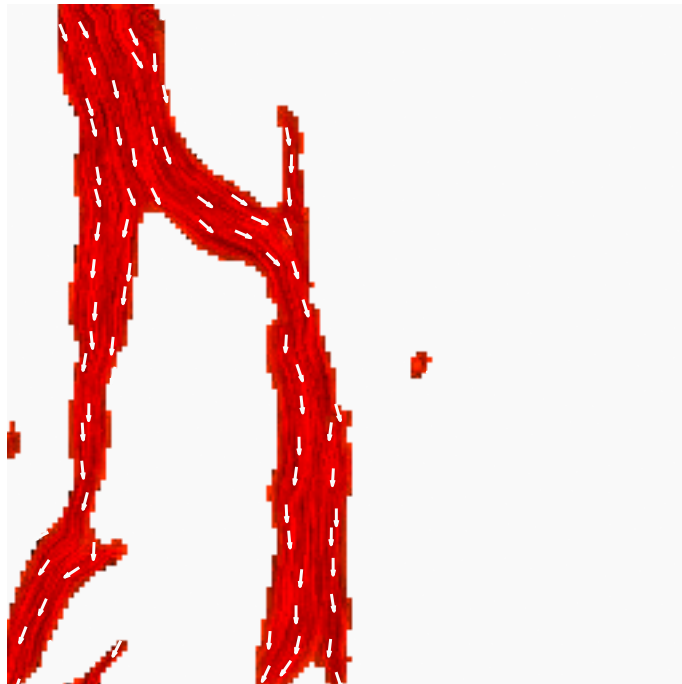


Figure 4.11: A streamline plot of the result in figure 4.9, showing v as well as ϕ (thresholded at ϕ_s).

Stability analysis of a long bar

“Geometry enlightens the intellect and sets one’s mind right. All of its proofs are very clear and orderly. It is hardly possible for errors to enter into geometrical reasoning, because it is well arranged and orderly. Thus, the mind that constantly applies itself to geometry is not likely to fall into error. In this convenient way, the person who knows geometry acquires intelligence.”

— Ibn Khaldun

Contents

5.1	Introduction	91
5.2	Stability analysis	92
5.2.1	Energy of the bar	92
5.2.1.1	Local energy of the bar	94
5.2.1.2	Nonlocal energy of the bar	95
5.2.1.3	Total energy of the bar	96
5.2.2	Stability conditions for the bar	96
5.2.2.1	First order stability conditions	96
5.2.2.2	Second order stability conditions	99
5.3	Overall model and parameter settings	99
5.3.1	Overall energy	99
5.3.2	Optimization and parameter settings	99
5.4	Conclusion	102

In this chapter, we analyse the stability of a network branch under the directed network model introduced in chapter 4. We focus on zero-frequency perturbations of the region boundary, which correspond to changes in the branch width. The resulting constraints necessary to produce stable networks eliminate some parameters, replace others by physical parameters such as network branch width, and place lower and upper bounds on the values of the rest. In the next chapter, we will validate the theoretical analysis via numerical experiments, and then will apply the model to the problem of road and hydrographic network extraction from multi-spectral VHR satellite images.

5.1 Introduction

A network-shaped region can be thought of as a set of branches joining at junctions. As with the undirected network model, we will assume that network branches are long enough

and straight enough that their stability can be analysed by considering the limit of a long, straight bar. Ideally, the analysis should proceed by first finding the energy minimizing $\phi_{R_{\text{Bar}}}$ and $v_{R_{\text{Bar}}}$ for the bar region, and then expanding around these values. In practice, there are two obstacles. First, $\phi_{R_{\text{Bar}}}$ and $v_{R_{\text{Bar}}}$ cannot be found exactly. Second, it is not possible to diagonalize exactly the second derivative operator, and thus hard to impose positive definiteness for stability. Approximate results are therefore necessary.

Figure 5.1 shows how the phase field functions behave for a stable network configuration which is obtained by running gradient descent to minimize the prior phase field energy E_P . The first row shows a stable network configuration (left) and a zoom on its central part showing ϕ and v (right). The latter shows the preferred vector field configuration along network branches. The second row shows the profiles of the functions ϕ (left) and $|v|$ (right), which minimize the energy of the network configuration shown on the right of the first row. The third row shows initial (left) and final (right) slices of ϕ and $|v|$, given in blue, across a network branch; the proposed approximations of ϕ and $|v|$ are shown in black. In this chapter, we define a four-parameter family of *ansatzes* for $\phi_{R_{\text{Bar}}}$ and $v_{R_{\text{Bar}}}$, and analyse the stability of this family. More sophisticated approaches are possible by expanding $\phi_{R_{\text{Bar}}}$, $v_{R_{\text{Bar}}}$, and the second derivative operator in some small parameter.

5.2 Stability analysis

In this section, we detail the stability analysis of a four-parameter family of *ansatzes* for $\phi_{R_{\text{Bar}}}$ and $v_{R_{\text{Bar}}}$. Figure 5.2 shows the *ansatz* for a directed bar. Two phase field variables are involved: the scalar field $\phi_{R_{\text{Bar}}}$ and the vector field $v_{R_{\text{Bar}}}$. The configuration is defined as follows: a scalar field $\phi_{R_{\text{Bar}}}$ which varies linearly from -1 to ϕ_m across a region interface of width w , otherwise being -1 outside and ϕ_m inside the bar, which has width w_0 ; and a divergence-free vector field $v_{R_{\text{Bar}}}$ whose magnitude varies linearly from 0 to v_m across the region interface, otherwise being 0 outside and v_m inside the bar. The four physical parameters w_0 , w , ϕ_m and v_m define the four-parameter family of *ansatzes* for the bar.

5.2.1 Energy of the bar

In this section, we calculate the energy of the bar *ansatz*. To compute the energy, we split the image domain into 3 regions: the internal region R , the external region \bar{R} and the interface R_C . The bar has two interfaces: a top interface R_{CT} and a bottom interface R_{CB} . The *ansatzes* for the scalar phase field and the magnitude of the vector phase field are, as has been described, given by

$$\phi_{R_{\text{Bar}}}(x) = \begin{cases} \frac{\phi_m+1}{w}x_2 - 1 & \text{if } 0 < x_2 < w, \\ \phi_m & \text{if } w < x_2 < w_0, \\ \frac{\phi_m+1}{w}(w_0 - x_2) + 1 & \text{if } w_0 < x_2 < w_0 + w, \\ -1 & \text{else.} \end{cases} \quad (5.1)$$

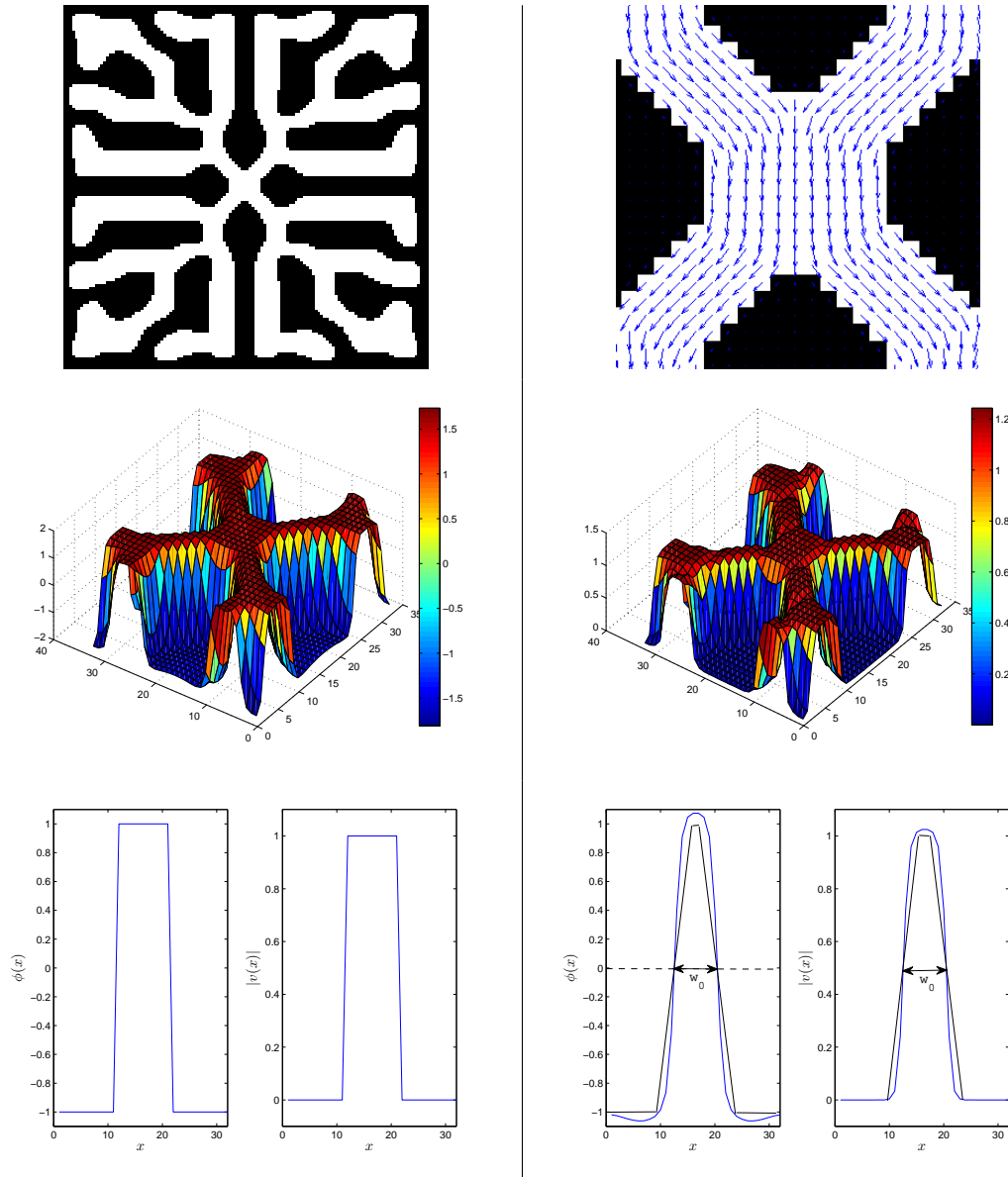


Figure 5.1: First row: a stable network configuration (left) and a zoom on its central part showing ϕ and v (right). Second row: profiles of functions ϕ (left) and $|v|$ (right) of the network shown on the right of the first row. Third row: initial (left) and final (right) slices of ϕ and $|v|$, given in blue, across a network branch after gradient descent; the proposed approximations of ϕ and $|v|$ are shown in black.

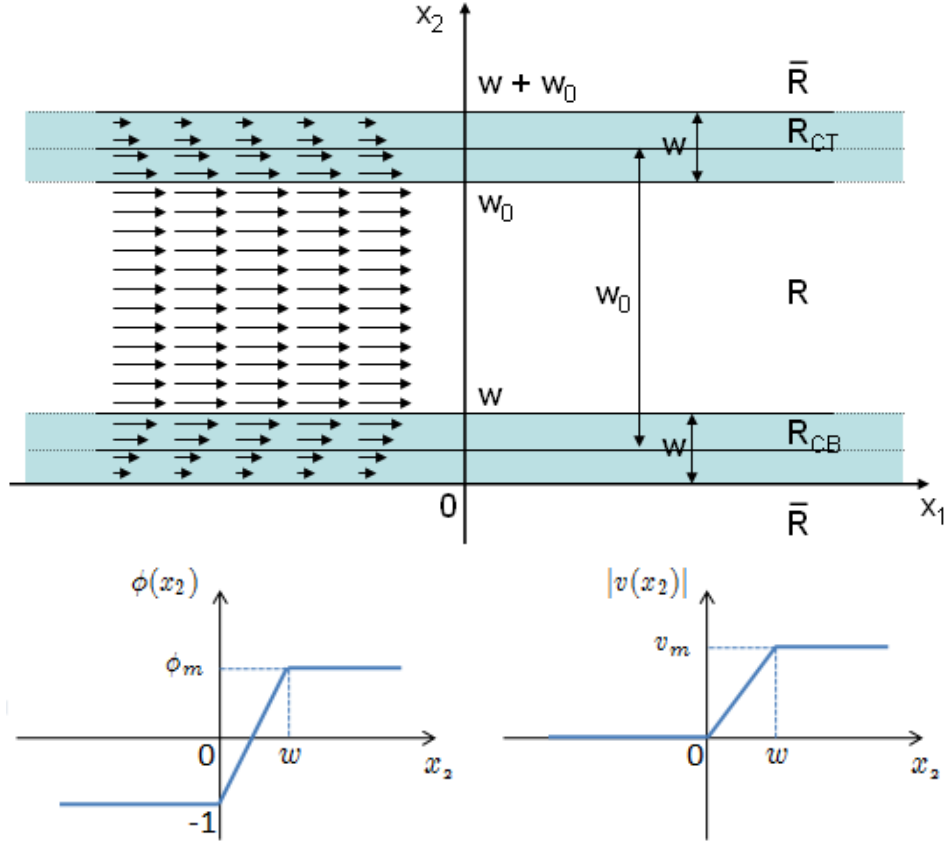


Figure 5.2: Directed bar *ansatz*, showing the parameterization in terms of the physical parameters w_0 , w , ϕ_m and v_m .

and

$$|v_{R\text{Bar}}(x)| = \begin{cases} \frac{v_m}{w} x_2 & \text{if } 0 < x_2 < w, \\ v_m & \text{if } w < x_2 < w_0, \\ \frac{v_m}{w} (w_0 - x_2) + 1 & \text{if } w_0 < x_2 < w_0 + w, \\ 0 & \text{else.} \end{cases} \quad (5.2)$$

5.2.1.1 Local energy of the bar

The local phase field energy is

$$E_0(\phi, v) = \int_{\Omega} d^2x \left\{ \frac{D}{2} \partial\phi \cdot \partial\phi + \tilde{W}(\phi, v) + \frac{D_v}{2} (\partial \cdot v)^2 + \frac{L_v}{2} \partial v : \partial v \right\}, \quad (5.3)$$

where $\tilde{W}(\phi, v) = W(\phi, v) - W(-1, 0)$. W is the ultralocal term given by equation (4.2). (This ensures that the energy of the background is zero, $\tilde{W}(-1, 0) = 0$, which facilitates the stability calculations.) Shifting the values of W by a constant value $W(-1, 0)$ does not change the minimizing functions of E_0 .

Substituting the bar *ansatzes* by their expressions given by equations (5.1) and (5.2), the total local bar energy becomes (cf. Appendix D.1)

$$\begin{aligned} E_0(\phi_{R_{\text{Bar}}}, v_{R_{\text{Bar}}}) &= E_{0,R} + E_{0,\bar{R}} + E_{0,R_C} \\ &= Lw_0\nu(\phi_m, v_m) + Lw\mu(\phi_m, v_m) + L\frac{D(\phi_m + 1)^2 + L_v v_m^2}{w}, \end{aligned}$$

where we define the total local bar energy per unit length as $e_0 = E_0/L$. The functions $\nu(\phi_m, v_m)$ and $\mu(\phi_m, v_m)$ are

$$\begin{aligned} \mu(\phi_m, v_m) &= -\frac{3v_m^4}{20} + \frac{v_m^2}{2} \left(\frac{\lambda_{22}}{10}(\phi_m + 1)(-3\phi_m + 2) \right. \\ &\quad \left. + \frac{\lambda_{21}}{6}(-3\phi_m + 1) + \frac{1}{3} \right) \\ &\quad + \frac{\lambda_{04}}{60}(\phi_m + 1)^2(-9\phi_m^2 + 12\phi_m + 1) \\ &\quad + \frac{\lambda_{03}}{6}(\phi_m + 1)^2(-\phi_m + 1) \\ &\quad + \frac{1}{24}(\lambda_{22} + \lambda_{21})(\phi_m + 1)^2, \\ \nu(\phi_m, v_m) &= W(\phi_m, v_m) - W(-1, 0) \\ &= \frac{v_m^4}{4} + \frac{v_m^2}{2} \left(\frac{\lambda_{22}}{2}(\phi_m^2 - 1) + \lambda_{21}(\phi_m - 1) - 1 \right) \\ &\quad + \frac{\lambda_{04}}{4}(\phi_m^2 - 1)^2 + \frac{\lambda_{03}}{3}(\phi_m + 1)^2(\phi_m - 2) \\ &\quad - \frac{1}{8}(\lambda_{22} + \lambda_{21})(\phi_m + 1)^2. \end{aligned}$$

5.2.1.2 Nonlocal energy of the bar

The contribution of the nonlocal phase field term given by equation (3.2) appears only along the boundary occupied by the region R_C . The nonlocal energy of the bar is (cf. Appendix D.1)

$$E_{\text{NL}}(\phi_{R_{\text{Bar}}}) = -Ld\beta(\phi_m + 1)^2 G_{00}(\hat{w}_0, \hat{w}),$$

where $\hat{w} = w/d$, $\hat{w}_0 = w_0/d$ and

$$G_{00}(\hat{w}_0, \hat{w}) = \frac{2}{\hat{w}^2} \int_0^{+\infty} \int_0^{\hat{w}} dz dx_2 \int_{-x_2}^{\hat{w}-x_2} dt \left\{ \Psi \left(\sqrt{z^2 + t^2} \right) - \Psi \left(\sqrt{z^2 + (\hat{w}_0 + t)^2} \right) \right\}.$$

We define the nonlocal energy per unit length as $e_{\text{NL}} = E_{\text{NL}}/L$.

5.2.1.3 Total energy of the bar

The total energy per unit length of the bar, $e_0 + e_{\text{NL}}$, is

$$e_{\text{P}}(\hat{w}_0, \hat{w}, \phi_m, v_m) = \hat{w}_0 \nu(\phi_m, v_m) + \hat{w} \mu(\phi_m, v_m) - \beta(\phi_m + 1)^2 G_{00}(\hat{w}_0, \hat{w}) + \frac{\hat{D}(\phi_m + 1)^2 + \hat{L}_v v_m^2}{\hat{w}}, \quad (5.4)$$

where $\hat{w} = w/d$, $\hat{w}_0 = w_0/d$, $\hat{D} = D/d^2$ and $\hat{L}_v = L_v/d^2$ are the dimensionless parameters.

The stability analysis of a network branch under the undirected network model described in section 3.1.1 was performed by Peng et al. (2008b). They found a bar energy similar to that in equation (5.4). We notice that the parameters μ and ν play the same roles as λ and α given in equation (3.1) respectively. The energy gap between the foreground and the background is equal to 2α in the case of the undirected network model and ν in the case of the directed network model. The parameter ν must be strictly positive to favour pixels belonging to the background: this effect is similar to the area force which tends to minimize the area of the region. The parameter μ controls the contribution of W across the region interface of width w : it has an effect similar to the parameter λ .

5.2.2 Stability conditions for the bar

The energy of a network branch is given by e_{P} . A network branch is stable in the four-parameter family of *ansatzes* if it minimizes $e_{\text{P}}(\hat{w}_0, \hat{w}, \phi_m, v_m)$ with respect to variations of \hat{w}_0 , \hat{w} , ϕ_m and v_m . This is equivalent to setting the first order variations of $e_{\text{P}}(\hat{w}_0, \hat{w}, \phi_m, v_m)$ equal to zero and requiring its Hessian matrix to be positive definite. The desired value of (ϕ_m, v_m) is $(1, 1)$ to describe the interior of the region R . These stability conditions produce parameter constraints.

5.2.2.1 First order stability conditions

The first order variations of e_{P} with respect to \hat{w}_0 , \hat{w} , ϕ_m and v_m are (cf. Appendix D.2)

$$\begin{aligned} \frac{\partial e_{\text{P}}(\hat{w}_0, \hat{w}, \phi_m, v_m)}{\partial \hat{w}_0} &= \nu(\phi_m, v_m) - \beta(\phi_m + 1)^2 G_{10}(\hat{w}_0, \hat{w}), \\ \frac{\partial e_{\text{P}}(\hat{w}_0, \hat{w}, \phi_m, v_m)}{\partial \hat{w}} &= \mu(\phi_m, v_m) - \frac{\hat{D}(\phi_m + 1)^2 + \hat{L}_v v_m^2}{\hat{w}^2} \\ &\quad - \beta(\phi_m + 1)^2 G_{11}(\hat{w}_0, \hat{w}), \\ \frac{\partial e_{\text{P}}(\hat{w}_0, \hat{w}, \phi_m, v_m)}{\partial \phi_m} &= \hat{w}_0 \nu_{\phi}(\phi_m, v_m) + \hat{w} \mu_{\phi}(\phi_m, v_m) - 2\beta(\phi_m + 1) G_{00}(\hat{w}_0, \hat{w}) \\ &\quad + 2 \frac{\hat{D}(\phi_m + 1)}{\hat{w}}, \\ \frac{\partial e_{\text{P}}(\hat{w}_0, \hat{w}, \phi_m, v_m)}{\partial v_m} &= \hat{w}_0 \nu_v(\phi_m, v_m) + \hat{w} \mu_v(\phi_m, v_m) + 2 \frac{\hat{L}_v v_m}{\hat{w}}, \end{aligned}$$

where $\nu_{\phi} = \partial \nu / \partial \phi_m$, $\mu_{\phi} = \partial \mu / \partial \phi_m$, $\nu_v = \partial \nu / \partial v_m$, $\mu_v = \partial \mu / \partial v_m$, $G_{10} = \partial G_{00} / \partial \hat{w}_0$ and $G_{11} = \partial G_{00} / \partial \hat{w}$. Setting the first order variations of e_{P} , evaluated at

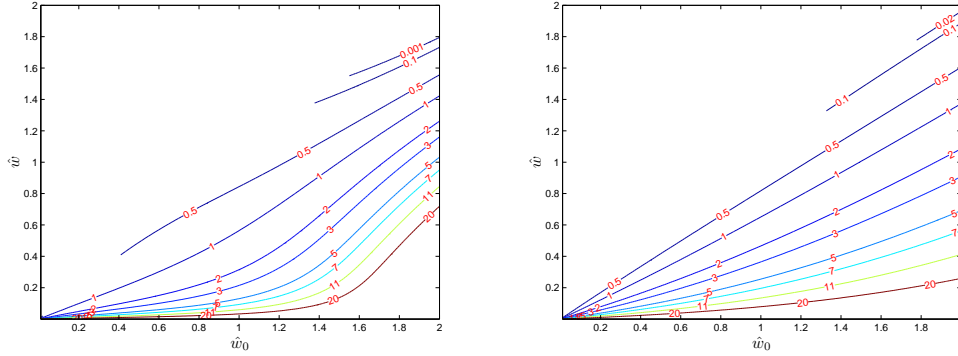


Figure 5.3: Example of solutions of equation (5.5) for some values of ρ^* using Rochery et al. (2005)'s interaction function (left) and K_0 (right). Curves are labeled by the values of ρ^* .

$(\hat{w}_0, \hat{w}, \phi_m, v_m) = (\hat{w}_0, \hat{w}, 1, 1)$, equal to zero, and after some mathematical manipulations, one can write the parameter constraints as

$$\rho^* - G(\hat{w}_0, \hat{w}) = 0, \quad (5.5)$$

$$\beta = \frac{\nu^*}{4G_{10}(\hat{w}_0, \hat{w})}, \quad (5.6)$$

$$\hat{D} = \frac{\hat{w}}{2} \left[\frac{\nu^* G_{00}(\hat{w}_0, \hat{w})}{2G_{10}(\hat{w}_0, \hat{w})} - \hat{w} \mu_\phi^* \right], \quad (5.7)$$

$$\hat{L}_v = -\frac{\hat{w}^2 \mu_v^*}{2}, \quad (5.8)$$

where $G(\hat{w}_0, \hat{w}) = [G_{00}(\hat{w}_0, \hat{w})/\hat{w} + G_{11}(\hat{w}_0, \hat{w})]/G_{10}(\hat{w}_0, \hat{w})$, $\rho^* = [\mu^* + \mu_\phi^* + \mu_v^*/2]/\nu^*$, $\nu^* = \nu(1, 1)$, $\mu^* = \mu(1, 1)$, $\mu_\phi^* = \mu_\phi(1, 1)$ and $\mu_v^* = \mu_v(1, 1)$. $\nu_\phi(1, 1)$ and $\nu_v(1, 1)$ are equal to 0 because $(1, 1)$ is a minimum of W . The starred parameters depend only on the 4 free potential parameters $\pi_\lambda = (\lambda_{22}, \lambda_{21}, \lambda_{04}, \lambda_{03})$. The parameter positivity conditions $\hat{D} > 0$ and $\hat{L}_v > 0$ generate lower and upper bounds on \hat{w}_0 , \hat{w} and π_λ . Equation (5.5) shows that, for fixed π_λ i.e. ρ^* is determined, the set of solutions in the plane (\hat{w}_0, \hat{w}) is the intersection of the surface representing the function G and the plane located at ρ^* . The result is then a set of curves in the plane (\hat{w}_0, \hat{w}) where each corresponds to a value of ρ^* . Figure 5.3 shows an example of solutions of equation (5.5) for some values of ρ^* using Rochery et al. (2005)'s interaction function (left) and K_0 (right).

Equation (5.6) shows that stability depends mainly on the scaled parameter $\hat{\beta} = \beta/\nu^*$. Figure 5.4 plots the behaviour of $\hat{\beta}$ against the scaled bar width \hat{w}_0 and the scaled interface width \hat{w} . The left-hand graph shows the behaviour of $\hat{\beta}$ when the interaction function Ψ is that introduced by Rochery et al. (2005). The right-hand graph shows the behaviour of $\hat{\beta}$ when Ψ is K_0 . For both graphs, we have plotted the surfaces as two half-surfaces: one is lighter (right-hand half-surface, smaller \hat{w}_0) than the other (left-hand half-surface, bigger \hat{w}_0). The valley between both half-surfaces corresponds to the minimum value of $\hat{\beta}$ for each value of \hat{w} .

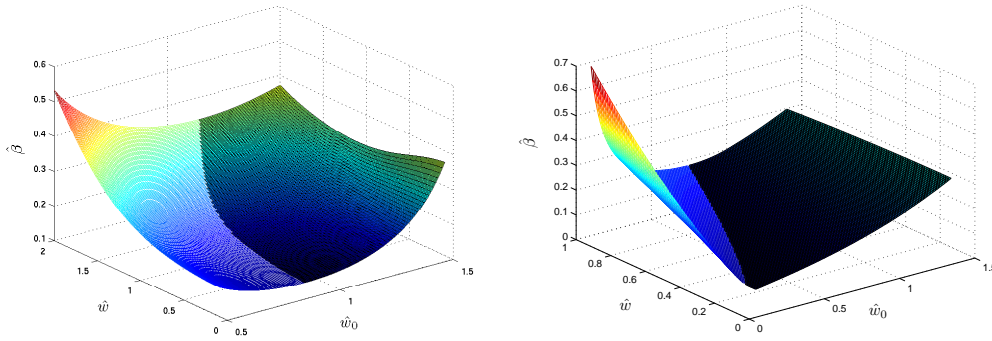


Figure 5.4: Left: behaviour of $\hat{\beta}$ using Rochery et al. (2005)'s interaction function. Right: behaviour of $\hat{\beta}$ using K_0 . The light and dark surfaces show the locations of maxima and minima respectively.

Both graphs show that: for each value $\hat{\beta} < \hat{\beta}_{\min} = \inf(1/4G_{10}(\hat{w}_0, \hat{w}))$ where $\hat{\beta}_{\min} = 0.1302$ (left) and 0.0879 (right), there are no possible values of (\hat{w}_0, \hat{w}) which satisfy the constraints and so the bar energy does not have minima; for each value $\hat{\beta} > \hat{\beta}_{\min}$ and for some chosen values of \hat{w} , there are two possible values of \hat{w}_0 which satisfy the constraints: the smaller width (left-hand half-surface) corresponds to an energy maximum and the bigger width (right-hand half-surface) corresponds to an energy minimum.

Figure 5.5 shows plots of bar energies against bar width using Rochery et al. (2005)'s interaction function (left) and K_0 (right). The latter has a flatter basin around the desired energy minimum than the former which constrains the range of widths more severely: this implies a larger range of stable widths when using K_0 .

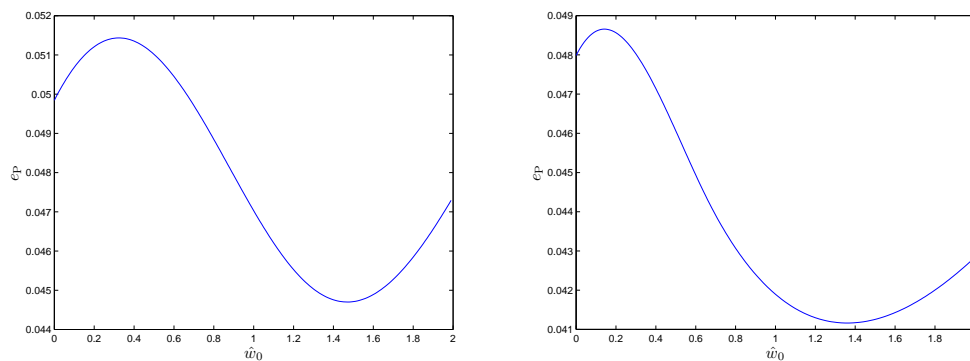


Figure 5.5: Bar energies against w_0 using Rochery et al. (2005)'s interaction function (left) and K_0 (right).

5.2.2.2 Second order stability conditions

The Hessian matrix H_{Bar} is

$$H_{\text{Bar}} = \begin{pmatrix} \frac{\partial^2 e_{\text{P}}}{\partial \hat{w}_0^2} & \frac{\partial^2 e_{\text{P}}}{\partial w \partial \hat{w}_0} & \frac{\partial^2 e_{\text{P}}}{\partial \phi_m \partial \hat{w}_0} & \frac{\partial^2 e_{\text{P}}}{\partial v_m \partial \hat{w}_0} \\ \frac{\partial^2 e_{\text{P}}}{\partial w \partial \hat{w}_0} & \frac{\partial^2 e_{\text{P}}}{\partial w^2} & \frac{\partial^2 e_{\text{P}}}{\partial \phi_m \partial w} & \frac{\partial^2 e_{\text{P}}}{\partial v_m \partial w} \\ \frac{\partial^2 e_{\text{P}}}{\partial \phi_m \partial \hat{w}_0} & \frac{\partial^2 e_{\text{P}}}{\partial \phi_m \partial w} & \frac{\partial^2 e_{\text{P}}}{\partial \phi_m^2} & \frac{\partial^2 e_{\text{P}}}{\partial v_m \partial \phi_m} \\ \frac{\partial^2 e_{\text{P}}}{\partial v_m \partial \hat{w}_0} & \frac{\partial^2 e_{\text{P}}}{\partial v_m \partial w} & \frac{\partial^2 e_{\text{P}}}{\partial v_m \partial \phi_m} & \frac{\partial^2 e_{\text{P}}}{\partial v_m^2} \end{pmatrix},$$

where H_{Bar} must be positive definite at $(\hat{w}_0, \hat{w}, 1, 1)$. This generates upper and lower bounds on the parameter values. This condition is tested numerically because we cannot compute the eigenvalues of H_{Bar} explicitly.

Figure 5.6 shows bar energies, e_{P} , against the physical parameters of the bar $\pi_{\text{B}} = (\hat{w}_0, \hat{w}, \phi_m, v_m)$. The desired energy minimum was chosen at $\pi_{\text{B}}^* = (1.36, 0.67, 1, 1)$.¹ We first choose π_{λ} , and then compute D , β and L_v using the parameter constraints given in the previous section. The first and second rows show 1D plot of bar energies, which have a minimum at the desired value π_{B}^* . The third row shows 2D contour plots of bar energies illustrating the location of the desired energy minimum.

5.3 Overall model and parameter settings

In this section, we define the overall model to be applied to real images, and describe the optimization process and how the parameter values are selected in practice.

5.3.1 Overall energy

To apply the model to real images, a likelihood energy E_{I} linking the region R to the data I is needed in addition to the prior term E_{P} . The problem we are dealing with is the extraction of road and hydrographic networks from multi-spectral VHR Quickbird images. E_{I} is studied in detail in section 3.3.2. The total energy to be minimized is then $E(\phi, v; I) = E_{\text{I}}(I, \phi) + \theta E_{\text{P}}(\phi, v)$ where $\theta > 0$ is a parameter which balances the two energy terms.

5.3.2 Optimization and parameter settings

In this work, we use gradient descent to seek energy minima. To do this, we need to compute the forces $\delta E_{\text{P}}/\delta \phi$ and $\delta E_{\text{P}}/\delta v$ (cf. Appendix B.1). The force of the data term, $\delta E_{\text{I}}/\delta \phi$, is given by equation (3.7). In practice, we implement the linear terms of the gov-

¹The parameter values were $(\lambda_{04}, \lambda_{03}, \lambda_{22}, \lambda_{21}, D, \beta, d, L_v, D_v) = (0.05, 0.025, 0.013, -0.6, 0.0007, 0.003, 1, 0.208, 0)$.

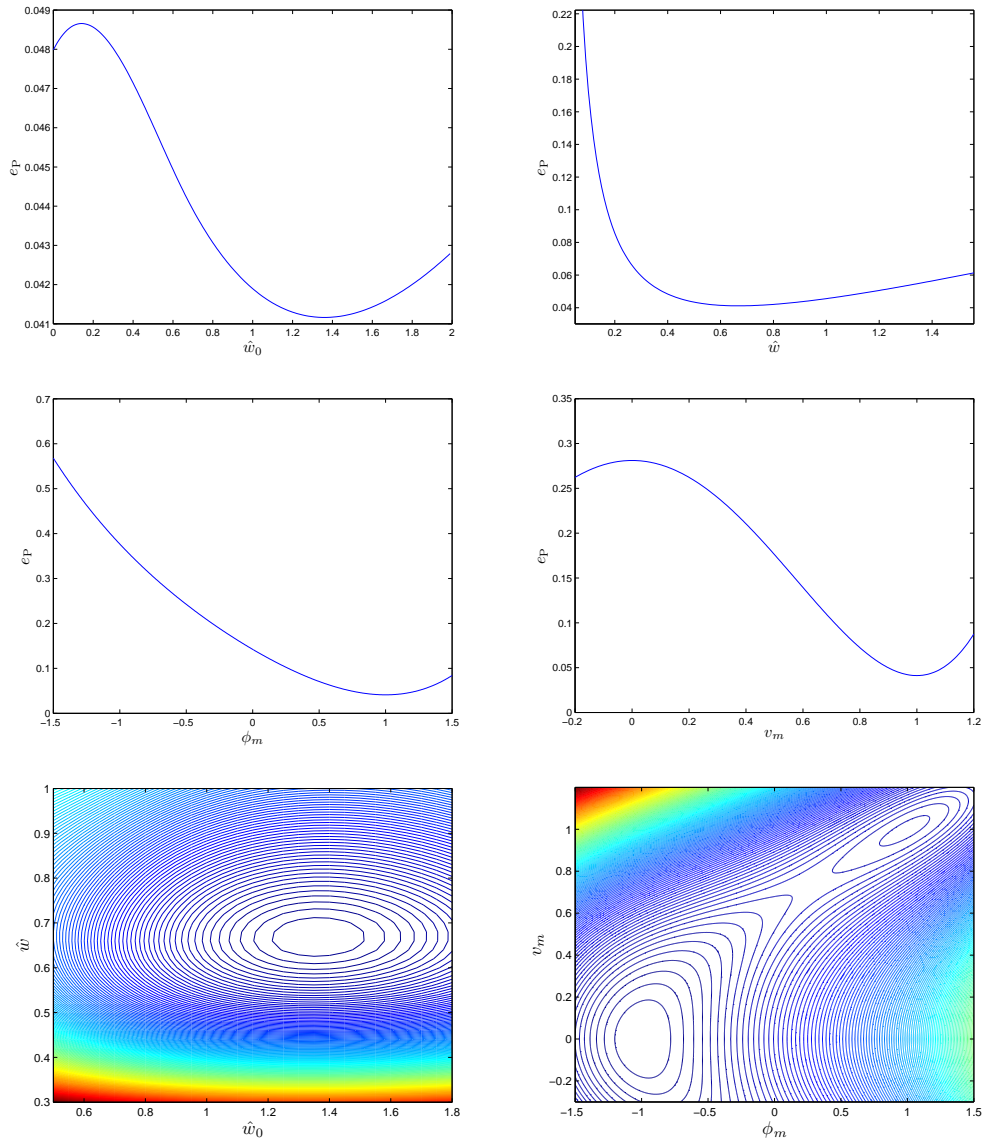


Figure 5.6: Bar energy e_P against the bar parameters \hat{w} , \hat{w}_0 , ϕ_m and v_m . Parameter values were chosen such that there is a bar energy minimum at $\pi_B^* = (1.36, 0.67, 1, 1)$.

erning equations in the Fourier domain, which speeds up the algorithm (*cf.* Appendix B.2):

$$\begin{aligned} \frac{\partial \phi}{\partial t} = & \frac{1}{2} \ln \frac{\pi_{\theta_R}}{\pi_{\theta_{\bar{R}}}} - \theta \left\{ \mathcal{F}^{-1} \left((D - \beta d^2 \hat{\Psi}(k)) k^2 \hat{\phi}(k) \right) \right. \\ & \left. + (\lambda_{22} \phi + \lambda_{21}) \frac{|v|^2}{2} + \lambda_{04} \phi^3 + \lambda_{03} \phi^2 + \lambda_{02} \phi + \lambda_{01} \right\}, \end{aligned} \quad (5.9)$$

$$\begin{aligned} \frac{\partial v}{\partial t} = & -\theta \left\{ \mathcal{F}^{-1} (L_v k^2 \hat{v}(k) + D_v k(k \cdot \hat{v}(k))) \right. \\ & \left. + (|v|^2 + \lambda_{22} \frac{\phi^2}{2} + \lambda_{21} \phi + \lambda_{20}) v \right\}, \end{aligned} \quad (5.10)$$

where $\hat{\cdot}$ and \mathcal{F}^{-1} are the Fourier transform of a function and the inverse Fourier transform respectively.

The unphysical free parameters of the prior model E_P are 9: $(\lambda_{04}, \lambda_{03}, \lambda_{22}, \lambda_{21}, D, \beta, d, L_v, D_v)$. Via the stability analysis for network modelling studied in section 5.2, the free parameters are reduced to 7: $(\lambda_{04}, \lambda_{03}, \lambda_{22}, \lambda_{21}, \hat{w}_0, \hat{w}, D_v)$ where \hat{w}_0 and \hat{w} are 2 physical parameters of the bar *ansatz*. The predicted bar width w_0 is an application-determined physical parameter. As described so far, the interaction function Ψ is chosen to be K_0 in order to allow a larger range of stable branch widths. To model networks, we fix the parameter values as follows:

1. fix the desired bar width w_0 depending of the application and constrain the interface width to have a reasonable value $2 < w < 4$,²
2. choose the 4 free parameter values π_λ to give the preferred profile of W ,
3. compute ν^* , μ^* , μ_ϕ^* , μ_v^* and then ρ^* , and solve (5.5) which gives the values of the scaled widths \hat{w}_0 and \hat{w} satisfying the condition $\hat{w} < \hat{w}_0$,
4. compute β , \hat{D} and \hat{L}_v using the parameter constraints given by (5.6), (5.7) and (5.8), and then compute $D = d^2 \hat{D}$ and $L_v = d^2 \hat{L}_v$ where $d = w_0 / \hat{w}_0$,
5. check numerically the positive definiteness of the Hessian matrix H_{Bar} studied in section 5.2.2.2,
6. choose the free parameter D_v ,
7. check numerically the Turing stability of the background and the foreground (*i.e.* positiveness of the 3 eigenvalues of the Hessian matrix \hat{H}) studied in section 4.3,
8. choose the remaining free parameter θ .

²The bar width w_0 and the interface width w must satisfy the condition $w_0 > w$ otherwise the bar model defined here fails.

5.4 Conclusion

In this chapter, we have conducted a theoretical study of a phase field HOAC model of directed networks in order to ascertain parameter ranges for which stable networks exist. This was done via a stability analysis of a long, straight bar that enabled some model parameters to be fixed in terms of the rest, others to be replaced by physically meaningful parameters, and lower and upper bounds to be placed on the remainder.

In the next chapter, we will validate the theoretical analysis via numerical experiments, and will apply the model to the problem of road and hydrographic network extraction from multi-spectral VHR satellite images.

Experimental results

“All life is an experiment. The more experiments you make the better.”

— Ralph Waldo Emerson

Contents

6.1	Introduction	103
6.2	Geometric experimental results	104
6.2.1	Geometric evolutions of a long bar	104
6.2.2	Geometric evolutions of a random configuration	105
6.2.3	Geometric evolutions for gap closure	108
6.3	Experimental results on real images	112
6.3.1	ML segmentation	113
6.3.2	MAP segmentation	119
6.4	Conclusion	120

In chapter 5, we conducted a theoretical analysis of the directed network model to constrain the parameter values in order to produce stable directed networks. In this chapter, we confirm the theoretical analysis by numerical experiments, and apply the model to the problem of road and hydrographic network extraction from multi-spectral VHR satellite images.

6.1 Introduction

In the first part of this thesis, we introduced a phase field higher-order active contour (HOAC) model for undirected networks via a stability analysis studied in chapter 2. Based on that, we introduced a phase field inflection point long bar model described in chapter 3 to improve parameter tuning and the results of segmentation of road networks from VHR satellite images.

To model directed networks, we have proposed a new directed network phase field HOAC model described in chapter 4. The new model is an extension of the undirected network model. Due to the amount of shape information needed to be incorporated into the model in order to describe efficiently the characteristic geometric properties of directed networks, the model possesses many free unphysical parameters which weight the different energy terms. This makes parameter tuning difficult. Chapter 5 conducted a theoretical analysis of the directed network model which facilitates significantly parameter tuning.

In this chapter, we describe two kinds of experiments. Firstly, we describe, in section 6.2, geometric experiments (*i.e.* only the prior term is used) to validate the theoretical

analysis in chapter 5: we show that the model favours directed networks with the predicted stable network branch width; and we also show that the directed network model closes gaps in the network thanks to the flow conservation property of the vector field. Secondly, we describe, in section 6.3, experiments on road and hydrographic network extraction from multi-spectral VHR satellite images using the overall directed network model defined in section 5.3.1; and we compare the results to those obtained using the undirected network model.

To minimize the energy, we use gradient descent. Section 5.3.2 describes the governing equations (5.9) and (5.10) for gradient descent and how we set the parameter values in practice to favour stable directed networks.

6.2 Geometric experimental results

In this section, we describe geometric evolutions: the prior model E_P is used without the presence of the data term and the parameter θ is fixed to 1 in the governing equations studied in section 5.3.2. In sections 6.2.1 and 6.2.2, we show numerical experiments to confirm the theoretical study described in section 5.2. In section 6.2.3, we describe a major advantage of the new directed network model for closing gaps in networks.

6.2.1 Geometric evolutions of a long bar

As a first test of the theoretical analysis, we show that straight bars evolve under gradient descent towards straight bars of the stable width predicted by theory. Figure 6.1 shows such evolutions using the directed network phase field model E_P and the interaction function Ψ is the one introduced in Rochery et al. (2005) for the first three rows and K_0 for the last three rows.¹

In all evolutions, we fixed $D_v = 0$, because the divergence term does not destabilize the bar when initialized as a constant vector field everywhere in the image domain. The width of the initial straight bar is 10. The first and fourth rows show that the bars evolve until they disappear because $\hat{\beta} < \hat{\beta}_{\min}$, where the bar energy does not have a minimum for $\hat{w}_0 \neq 0$. The first column of figure 6.2 shows that the bar energy e_P given by equation (5.4), corresponding to the fourth evolution, has a minimum in the directions \hat{w} , ϕ_m and v_m whereas in the direction \hat{w}_0 , it does not have a minimum.

On the other hand, the second and third rows show that straight bars evolve toward straight bars with the desired stable widths $w_0 = 6$ and 14, respectively, when $\hat{\beta} > \hat{\beta}_{\min}$. The final widths increase or decrease as a function of the desired stable width: in this case, the stable widths are 6 and 14. Bars that have widths less than 14 widen until reaching the stable width 14, while bars that have widths greater than 6 shrink until reaching the stable width 6.

The final two rows show the same kind of evolutions as in rows 2 and 3 except that the stable widths are 3 and 6, and using K_0 . The corresponding bar energies are given

¹From top to bottom, parameter values were: $(\lambda_{04}, \lambda_{03}, \lambda_{22}, \lambda_{21}, D, \beta, d, L_v, D_v) = (0.1, 0.143, -0.303, -0.6, 0.046, 0.001, 4.76, 0.024, 0), (0.1, 0.143, -0.303, -0.6, 0.046, 0.002, 4.76, 0.024, 0), (0.25, 0.0367, -0.018, -0.6, 0.193, 0.0027, 9.9, 0.4506, 0), (0.1, -0.064, 0.232, -0.6, 0.065, 0.0027, 3.66, 0.5524, 0), (0.112, 0.019, -0.051, -0.6, 0.055, 0.011, 2.78, 0.115, 0)$ and $(0.1, -0.064, 0.232, -0.6, 0.065, 0.0077, 3.66, 0.5524, 0)$.

in second and third columns of figure 6.2 respectively; the bar energy e_P has indeed a minimum in all the directions \hat{w}_0 , \hat{w} , ϕ_m and v_m .

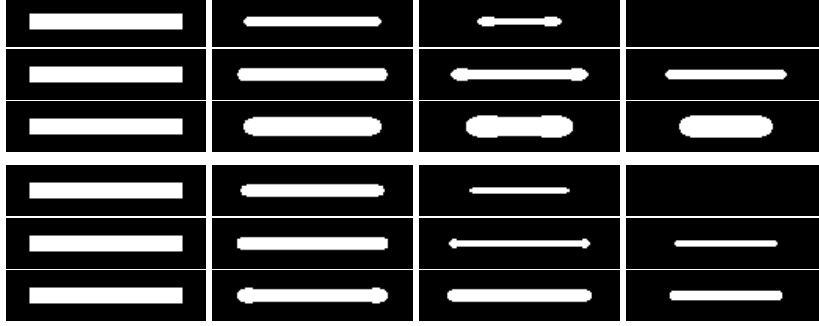


Figure 6.1: Geometric evolutions of bars using the directed network phase field model E_P . Time runs from left to right. For the first three rows we use Rochery et al. (2005)'s interaction function and K_0 for the last three rows. First column: initial configuration which consists of a set of straight bar of width 10. The function ϕ is -1 in the background and ϕ_s in the foreground, and the initial vector field is $(1, 0)$. 1st and 4th rows: when $\hat{\beta} < \hat{\beta}_{\min}$, the initial bars vanish; 2nd, 3rd, 5th and 6th rows: when $\hat{\beta} > \hat{\beta}_{\min}$, the bars evolve toward bars which have the predicted stable widths $w_0 = 6, 14, 3$ and 6 respectively. The regions are obtained by thresholding the function ϕ at 0.

6.2.2 Geometric evolutions of a random configuration

As a second test of the theoretical analysis, we present experiments that show that starting from a random configuration of ϕ and v , the region evolves under gradient descent to a network of the predicted width.

Figure 6.3 shows such geometric evolutions of a uniformly random initial configuration.² At each point of the image domain, the pair $(\phi, |v|)$ was initialized randomly to be either $(-1, 0)$ or $(1, 1)$. The orientation of v was chosen uniformly on the circle. Time runs from left to right. We use Rochery et al. (2005)'s interaction function for the first four evolutions and K_0 for the last four. Evolutions 1 – 2 and 5 – 6 use parameter values computed using the parameter constraints where the desired stable width is $w_0 = 5$, while evolutions 3 – 4 and 7 – 8 use the desired stable width $w_0 = 8$. All evolutions show that the initial configuration evolves to a stable network-like region with an approximately constant branch width equal to the desired stable width. This validates the stability analysis calculations of the directed long bar studied in section 5.2.

As explained in section 5.2.1.3, the parameter $\nu^* = \nu(1, 1)$, where we set $(\phi_m, v_m) = (1, 1)$ which corresponds to the stable state, measures the gap of the ultralocal energy W

²From top to bottom, parameter values were: $(\lambda_{04}, \lambda_{03}, \lambda_{22}, \lambda_{21}, D, \beta, d, L_v, D_v) = (0.4, 0.029, 0.121, -0.8, 0.239, 0.0135, 3.51, 0.077, 10)$, $(0.4, 0.01, 0.13, -0.8, 0.285, 0.016, 3.7, 0.096, 10)$, $(0.25, 0.062, 0.093, -0.8, 0.194, 0.005, 5.85, 0.082, 10)$, $(0.4, 0.029, 0.121, -0.8, 0.237, 0.007, 8, 0.092, 10)$, $(0.4, 0.029, 0.121, -0.8, 0.273, 0.013, 3.97, 0.079, 10)$, $(0.4, 0.01, 0.132, -0.8, 0.274, 0.01, 8.06, 0.091, 10)$, $(0.4, -0.122, 0.725, -1, 0.707, 0.017, 5.3, 0.584, 1)$ and $(0.4, -0.202, 0.699, -0.8, 0.547, 0.012, 10.81, 1.055, 1)$.

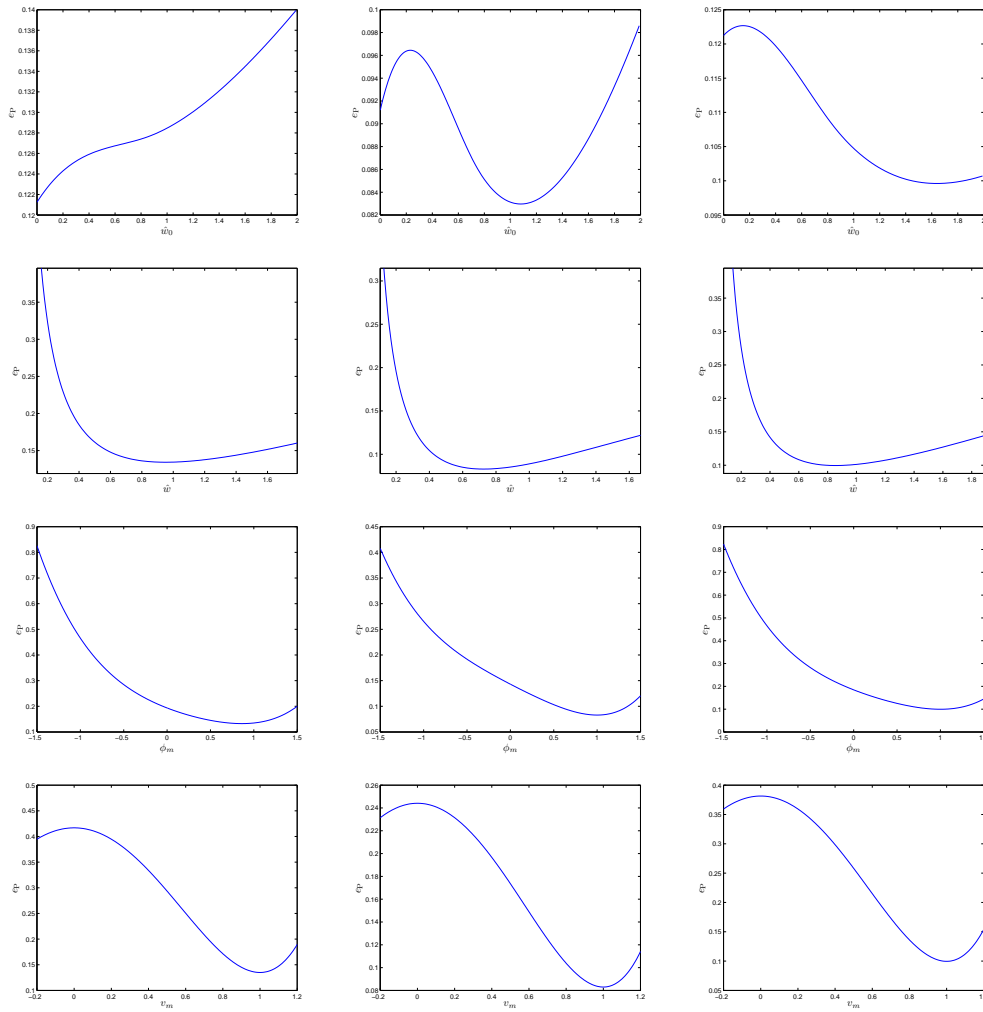


Figure 6.2: From top to bottom, the bar energies e_P against the bar parameters \hat{w} , \hat{w}_0 , ϕ_m and v_m ; from left to right, the columns correspond to the last three bar evolutions in figure 6.1 from top to bottom respectively.

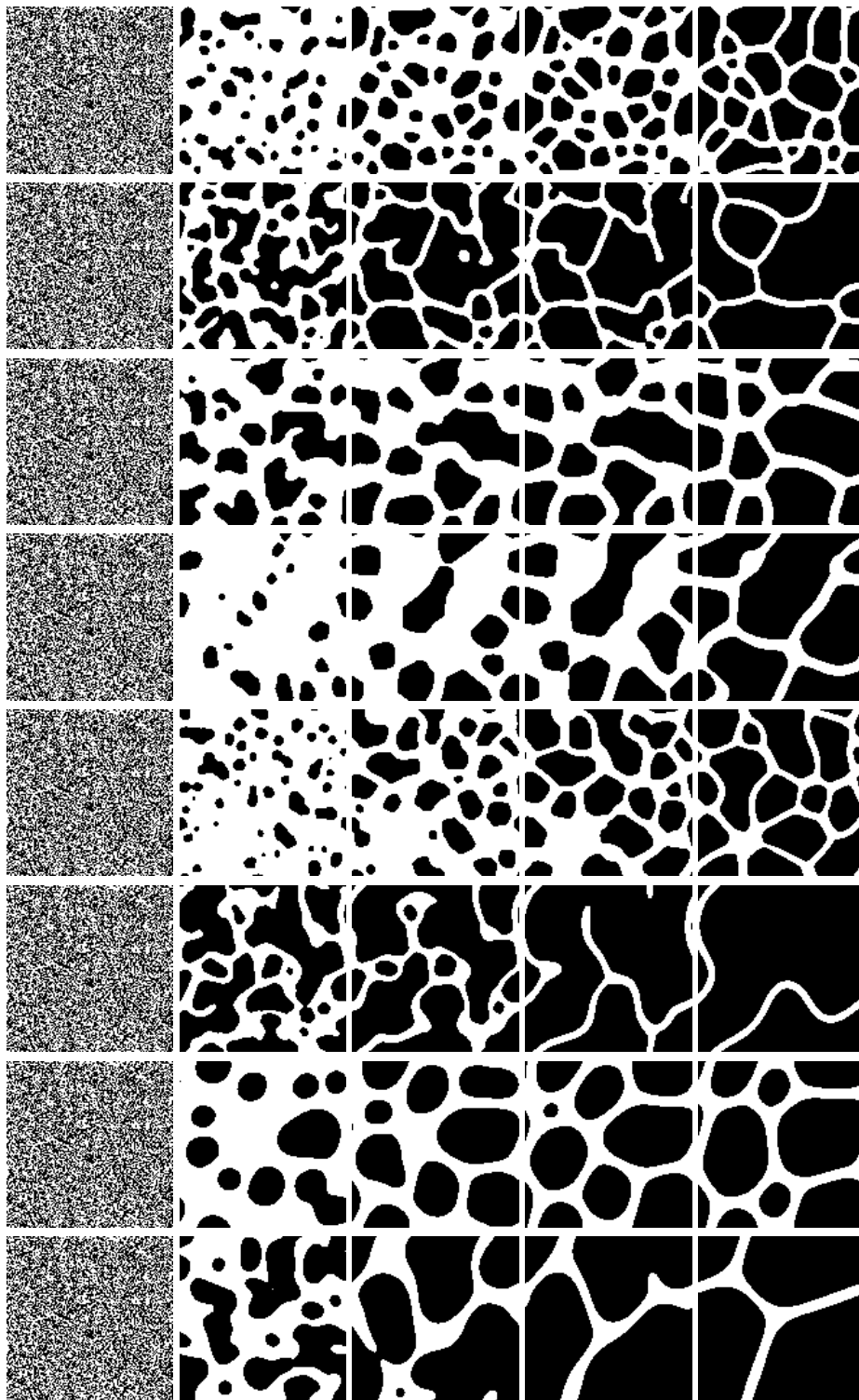


Figure 6.3: Geometric evolutions of a random initial configuration. Time runs from left to right. For the first four rows we use Rochery et al. (2005)'s interaction function while K_0 is used for the last four rows. Parameter values were chosen as a function of the desired stable width. The latter is $w_0 = 5$ for evolutions 1 – 2 and 5 – 6, and $w_0 = 8$ for evolutions 3 – 4 and 7 – 8. All evolutions show that the initial configuration evolves towards a line network-like region where branches have approximately a constant width equal to the desired stable width.

between the foreground and the background. It is taken to be positive to favour pixels belonging to the background. It controls the area of the region R (the network). The energy gap $\nu_i^* = \{(0.05, 0.07), (0.02, 0.05), (0.05, 0.07), (0.05, 0.07)\}$ where $i = 1..8$ is the evolution number from top to bottom. For each pair of evolutions, it is clear that when ν^* increases, the area occupied by the network decreases.

The experiments in figure 6.3 use parameter settings where the weight of the divergence term is not large ($D_v = 1$ or 10). Figure 6.4 shows the same kind of experiments but with large values of D_v to highlight the contribution of the divergence term.³ The evolutions in the first two rows have predicted stable width $w_0 = 5$, while the one in the third row has predicted stable width $w_0 = 8$. In all cases, the initial configuration evolves to a stable network region with branch widths equal to the predicted value, except near junctions, where branch width changes slowly to accommodate flow conservation. The effect of large values of D_v is to enforce the divergence of v to be 0 everywhere in the image domain leading to flow/width conservation along branches and at junctions. Figure 6.5 shows the scalar phase field ϕ (left) and the vector field magnitude $|v|$ (right) corresponding to the converged configuration of the third experiment in figure 6.4. It shows that indeed $(\phi, |v|)$ assigns approximately $(-1, 0)$ outside the network region and $(1, 1)$ inside; the transition of both functions from the exterior to interior is smooth.

Figure 6.6 shows, in the top-right, the vector field of the central two junctions of the converged configuration of the second evolution in figure 6.4. Figure 6.6 shows, in the bottom, the vector field of the converged configuration of the third evolution in figure 6.4. Both configurations show that the vector field is indeed: smooth; running along network branches (parallel to the boundaries of the network branches); approximately 0 outside the network region, of unit magnitude inside, and its magnitude varies smoothly from 0 to 1 across the network branch boundaries; approximately conserved everywhere where along branches the width changes slowly and at junctions, total incoming width equals total outgoing width. In the top-left in figure 6.6, we show a zoom on the top-right quadrant of the converged configuration of the first evolution in figure 6.4. It shows that the vector field converges to a configuration with a rotational effect. That configuration is still divergence-free but the smoothing term is not strong enough to remedy it.

6.2.3 Geometric evolutions for gap closure

As mentioned in the introduction of this thesis, the problem of occlusions is present in the images we are dealing with. This leads to gaps in the network entity to be extracted from the image. This problem can be solved by the contribution of the divergence term in the prior directed network model E_P . The undirected network model described in section 3.1.1 does not close gaps because the extremities of two separated branches repel, due to the nonlocal term, and there are no forces attracting one extremity to the other. In the case of the directed network model, the flow conservation property of the vector field encourages branch extremities to not end but to elongate, and then to join and thus close gaps.

Figure 6.7 shows, from left to right, three geometric evolutions of an initial configuration of two separated branches using the model E_P . Time runs from top to bottom.

³From top to bottom, the parameter values were: $(\lambda_{04}, \lambda_{03}, \lambda_{22}, \lambda_{21}, D, \beta, d, L_v, D_v) = (0.25, 0.0625, 0.0932, -0.8, 0.1045, 0.0054, 4, 0.0391, 100), (0.25, 0.0625, 0.0932, -0.8, 0.111, 0.0061, 3.65, 0.0412, 50)$ and $(0.4, -0.1217, 0.7246, -1, 0.4566, 0.0083, 10.8, 0.4334, 100)$.

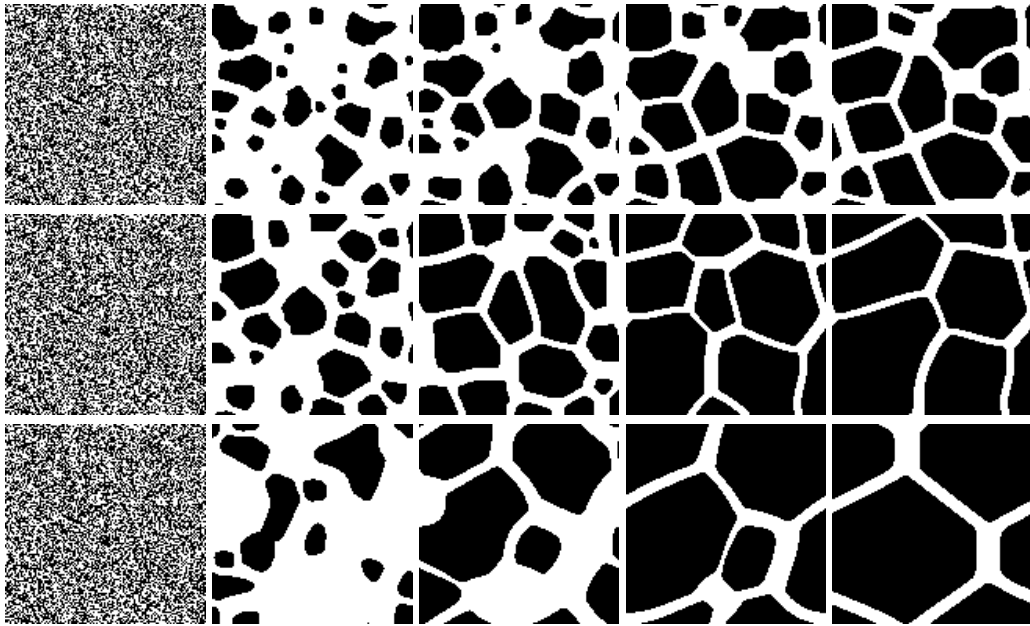


Figure 6.4: Geometric evolutions starting from a random initial configuration. Time runs from left to right. Parameter values were chosen as a function of the predicted stable width, which was 5 for the first and second rows and 8 for the third row. The regions are obtained by thresholding the function ϕ at 0.

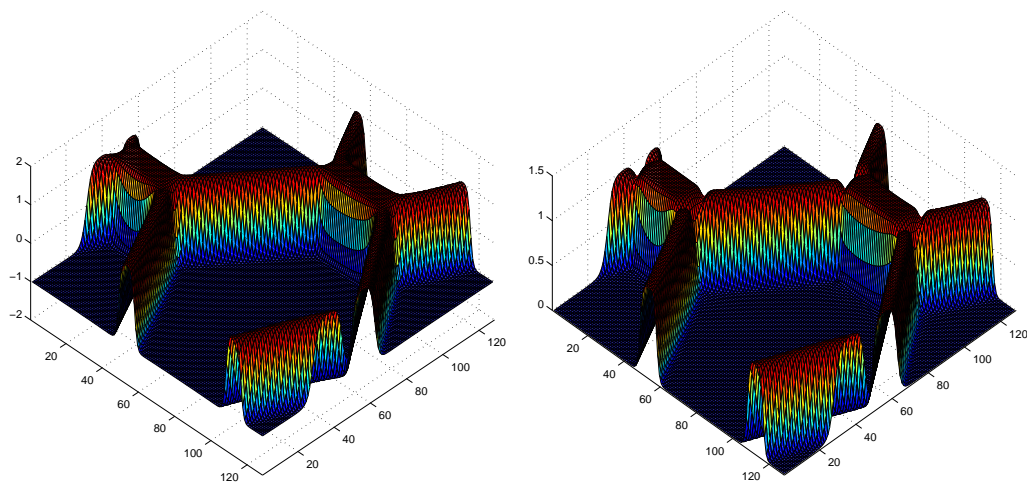


Figure 6.5: The phase field function ϕ (left) and the magnitude of the vector phase field function $|v|$ (right) of the converged configuration of the third experiment in figure 6.4.

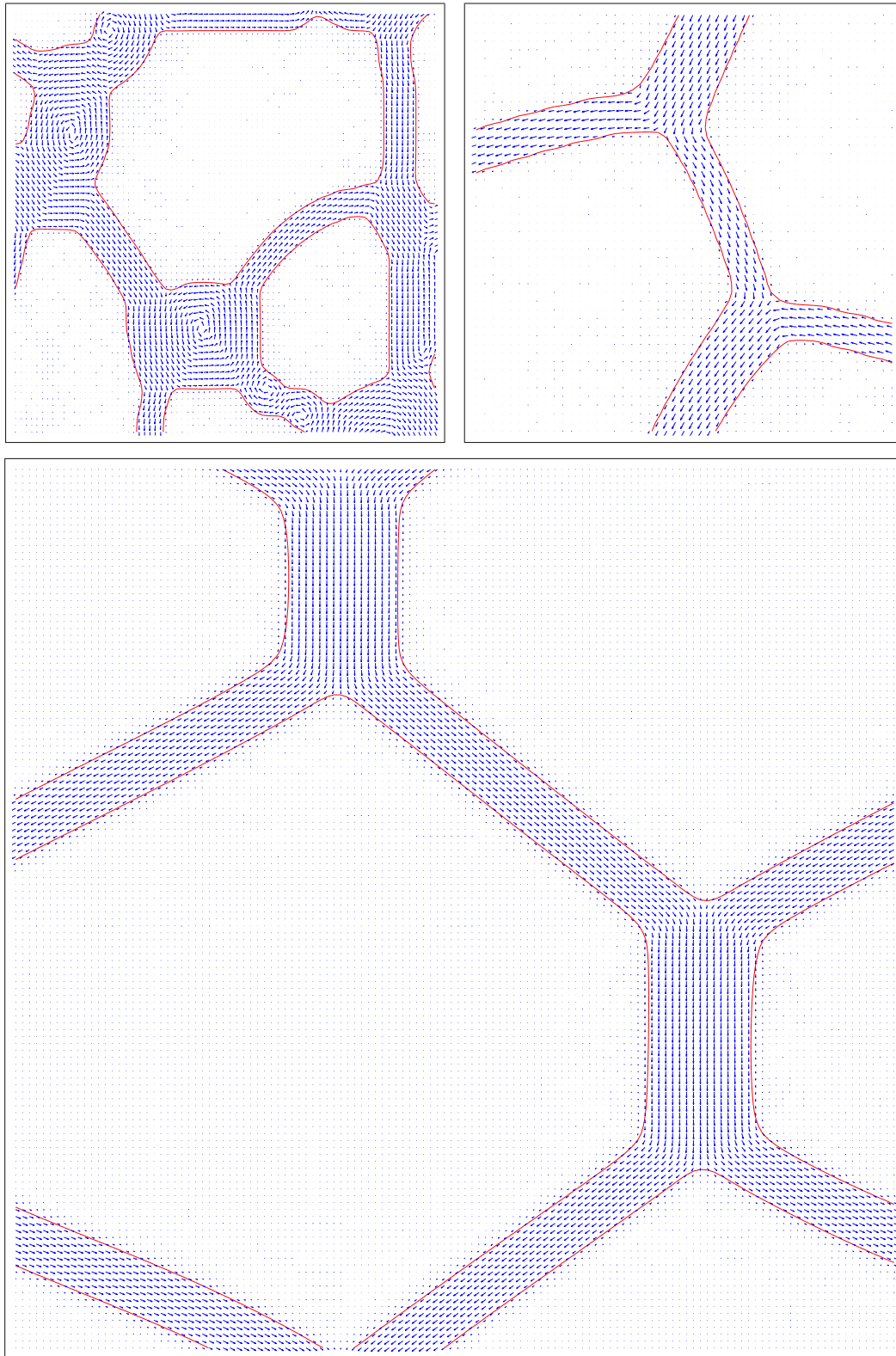


Figure 6.6: The final configuration of v and ϕ (thresholded at 0): (top-left) a zoom on the top-right quadrant, (top-right) a zoom on the central two junctions, and (bottom) a zoom of the converged configurations of the first, second and third evolutions in figure 6.4 respectively.

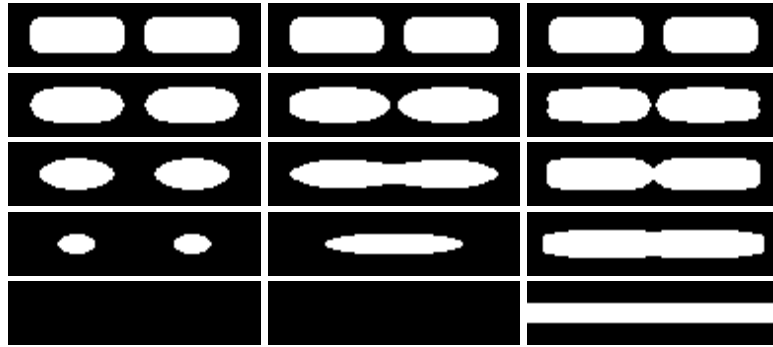


Figure 6.7: Geometric evolutions of branches using the prior directed network model E_P . Time runs from top to bottom. ϕ is initialized to be -1 outside the branches and 1 inside, and v is initialized to be 0 outside and of unit magnitude inside, and running along the branches. Parameter values are the same for the three experiments except the divergence weight D_v is 1 , 10 and 100 from left to right. The initial width of branches is 18 and the stable width is fixed to 10 . From left to right: branches shrink until they disappear; branch extremities join each other to form a single branch, and then the latter shrinks until it disappears; branch extremities join each other to form a single branch, and the latter lengthens. Regions are obtained by thresholding ϕ at 0 .

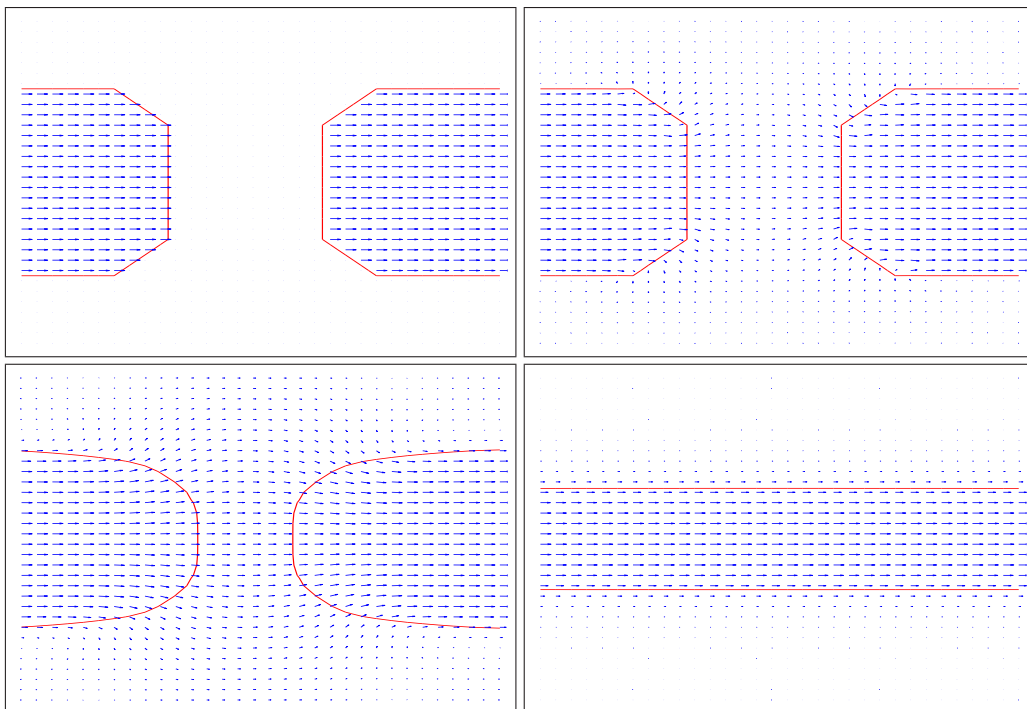


Figure 6.8: Configurations of v and ϕ (thresholded at 0) of a zoom on the central gap corresponding to the third experiment in figure 6.7. Time runs from left to right, and from top to bottom.

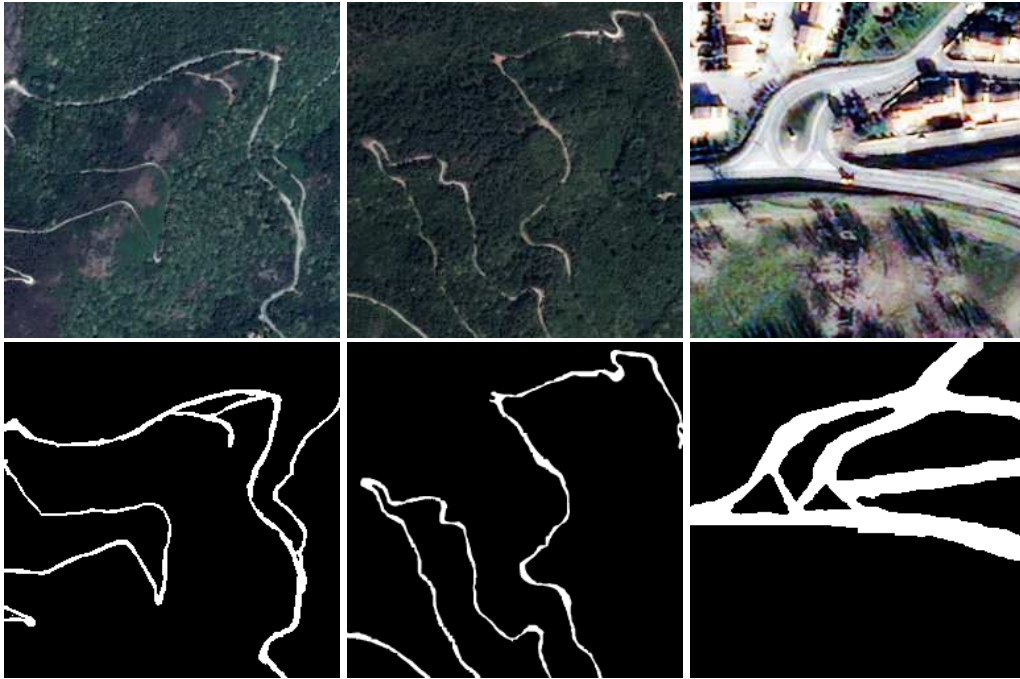


Figure 6.9: Three multi-spectral Quickbird images showing road networks, and their reference segmentations extracted manually. The resolution of images 1 and 2 is $1/4$ the original resolution (2.44m); image 3 is at full resolution (0.61m). Images 1, 2 and 3: RGB channels of the images. (Original images ©DigitalGlobe, CNES processing, images acquired via ORFEO Accompaniment Program.)

Parameter values were the same for the three evolutions⁴ except that the parameter D_v is, from left to right, 1, 10 and 100. The stable branch width is chosen to be 10. The first evolution shows that the initial branches shrink until they disappear because the divergence term weighted by $D_v = 1$ is weak compared to the other terms, so that the directed network model behaves similarly to the undirected network model. The second evolution, where $D_v = 10$, shows that the central gap is closed but still the resulting branch shrinks until it disappears. This means that for $D_v = 10$ the force is not strong enough to elongate branch extremities when the gap is relatively large. The third evolution, where $D_v = 100$, shows that the model is able to close the central gap and elongate the resulting branch until all gaps are closed. Figure 6.8 shows an evolution of the vector field configuration of a zoom on the central gap corresponding to the third column of figure 6.7.

6.3 Experimental results on real images

In this section, we apply the model to multi-spectral VHR satellite images for road and hydrographic network segmentation. The channels are red, green, blue and infra-red. Figures 6.9 and 6.10 show examples of images of road networks and hydrographic networks

⁴The parameter values were: $(\lambda_{04}, \lambda_{03}, \lambda_{22}, \lambda_{21}, D, \beta, d, L_v) = (0.1, 0.0387, -0.0192, -0.6, 0.0351, 0.001, 20.41, 0.2964)$.

respectively, and their reference segmentations extracted manually. In section 6.3.1, we describe segmentations of the real images using a Maximum Likelihood (ML) estimate and compare different data models. In section 6.3.2, we describe segmentations using a maximum *a posteriori* (MAP) estimate and compare the undirected and directed network models.

6.3.1 ML segmentation

In section 3.4, the road network segmentation performance of a phase field HOAC model for undirected networks was tested using two classes of likelihoods (the same class was used for both R and \bar{R}): a multivariate Gaussian (MG) and a mixture of two multivariate Gaussians (MMG). In maximum likelihood segmentations, the performance was mixed, but when combined with the prior energy, the MMG model was found to outperform the MG model, with the improvement being most significant when the image was very heterogeneous. Here, we test the maximum likelihood performance of these two likelihood classes on the real images, and compare them to segmentations obtained using the normalized difference vegetation index ($NDVI = (I - R)/(I + R)$) (Rouse et al., 1973; Tucker, 1979) and the normalized difference water index ($NDWI = -(I - G)/(I + G)$) (McFeeters, 1996). We apply the former to images of road networks in which the background is mostly vegetation, and the latter to images of hydrographic networks.

The second, third, and fourth rows of figure 6.11 show maximum likelihood (ML) segmentation results for road networks using NDVI, MG, and MMG respectively. The second, third, and fourth rows of figures 6.12 and 6.13 show ML segmentation results for hydrographic networks using NDWI, MG, and MMG respectively.

Table 6.1 shows quantitative evaluations of the quality of the ML segmentations using NDVI, MG, and MMG. The bold numbers show the best ML segmentation method. In all experiments in figure 6.11, the NDVI results show lower performance, according to the quality measure, than the MG and MMG results. The NDVI results on the first and second images show that most of the hidden parts of the network are not retrieved because they resemble vegetation more than road network.

Table 6.2 shows quantitative evaluations of the quality of the ML segmentations using NDWI, MG, and MMG. The NDWI results on the second and third images in figure 6.12 and the second image in figure 6.13 show better performance, according to the quality measure, than the MG and MMG results. On the other hand, as in the case of NDVI results for road networks, the NDWI results on these images show that most of the hidden parts of the network are not retrieved because they resemble background more than hydrographic network.

The result is the presence of many lengthy gaps in the ML segmentation using NDVI/NDWI. Because these gaps are so long, it is very unlikely that the prior term would close them. In contrast, the MG and MMG segmentations include most of the network, but also many points of the background, which the prior model should be able to eliminate. When coupled with the results in section 3.4 showing that MMG outperforms MG, these results lead us to choose the MMG model to construct the likelihood energy E_I . In the case of the MMG model, E_I is given by equation (3.9).

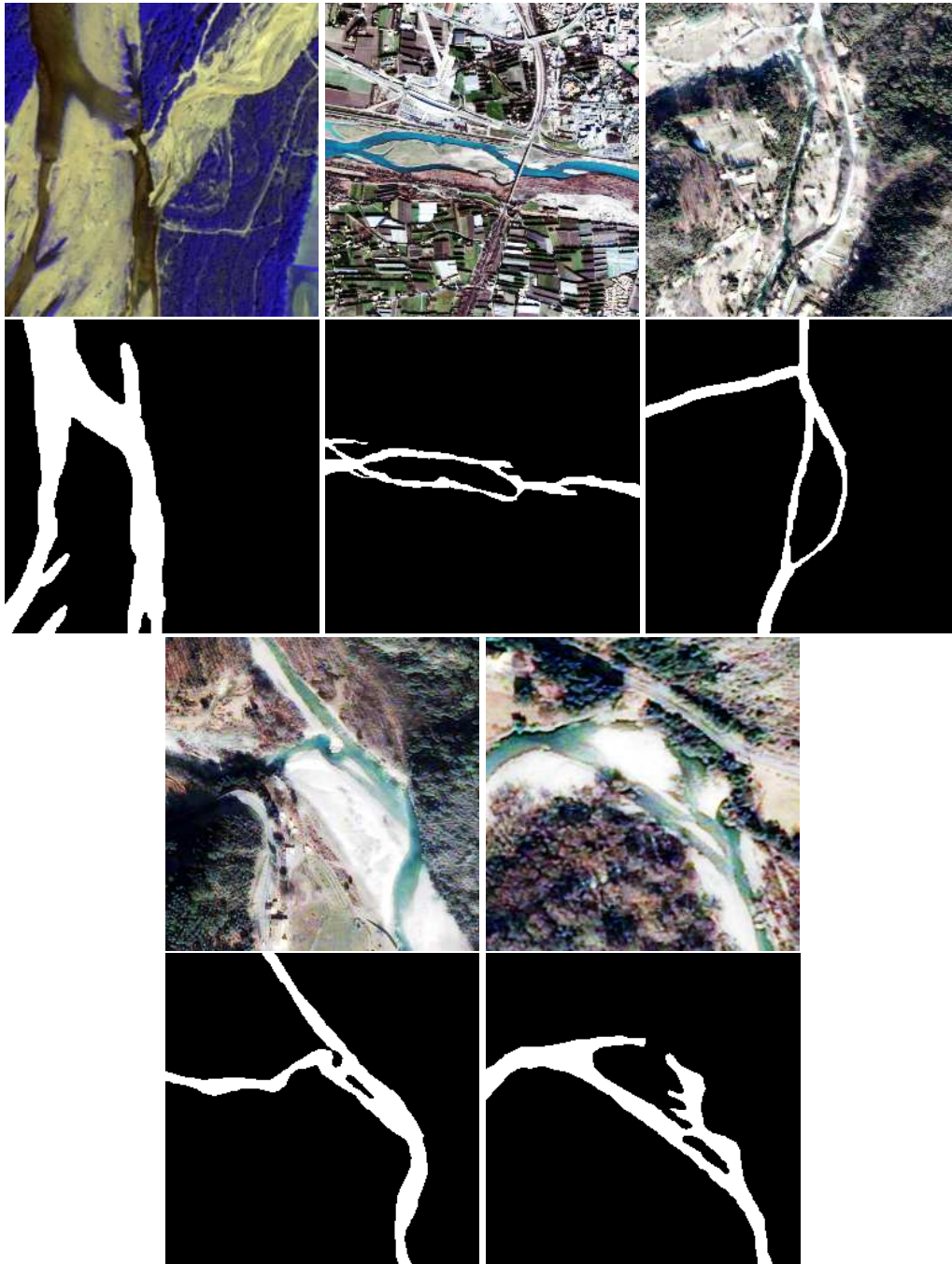


Figure 6.10: Five multi-spectral Quickbird images showing hydrographic networks, and their reference segmentations extracted manually. The resolution of images 1 and 3 is $1/4$ the original resolution (2.44m); the resolution of image 2 is $1/16$ the original resolution (9.76m); the resolution of image 4 is $1/2$ the original resolution (1.22m); image 5 is at full resolution (0.61m). Images 2, 3, 4 and 5: RGB channels of the images. Image 1: GBI (mapped to RGB) channels of the image. (Original images ©DigitalGlobe, CNES processing, images acquired via ORFEO Accompaniment Program.)

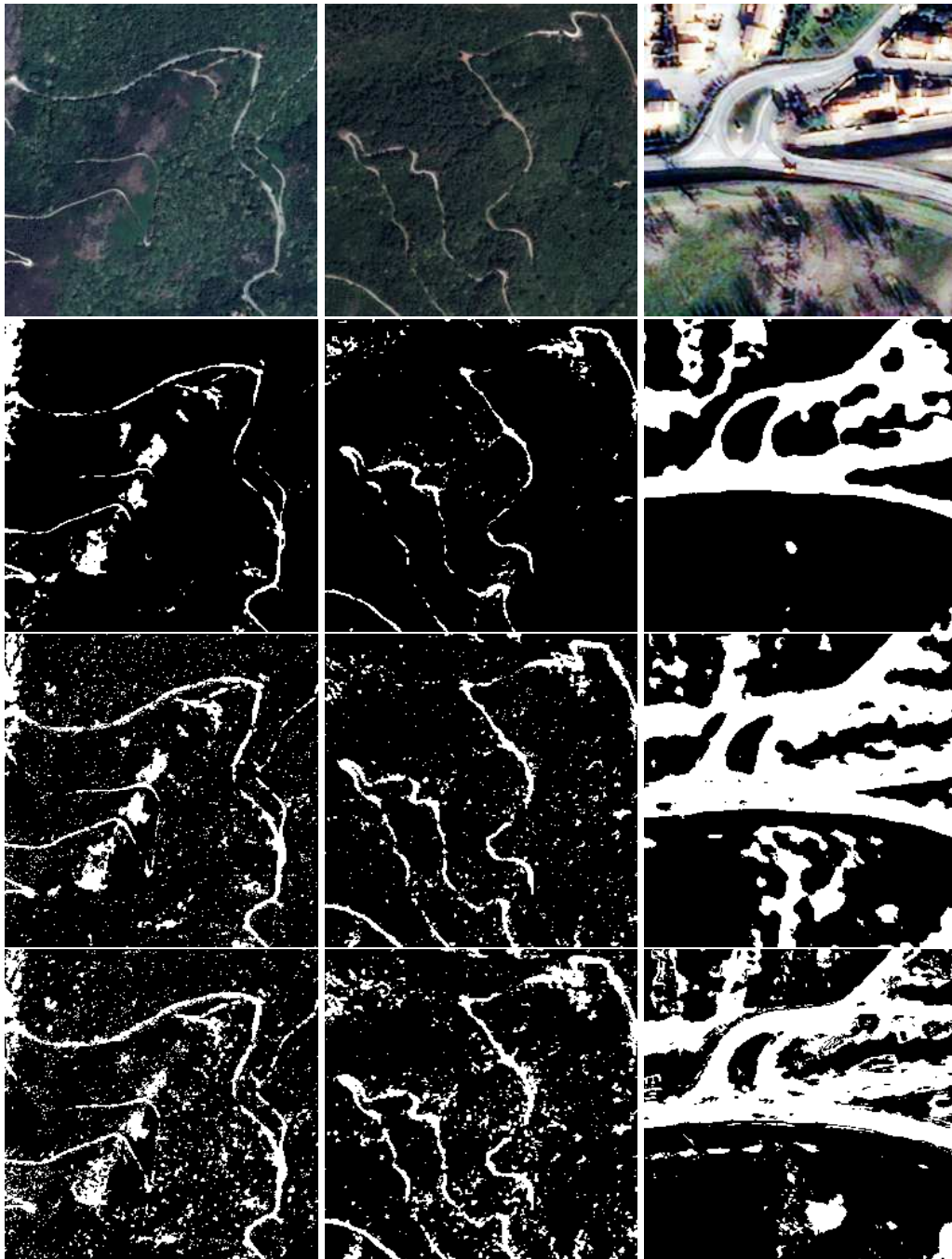


Figure 6.11: From top to bottom: original images of road networks; segmentations obtained using NDVI and optimal thresholding; ML segmentations using the MG model; ML segmentations using the MMG model.

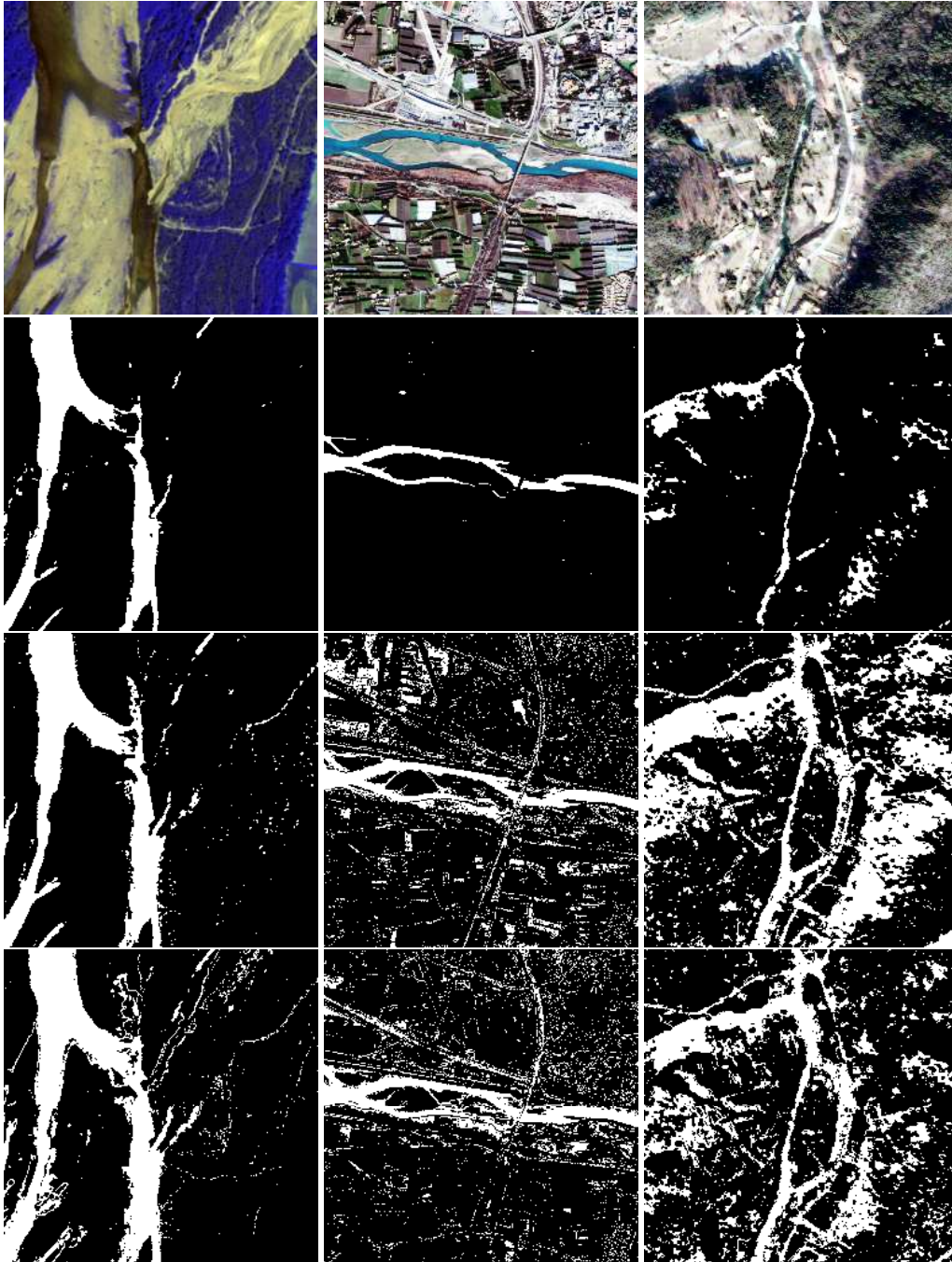


Figure 6.12: From top to bottom: original images of hydrographic networks; segmentations obtained using NDWI and optimal thresholding; ML segmentations using the MG model; ML segmentations using the MMG model.

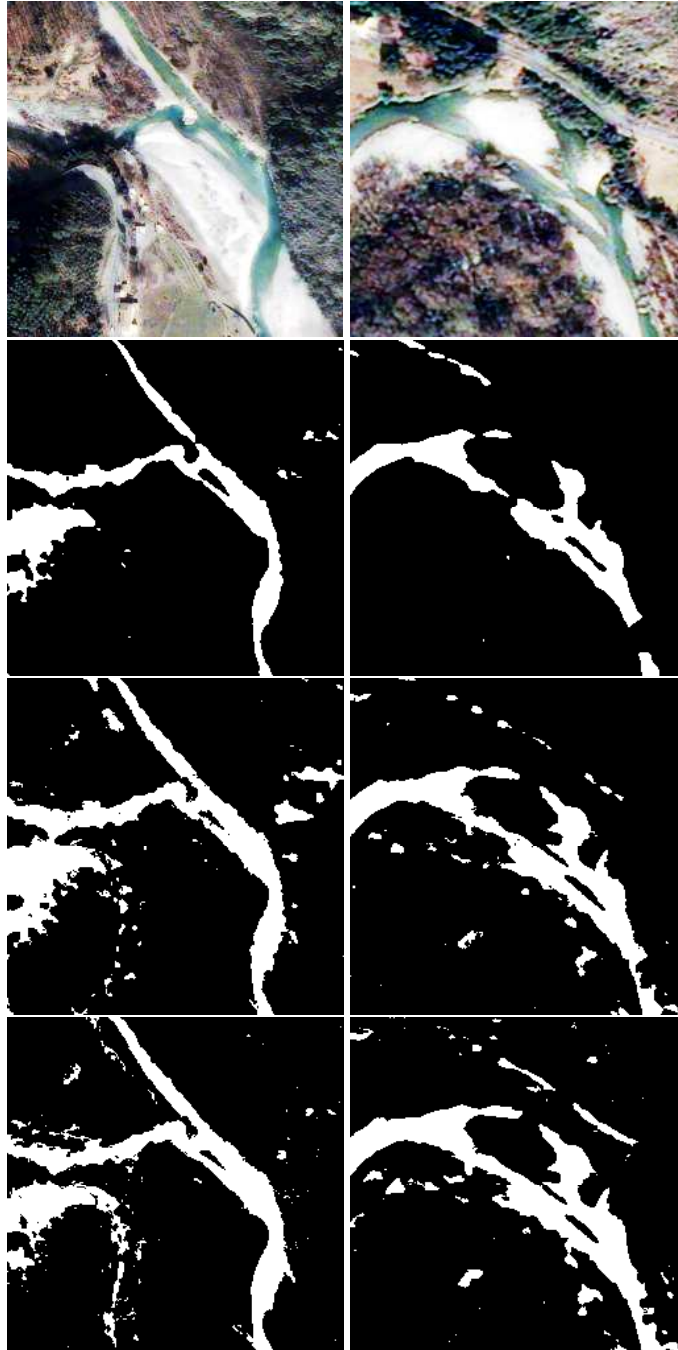


Figure 6.13: From top to bottom: original images of hydrographic networks; segmentations obtained using NDWI and optimal thresholding; ML segmentations using the MG model; ML segmentations using the MMG model.

Image	Method	Completeness	Correctness	Quality
1	NDVI	0.4296	0.3965	0.2598
	MG	0.6920	0.3423	0.2970
	MMG	0.7510	0.3000	0.2728
2	NDVI	0.4745	0.6536	0.3791
	MG	0.7166	0.4958	0.4145
	MMG	0.7983	0.3521	0.3233
3	NDVI	0.6776	0.4517	0.3718
	MG	0.9060	0.4099	0.3932
	MMG	0.8634	0.4641	0.4323

Table 6.1: Quantitative evaluations of the ML segmentations given in figure 6.11. The numbers 1, 2, and 3 correspond to the three images in figure 6.11, from left to right. Completeness= $TP/(TP + FN)$, correctness= $TP/(TP + FP)$ and quality = $TP/(TP + FP + FN)$. T, F, P, and N correspond to true, false, positive, and negative respectively.

Image	Method	Completeness	Correctness	Quality
1	NDWI	0.6280	0.9446	0.6057
	MG	0.7835	0.8468	0.6862
	MMG	0.8485	0.7424	0.6555
2	NDWI	0.6574	0.8352	0.5819
	MG	0.8109	0.2189	0.2082
	MMG	0.8312	0.2414	0.2301
3	NDWI	0.3588	0.3363	0.2102
	MG	0.7924	0.1378	0.1338
	MMG	0.7846	0.1816	0.1730
4	NDWI	0.7692	0.6105	0.5160
	MG	0.9127	0.4765	0.4557
	MMG	0.9361	0.5381	0.5190
5	NDWI	0.7995	0.8477	0.6990
	MG	0.9067	0.7140	0.6651
	MMG	0.9445	0.6233	0.6012

Table 6.2: Quantitative evaluations of the ML segmentations given in figures 6.12 and 6.13. The numbers 1, 2 and 3 (4 and 5) correspond to the images in figure 6.12 (6.13), from left to right. Completeness= $TP/(TP + FN)$, correctness= $TP/(TP + FP)$ and quality = $TP/(TP + FP + FN)$. T, F, P, and N correspond to true, false, positive, and negative respectively.

6.3.2 MAP segmentation

Figure 6.14 shows the MAP segmentation results for road networks obtained using the undirected network model (first column),⁵ E_P^s , and the directed network model (second column),⁶ E_P . Figures 6.15 and 6.16 show the MAP segmentation results for hydrographic networks obtained using the undirected network model (first column),⁷ E_P^s , and the directed network model (second column),⁸ E_P .

The undirected network model favours network structures in which all branches have the same width. Consequently, network branches which have widths significantly different from the average are not extracted. The result on the third image in figure 6.15 shows clearly the false negative in the central part of the network branch, where the width is about half the average width. Similarly, the results on the third image in figure 6.14 and on the second image in figure 6.15 show a false positive at the central two loops of the network and at the bottom of the central loop of the network respectively, where the true branch width is small. The result on the first image in figure 6.15 again shows a small false negative piece in the network junction at the bottom. The two images in figure 6.16 show also false positive in the central loop in each image, and in the horizontal branch in the first image where the branch width of the segmentation changes significantly along the branch.

The directed network model remedies these problems. The first and second images in figure 6.14 and the third image in figure 6.15 show many gaps in the road network and hydrographic network, respectively, due mainly to the presence of trees. These gaps cannot be closed using the undirected network model. The directed network model can close these gaps because flow conservation tends to prolong network branches. Tables 6.3 and 6.4 show that, in all experiments, the directed network model outperforms the undirected network model.

In all experiments obtained using the directed network model, the role of the divergence term at junctions is clear. The divergence-free property of the vector field favours junctions where total incoming branch width equals total outgoing branch width. Figure 6.17 shows streamline plots of the final vector field configuration superimposed on the thresholded ϕ corresponding to the third result in figure 6.14 and the first result in figure 6.15. The vector field is indeed of constant (unit) magnitude inside the network, parallel to the network boundaries, and smooth; the flow is approximately conserved along network branches and in particular at junctions, where the total incoming flow is approximately equal to total outgoing flow. Similarly, figure 6.18 shows the final vector field configurations of some zoomed parts of the segmentations given in figures 6.15 and 6.16.

⁵The parameter values were, from top to bottom: $(\lambda, \alpha, D, \beta, d) = (5.6, 0.851, 3.75, 0.1472, 3.41)$, $(4.88, 0.3486, 3, 0.0603, 2.27)$ and $(24.54, 1.5, 15, 0.2592, 9.09)$.

⁶The parameter values were, from top to bottom: $(\lambda_{04}, \lambda_{03}, \lambda_{22}, \lambda_{21}, D, \beta, d, L_v, D_v, \theta) = (0.3375, -0.1767, 0.2712, -0.6, 0.2645, 0.0629, 1.68, 0.2649, 100, 33.33)$, $(0.1, 0.0164, 0.1162, -0.8, 0.0512, 0.0205, 1.45, 0.0227, 200, 100)$ and $(0.4, -0.018, 0.15, -0.8, 0.548, 0.0316, 3.45, 0.150, 50, 25)$.

⁷The parameter values were, from top to bottom and from figure 6.15 to figure 6.16: $(\lambda, \alpha, D, \beta, d) = (18.74, 0.0775, 11.25, 0.0134, 34.1)$, $(4.88, 0.3327, 3, 0.0575, 4.54)$, $(19.88, 0.6654, 12, 0.1151, 9.1)$, $(12.01, 1.0804, 7.5, 0.1869, 5.68)$ and $(14.27, 1.439, 9, 0.2489, 5.68)$.

⁸The parameter values were, from top to bottom and from figure 6.15 to figure 6.16: $(\lambda_{04}, \lambda_{03}, \lambda_{22}, \lambda_{21}, D, \beta, d, L_v, D_v, \theta) = (0.412, -0.0008, 0.0022, -0.6, 0.257, 0.0083, 8.33, 0.275, 50, 25)$, $(0.2650, -0.1659, 0.5023, -0.8, 0.1926, 0.0387, 2.027, 0.2023, 100, 16.66)$, $(0.4525, -0.2629, 0.6611, -0.8, 0.3585, 0.0289, 5.12, 0.4224, 10, 22.22)$, $(0.4625, -0.2918, 0.778, -1, 0.8786, 0.105, 2.228, 0.3536, 100, 25)$ and $(0.4375, -0.2557, 0.6818, -0.8, 0.3597, 0.0329, 3.81, 0.432, 10, 15)$.

Figure 6.19 shows the segmentation of a hydrographic network from a colour optical image.⁹ The likelihood model used was the same, but with one less band. The flow conservation property and its geometric consequences enable the algorithm to avoid confounding factors in the background and segment the network to a good accuracy.

Image	Method	Completeness	Correctness	Quality
1	UNM	0.5997	0.6411	0.4490
	DNM	0.6084	0.7906	0.5240
2	UNM	0.6799	0.6919	0.5219
	DNM	0.6231	0.7978	0.6779
3	UNM	0.7118	0.6840	0.4957
	DNM	0.5894	0.7051	0.5435

Table 6.3: Quantitative evaluations of experiments of the three images given in figure 6.14. T, F, P, N, UNM and DNM correspond to true, false, positive, negative, undirected network model and directed network model respectively.

Image	Method	Completeness	Correctness	Quality
1	UNM	0.8439	0.9168	0.7739
	DNM	0.8202	0.9489	0.7924
2	UNM	0.9094	0.6999	0.6043
	DNM	0.8484	0.7856	0.6889
3	UNM	0.5421	0.6411	0.4158
	DNM	0.7702	0.6251	0.6513
4	UNM	0.8916	0.8757	0.7914
	DNM	0.7067	0.9394	0.8722
5	UNM	0.8649	0.8724	0.7678
	DNM	0.8766	0.8881	0.7894

Table 6.4: Quantitative evaluations of experiments of the three images given in figure 6.15 (1, 2 and 3) and of the two images given in figure 6.16 (4 and 5). T, F, P, N, UNM and DNM correspond to true, false, positive, negative, undirected network model and directed network model respectively.

6.4 Conclusion

In this chapter, we validated the theoretical analysis of the directed network model, studied in chapter 5, via numerical experiments and we described a major advantage of the model: closing gaps in the network. We then added a likelihood energy and tested the model on the problem of road and hydrographic network extraction from multi-spectral VHR satellite images, showing that the directed network model outperforms the undirected network model.

⁹Parameter values were: $(\lambda_{04}, \lambda_{03}, \lambda_{22}, \lambda_{21}, D, \beta, d, L_v, D_v, \theta) = (0.25, 0.0323, 0.1138, -0.8, 0.1903, 0.0176, 2.56, 0.0644, 100, 0.07)$.

On the other hand, the directed network model has difficulties compared to the undirected network model. Firstly, the number of free parameters, after performing the stability analysis, is large (7 parameters). This makes parameter learning hard. Secondly, in our work, we have used a local optimizer (gradient descent algorithm) to seek energy minima, which renders parameter tuning harder in the sense that a parameter setting which gives a local minimum corresponding to a bad segmentation, may give a global minimum corresponding to a good segmentation, and vice-versa. Thirdly, the weight of the divergence term, D_v , must be large in order to have a very low divergence of the vector field. This implies a very small time step in the gradient descent algorithm and thus slow convergence. In addition to that, we have two governing equations (one for the scalar field and the other for the vector field) to compute at each iteration which consumes time.

Thus important future directions are estimation of the parameter values of the new model and reduction of the execution time needed to find a good segmentation.

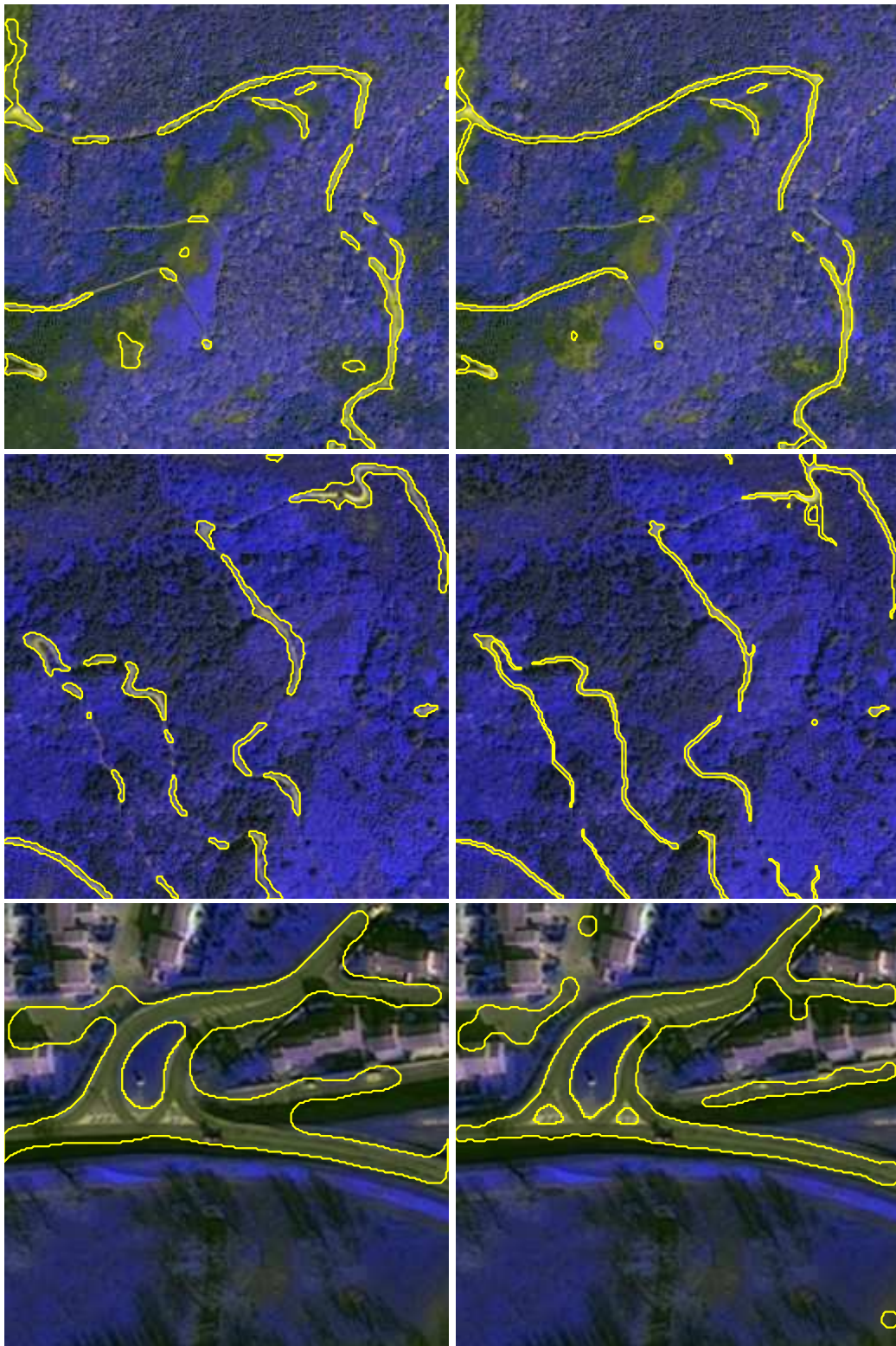


Figure 6.14: Road network segmentations using the undirected network model (first column) and the directed network model (second column). Regions are obtained by thresholding ϕ at 0.

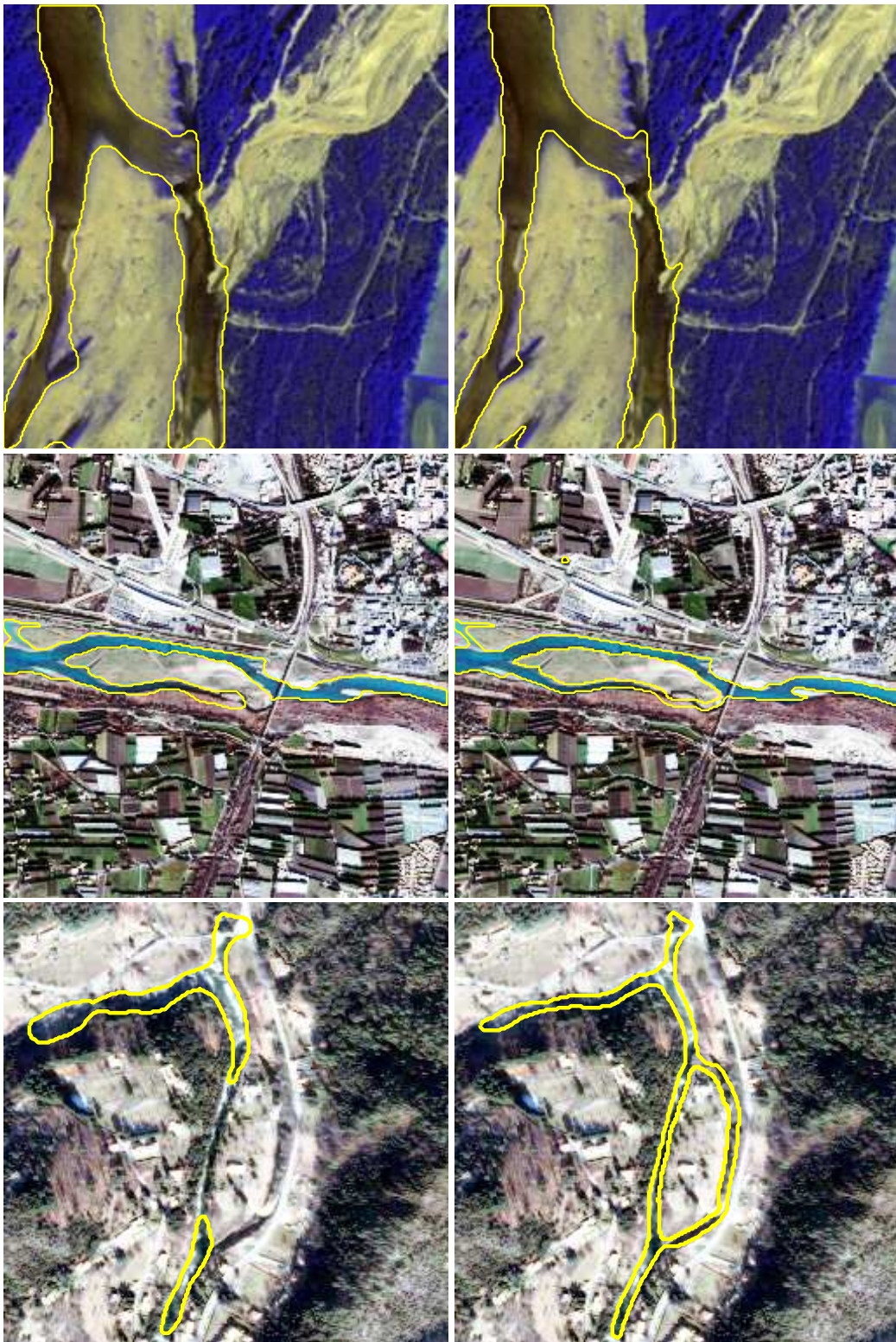


Figure 6.15: Hydrographic network segmentations using the undirected network model (first column) and the directed network model (second column). Regions are obtained by thresholding ϕ at 0.



Figure 6.16: Hydrographic network segmentations using the undirected network model (first column) and the directed network model (second column). Regions are obtained by thresholding ϕ at 0.

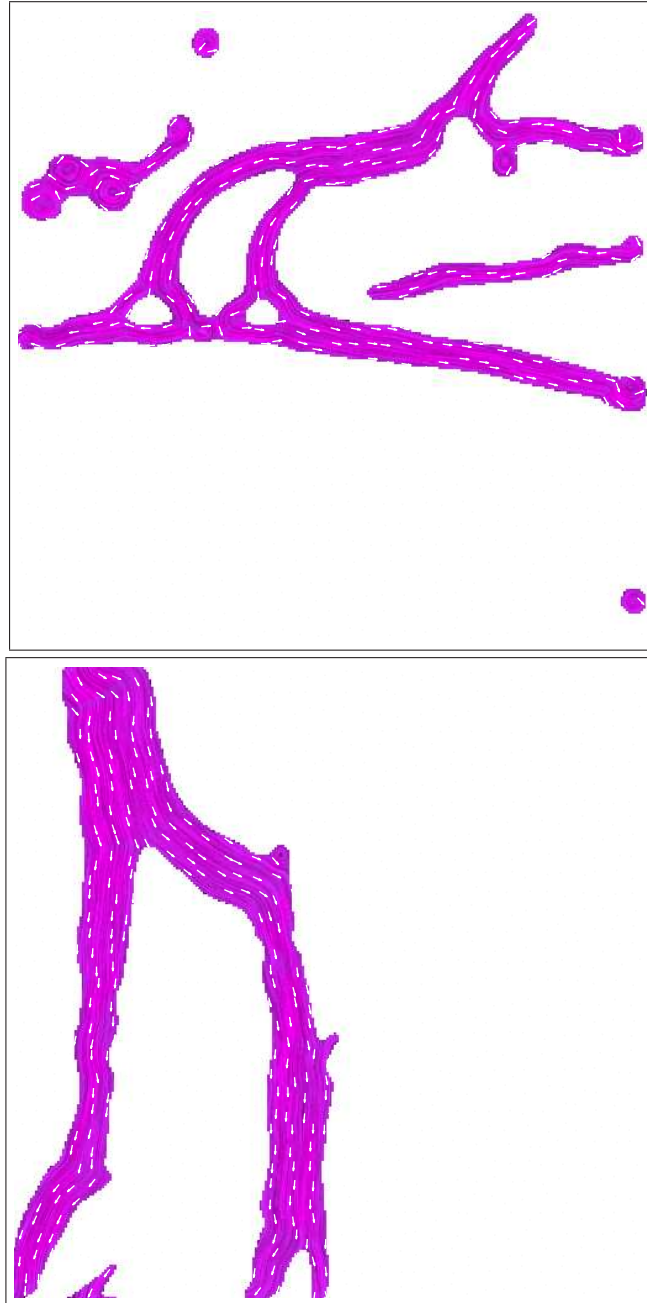


Figure 6.17: The final configuration of v and ϕ (thresholded at 0) corresponding to the third segmentation in figure 6.14 and first segmentation in figure 6.15. The vector field is indeed zero outside the network and of constant (unit) magnitude inside, smooth, parallel to branch boundaries, and conserved along network branches and at junctions.

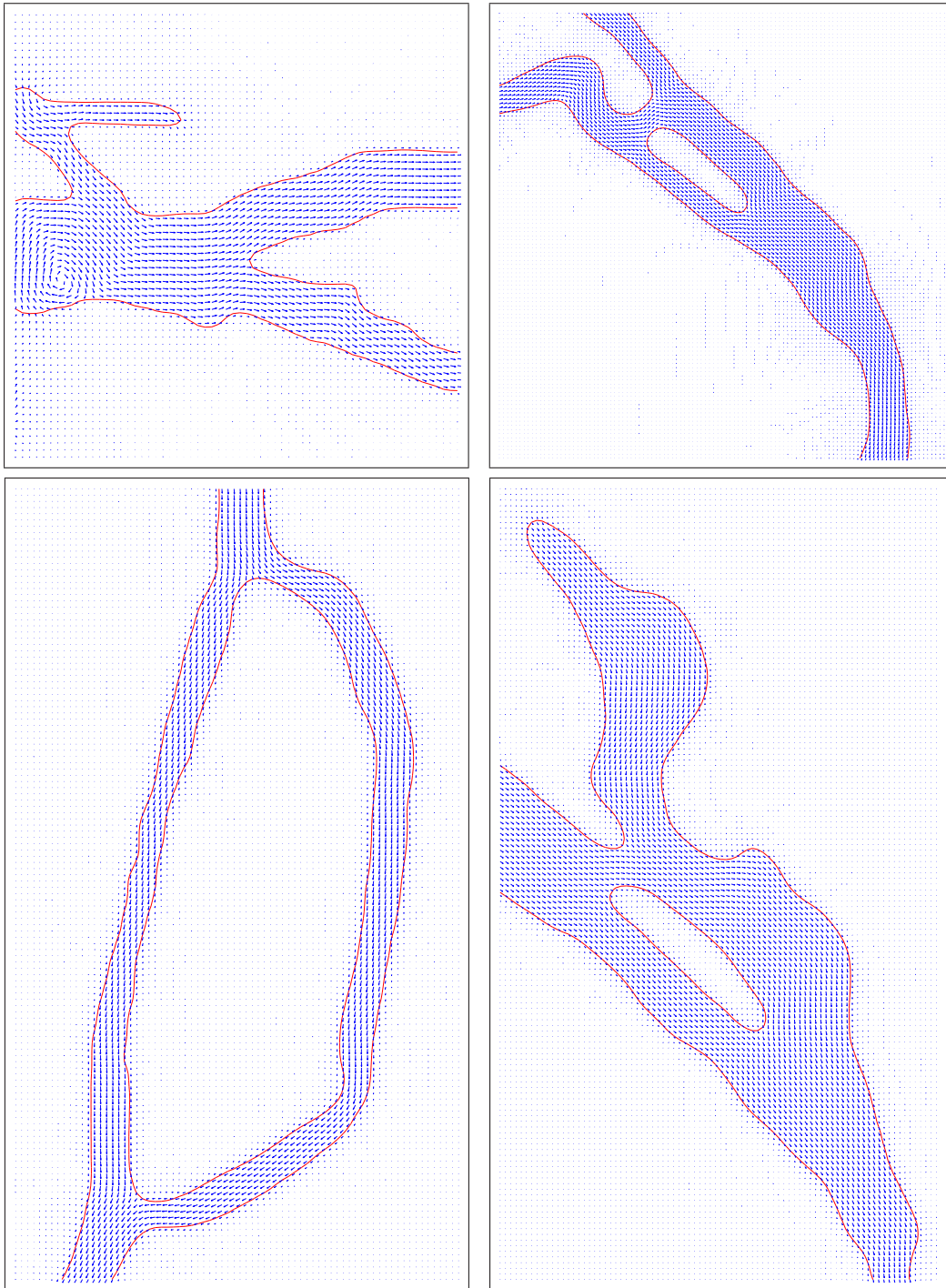


Figure 6.18: The final configuration of v and ϕ (thresholded at 0): (top-left) zoom on the left part of the network of the second image and (bottom-left) on the central loop of the network of the third image in figure 6.15; (top-right) zoom on the central loop of the network of the first image and (bottom-right) the second image in figure 6.16.



Figure 6.19: Hydrographic network segmentation from a colour image using the directed network model. Flow conservation is satisfied at junctions, illustrated by a significant change of width, and along branches, as illustrated by a slow change of width. ((©2010 Google - Imagery ©2010 TerraMetrics, Map data ©2010 Tele Atlas.)

Conclusion and perspectives

“The important thing is not to stop questioning. Curiosity has its own reason for existing.”

— Albert Einstein

Summary

The purpose of this work was to build variational models for network modelling for road and hydrographic network extraction from multi-spectral VHR Quickbird images. More concretely, we focused on developing specific and sophisticated shape priors for undirected and directed network modelling.

We first improved the HOAC model for undirected network modelling. We conducted a stability analysis of a long bar under the HOAC model which aims to constrain the parameter values to obtain stable networks with a predicted stable branch width. Due to the topological complexity of a network, *i.e.* a network may have many loops, a phase field formalism is used to allow full topological freedom, a neutral initialization for the algorithm, and reduced execution time. An equivalence was shown between the explicit, *i.e.* HOAC, and the implicit, *i.e.* nonlocal phase field, representation of the region of interest. The result is that one can use nonlocal phase fields instead of HOACs. Based on that, we studied the inflection point energy under undirected network phase field HOACs, and we showed that it outperforms the non-inflection point energy for road network extraction from Quickbird images.

Hydrographic networks have different geometric properties to road networks. There is an orientation to the ‘flow’ they carry through their branches. This has an effect on the geometric properties of the network. We introduced a new family of phase field HOACs that incorporates, in addition to the standard scalar field function, a vector field describing the ‘flow’ through the network branches. The vector field is enforced to be zero outside the network and of unit magnitude inside, smooth, parallel to the region boundary and divergence-free. The vector field is strongly encouraged to be divergence-free so that the proposed directed network model favours geometric structures which preserve the ‘flow’ in some sense: along branches, the width changes slowly; and at junctions, total incoming branch width approximately equals total outgoing branch width. A stability analysis of a directed straight, long bar was conducted to constrain the parameter values and express some parameters as a function of the others. We were able to express some of the model parameters as a function of the physical parameters of the bar which some of them are the predicted branch network width and the interface width. We applied our directed network phase field HOAC model to the extraction of hydrographic and road networks from Quickbird images. The results showed that the directed network model outperforms the undirected network model for hydrographic network extractions from images. The proposed model allowed: to close the gaps of networks present in real images thanks to the ‘flow’ conservation property which allows to prolong network branches; to extract network branches which have significantly different widths thanks to the suitable choice of the interaction function.

Phase fields and Markov random fields

In general, Bayesian inference-based segmentation methods involve parametric models. In this case, the solution of the problem depends strongly on the values of the model parameters. In this thesis, the parameter values, of both the undirected and directed network models, were fixed manually. A more ambitious way to solve the problem of parameter tuning is to estimate them.

Parameter estimation requires a probabilistic formulation of the model and in particular the normalizing constants of the Gibbs distribution corresponding to the model energy. As described in the first chapter, the phase field HOAC model introduced by (Rochery et al., 2005, 2006) was also used to detect circular shapes, via a stability analysis conducted by (Horvath et al., 2009), in addition to network structures. Blaskovics et al. (2009) proposed a new Markov Random Field (MRF) model incorporating a strong shape prior to detect circular shapes. The authors used the phase field formulation of the ‘gas of circles’ model to construct the new MRF model. The continuous phase field function is discretized and assigns the two labels ± 1 . The MRF model uses the discretized function and defines long-range interactions to favour circular shapes. The authors were able to approximate the parameters of the MRF model as a function of those of the phase field model which uses a continuous function. Performing this equivalence between the discrete and continuous models, new ways will be opened to solve the challenging problem of parameter estimation.

Active contours and marked point processes

Marked Point Processes (MPP) have a long history applied to the problem of object extraction from images. Particularly, MPPs were used for the extraction of road networks (Lacoste et al., 2004, 2005, 2010), buildings (Ortner et al., 2007), and trees (Perrin et al., 2005). These works represent the objects by simplified shapes *e.g.* ellipses, discs or rectangles.

Kulikova et al. (2010) proposed a new MPP model which incorporates strong prior shape information for the extraction of multiple, arbitrarily-shaped objects. The authors constructed, first, a single-object model which combines a data term and a prior term. The prior term incorporates, in addition to a smoothing term, a HOAC term which describes specific shapes of the object. Secondly, a multiple-object model is built based on sampling from a Gibbs distribution, and each object evolves with respect to the single-object model. A birth-and-death algorithm was used to speed up the convergence.

The incorporation of active contours into a MPP framework has several advantages: possible overlap between objects; the topology of the object changes automatically, and efficient computation thanks to birth-and-death dynamics. This opens new directions to describe arbitrarily-shaped objects in scenes of high complexity containing overlapping objects. In the case of road or hydrographic networks, a challenging problem appears if two or more network branches overlap *e.g.* a bridge crossing a river or road, which produces an overlapping in the observed image: one way to handle this is through MPP.

Perspectives

To improve the model, we list a few perspectives:

1. Some of the results obtained using the directed network model still have false positives. The main reason is that the gradient descent algorithm becomes locally stuck in a local minimum, so that some of the background remains classified as network even if this is globally energetically unfavourable. So, one may think to use a global minimization algorithm to seek global minima *e.g.* simulated annealing.
2. Some of the results obtained using the directed network model still have false negatives. The main reason are long gaps in the visible network caused by occlusions. More investigations on parameter tuning will help to understand why gap closure may fail for some parts of the network and may succeed for other parts.
3. Our data model is taken to be either a multivariate Gaussian or a multivariate mixture of two Gaussians. They gave very encouraging results for road and hydrographic network extraction. Many other possibilities may be useful to outperform the segmentation results: one can incorporate multiscale features, *e.g.* wavelets, or texture features. This will help in the case of VHR remote sensing images where the network branches are very large.
4. One can think to accelerate the algorithm convergence. In our work we used gradient descent to seek minima. Many other algorithms may help to speed up the convergence *e.g.* conjugate gradient descent, implicit methods...
5. The stability analysis performed in this work allowed us to express some of the model parameters as a function of the others so as to favor stable networks. Nevertheless, the model still has several free parameters. Parameter estimation techniques could be used to estimate these parameters rather than fixing them manually. Implementing this is very difficult task, however, due to the complexity of the model, and the lack of knowledge of the normalizing constant of the Gibbs distribution defined by the model energy.

Stability calculations for a long bar under the undirected network HOAC model

Contents

A.1 Length of the contour	133
A.2 Area of the contour	134
A.3 The quadratic energy $E_Q(\gamma)$	134
A.3.1 Inner product of tangent vectors	135
A.3.2 Quadratic distance	135
A.3.3 Interaction function	135
A.3.4 Computation of $G(t_\mu, t'_\nu)$	136

In this appendix, we detail the stability calculations of each term of the total geometric energy given by equation (2.1). We Taylor-expand these terms to second order around a long bar of width w_0 .

A.1 Length of the contour

The derivative of the contour γ given by equation (2.6) is

$$\begin{aligned} \dot{\gamma}_\mu(t_\mu) &= \begin{cases} \dot{x}_\mu(t_\mu) &= \pm_\mu l \\ \dot{y}_\mu(t_\mu) &= \delta y_\mu(t_\mu) \end{cases} \\ &= \begin{cases} \dot{x}_\mu(t_\mu) &= \pm_\mu l \\ \dot{y}_\mu(t_\mu) &= \sum_{k_\mu} i k_\mu l a_{\mu, k_\mu} e^{i k_\mu t_\mu} . \end{cases} \end{aligned}$$

The length of the contour is defined as

$$L(\gamma) = \sum_\mu \int_{\square\gamma_\mu} |\dot{\gamma}_\mu(t_\mu)| dt_\mu ,$$

where the tangent vector is given by

$$|\dot{\gamma}_\mu(t_\mu)| = l \left[1 - \sum_{k_\mu, k'_\mu} a_{\mu, k_\mu} a_{\mu, k'_\mu} k_\mu k'_\mu e^{i(k_\mu + k'_\mu)t_\mu} \right]^{\frac{1}{2}} . \quad (\text{A.1})$$

Expanding equation A.1 in a Taylor series to second order and using the fact that

$$\int_{\square\gamma_\mu} e^{ikt_\mu} dt_\mu = \delta(k) , \quad (\text{A.2})$$

and

$$\sqrt{1+x} \simeq 1 + \frac{1}{2}x ,$$

we obtain

$$\int_{\square\gamma_\mu} |\dot{\gamma}_\mu(t_\mu)| dt_\mu \simeq l \left[1 + \frac{1}{2} \sum_{k_\mu} |a_{\mu,k_\mu}|^2 |k_\mu|^2 \right] .$$

Then the length of the contour becomes to second order

$$\begin{aligned} L(\gamma) &\simeq l \left[2 + \frac{1}{2} \sum_{\mu} \sum_{k_\mu} |a_{\mu,k_\mu}|^2 |k_\mu|^2 \right] \\ &= l \left[2 + \frac{1}{2} \sum_k k^2 (|a_{1,k}|^2 + |a_{2,k}|^2) \right] . \end{aligned} \quad (\text{A.3})$$

A.2 Area of the contour

The area of the contour γ is defined as

$$\begin{aligned} A(\gamma) &= \int_{\square\gamma_1} l(y_1(t_1) - y_2(-t_1)) dt_1 \\ &= \int_{\square\gamma_1} l(w_0 + \delta y_1(t_1) - \delta y_2(-t_1)) dt_1 , \end{aligned}$$

and using the expression for the perturbations expressed in terms of Fourier coefficients, and the integral value given by equation (A.2), we obtain

$$\begin{aligned} A(\gamma) &= l[w_0 + (a_{1,0} - a_{2,0})] \\ &= l[w_0 + \sum_{\mu} \pm_{\mu} a_{\mu,0}] . \end{aligned} \quad (\text{A.4})$$

A.3 The quadratic energy $E_Q(\gamma)$

The general expression for the quadratic energy $E_Q(\gamma)$ can be written as

$$E_Q(\gamma) = \sum_{\mu,\nu} \iint_{(\square\gamma_\mu, \square\gamma_\nu)} dt_\mu dt'_\nu G(t_\mu, t'_\nu) , \quad (\text{A.5a})$$

where G is the energy interaction of a pair of points t_μ and t'_ν , which can be defined as

$$G(t_\mu, t'_\nu) = \dot{\gamma}_\mu(t_\mu) \dot{\gamma}_\nu(t'_\nu) \Psi(|\gamma_\mu(t_\mu) - \gamma_\nu(t'_\nu)|) . \quad (\text{A.5b})$$

A.3.1 Inner product of tangent vectors

The inner product of the tangent vectors $\dot{\gamma}_\mu(t_\mu)$ and $\dot{\gamma}_\nu(t'_\nu)$ is given by

$$\begin{aligned}\dot{\gamma}_\mu(t_\mu) \dot{\gamma}_\nu(t'_\nu) &= \dot{x}_\mu(t_\mu) \dot{x}_\nu(t'_\nu) + \dot{y}_\mu(t_\mu) \dot{y}_\nu(t'_\nu) \\ &= \pm_\mu \pm_\nu l^2 + \dot{\delta}y_\mu(t_\mu) \dot{\delta}y_\nu(t'_\nu) .\end{aligned}\tag{A.6}$$

A.3.2 Quadratic distance

Using the expression for the contour given by equation (2.6), we can compute the squared distance between two contour points:

$$\begin{aligned}|\gamma_\mu(t_\mu) - \gamma_\nu(t'_\nu)|^2 &= (x_\mu(t_\mu) - x_\nu(t'_\nu))^2 + (y_\mu(t_\mu) - y_\nu(t'_\nu))^2 \\ &= [\pm_\mu l t_\mu - \pm_\nu l t'_\nu]^2 + \left[\frac{w_0}{2}(\pm_\mu - \pm_\nu) + \delta y_\mu(t_\mu) - \delta y_\nu(t'_\nu)\right]^2 .\end{aligned}$$

Let $\Delta_{\mu,\nu}^2 = (\pm_\mu l t_\mu - \pm_\nu l t'_\nu)^2$ and $X_0^2 = \Delta_{\mu,\nu}^2 + \frac{w_0^2}{2}(1 - \pm_\mu \pm_\nu)$. We then obtain

$$\begin{aligned}|\gamma_\mu(t_\mu) - \gamma_\nu(t'_\nu)|^2 &= X_0^2 + (\delta y_\mu(t_\mu))^2 + (\delta y_\nu(t'_\nu))^2 + w_0(\pm_\mu - \pm_\nu)\delta y_\mu(t_\mu) \\ &\quad - w_0(\pm_\mu - \pm_\nu)\delta y_\nu(t'_\nu) - 2\delta y_\mu(t_\mu)\delta y_\nu(t'_\nu) ,\end{aligned}$$

which, after expansion in a Taylor series to second order around X_0 , becomes

$$\begin{aligned}|\gamma_\mu(t_\mu) - \gamma_\nu(t'_\nu)| &\simeq X_0 + \frac{1}{2X_0}w_0(\pm_\mu - \pm_\nu)\delta y_\mu(t_\mu) - \frac{1}{2X_0}w_0(\pm_\mu - \pm_\nu)\delta y_\nu(t'_\nu) \\ &\quad + \frac{4X_0^2 - w_0^2(\pm_\mu - \pm_\nu)^2}{8X_0^3}(\delta y_\mu(t_\mu))^2 + \frac{4X_0^2 - w_0^2(\pm_\mu - \pm_\nu)^2}{8X_0^3}(\delta y_\nu(t'_\nu))^2 \\ &\quad - 2\frac{4X_0^2 - w_0^2(\pm_\mu - \pm_\nu)^2}{8X_0^3}\delta y_\mu(t_\mu)\delta y_\nu(t'_\nu) .\end{aligned}$$

To simplify the last expression, we define $X_1 = \frac{1}{2X_0}w_0(\pm_\mu - \pm_\nu)$, $X_2 = \frac{1}{2X_0}(1 - X_1^2)$ and $\Delta\delta y_{\mu,\nu} = \delta y_\mu(t_\mu) - \delta y_\nu(t'_\nu)$:

$$|\gamma_\mu(t_\mu) - \gamma_\nu(t'_\nu)| \simeq X_0 + X_1\Delta\delta y_{\mu,\nu} + X_2(\Delta\delta y_{\mu,\nu})^2 .$$

A.3.3 Interaction function

Expanding the interaction function in a Taylor series to second order around X_0 , we obtain

$$\begin{aligned}\Phi(|\gamma_\mu(t_\mu) - \gamma_\nu(t'_\nu)|) &\simeq \Psi(X_0) + [X_1\Delta\delta y_{\mu,\nu} + X_2(\Delta\delta y_{\mu,\nu})^2] \Psi'(X_0) \\ &\quad + \frac{\Psi''(X_0)}{2}X_1^2(\Delta\delta y_{\mu,\nu})^2 \\ &= \Psi(X_0) + X_1\Psi'(X_0)\Delta\delta y_{\mu,\nu} \\ &\quad + \left[X_2\Psi'(X_0) + \frac{X_1^2}{2}\Psi''(X_0)\right] (\Delta\delta y_{\mu,\nu})^2 .\end{aligned}\tag{A.7}$$

A.3.4 Computation of $G(t_\mu, t'_\nu)$

Substituting the expressions given by equations A.6 and A.7 in A.5b, we find

$$\begin{aligned}
 G(t_\mu, t'_\nu) &= \left\{ \Psi(X_0) + X_1 \Psi'(X_0) \Delta \delta y_{\mu, \nu} + \left[X_2 \Psi'(X_0) + \frac{X_1^2}{2} \Psi''(X_0) \right] (\Delta \delta y_{\mu, \nu})^2 \right\} \\
 &\quad * \left\{ \pm_\mu \pm_\nu l^2 + \dot{\delta} y_\mu(t_\mu) \dot{\delta} y_\nu(t'_\nu) \right\} \\
 &= \underbrace{\pm_\mu \pm_\nu l^2 \Psi(X_0)}_{F_{00}} \\
 &\quad + \underbrace{\pm_\mu \pm_\nu l^2 X_1 \Psi'(X_0)}_{F_{10}} \Delta \delta y_{\mu, \nu} \\
 &\quad + \underbrace{\pm_\mu \pm_\nu l^2 \left[X_2 \Psi'(X_0) + \frac{X_1^2}{2} \Psi''(X_0) \right]}_{F_{20}} (\Delta \delta y_{\mu, \nu})^2 \\
 &\quad + \underbrace{\Psi(X_0)}_{F_{21}} \dot{\delta} y_\mu(t_\mu) \dot{\delta} y_\nu(t'_\nu),
 \end{aligned}$$

and so, the total quadratic energy becomes

$$\begin{aligned}
 \sum_{\mu, \nu} \int_{\square\gamma_\mu} \int_{\square\gamma_\nu} G(t_\mu, t'_\nu) dt_\mu dt'_\nu &= \sum_{\mu, \nu} \int_{\square\gamma_\mu} \int_{\square\gamma_\nu} F_{00}(t_\mu, t'_\nu) dt_\mu dt'_\nu \\
 &\quad + \sum_{\mu, \nu} \int_{\square\gamma_\mu} \int_{\square\gamma_\nu} F_{10}(t_\mu, t'_\nu) \Delta \delta y_{\mu, \nu} dt_\mu dt'_\nu \\
 &\quad + \sum_{\mu, \nu} \int_{\square\gamma_\mu} \int_{\square\gamma_\nu} F_{20}(t_\mu, t'_\nu) (\Delta \delta y_{\mu, \nu})^2 dt_\mu dt'_\nu \\
 &\quad + \sum_{\mu, \nu} \int_{\square\gamma_\mu} \int_{\square\gamma_\nu} F_{21}(t_\mu, t'_\nu) \dot{\delta} y_\mu(t_\mu) \dot{\delta} y_\nu(t'_\nu) dt_\mu dt'_\nu.
 \end{aligned} \tag{A.8}$$

To compute these integrals, we make a change of variables to simplify the calculations. These integrals can be written as

$$\int_{\square\gamma_\mu} \int_{\square\gamma_\nu} f(t_\mu, t'_\nu) dt_\mu dt'_\nu, \tag{A.9}$$

where $f(t_\mu, t'_\nu)$ is a function which depends on $\pm_\mu l t_\mu$ and $\pm_\nu l t'_\nu$. Making a first change of variables, $s_\mu = l t_\mu$ and $s'_\nu = l t'_\nu$, equation A.9 becomes

$$\int_{-\frac{1}{2}}^{\frac{1}{2}} \int_{-\frac{1}{2}}^{\frac{1}{2}} f(t_\mu, t'_\nu) dt_\mu dt'_\nu = \frac{1}{l^2} \int_{-\frac{1}{2}}^{\frac{1}{2}} \int_{-\frac{1}{2}}^{\frac{1}{2}} f(s_\mu, s'_\nu) ds'_\nu ds_\mu.$$

The functions F_{ij} depend on $(\pm_\mu s_\mu - \pm_\nu s'_\nu)$, so a second change of variables can be made: $x = \pm_\mu s_\mu - \pm_\nu s'_\nu$ and $y = \pm_\mu s_\mu + \pm_\nu s'_\nu$ which give $s_\mu = \pm_\mu \frac{y+x}{2}$ and $s'_\nu = \pm_\nu \frac{y-x}{2}$.

The variables s_μ and s'_ν lie between $-\frac{l}{2}$ and $\frac{l}{2}$, so the new integration domain is defined as: $\{(x, y) \mid -l \leq x \leq l, -l + |x| \leq y \leq l - |x|\}$. We obtain

$$\int_{-\frac{l}{2}}^{\frac{l}{2}} \int_{-\frac{l}{2}}^{\frac{l}{2}} f(t_\mu, t'_\nu) dt_\mu dt'_\nu = \frac{1}{2l^2} \int_{-l}^l dx \int_{-l+|x|}^{l-|x|} f(x, y) dy .$$

The expression for $f(x, y)$ can always be written as a product of two functions: the first function depends on the interaction function Ψ given by equation 2.2 and its derivatives, embedded in the expressions for F_{ij} , which are equal to zero for a distance x greater than a given threshold which characterizes the interaction range of Ψ ; the second function is written as an exponential function describing the contribution of the Fourier perturbations. Then, we can approximate the integration domain by $\{(x, y) \mid -l \leq x \leq l, -l \leq y \leq l\}$. After these simple mathematical manipulations, we obtain

$$\int_{-\frac{l}{2}}^{\frac{l}{2}} \int_{-\frac{l}{2}}^{\frac{l}{2}} f(t_\mu, t'_\nu) dt_\mu dt'_\nu = \frac{1}{2l^2} \int_{-l}^l \int_{-l}^l f(x, y) dx dy . \quad (\text{A.10})$$

We now compute the different double integrals in equation (A.8) using the equality given by equation A.10.

$$\begin{aligned} & \int_{\square_{\gamma_\mu}} \int_{\square_{\gamma_\nu}} F_{00}(t_\mu, t'_\nu) dt_\mu dt'_\nu = \pm_\mu \pm_\nu l \int_{-l}^l \Psi(X_0(x)) dx ; \\ & \int_{\square_{\gamma_\mu}} \int_{\square_{\gamma_\nu}} F_{10}(t_\mu, t'_\nu) \Delta \delta y_{\mu, \nu} dt_\mu dt'_\nu = \\ & \int_{\square_{\gamma_\mu}} \int_{\square_{\gamma_\nu}} F_{10}(t_\mu, t'_\nu) \left(\sum_{k_\mu} a_{\mu, k_\mu} e^{ik_\mu t_\mu} - \sum_{k_\nu} a_{\nu, k_\nu} e^{ik_\nu t'_\nu} \right) dt_\mu dt'_\nu \\ & = \frac{1}{2l^2} \left\{ \int_{-l}^l \int_{-l}^l F_{10}(x) \sum_{k_\mu} a_{\mu, k_\mu} e^{\pm_\mu ik_\mu \frac{y+x}{2}} dx dy \right. \\ & \quad \left. - \int_{-l}^l \int_{-l}^l F_{10}(x) \sum_{k_\nu} a_{\nu, k_\nu} e^{\pm_\nu ik_\nu \frac{y-x}{2}} dx dy \right\} \\ & = \frac{1}{2l^2} \left\{ \sum_{k_\mu} a_{\mu, k_\mu} \int_{-l}^l F_{10}(x) e^{\pm_\mu ik_\mu \frac{x}{2}} \underbrace{\left(\int_{-l}^l e^{\pm_\mu ik_\mu \frac{y}{2}} dy \right)}_{2l\delta(k_\mu)} dx \right. \\ & \quad \left. - \sum_{k_\nu} a_{\nu, k_\nu} \int_{-l}^l F_{10}(x) e^{-\pm_\nu ik_\nu \frac{x}{2}} \left(\int_{-l}^l e^{-\pm_\nu ik_\nu \frac{y}{2}} dy \right) dx \right\} \\ & = \pm_\mu \pm_\nu l (a_{\mu, 0} - a_{\nu, 0}) \int_{-l}^l X_1(x) \Psi'(X_0(x)) dx ; \end{aligned}$$

$$\begin{aligned}
 \int_{\square\gamma_\mu} \int_{\square\gamma_\nu} F_{20}(t_\mu, t'_\nu) (\Delta\delta y_{\mu,\nu})^2 dt_\mu dt'_\nu &= \underbrace{\int_{\square\gamma_\mu} \int_{\square\gamma_\nu} F_{20}(t_\mu, t'_\nu) (\delta y_\mu(t_\mu))^2 dt_\mu dt'_\nu}_{I_1} \\
 &+ \underbrace{\int_{\square\gamma_\mu} \int_{\square\gamma_\nu} F_{20}(t_\mu, t'_\nu) (\delta y_\nu(t'_\nu))^2 dt_\mu dt'_\nu}_{I_2} \\
 &- 2 \underbrace{\int_{\square\gamma_\mu} \int_{\square\gamma_\nu} F_{20}(t_\mu, t'_\nu) \delta y_\mu(t_\mu) \delta y_\nu(t'_\nu) dt_\mu dt'_\nu}_{I_3} ;
 \end{aligned} \tag{A.11}$$

$$\begin{aligned}
 I_1 &= \int_{\square\gamma_\mu} \int_{\square\gamma_\nu} F_{20}(t_\mu, t'_\nu) \sum_{k_\mu, k'_\mu} a_{\mu, k_\mu} a_{\mu, k'_\mu} e^{i(k_\mu + k'_\mu)t_\mu} dt_\mu dt'_\nu \\
 &= \frac{1}{2l^2} \sum_{k_\mu, k'_\mu} a_{\mu, k_\mu} a_{\mu, k'_\mu} \int_{-l}^l F_{20}(x) e^{\pm i(k_\mu + k'_\mu)\frac{x}{2}} dx \underbrace{\int_{-l}^l e^{\pm i(k_\mu + k'_\mu)\frac{y}{2}} dy}_{2l\delta(k_\mu + k'_\mu)} \\
 &= \frac{1}{l} \sum_{k_\mu} |a_{\mu, k_\mu}|^2 \int_{-l}^l F_{20}(x) dx \\
 &= \frac{1}{l} \sum_k |a_{\mu, k}|^2 \int_{-l}^l F_{20}(x) dx ,
 \end{aligned}$$

and due to the symmetry of μ and ν in the expressions for I_1 and I_2 , we find

$$I_2 = \frac{1}{l} \sum_k |a_{\nu, k}|^2 \int_{-l}^l F_{20}(x) dx ,$$

and finally

$$\begin{aligned}
 I_3 &= \int_{\square\gamma_\mu} \int_{\square\gamma_\nu} F_{20}(t_\mu, t'_\nu) \sum_{k_\mu, k_\nu} a_{\mu, k_\mu} a_{\nu, k_\nu} e^{ik_\mu t_\mu} e^{ik_\nu t'_\nu} dt_\mu dt'_\nu \\
 &= \frac{1}{2l^2} \sum_{k_\mu, k_\nu} a_{\mu, k_\mu} a_{\nu, k_\nu} \int_{-l}^l F_{20}(x) e^{i(\pm_\mu k_\mu - \pm_\nu k_\nu)\frac{x}{2}} dx \underbrace{\int_{-l}^l e^{i(\pm_\mu k_\mu + \pm_\nu k_\nu)\frac{y}{2}} dy}_{2l\delta(\pm_\mu k_\mu + \pm_\nu k_\nu)} \\
 &= \frac{1}{l} \sum_k a_{\mu, k} a_{\nu, -\pm_\mu \pm_\nu k} \int_{-l}^l F_{20}(x) e^{\pm_\mu i k x} dx .
 \end{aligned}$$

Substituting the expressions for I_1 , I_2 and I_3 in equation A.11, one has

$$\begin{aligned} & \int_{\square\gamma_\mu} \int_{\square\gamma_\nu} F_{20}(t_\mu, t'_\nu) (\Delta\delta y_{\mu,\nu})^2 dt_\mu dt'_\nu = \frac{1}{l} \sum_k |a_{\mu,k}|^2 \int_{-l}^l F_{20}(x) dx \\ & + \frac{1}{l} \sum_k |a_{\nu,k}|^2 \int_{-l}^l F_{20}(x) dx - 2\frac{1}{l} \sum_k a_{\mu,k} a_{\nu,-\pm_\mu \pm_\nu k} \int_{-l}^l F_{20}(x) e^{\pm_\mu ikx} dx \\ & = \frac{1}{l} \sum_k \left\{ (|a_{\mu,k}|^2 + |a_{\nu,k}|^2) \int_{-l}^l F_{20}(x) dx - 2a_{\mu,k} a_{\nu,-\pm_\mu \pm_\nu k} \int_{-l}^l F_{20}(x) e^{\pm_\mu ikx} dx \right\}; \end{aligned}$$

$$\begin{aligned} & \int_{\square\gamma_\mu} \int_{\square\gamma_\nu} F_{21}(t_\mu, t'_\nu) \delta y_\mu(t_\mu) \delta y_\nu(t'_\nu) dt_\mu dt'_\nu = \\ & \int_{\square\gamma_\mu} \int_{\square\gamma_\nu} F_{21}(t_\mu, t'_\nu) \sum_{k_\mu, k_\nu} a_{\mu, k_\mu} a_{\nu, k_\nu} i^2 l^2 k_\mu k_\nu e^{ik_\mu t_\mu} e^{ik_\nu t'_\nu} dt_\mu dt'_\nu \\ & = -\frac{1}{2l^2} \sum_{k_\mu, k_\nu} a_{\mu, k_\mu} a_{\nu, k_\nu} l^2 k_\mu k_\nu \int_{-l}^l F_{21}(x) e^{i(\pm_\mu k_\mu - \pm_\nu k_\nu) \frac{x}{2}} dx \underbrace{\int_{-l}^l e^{i(\pm_\mu k_\mu + \pm_\nu k_\nu) \frac{y}{2}} dy}_{2l\delta(\pm_\mu k_\mu + \pm_\nu k_\nu)} \\ & = l \sum_k k^2 a_{\mu,k} a_{\nu,-\pm_\mu \pm_\nu k} \int_{-l}^l \Psi(X_0(x)) e^{\pm_\mu ikx} dx; \end{aligned}$$

Substituting the double integrals in equation (A.8) by their expressions computed previously, we obtain

$$\begin{aligned} & \sum_{\mu,\nu} \int_{\square\gamma_\mu} \int_{\square\gamma_\nu} G(t_\mu, t'_\nu) dt_\mu dt'_\nu = \sum_{\mu,\nu} \pm_\mu \pm_\nu l \int_{-l}^l \Psi(X_0(x)) dx \\ & + \sum_{\mu,\nu} \pm_\mu \pm_\nu l (a_{\mu,0} - a_{\nu,0}) \int_{-l}^l X_1(x) \Psi'(X_0(x)) dx \\ & + \sum_{\mu,\nu} \sum_k \pm_\mu \pm_\nu l (|a_{\mu,k}|^2 + |a_{\nu,k}|^2) \int_{-l}^l \left[X_2(x) \Psi'(X_0(x)) + \frac{X_1^2}{2} \Psi''(X_0(x)) \right] dx \\ & + \sum_{\mu,\nu} \sum_k -2 \pm_\mu \pm_\nu l a_{\mu,k} a_{\nu,-\pm_\mu \pm_\nu k} \int_{-l}^l \left[X_2(x) \Psi'(X_0(x)) + \frac{X_1^2}{2} \Psi''(X_0(x)) \right] e^{\pm_\mu ikx} dx \\ & + \sum_{\mu,\nu} \sum_k \pm_\mu \pm_\nu l k^2 a_{\mu,k} a_{\nu,-\pm_\mu \pm_\nu k} \int_{-l}^l \Psi(X_0(x)) e^{\pm_\mu ikx} dx. \end{aligned}$$

To compute the total quadratic energy E_Q , we separate two cases:

First case: $\pm_\mu \pm_\nu = 1$, which gives $X_0(x) = |x|$, $X_1(x) = 0$ and $X_2(x) = \frac{1}{2|x|}$. We then get

$$\begin{aligned}
 E_Q^{\pm_\mu \pm_\nu = 1}(\gamma) &= E_Q(\gamma_1, \gamma_1) + E_Q(\gamma_2, \gamma_2) \\
 &= \sum_{\pm_\mu \pm_\nu = 1} \pm_\mu \pm_\nu l \int_{-l}^l \Psi(X_0(x)) dx \\
 &+ \sum_{\pm_\mu \pm_\nu = 1} \sum_k \pm_\mu \pm_\nu l (|a_{\mu,k}|^2 + |a_{\nu,k}|^2) \int_{-l}^l \frac{1}{2|x|} \Psi'(|x|) dx \\
 &+ \sum_{\pm_\mu \pm_\nu = 1} \sum_k -2 \pm_\mu \pm_\nu l a_{\mu,k} a_{\nu, -\pm_\mu \pm_\nu k} \int_{-l}^l \frac{1}{2|x|} \Psi'(|x|) e^{\pm_\mu i k x} dx \\
 &+ \sum_{\pm_\mu \pm_\nu = 1} \sum_k \pm_\mu \pm_\nu l k^2 a_{\mu,k} a_{\nu, -\pm_\mu \pm_\nu k} \int_{-l}^l \Psi(|x|) e^{\pm_\mu i k x} dx \\
 &= 2l \int_{-l}^l \Psi(|x|) dx \\
 &+ 2l \sum_k (|a_{1,k}|^2 + |a_{2,k}|^2) \int_{-l}^l \frac{1}{2|x|} \Psi'(|x|) dx \\
 &- 2l \sum_k (|a_{1,k}|^2 + |a_{2,k}|^2) \int_{-l}^l \frac{1}{2|x|} \Psi'(|x|) e^{i k x} dx \\
 &+ l \sum_k k^2 (|a_{1,k}|^2 + |a_{2,k}|^2) \int_{-l}^l \Psi(|x|) e^{i k x} dx \\
 &= 2l \int_{-l}^l \Psi(|x|) dx \\
 &+ l \sum_k (|a_{1,k}|^2 + |a_{2,k}|^2) \int_{-l}^l \frac{1}{|x|} \Psi'(|x|) - \frac{1}{|x|} \Psi'(|x|) e^{i k x} + k^2 \Psi(|x|) e^{i k x} dx .
 \end{aligned}$$

Second case: $\pm_\mu \pm_\nu = -1$, which gives $X_0(x) = \sqrt{x^2 + w_0^2}$, $X_1(x) = \pm_\mu \frac{w_0}{\sqrt{x^2 + w_0^2}}$ and $X_2(x) = \frac{x^2}{2(x^2 + w_0^2)^{\frac{3}{2}}}$. We then get

$$\begin{aligned}
E_Q^{\pm_\mu \pm_\nu = -1}(\gamma) &= E_Q(\gamma_1, \gamma_2) + E_Q(\gamma_2, \gamma_1) \\
&= \sum_{\pm_\mu \pm_\nu = -1} -l \int_{-l}^l \Psi(X_0(x)) dx \\
&+ \sum_{\pm_\mu \pm_\nu = -1} -l(a_{\mu,0} - a_{\nu,0}) \int_{-l}^l \pm_\mu \frac{w_0}{\sqrt{x^2 + w_0^2}} \Psi'(\sqrt{x^2 + w_0^2}) dx \\
&+ \sum_{\pm_\mu \pm_\nu = -1} \sum_k -l(|a_{\mu,k}|^2 + |a_{\nu,k}|^2) \int_{-l}^l \left\{ \frac{x^2}{2(x^2 + w_0^2)^{\frac{3}{2}}} \Psi'(\sqrt{x^2 + w_0^2}) \right. \\
&+ \left. \frac{w_0^2}{2(x^2 + w_0^2)} \Psi''(\sqrt{x^2 + w_0^2}) \right\} dx \\
&+ \sum_{\pm_\mu \pm_\nu = -1} \sum_k 2l a_{\mu,k} a_{\nu,k} \int_{-l}^l \left\{ \frac{x^2}{2(x^2 + w_0^2)^{\frac{3}{2}}} \Psi'(\sqrt{x^2 + w_0^2}) \right. \\
&+ \left. \frac{w_0^2}{2(x^2 + w_0^2)} \Psi''(\sqrt{x^2 + w_0^2}) \right\} e^{\pm_\mu ikx} dx \\
&+ \sum_{\pm_\mu \pm_\nu = -1} \sum_k -l k^2 a_{\mu,k} a_{\nu,k} \int_{-l}^l \Psi(\sqrt{x^2 + w_0^2}) e^{\pm_\mu ikx} dx \\
&= -2l \int_{-l}^l \Psi(\sqrt{x^2 + w_0^2}) dx - 2l(a_{1,0} - a_{2,0}) \int_{-l}^l \frac{w_0}{\sqrt{x^2 + w_0^2}} \Psi'(\sqrt{x^2 + w_0^2}) dx \\
&- 2l \sum_k (|a_{1,k}|^2 + |a_{2,k}|^2) \int_{-l}^l \frac{x^2}{2(x^2 + w_0^2)^{\frac{3}{2}}} \Psi'(\sqrt{x^2 + w_0^2}) + \frac{w_0^2}{2(x^2 + w_0^2)} \Psi''(\sqrt{x^2 + w_0^2}) dx \\
&+ 2l \sum_k (a_{1,k} a_{2,k} + a_{1,-k} a_{2,-k}) \int_{-l}^l \left\{ \frac{x^2}{2(x^2 + w_0^2)^{\frac{3}{2}}} \Psi'(\sqrt{x^2 + w_0^2}) \right. \\
&+ \left. \frac{w_0^2}{2(x^2 + w_0^2)} \Psi''(\sqrt{x^2 + w_0^2}) \right\} e^{ikx} dx \\
&- l \sum_k (a_{1,k} a_{2,k} + a_{1,-k} a_{2,-k}) \int_{-l}^l k^2 \Psi(\sqrt{x^2 + w_0^2}) e^{ikx} dx .
\end{aligned}$$

The total quadratic energy of the contour γ is then given by

$$\begin{aligned}
E_Q(\gamma) &= E_Q^{\pm\mu\pm\nu=1}(\gamma) + E_Q^{\pm\mu\pm\nu=-1}(\gamma) \\
&= 2l \int_{-l}^l \Psi(|x|) dx - 2l \int_{-l}^l \Psi(\sqrt{x^2 + w_0^2}) dx \\
&\quad - 2l(a_{1,0} - a_{2,0}) \int_{-l}^l \frac{w_0}{\sqrt{x^2 + w_0^2}} \Psi'(\sqrt{x^2 + w_0^2}) dx \\
&\quad + l \sum_k (|a_{1,k}|^2 + |a_{2,k}|^2) \int_{-l}^l \frac{1}{|x|} \Psi'(|x|) - \frac{1}{|x|} \Psi'(|x|) e^{ikx} + k^2 \Psi(|x|) e^{ikx} dx \\
&\quad - l \sum_k (|a_{1,k}|^2 + |a_{2,k}|^2) \int_{-l}^l \left\{ \frac{x^2}{(x^2 + w_0^2)^{\frac{3}{2}}} \Psi'(\sqrt{x^2 + w_0^2}) \right. \\
&\quad \left. + \frac{w_0^2}{x^2 + w_0^2} \Psi''(\sqrt{x^2 + w_0^2}) \right\} dx \\
&\quad + l \sum_k (a_{1,k} a_{2,k} + a_{1,-k} a_{2,-k}) \int_{-l}^l \left\{ \frac{x^2}{(x^2 + w_0^2)^{\frac{3}{2}}} \Psi'(\sqrt{x^2 + w_0^2}) \right. \\
&\quad \left. + \frac{w_0^2}{(x^2 + w_0^2)} \Psi''(\sqrt{x^2 + w_0^2}) \right\} e^{ikx} dx \\
&\quad - l \sum_k (a_{1,k} a_{2,k} + a_{1,-k} a_{2,-k}) \int_{-l}^l k^2 \Psi(\sqrt{x^2 + w_0^2}) e^{ikx} dx .
\end{aligned} \tag{A.12}$$

Substituting the length, the area and the quadratic terms by their expressions given by equations (A.3), (A.4) and (A.12) in the expression for the geometric energy E_P of the contour γ given by equation (2.1), we find

$$\begin{aligned}
E_P^{(2)}(\gamma) &= \lambda_C l \left[2 + \frac{1}{2} \sum_k k^2 (|a_{1,k}|^2 + |a_{2,k}|^2) \right] \\
&+ \alpha_C l [w + (a_{1,0} - a_{2,0})] \\
&- \frac{\beta_C}{2} 2l \int_{-l}^l \Psi(|x|) - \Psi(\sqrt{x^2 + w_0^2}) dx \\
&+ \frac{\beta_C}{2} 2l(a_{1,0} - a_{2,0}) \int_{-l}^l \frac{w_0}{\sqrt{x^2 + w_0^2}} \Psi'(\sqrt{x^2 + w_0^2}) dx \\
&- \frac{\beta_C}{2} l \sum_k (|a_{1,k}|^2 + |a_{2,k}|^2) \int_{-l}^l \frac{1}{|x|} \Psi'(|x|) - \frac{1}{|x|} \Psi'(|x|) e^{ikx} + k^2 \Psi(|x|) e^{ikx} dx \\
&+ \frac{\beta_C}{2} l \sum_k (|a_{1,k}|^2 + |a_{2,k}|^2) \int_{-l}^l \frac{x^2}{(x^2 + w_0^2)^{\frac{3}{2}}} \Psi'(\sqrt{x^2 + w_0^2}) + \frac{w_0^2}{x^2 + w_0^2} \Psi''(\sqrt{x^2 + w_0^2}) dx \\
&- \frac{\beta_C}{2} l \sum_k (a_{1,k} a_{2,k} + a_{1,-k} a_{2,-k}) \int_{-l}^l \left[\frac{x^2}{(x^2 + w_0^2)^{\frac{3}{2}}} \Psi'(\sqrt{x^2 + w_0^2}) \right. \\
&+ \left. \frac{w_0^2}{(x^2 + w_0^2)} \Psi''(\sqrt{x^2 + w_0^2}) \right] e^{ikx} dx \\
&+ \frac{\beta_C}{2} l \sum_k (a_{1,k} a_{2,k} + a_{1,-k} a_{2,-k}) \int_{-l}^l k^2 \Psi(\sqrt{x^2 + w_0^2}) e^{ikx} dx .
\end{aligned}$$

The bar length, l , is very big compared to the bar width, w_0 , in order that we can ignore the effect of both bar extremities, and we will take the $l \rightarrow +\infty$ limit. To simplify the expression for the energy, we define

$$\begin{aligned}
G_{00}(w_0) &= \int_{-\infty}^{+\infty} \Psi(|x|) - \Psi(\sqrt{x^2 + w_0^2}) dx , \\
G_{10}(w_0) &= \int_{-\infty}^{+\infty} \frac{-w_0}{\sqrt{x^2 + w_0^2}} \Psi'(\sqrt{x^2 + w_0^2}) dx , \\
G_{20}(w_0, k) &= \int_{-\infty}^{+\infty} \left\{ \frac{x^2}{(x^2 + w_0^2)^{\frac{3}{2}}} \Psi'(\sqrt{x^2 + w_0^2}) + \frac{w_0^2}{(x^2 + w_0^2)} \Psi''(\sqrt{x^2 + w_0^2}) \right. \\
&\quad \left. - \frac{1}{|x|} \Psi'(|x|) (1 - e^{ikx}) - k^2 \Psi(|x|) e^{ikx} \right\} dx , \\
G_{21}(w_0, k) &= \int_{-\infty}^{+\infty} \left\{ -\frac{x^2}{(x^2 + w_0^2)^{\frac{3}{2}}} \Psi'(\sqrt{x^2 + w_0^2}) - \frac{w_0^2}{(x^2 + w_0^2)} \Psi''(\sqrt{x^2 + w_0^2}) \right. \\
&\quad \left. + k^2 \Psi(\sqrt{x^2 + w_0^2}) \right\} e^{ikx} dx .
\end{aligned}$$

Variational calculations for the directed network model

Contents

B.1	First derivatives of phase field terms	145
B.1.1	Derivative of the term weighted by D	145
B.1.2	Derivative of the term weighted by D_v	145
B.1.3	Derivative of the term weighted by L_v	146
B.1.4	Derivative of the nonlocal term	146
B.2	Fourier transform of the linear derivatives	147

Here we detail the variational calculations for the phase field energy given by equation (4.1). For each energy term, we compute the energy of $\phi + \delta\phi$ and $v + \delta v$ and we try to express it as the following: $E(\phi + \delta\phi, v + \delta v) = E(\phi, v) + \langle E_1(\phi, v) | \delta(\phi, v) \rangle$. The derivative is then $E_1(\phi, v)$.

B.1 First derivatives of phase field terms

B.1.1 Derivative of the term weighted by D

$$\begin{aligned} E(\phi + \delta\phi) &= \frac{1}{2} \int \partial(\phi + \delta\phi) \cdot \partial(\phi + \delta\phi) = \frac{1}{2} \int \partial\phi \cdot \partial\phi + 2\partial\phi \cdot \partial\delta\phi \\ &= E(\phi) - \int (\partial \cdot \partial\phi) \delta\phi, \end{aligned}$$

and so

$$\frac{\delta}{\delta\phi} \int \frac{1}{2} \partial\phi \cdot \partial\phi = -\partial^2\phi.$$

B.1.2 Derivative of the term weighted by D_v

$$\begin{aligned} E(v + \delta v) &= \frac{1}{2} \int (\partial \cdot (v + \delta v))^2 = \frac{1}{2} \int (\partial \cdot v + \partial \cdot \delta v)^2 \\ &= \frac{1}{2} \int (\partial \cdot v)^2 + 2(\partial \cdot v)(\partial \cdot \delta v) = E(v) - \int \partial(\partial \cdot v) \cdot \delta v, \end{aligned}$$

and so

$$\frac{\delta}{\delta v} \int \frac{1}{2} (\partial \cdot v)^2 = -\partial(\partial \cdot v) .$$

B.1.3 Derivative of the term weighted by L_v

$$\begin{aligned} E(v + \delta v) &= \frac{1}{2} \int (\partial_m(v^n + \delta v^n))^2 = \frac{1}{2} \int (\partial_m v^n + \partial_m \delta v^n)^2 \\ &= \frac{1}{2} \int (\partial_m v^n)^2 + 2(\partial_m v^n)(\partial_m \delta v^n) = E(v) - \int \partial_m(\partial_m v^n) \delta v^n , \end{aligned}$$

and so

$$\frac{\delta}{\delta v} \int \frac{1}{2} (\partial_m v^n)^2 = -\partial^2 v .$$

B.1.4 Derivative of the nonlocal term

$$\begin{aligned} E(\phi + \delta\phi) &= -\frac{1}{2} \iint \partial(\phi + \delta\phi) \cdot \partial(\phi' + \delta\phi') \Psi \\ &= E(\phi) - \frac{1}{2} \iint \partial\phi \cdot \partial\delta\phi' \Psi - \frac{1}{2} \iint \partial\delta\phi \cdot \partial\phi' \Psi \\ &= E(\phi) - \iint \partial\phi' \cdot \partial\delta\phi \Psi \\ &= E(\phi) + \iint (\partial \cdot (\partial\phi' \Psi)) \delta\phi \\ &= E(\phi) + \iint \partial\phi' \cdot \partial\Psi \delta\phi , \end{aligned}$$

and so

$$\begin{aligned} \frac{\delta}{\delta\phi} \left\{ -\frac{1}{2} \iint_{\Omega^2} d^2x' \partial\phi(x) \cdot \partial\phi(x') \Psi(x-x') \right\} &= \int_{\Omega} d^2x' \partial\phi(x') \cdot \partial\Psi(x-x') \\ &= - \int_{\Omega} d^2x' \phi(x') \partial' \partial\Psi(x-x') \\ &= \int_{\Omega} d^2x' \phi(x') \partial^2 \Psi(x-x') \\ &= \phi(x) * \partial^2 \Psi(x) . \end{aligned}$$

B.2 Fourier transform of the linear derivatives

Let $\hat{\phi}$ the Fourier transform of ϕ and $\square = -\partial^2$ the negative Laplacian. The Fourier transform of the negative Laplacian of ϕ is

$$\begin{aligned}\mathcal{F}(\square\phi) &= \int \frac{d^2x}{2\pi} e^{-ik\cdot x} \square\phi = \int \frac{d^2x}{2\pi} e^{-ik\cdot x} (-\partial \cdot \partial\phi) \\ &= \int \frac{d^2x}{2\pi} (-ik)e^{-ik\cdot x} \partial\phi = \int \frac{d^2x}{2\pi} k^2 e^{-ik\cdot x} \phi = k^2 \hat{\phi}(k),\end{aligned}$$

where we made two integrations by parts.

The Fourier transform of the derivative of the nonlocal term, *i.e.* the convolution product $-\square\Psi * \phi$, is

$$\mathcal{F}(-\square\Psi * \phi) = -k^2 \hat{\Psi}(k) \hat{\phi}(k).$$

The Fourier transform of the divergence derivative $-\partial(\partial \cdot v)$ is

$$\begin{aligned}\mathcal{F}(-\partial_m(\partial_n v^n)) &= \int \frac{d^2x}{2\pi} e^{-ik\cdot x} (-\partial_m(\partial_n v^n)) = \int \frac{d^2x}{2\pi} (-ik_m) e^{-ik\cdot x} \partial_n v^n \\ &= \int \frac{d^2x}{2\pi} k_m k_n e^{-ik\cdot x} v^n = k_m k_n \hat{v}^n = k_m (k \cdot \hat{v}(k)).\end{aligned}$$

The Fourier transform of the derivative of the smoothing term $-\partial^2 v$ is

$$\begin{aligned}\mathcal{F}(-\partial_m(\partial_m v^n)) &= \int \frac{d^2x}{2\pi} e^{-ik\cdot x} (-\partial_m(\partial_m v^n)) = \int \frac{d^2x}{2\pi} (-ik_m) e^{-ik\cdot x} \partial_m v^n \\ &= \int \frac{d^2x}{2\pi} k_m k_m e^{-ik\cdot x} v^n = k^2 \hat{v}^n(k).\end{aligned}$$

Turing stability calculations for the directed network model

Contents

C.1 Stability of the background	151
C.1.1 Particular case: $L_v = 0$ and $\Psi = K_0$	152
C.2 Stability of the foreground	152
C.2.1 Particular case: $L_v = 0$ and $\Psi = K_0$	153

In this appendix, we detail the stability analysis of the background and the foreground under the total phase field HOAC model, $E_P = E_0 + E_{NL}$, where E_0 is

$$E_0(\phi, v) = \int_{\Omega} d^2x \left\{ \frac{D}{2} \partial\phi \cdot \partial\phi + \frac{D_v}{2} (\partial \cdot v)^2 + \frac{L_v}{2} \partial v : \partial v + \frac{A_v}{2} (\partial\phi \cdot v)^2 + W(\phi, v) \right\}. \quad (\text{C.1})$$

The local phase field model given by equation (4.1) is obtained by setting $A_v = 0$. We study, firstly, the first order stability conditions and, secondly, the positivity conditions for the eigenvalues of the Hessian matrix \hat{H} expressed in the Fourier domain and evaluated at the desired stable configurations (*i.e.* the background and the foreground). The Hessian matrix \hat{H} is given by equation (4.3). This will generate constraints on the model parameters.

The first order stability conditions, *i.e.* that the first order variations of the energy be equal to zero, of the background and the foreground constrain the parameters of the potential W as the follows:

$$\lambda_{20} = -1 - \frac{\lambda_{22}}{2} - \lambda_{21}, \quad (\text{C.2})$$

$$\lambda_{01} = -\frac{\lambda_{22}}{4} - \frac{\lambda_{21}}{4} - \lambda_{03}, \quad (\text{C.3})$$

$$\lambda_{02} = -\frac{\lambda_{22}}{4} - \frac{\lambda_{21}}{4} - \lambda_{04}. \quad (\text{C.4})$$

Thus the number of free parameters of the potential W is reduced from 7 to 4.

The second order stability conditions, that the Hessian matrix be positive definite at the desired local minima, give upper and lower bounds for the parameter values. The Hessian matrix is given by equation (4.3). \hat{H} is positive definite iff its eigenvalues are strictly positives for all frequencies k . It is simpler to study the three invariants of \hat{H} given below

instead of the eigenvalues. The positivity conditions of the eigenvalues are equivalent to those of the invariants. A state (ϕ_0, v_0) is stable iff the 3 invariants of \hat{H} evaluated at this point are strictly positive for all frequencies k . The 3 invariants of \hat{H} are

$$\begin{aligned}
I_1 &= \text{tr}(\hat{H}) = A_v(k \cdot v_0)^2 + D_v k^2 + 2L_v k^2 + 2v_0^2 + [D - \beta\hat{G}(k)]k^2 + F_{11} + 2F_{22} , \\
I_2 &= \frac{1}{2} \left(\text{tr}(\hat{H})^2 - \text{tr}(\hat{H}^2) \right) \\
&= \underbrace{(D_v k^2 + 2L_v k^2 + 2F_{22} + 2v_0^2)}_Y \left(\underbrace{A_v(k \cdot v_0)^2 + [D - \beta\hat{G}(k)]k^2 + F_{11}}_X + L_v k^2 + F_{22} \right) \\
&\quad - (L_v k^2 + F_{22})^2 - F_{12}^2 v_0^2 + 2D_v (k \times v_0)^2 , \\
I_3 &= \det(\hat{H}) \\
&= \left(A_v(k \cdot v_0)^2 + [D - \beta\hat{G}(k)]k^2 + F_{11} \right) \left((F_{22} + L_v k^2)(D_v k^2 + 2L_v k^2 + 2F_{22} + 2v_0^2) \right. \\
&\quad \left. - (F_{22} + L_v k^2)^2 + 2D_v (k \times v_0)^2 \right) - F_{12}^2 [(F_{22} + L_v k^2)v_0^2 + D_v (k \times v_0)^2] ,
\end{aligned}$$

where tr and \det are the trace and the determinant of a matrix respectively; \times is the cross product between two vectors. The invariants can be written as

$$\begin{aligned}
I_1 &= X + Y > 0 \quad \forall k , \\
I_2 &= Y(X + L_v k^2 + F_{22}) + 2D_v (k \times v_0)^2 - (F_{22} + L_v k^2)^2 - F_{12}^2 v_0^2 > 0 \quad \forall k , \\
I_3 &= X[(F_{22} + L_v k^2)Y - (F_{22} + L_v k^2)^2 + 2D_v (k \times v_0)^2] - F_{12}^2 [(F_{22} + L_v k^2)v_0^2 \\
&\quad + D_v (k \times v_0)^2] > 0 \quad \forall k .
\end{aligned}$$

First, we study the case of $k = 0$. The eigenvalues of \hat{H} are

$$\begin{aligned}
\lambda_1 &= F_{22} , \\
\lambda_2 &= \frac{1}{2} \left(F + F_{11} - \sqrt{(F - F_{11})^2 + 4F_{12}^2 v_0^2} \right) , \\
\lambda_3 &= \frac{1}{2} \left(F + F_{11} + \sqrt{(F - F_{11})^2 + 4F_{12}^2 v_0^2} \right) ,
\end{aligned}$$

where $F = F_{22} + 2v_0^2$. The stability conditions require that, first, $F_{11} > 0$ and, second, $0 < \lambda_2$ (because $\lambda_2 < \lambda_3$) which gives $F + F_{11} > 0$ and $F - F_{11} - F_{12}^2 v_0^2 > 0$, the latter gives $F_{11} > 0$ because $F > 0$. Then, the inequality system S_0 , which corresponds to $k = 0$, is

$$S_0 = \begin{cases} F_{11} > 0 , \\ F_{22} > 0 , \\ F_{11}(F_{22} + 2v_0^2) - F_{12}^2 v_0^2 > 0 . \end{cases}$$

The positivity conditions of the 3 invariants are then summarized as

$$S = \begin{cases} X + Y > 0 \quad \forall k , \\ Y(X + L_v k^2 + F_{22}) + 2D_v(k \times v_0)^2 > 0 \quad \forall k , \\ Y(X + L_v k^2 + F_{22}) + 2D_v(k \times v_0)^2 - (F_{22} + L_v k^2)^2 - F_{12}^2 v_0^2 > 0 \quad \forall k , \\ X[(F_{22} + L_v k^2)Y - (F_{22} + L_v k^2)^2 + 2D_v(k \times v_0)^2] > 0 \quad \forall k , \\ X[(F_{22} + L_v k^2)Y - (F_{22} + L_v k^2)^2 + 2D_v(k \times v_0)^2] \\ - F_{12}^2[(F_{22} + L_v k^2)v_0^2 + D_v(k \times v_0)^2] > 0 \quad \forall k . \end{cases}$$

The fourth inequality is satisfied if $X > 0$ because $F_{22}(Y - F_{22}) > 0$. And due to $Y > 0$, we get

$$S = \begin{cases} X > 0 \quad \forall k , \\ Y(X + L_v k^2 + F_{22}) + 2D_v(k \times v_0)^2 - (F_{22} + L_v k^2)^2 - F_{12}^2 v_0^2 > 0 \quad \forall k , \\ X[(F_{22} + L_v k^2)Y - (F_{22} + L_v k^2)^2 + 2D_v(k \times v_0)^2] \\ - F_{12}^2[(F_{22} + L_v k^2)v_0^2 + D_v(k \times v_0)^2] > 0 \quad \forall k . \end{cases} \quad (\text{C.5})$$

To conclude, the point (ϕ_0, v_0) is stable iff S is satisfied. The zero frequency constraints, *i.e.* the system S_0 , involve only terms coming from the W . A way to solve the constraints given by the system S (*i.e.* the form $f(k) > 0 \quad \forall k$) can be treated in 2 steps: 1) prove that f is bounded below at $k = k^*$ and 2) $f(k^*) > 0$. A way to prove that a function f is bounded below is to prove that f has a minimum at k^* .

C.1 Stability of the background

When $(\phi_0, v_0) = (-1, 0)$, *i.e.* $(\phi_0, v_0^1, v_0^2) = (-1, 0, 0)$, the functions F_{ij} become

$$\begin{aligned} F_{11}^b &= 3\lambda_{04} - 2\lambda_{03} + \lambda_{02} , \\ F_{22}^b &= \frac{\lambda_{22}}{2} - \lambda_{21} + \lambda_{20} , \end{aligned}$$

and replacing the parameters λ_{02} and λ_{20} by their expressions given by (D.2), (D.3) and (D.4), one can get

$$\begin{aligned} F_{11}^b &= 2\lambda_{04} - 2\lambda_{03} - \frac{\lambda_{22}}{4} - \frac{\lambda_{21}}{4} , \\ F_{22}^b &= -2\lambda_{21} - 1 . \end{aligned}$$

The systems S_0 and S are reduced to

$$S_b = \begin{cases} F_{11}^b > 0 , \\ F_{22}^b > 0 , \\ X^b > 0 . \end{cases} \quad (\text{C.6})$$

C.1.1 Particular case: $L_v = 0$ and $\Psi = K_0$

Here, we restrict the stability calculations to the case in which $L_v = 0$ and the interaction function $\Psi = K_0$ where K_0 corresponds to a modified Bessel function of the second kind of order 0. Its Fourier transform is given by $\hat{\Psi}(k) = 1/(m^2 + k^2)$ where m is an interaction range parameter in the Fourier domain like the parameter d in the spatial domain given in equation (3.2). Replacing $\hat{\Psi}$ by its expression, one can write

$$X^b(k) = \frac{Dk^4 + (Dm^2 - \beta)k^2}{m^2 + k^2} + F_{11}^b,$$

and its derivative with respect to k , while introducing the variable $w = k^2$, is $\frac{\partial X^b(k)}{\partial k} = 2k \frac{\partial X^b(w)}{\partial w}$ where

$$\frac{\partial X^b(w)}{\partial w} = \frac{Dw^2 + 2Dm^2w - (\beta - Dm^2)m^2}{(m^2 + w)^2} = 0,$$

which has one solution $w^* = (-Dm^2 + m\sqrt{D\beta})/D$ if $\beta > Dm^2$, and $X^b(w^*) = F_{11}^b - (\sqrt{\beta} - m\sqrt{D})^2 < X^b(0) = F_{11}^b$. So the constraint $X^b(k) > 0 \forall k$ becomes:

$$\begin{cases} \text{if } \beta \leq Dm^2 & \text{then } X^b(0) = F_{11}^b > 0 \\ \text{if } Dm^2 < \beta < (m\sqrt{D} + \sqrt{F_{11}^b})^2 & \text{then } X^b(w^*) > 0 \\ \text{if } \beta \geq (m\sqrt{D} + \sqrt{F_{11}^b})^2 & \text{then } X^b(w^*) < 0, \end{cases} \quad (\text{C.7})$$

and so the conclusion is: $X^b(k) > 0 \forall k$ is satisfied if $0 < \beta < (m\sqrt{D} + \sqrt{F_{11}^b})^2$.

C.2 Stability of the foreground

When $(\phi_0, v_0) = (1, 1)$, i.e. $(\phi_0, |v_0|) = (\phi_0, \sqrt{(v_0^1)^2 + (v_0^2)^2}) = (1, 1)$, the functions F_{ij} become

$$\begin{aligned} F_{11}^f &= \frac{\lambda_{22}}{2} + 3\lambda_{04} + 2\lambda_{03} + \lambda_{02}, \\ F_{22}^f &= 1 + \frac{\lambda_{22}}{2} + \lambda_{21} + \lambda_{20}, \\ F_{12}^f &= (\lambda_{22} + \lambda_{21}), \end{aligned}$$

and replacing the parameters λ_{02} and λ_{20} by their expressions given by (D.4) and (D.2), one can get

$$\begin{aligned} F_{11}^f &= 2\lambda_{04} + 2\lambda_{03} + \frac{\lambda_{22}}{4} - \frac{\lambda_{21}}{4}, \\ F_{22}^f &= 0, \\ F_{12}^f &= (\lambda_{22} + \lambda_{21}). \end{aligned}$$

Due to the Euclidean invariance of v_0 , we put $v_0 = (1, 0)$ and so $(k \cdot v_0)^2 = k_1^2 = w_1$ and $(k \times v_0)^2 = k_2^2 = w_2$ where $w_1 + w_2 = w$. The systems S_0 and S are reduced to

$$S_f = \begin{cases} F_{11}^f > 0 \\ 2F_{11}^f - (F_{12}^f)^2 > 0 \\ X^f > 0 \forall k \\ Z^f = 2X^f - (F_{12}^f)^2 > 0 \forall k, \end{cases} \quad (\text{C.8})$$

because $Y^f X^f + 2D_v(k \times v_0)^2 > 2X^f$. Of course, the fourth constraint implies the third one.

C.2.1 Particular case: $L_v = 0$ and $\Psi = K_0$

The minima of Z^f are the same as those of X^f ; so we seek the minima of X^f . After simple calculations, one can write

$$X^f(k_1, k_2) = X^f(w_1, w) = \frac{\tilde{D}w^2 + A_v w_1 w + A_v m^2 w_1 + (Dm^2 - \beta)w}{m^2 + w} + F_{11}^f.$$

The partial derivatives of X^f can be computed as

$$\frac{\partial X^f(k_1, k_2)}{\partial k_i} = 2k_i \frac{\partial X^f(w_1, w)}{\partial w_i}, \quad (\text{C.9})$$

where $i = 1, 2$ and $\tilde{D} = D + D_v$. After calculations, we obtain

$$\begin{aligned} \frac{\partial X^f(w_1, w)}{\partial w_1} &= \frac{(A_v + \tilde{D})w^2 + 2(A_v + \tilde{D})m^2 w + (A_v m^2 + Dm^2 - \beta)m^2}{(m^2 + w)^2} = 0 \\ \frac{\partial X^f(w_2, w)}{\partial w_2} &= \frac{\tilde{D}w^2 + 2\tilde{D}m^2 w + (Dm^2 - \beta)m^2}{(m^2 + w)^2} = 0, \end{aligned}$$

which are equivalent to

$$\begin{cases} (w + m^2)^2 = 0 \\ \tilde{D}w^2 + 2\tilde{D}m^2 w + (Dm^2 - \beta)m^2 = 0, \end{cases}$$

where only the second equation has, when $\beta > Dm^2$, a solution $w^* = -m^2 + m\sqrt{(\beta + D_v m^2)/\tilde{D}}$ because $w = k^2 \geq 0$. Then, the solutions of the equations given by (C.9) are as follows:

$$\begin{cases} \text{if } \beta \leq Dm^2 & \text{then } (k_1^*, k_2^*) = (0, 0) > 0 \\ \text{if } Dm^2 > \beta & \text{then } (k_1^*, k_2^*) = (0, \sqrt{w^* - w_1^*}) = (0, \sqrt{w^*}) > 0. \end{cases}$$

The constraint $Z^f(k_1, k_2) > 0, \forall k_1, k_2$ is then equivalent to $Z^f(w^*) = -2\tilde{D}(m - \Gamma)^2 + 2F_{11}^f - (F_{12}^f)^2 > 0$ where $\Gamma = \sqrt{(\beta + D_v m^2)/\tilde{D}}$. We then get

$$\begin{cases} \text{if } \beta \leq Dm^2 & \text{then } Z^f(0) = 2F_{11}^f - (F_{12}^f)^2 > 0 \\ \text{if } Dm^2 < \beta < \tilde{D} \left(m + \sqrt{(2F_{11}^f - (F_{12}^f)^2)/(2\tilde{D})} \right)^2 - D_v m^2 & \text{then } Z^f(w^*) > 0 \\ \text{if } \beta \geq \tilde{D} \left(m + \sqrt{(2F_{11}^f - (F_{12}^f)^2)/(2\tilde{D})} \right)^2 - D_v m^2 & \text{then } Z^f(w^*) < 0, \end{cases}$$

and so the conclusion is:

$$Z^f(k) > 0, \forall k \Leftrightarrow 0 < \beta < \tilde{D} \left(m + \sqrt{(2F_{11}^f - (F_{12}^f)^2)/(2\tilde{D})} \right)^2 - D_v m^2.$$

Stability calculations for a long bar under the directed network HOAC model

Contents

D.1 Energy of the long bar	155
D.1.1 Contribution of the local term	155
D.1.2 Contribution of the nonlocal term	158
D.1.3 Total bar energy	158
D.2 Stability constraints	159
D.2.1 First order stability conditions	159
D.2.2 Second order stability conditions	161
D.2.3 Derivatives of the function K_0	163

In this appendix, we detail the stability calculations for the directed long bar studied in chapter 5.

D.1 Energy of the long bar

D.1.1 Contribution of the local term

The local phase field model is

$$E_{P,0} = \int_{\Omega} d^2x \left\{ \frac{D}{2} \partial\phi \cdot \partial\phi + \tilde{W}(\phi, v) + \frac{D_v}{2} (\partial \cdot v)^2 + \frac{L_v}{2} \partial v : \partial v \right\}, \quad (\text{D.1})$$

where $\tilde{W}(\phi, v) = W(\phi, v) - W(-1, 0)$, where the generic form of $W(\phi, v)$ is given by equation (4.2). The first order stability conditions, *i.e.* that the first order variations of the energy equal zero, of the background and the foreground constrain the parameters of W as the follows (*cf.* Appendix C):

$$\lambda_{20} = -1 - \frac{\lambda_{22}}{2} - \lambda_{21}, \quad (\text{D.2})$$

$$\lambda_{01} = -\frac{\lambda_{22}}{4} - \frac{\lambda_{21}}{4} - \lambda_{03}, \quad (\text{D.3})$$

$$\lambda_{02} = -\frac{\lambda_{22}}{4} - \frac{\lambda_{21}}{4} - \lambda_{04}. \quad (\text{D.4})$$

The local energy contributions of R and \bar{R} are

$$E_{0,R} = \int_{-\infty}^{+\infty} \int_w^{w_0} dx_1 dx_2 \tilde{W}(\phi_m, v_m) = L(w_0 - w)(W(\phi_m, v_m) - W(-1, 0)),$$

$$E_{0,\bar{R}} = \int_{-\infty}^{+\infty} \int_{\bar{R}} dx_1 dx_2 \tilde{W}(-1, 0) = 0,$$

and due to the symmetry of the bar, the contributions of R_{CB} and R_{CT} are equal:

$$E_{0,R_{CB}} = \int_{-\infty}^{+\infty} \int_0^w dx_1 dx_2 \frac{D - (\phi_m + 1) - (\phi_m + 1)}{2} \frac{L_v - v_m - v_m}{w} + \tilde{W}(\phi_{R_{Bar}}, v_{R_{Bar}})$$

$$= L \frac{D}{2} \frac{(\phi_m + 1)^2}{w} + L \frac{L_v v_m^2}{2 w} - LwW(-1, 0) + \int_{-\infty}^{+\infty} \int_0^w dx_1 dx_2 W(\phi_{R_{Bar}}, v_{R_{Bar}}),$$

where

$$\int_{-\infty}^{+\infty} \int_0^w dx_1 dx_2 W(\phi_{R_{Bar}}, v_{R_{Bar}}) = \int_{-\infty}^{+\infty} \int_0^w dx_1 dx_2 \left\{ \frac{v_m^4 x_2^4}{4w^4} + \left[\frac{\lambda_{22}}{2} \left(\frac{\phi_m + 1}{w} x_2 - 1 \right)^2 + \lambda_{21} \left(\frac{\phi_m + 1}{w} x_2 - 1 \right) + \lambda_{20} \right] \frac{v_m^2 x_2^2}{2w^2} + \frac{\lambda_{04}}{4} \left(\frac{\phi_m + 1}{w} x_2 - 1 \right)^4 + \frac{\lambda_{03}}{3} \left(\frac{\phi_m + 1}{w} x_2 - 1 \right)^3 + \frac{\lambda_{02}}{2} \left(\frac{\phi_m + 1}{w} x_2 - 1 \right)^2 + \lambda_{01} \left(\frac{\phi_m + 1}{w} x_2 - 1 \right) \right\}$$

$$= \int_{-\infty}^{+\infty} \int_0^w dx_1 dx_2 \left\{ \frac{v_m^4 x_2^4}{4w^4} + \left[\frac{\lambda_{22}}{2} \left(\frac{(\phi_m + 1)^2}{w^2} x_2^4 - \frac{2(\phi_m + 1)}{w} x_2^3 + x_2^2 \right) + \lambda_{21} \left(\frac{\phi_m + 1}{w} x_2^3 - x_2^2 \right) + \lambda_{20} x_2^2 \right] \frac{v_m^2}{2w^2} + \frac{\lambda_{04}}{4} \left(\frac{\phi_m + 1}{w} x_2 - 1 \right)^4 + \frac{\lambda_{03}}{3} \left(\frac{\phi_m + 1}{w} x_2 - 1 \right)^3 + \frac{\lambda_{02}}{2} \left(\frac{\phi_m + 1}{w} x_2 - 1 \right)^2 + \lambda_{01} \left(\frac{\phi_m + 1}{w} x_2 - 1 \right) \right\}$$

$$= L \left\{ \frac{v_m^4 x_2^5}{20w^4} + \left[\frac{\lambda_{22}}{2} \left(\frac{(\phi_m + 1)^2}{5w^2} x_2^5 - \frac{(\phi_m + 1)x_2^4}{2w} + \frac{x_2^3}{3} \right) + \lambda_{21} \left(\frac{(\phi_m + 1)x_2^4}{4w} - \frac{x_2^3}{3} \right) + \lambda_{20} \frac{x_2^3}{3} \right] \frac{v_m^2}{2w^2} + \frac{\lambda_{04}}{20} \frac{w}{\phi_m + 1} \left(\frac{\phi_m + 1}{w} x_2 - 1 \right)^5 + \frac{\lambda_{03}}{12} \frac{w}{\phi_m + 1} \left(\frac{\phi_m + 1}{w} x_2 - 1 \right)^4 + \frac{\lambda_{02}}{6} \frac{w}{\phi_m + 1} \left(\frac{\phi_m + 1}{w} x_2 - 1 \right)^3 + \frac{\lambda_{01}}{2} \frac{w}{\phi_m + 1} \left(\frac{\phi_m + 1}{w} x_2 - 1 \right)^2 \right\}_0^w$$

$$= \frac{Lw}{2} \left[\frac{v_m^4}{10} + \frac{v_m^2}{2} \left(\lambda_{22} \left(\frac{\phi_m^2}{5} - \frac{\phi_m}{10} + \frac{1}{30} \right) + \lambda_{21} \left(\frac{\phi_m}{2} - \frac{1}{6} \right) + \frac{2\lambda_{20}}{3} \right) + \frac{\lambda_{04}}{10} (\phi_m^4 - \phi_m^3 + \phi_m^2 - \phi_m + 1) + \frac{\lambda_{03}}{6} (\phi_m - 1)(\phi_m^2 + 1) + \frac{\lambda_{02}}{3} (\phi_m^2 - \phi_m + 1) + \lambda_{01} (\phi_m - 1) \right]$$

$$= \frac{Lw}{2} C(\phi_m, v_m),$$

and the total contribution of R_{CB} and R_{CT} is then

$$\begin{aligned} E_{0,R_C} &= 2E_{R_{CB},0} \\ &= LwC(\phi_m, v_m) - 2LwW(-1, 0) + L\frac{D(\phi_m + 1)^2 + L_v v_m^2}{w}, \end{aligned}$$

Combining the local term contributions, the total local bar energy becomes

$$\begin{aligned} E_0(\phi_{R_{Bar}}, v_{R_{Bar}}) &= E_{0,R} + E_{0,\bar{R}} + E_{0,R_C} \\ &= Lw_0 (W(\phi_m, v_m) - W(-1, 0)) \\ &\quad + Lw (C(\phi_m, v_m) - W(\phi_m, v_m) - W(-1, 0)) \\ &\quad + L\frac{D(\phi_m + 1)^2 + L_v v_m^2}{w}, \end{aligned}$$

where we define the total local bar energy per unit length $e_0(w, w_0) = E_0/L$, which can be written as

$$\begin{aligned} e_0(w, w_0) &= w_0 \underbrace{(W(\phi_m, v_m) - W(-1, 0))}_{\nu(\phi_m, v_m)} \\ &\quad + w \underbrace{(C(\phi_m, v_m) - W(\phi_m, v_m) - W(-1, 0))}_{\mu(\phi_m, v_m)} \\ &\quad + \frac{D(\phi_m + 1)^2 + L_v v_m^2}{w}, \end{aligned}$$

where

$$\begin{aligned} W(-1, 0) &= \frac{\lambda_{04}}{4} - \frac{\lambda_{03}}{3} + \frac{\lambda_{02}}{2} - \lambda_{01} \\ &= -\frac{\lambda_{04}}{4} + \frac{2\lambda_{03}}{3} + \frac{\lambda_{22}}{8} + \frac{\lambda_{21}}{8}; \\ W(1, 1) &= \frac{1}{4} + \frac{\lambda_{22}}{4} + \frac{\lambda_{21}}{2} + \frac{\lambda_{20}}{2} + \frac{\lambda_{04}}{4} + \frac{\lambda_{03}}{3} + \frac{\lambda_{02}}{2} + \lambda_{01} \\ &= -\frac{1}{4} - \frac{\lambda_{04}}{4} - \frac{2\lambda_{03}}{3} - \frac{3\lambda_{22}}{8} - \frac{3\lambda_{21}}{8}; \\ \mu(\phi_m, v_m) &= -\frac{3v_m^4}{20} + \frac{v_m^2}{2} \left(\frac{\lambda_{22}}{10}(\phi_m + 1)(-3\phi_m + 2) + \frac{\lambda_{21}}{6}(-3\phi_m + 1) + \frac{1}{3} \right) \\ &\quad + \frac{\lambda_{04}}{60}(\phi_m + 1)^2(-9\phi_m^2 + 12\phi_m + 1) \\ &\quad + \frac{\lambda_{03}}{6}(\phi_m + 1)^2(-\phi_m + 1) \\ &\quad + \frac{1}{24}(\lambda_{22} + \lambda_{21})(\phi_m + 1)^2; \\ \nu(\phi_m, v_m) &= \frac{v_m^4}{4} + \frac{v_m^2}{2} \left(\frac{\lambda_{22}}{2}(\phi_m^2 - 1) + \lambda_{21}(\phi_m - 1) - 1 \right) \\ &\quad + \frac{\lambda_{04}}{4}(\phi_m^2 - 1)^2 + \frac{\lambda_{03}}{3}(\phi_m + 1)^2(\phi_m - 2) \\ &\quad - \frac{1}{8}(\lambda_{22} + \lambda_{21})(\phi_m + 1)^2; \end{aligned}$$

D.1.2 Contribution of the nonlocal term

The contribution of the nonlocal phase field term given by equation (3.2) appears only along the boundary occupied by the region R_C :

$$\begin{aligned}
 E_{\text{NL}}(\phi_{R_{Bar}}) &= -\frac{\beta}{2} \iint_{\Omega^2} d^2x d^2x' \frac{(\phi_m + 1)^2}{w^2} \hat{n}(x) \cdot \hat{n}(x') \Psi\left(\frac{|x - x'|}{d}\right) \\
 &= -\frac{\beta(\phi_m + 1)^2}{w^2} \left[\iint_{R_{CB} \times R_{CB}} d^2x d^2x' \Psi\left(\frac{|x - x'|}{d}\right) \right. \\
 &\quad \left. - \iint_{R_{CB} \times R_{CT}} d^2x d^2x' \Psi\left(\frac{|x - x'|}{d}\right) \right] \\
 &= -\frac{\beta(\phi_m + 1)^2}{w^2} \left[\int_{-\infty}^{+\infty} \int_{-\infty}^{+\infty} \int_0^w dx_1 dx'_1 dx_2 \right. \\
 &\quad \left. \left\{ \int_0^w dx'_2 \Psi\left(\frac{\sqrt{(x_1 - x'_1)^2 + (x_2 - x'_2)^2}}{d}\right) \right. \right. \\
 &\quad \left. \left. - \int_{w_0}^{w_0+w} dx'_2 \Psi\left(\frac{\sqrt{(x_1 - x'_1)^2 + (x_2 - x'_2)^2}}{d}\right) \right\} \right] \\
 &= -\frac{\beta(\phi_m + 1)^2}{w^2} \int_{-\infty}^{+\infty} \int_{-\infty}^{+\infty} \int_0^w \int_0^w dx_1 dx'_1 dx_2 dx'_2 \\
 &\quad \left\{ \Psi\left(\frac{\sqrt{(x_1 - x'_1)^2 + (x_2 - x'_2)^2}}{d}\right) \right. \\
 &\quad \left. - \Psi\left(\frac{\sqrt{(x_1 - x'_1)^2 + (w_0 + x'_2 - x_2)^2}}{d}\right) \right\},
 \end{aligned}$$

where (x_1, x_2) and (x'_1, x'_2) are the coordinates of x and x' respectively and \hat{n} is the normal unit vector. Making the change of variables $z = (x_1 - x'_1)/d$ and $t = (x'_2 - x_2)/d$, one has

$$E_{\text{NL}}(\phi_{R_{Bar}}) = -Ld\beta(\phi_m + 1)^2 G_{00}(\hat{w}_0, \hat{w}),$$

where $\hat{w} = w/d$, $\hat{w}_0 = w_0/d$, $G_{00}(\hat{w}_0, \hat{w}) = \frac{2}{\hat{w}^2} I_{00}(\hat{w}_0, \hat{w})$, $I_{00}(\hat{w}_0, \hat{w}) = \int_0^{+\infty} dz I(\hat{w}_0, \hat{w}, z)$ and

$$I(\hat{w}_0, \hat{w}, z) = \int_0^{\hat{w}} dx_2 \int_{-x_2}^{\hat{w}-x_2} dt \left\{ \Psi\left(\sqrt{z^2 + t^2}\right) - \Psi\left(\sqrt{z^2 + (\hat{w}_0 + t)^2}\right) \right\}.$$

We define the nonlocal energy per unit length as $e_{\text{NL}} = E_{\text{NL}}/L$.

D.1.3 Total bar energy

The total phase field energy per unit length of the bar is

$$\begin{aligned}
 e_{\text{P}}(\hat{w}_0, \hat{w}, \phi_m, v_m) &= e_0 + e_{\text{NL}} \\
 &= d\hat{w}_0\nu(\phi_m, v_m) + d\hat{w}\mu(\phi_m, v_m) + d\frac{\hat{D}(\phi_m + 1)^2 + \hat{L}_v v_m^2}{\hat{w}} \\
 &\quad - d\beta(\phi_m + 1)^2 G_{00}(\hat{w}_0, \hat{w}),
 \end{aligned}$$

where $\hat{w}_0 = w_0/d$, $\hat{D} = D/d^2$, $\hat{L}_v = L_v/d^2$. The interaction range d appears as a multiplicative term in the bar energy and does not change the energy minima. We put it equal to 1 for better readability.

D.2 Stability constraints

D.2.1 First order stability conditions

The first order stability conditions consist of putting the first partial derivatives of the bar energy equal to zero. The first partial derivatives are:

$$\begin{aligned} \frac{\partial e_P(\hat{w}_0, \hat{w}, \phi_m, v_m)}{\partial \hat{w}_0} &= \nu(\phi_m, v_m) - \beta(\phi_m + 1)^2 G_{10}(\hat{w}_0, \hat{w}), \\ \frac{\partial e_P(\hat{w}_0, \hat{w}, \phi_m, v_m)}{\partial \hat{w}} &= \mu(\phi_m, v_m) - \frac{\hat{D}(\phi_m + 1)^2 + \hat{L}_v v_m^2}{\hat{w}^2} - \beta(\phi_m + 1)^2 G_{11}(\hat{w}_0, \hat{w}), \\ \frac{\partial e_P(\hat{w}_0, \hat{w}, \phi_m, v_m)}{\partial \phi_m} &= \hat{w}_0 \nu_\phi(\phi_m, v_m) + \hat{w} \mu_\phi(\phi_m, v_m) - 2\beta(\phi_m + 1) G_{00}(\hat{w}_0, \hat{w}) \\ &\quad + 2 \frac{\hat{D}(\phi_m + 1)}{\hat{w}}, \\ \frac{\partial e_P(\hat{w}_0, \hat{w}, \phi_m, v_m)}{\partial v_m} &= \hat{w}_0 \nu_v(\phi_m, v_m) + \hat{w} \mu_v(\phi_m, v_m) + 2 \frac{\hat{L}_v v_m}{\hat{w}}, \end{aligned}$$

where

$$\begin{aligned} \mu_\phi(\phi_m, v_m) &= \frac{\partial \mu(\phi_m, v_m)}{\partial \phi_m} \\ &= \frac{v_m^2}{2} \left(\lambda_{22} \left(-\frac{3\phi_m}{5} - \frac{1}{10} \right) - \frac{\lambda_{21}}{2} \right) \\ &\quad + \frac{\lambda_{04}}{30} (-18\phi_m^3 - 9\phi_m^2 + 16\phi_m + 7) + \frac{\lambda_{03}}{6} (-3\phi_m^2 - 2\phi_m + 1) \\ &\quad + \frac{1}{12} (\lambda_{22} + \lambda_{21}) (\phi_m + 1); \\ \mu_v(\phi_m, v_m) &= \frac{\partial \mu(\phi_m, v_m)}{\partial v_m} \\ &= -\frac{3v_m^3}{5} + v_m \left(\lambda_{22} \left(-\frac{3\phi_m^2}{10} - \frac{\phi_m}{10} + \frac{1}{5} \right) + \lambda_{21} \left(-\frac{\phi_m}{2} + \frac{1}{6} \right) + \frac{1}{3} \right); \\ \nu_\phi(\phi_m, v_m) &= \frac{\partial \nu(\phi_m, v_m)}{\partial \phi_m} \\ &= \frac{v_m^2}{2} (\lambda_{22} \phi_m + \lambda_{21}) + \lambda_{04} (\phi_m^3 - \phi_m) + \lambda_{03} (\phi_m^2 - 1) \\ &\quad - \frac{1}{4} (\lambda_{22} + \lambda_{21}) (\phi_m + 1); \\ \nu_v(\phi_m, v_m) &= \frac{\partial \nu(\phi_m, v_m)}{\partial v_m} \\ &= v_m^3 + v_m \left(\frac{\lambda_{22}}{2} (\phi_m^2 - 1) + \lambda_{21} (\phi_m - 1) - 1 \right); \end{aligned}$$

$$G_{10}(\hat{w}_0, \hat{w}) = \frac{\partial G_{00}(\hat{w}_0, \hat{w})}{\partial \hat{w}_0} = -\frac{2}{\hat{w}^2} \int_0^{+\infty} \int_0^{\hat{w}} \int_0^{\hat{w}} dz dx_2 dx'_2 \left\{ \frac{\hat{w}_0 + x'_2 - x_2}{\sqrt{z^2 + (\hat{w}_0 + x'_2 - x_2)^2}} \Psi' \left(\sqrt{z^2 + (\hat{w}_0 + x'_2 - x_2)^2} \right) \right\};$$

$$G_{11}(\hat{w}_0, \hat{w}) = \frac{\partial G_{00}(\hat{w}_0, \hat{w})}{\partial \hat{w}} = -\frac{4}{\hat{w}^3} I_{00}(\hat{w}_0, \hat{w}) + \frac{2}{\hat{w}^2} \frac{\partial I_{00}(\hat{w}_0, \hat{w})}{\partial \hat{w}} = -\frac{2}{\hat{w}} G_{00}(\hat{w}_0, \hat{w}) + \frac{2}{\hat{w}^2} I_{11}(\hat{w}_0, \hat{w}),$$

where $I_{11} = \frac{\partial I_{00}}{\partial \hat{w}_0} = \int_0^{+\infty} dz \frac{\partial I(\hat{w}_0, \hat{w}, z)}{\partial \hat{w}_0}$ and

$$\begin{aligned} \frac{\partial I}{\partial \hat{w}} &= \frac{\partial}{\partial \hat{w}} \left\{ \int_0^{\hat{w}} \int_0^{\hat{w}} dx_2 dx'_2 \Psi \left(\sqrt{z^2 + (x'_2 - x_2)^2} \right) - \Psi \left(\sqrt{z^2 + (\hat{w}_0 + x'_2 - x_2)^2} \right) \right\} \\ &= \left[\int_0^{\hat{w}} dx'_2 \Psi \left(\sqrt{z^2 + (x'_2 - x_2)^2} \right) - \Psi \left(\sqrt{z^2 + (\hat{w}_0 + x'_2 - x_2)^2} \right) \right]_{x_2=\hat{w}} \\ &+ \int_0^{\hat{w}} dx_2 \frac{\partial}{\partial \hat{w}} \int_0^{\hat{w}} dx'_2 \Psi \left(\sqrt{z^2 + (x'_2 - x_2)^2} \right) - \Psi \left(\sqrt{z^2 + (\hat{w}_0 + x'_2 - x_2)^2} \right) \\ &= \int_0^{\hat{w}} dx'_2 \Psi \left(\sqrt{z^2 + (x'_2 - \hat{w})^2} \right) - \Psi \left(\sqrt{z^2 + (\hat{w}_0 + x'_2 - \hat{w})^2} \right) \\ &+ \int_0^{\hat{w}} dx_2 \Psi \left(\sqrt{z^2 + (\hat{w} - x_2)^2} \right) - \Psi \left(\sqrt{z^2 + (\hat{w}_0 + \hat{w} - x_2)^2} \right) \\ &= 2 \int_0^{\hat{w}} dx_2 \Psi \left(\sqrt{z^2 + (x_2 - \hat{w})^2} \right) \\ &- \int_0^{\hat{w}} dx_2 \Psi \left(\sqrt{z^2 + (\hat{w}_0 + x_2 - \hat{w})^2} \right) - \int_0^{\hat{w}} dx_2 \Psi \left(\sqrt{z^2 + (\hat{w}_0 + \hat{w} - x_2)^2} \right) \\ &= 2 \int_0^{\hat{w}} dt \Psi \left(\sqrt{z^2 + t^2} \right) - \int_{\hat{w}_0 - \hat{w}}^{\hat{w}_0 + \hat{w}} dt \Psi \left(\sqrt{z^2 + t^2} \right). \end{aligned}$$

Putting the first partial derivatives of the bar energy equal to zero, and after some mathematical manipulations, one finds the 4 parameter constraints:

$$\begin{aligned} &\hat{w} \left[\mu(\phi_m, v_m) + \frac{\phi_m + 1}{2} \mu_\phi(\phi_m, v_m) + \frac{v_m}{2} \mu_v(\phi_m, v_m) \right] \\ &+ \hat{w}_0 \left[\frac{\phi_m + 1}{2} \nu_\phi(\phi_m, v_m) + \frac{v_m}{2} \nu_v(\phi_m, v_m) \right] \\ &- \frac{\nu(\phi_m, v_m)}{G_{10}(\hat{w}_0, \hat{w})} [G_{00}(\hat{w}_0, \hat{w}) + \hat{w} G_{10}(\hat{w}_0, \hat{w})] = 0; \end{aligned} \quad (\text{D.5})$$

$$\beta = \frac{\nu(\phi_m, v_m)}{(\phi_m + 1)^2 G_{10}(\hat{w}_0, \hat{w})}; \quad (\text{D.6})$$

$$\hat{D} = \frac{\hat{w}}{\phi_m + 1} \left[\frac{\nu(\phi_m, v_m) G_{00}(\hat{w}_0, \hat{w})}{(\phi_m + 1) G_{10}(\hat{w}_0, \hat{w})} - \hat{w}_0 \nu_\phi(\phi_m, v_m) - \hat{w} \mu_\phi(\phi_m, v_m) \right]; \quad (\text{D.7})$$

$$\hat{L}_v = -\frac{\hat{w}}{2v_m} [\hat{w}_0 \nu_v(\phi_m, v_m) + \hat{w} \mu_v(\phi_m, v_m)]; \quad (\text{D.8})$$

D.2.2 Second order stability conditions

The second order stability condition says that the Hessian matrix H_{Bar} , evaluated at the desired physical parameters $(\hat{w}_0, \hat{w}, \phi_m, v_m) = (\hat{w}_0, \hat{w}, 1, 1)$, must be positive definite. H_{Bar} is given by

$$H_{\text{Bar}} = \begin{pmatrix} \frac{\partial^2 e_{\text{P}}}{\partial \hat{w}_0^2} & \frac{\partial^2 e_{\text{P}}}{\partial w \partial \hat{w}_0} & \frac{\partial^2 e_{\text{P}}}{\partial \phi_m \partial \hat{w}_0} & \frac{\partial^2 e_{\text{P}}}{\partial v_m \partial \hat{w}_0} \\ \frac{\partial^2 e_{\text{P}}}{\partial w \partial \hat{w}_0} & \frac{\partial^2 e_{\text{P}}}{\partial w^2} & \frac{\partial^2 e_{\text{P}}}{\partial \phi_m \partial w} & \frac{\partial^2 e_{\text{P}}}{\partial v_m \partial w} \\ \frac{\partial^2 e_{\text{P}}}{\partial \phi_m \partial \hat{w}_0} & \frac{\partial^2 e_{\text{P}}}{\partial \phi_m \partial w} & \frac{\partial^2 e_{\text{P}}}{\partial \phi_m^2} & \frac{\partial^2 e_{\text{P}}}{\partial v_m \partial \phi_m} \\ \frac{\partial^2 e_{\text{P}}}{\partial v_m \partial \hat{w}_0} & \frac{\partial^2 e_{\text{P}}}{\partial v_m \partial w} & \frac{\partial^2 e_{\text{P}}}{\partial v_m \partial \phi_m} & \frac{\partial^2 e_{\text{P}}}{\partial v_m^2} \end{pmatrix}.$$

The second order variations of the bar energy are

$$\begin{aligned} \frac{\partial^2 e_{\text{P}}(\hat{w}_0, \hat{w}, \phi_m, v_m)}{\partial \hat{w}_0^2} &= \beta(\phi_m + 1)^2 G_{20}(\hat{w}_0, \hat{w}), \\ \frac{\partial^2 e_{\text{P}}(\hat{w}_0, \hat{w}, \phi_m, v_m)}{\partial \hat{w} \partial \hat{w}_0} &= \beta(\phi_m + 1)^2 G_{21}(\hat{w}_0, \hat{w}), \\ \frac{\partial^2 e_{\text{P}}(\hat{w}_0, \hat{w}, \phi_m, v_m)}{\partial \phi_m \partial \hat{w}_0} &= \nu_\phi(\phi_m, v_m) - 2\beta(\phi_m + 1)G_{10}(\hat{w}_0, \hat{w}), \\ \frac{\partial^2 e_{\text{P}}(\hat{w}_0, \hat{w}, \phi_m, v_m)}{\partial v_m \partial \hat{w}_0} &= \nu_v(\phi_m, v_m), \\ \frac{\partial^2 e_{\text{P}}(\hat{w}_0, \hat{w}, \phi_m, v_m)}{\partial \hat{w}^2} &= 2\frac{\hat{D}(\phi_m + 1)^2 + \hat{L}_v v_m^2}{\hat{w}^3} - \beta(\phi_m + 1)^2 G_{22}(\hat{w}_0, \hat{w}), \\ \frac{\partial^2 e_{\text{P}}(\hat{w}_0, \hat{w}, \phi_m, v_m)}{\partial \phi_m \partial \hat{w}} &= \mu_\phi(\phi_m, v_m) - 2\hat{D}\frac{\phi_m + 1}{\hat{w}^2} - 2\beta(\phi_m + 1)G_{11}(\hat{w}_0, \hat{w}), \\ \frac{\partial^2 e_{\text{P}}(\hat{w}_0, \hat{w}, \phi_m, v_m)}{\partial v_m \partial \hat{w}} &= \mu_v(\phi_m, v_m) - 2\hat{L}_v \frac{v_m}{\hat{w}^2}, \\ \frac{\partial^2 e_{\text{P}}(\hat{w}_0, \hat{w}, \phi_m, v_m)}{\partial \phi_m^2} &= \hat{w}_0 \nu_{\phi\phi}(\phi_m, v_m) - 2\beta G_{00}(\hat{w}_0, \hat{w}) + \hat{w} \mu_{\phi\phi}(\phi_m, v_m) + 2\frac{\hat{D}}{\hat{w}}, \\ \frac{\partial^2 e_{\text{P}}(\hat{w}_0, \hat{w}, \phi_m, v_m)}{\partial v_m \partial \phi_m} &= \hat{w}_0 \nu_{v\phi}(\phi_m, v_m) + \hat{w} \mu_{v\phi}(\phi_m, v_m), \\ \frac{\partial^2 e_{\text{P}}(\hat{w}_0, \hat{w}, \phi_m, v_m)}{\partial v_m^2} &= \hat{w}_0 \nu_{vv}(\phi_m, v_m) + \hat{w} \mu_{vv}(\phi_m, v_m) + 2\frac{\hat{L}_v}{\hat{w}}, \end{aligned}$$

where

$$\begin{aligned} \mu_{\phi\phi}(\phi_m, v_m) &= \frac{\partial^2 \mu(\phi_m, v_m)}{\partial \phi_m^2} \\ &= -\frac{3}{10} \lambda_{22} v_m^2 + \frac{\lambda_{04}}{15} (-27\phi_m^2 - 9\phi_m + 8) - \frac{\lambda_{03}}{3} (3\phi_m + 1) \\ &\quad + \frac{1}{12} (\lambda_{22} + \lambda_{21}); \\ \mu_{vv}(\phi_m, v_m) &= \frac{\partial^2 \mu(\phi_m, v_m)}{\partial v_m^2} \\ &= -\frac{9v_m^2}{5} + \lambda_{22} \left(-\frac{3\phi_m^2}{10} - \frac{\phi_m}{10} + \frac{1}{5}\right) + \lambda_{21} \left(-\frac{\phi_m}{2} + \frac{1}{6}\right) + \frac{1}{3}; \end{aligned}$$

$$\begin{aligned}
 \mu_{v\phi}(\phi_m, v_m) &= \frac{\partial^2 \mu(\phi_m, v_m)}{\partial v_m \partial \phi_m} \\
 &= v_m \left(\lambda_{22} \left(-\frac{3\phi_m}{5} - \frac{1}{10} \right) - \frac{\lambda_{21}}{2} \right) ; \\
 \nu_{\phi\phi}(\phi_m, v_m) &= \frac{\partial^2 \nu(\phi_m, v_m)}{\partial \phi_m^2} \\
 &= \lambda_{22} \frac{v_m^2}{2} + \lambda_{04} (3\phi_m^2 - 1) + 2\lambda_{03} \phi_m - \frac{1}{4} (\lambda_{22} + \lambda_{21}) ; \\
 \nu_{vv}(\phi_m, v_m) &= \frac{\partial^2 \nu(\phi_m, v_m)}{\partial v_m^2} \\
 &= 3v_m^2 + \frac{\lambda_{22}}{2} (\phi_m^2 - 1) + \lambda_{21} (\phi_m - 1) - 1 ; \\
 \nu_{v\phi}(\phi_m, v_m) &= \frac{\partial^2 \nu(\phi_m, v_m)}{\partial v_m \partial \phi_m} \\
 &= v_m (\lambda_{22} \phi_m + \lambda_{21}) ; \\
 G_{20}(\hat{w}_0, \hat{w}) &= -\frac{\partial G_{10}(\hat{w}_0, \hat{w})}{\partial \hat{w}_0} \\
 &= \frac{2}{\hat{w}^2} \int_0^{+\infty} \int_0^{\hat{w}} \int_0^{\hat{w}} dz dx_2 dx'_2 \\
 &\quad \left\{ \frac{z_2}{(z^2 + (\hat{w}_0 + x'_2 - x_2)^2)^{3/2}} \Psi' \left(\sqrt{z^2 + (\hat{w}_0 + x'_2 - x_2)^2} \right) \right. \\
 &\quad \left. \frac{(\hat{w}_0 + x'_2 - x_2)^2}{z^2 + (\hat{w}_0 + x'_2 - x_2)^2} \Psi'' \left(\sqrt{z^2 + (\hat{w}_0 + x'_2 - x_2)^2} \right) \right\} \\
 &= \frac{2}{\hat{w}^2} \int_0^{+\infty} dz \int_0^{\hat{w}} dx_2 \int_{\hat{w}_0 - x_2}^{\hat{w} + \hat{w}_0 - x_2} dt \\
 &\quad \left\{ \frac{z^2}{(z^2 + t^2)^{3/2}} \Psi' \left(\sqrt{z^2 + t^2} \right) + \frac{t^2}{z^2 + t^2} \Psi'' \left(\sqrt{z^2 + t^2} \right) \right\} ; \\
 G_{21}(\hat{w}_0, \hat{w}) &= -\frac{\partial G_{10}(\hat{w}_0, \hat{w})}{\partial \hat{w}} \\
 &= \frac{2}{\hat{w}} G_{10} + \frac{2}{\hat{w}^2} I_{21} ; \\
 I_{21} &= \int_0^{+\infty} \int_{-\hat{w}}^{\hat{w}} dz dt \frac{\hat{w}_0 + t}{\sqrt{z^2 + (\hat{w}_0 + t)^2}} \Psi' \left(\sqrt{z^2 + (\hat{w}_0 + t)^2} \right) \\
 &= \int_0^{+\infty} \int_{\hat{w}_0 - \hat{w}}^{\hat{w}_0 + \hat{w}} dt dz \frac{t}{\sqrt{z^2 + t^2}} \Psi' \left(\sqrt{z^2 + t^2} \right) ; \\
 G_{22}(\hat{w}_0, \hat{w}) &= \frac{\partial G_{11}(\hat{w}_0, \hat{w})}{\partial \hat{w}} \\
 &= \frac{6}{\hat{w}^2} G_{00} - \frac{8}{\hat{w}^3} I_{11} + \frac{2}{\hat{w}^2} I_{22} ; \\
 I_{22} &= \int_0^{+\infty} dz \left\{ 2\Psi \left(\sqrt{z^2 + \hat{w}^2} \right) \right. \\
 &\quad \left. - \Psi \left(\sqrt{z^2 + (\hat{w}_0 + \hat{w})^2} \right) - \Psi \left(\sqrt{z^2 + (\hat{w}_0 - \hat{w})^2} \right) \right\} .
 \end{aligned}$$

D.2.3 Derivatives of the function K_0

To compute the derivatives of the modified Bessel function of the second kind of order ν denoted $K_\nu(z)$, we use these formulae:

$$\begin{aligned}\frac{\partial K_0(z)}{\partial z} &= -K_1(z) , \\ \frac{\partial K_\nu(z)}{\partial z} &= -\frac{1}{2} (K_{\nu-1}(z) + K_{\nu+1}(z)) .\end{aligned}$$

We denote on $'$ the derivative with respect to z . Using the above formulae, one can compute the first three derivatives of $K_0(z)$:

$$\begin{aligned}K_0'(z) &= -K_1(z) , \\ K_0''(z) &= \frac{1}{2} (K_0(z) + K_2(z)) , \\ K_0'''(z) &= -\frac{1}{4} (K_1(z) + K_3(z)) .\end{aligned}$$

Publications and scientific activities of the author

Journal papers

1. A. El Ghou, I. H. Jermyn and J. Zerubia. On directed network modelling. *IEEE Transaction on PAMI*. Under review.

Conference papers

2010

1. A. El Ghou, I. H. Jermyn and J. Zerubia. A theoretical and numerical study of a phase field higher-order active contour model of directed networks. *ACCV, Asian Conference on Computer Vision*. Queenstown, New Zealand, November 2010.
2. A. El Ghou, I. H. Jermyn and J. Zerubia. Segmentation of networks from VHR remote sensing images using a directed phase field HOAC model. *ISPRS Technical Commission III Symposium on Photogrammetry Computer Vision and Image Analysis*. Paris, September 2010.

2009

1. A. El Ghou, I. H. Jermyn and J. Zerubia. A phase field higher-order active contour model of directed networks. In *2nd IEEE Workshop on Non-Rigid Shape Analysis and Deformable Image Alignment, at ICCV*. Kyoto, Japan, September 2009.
2. A. El Ghou, I. H. Jermyn and J. Zerubia. Inflection point model under phase field higher-order active contours for network extraction from VHR satellite images. *EU-SIPCO, European Signal Processing Conference*. Glasgow, Scotland, August 2009.

2008

1. A. El Ghou, I. H. Jermyn and J. Zerubia. Phase diagram of a long bar under a higher-order active contour energy: application to hydrographic network extraction from VHR satellite images. *ICPR, International Conference on Pattern Recognition*. Tampa, Florida, USA, December 2008.
2. A. El Ghou, I. H. Jermyn and J. Zerubia. Diagramme de phase d'une énergie de type contour actif d'ordre supérieur : le cas d'une barre longue. *RFIA, Reconnaissance des Formes et Intelligence Artificielle*. Amiens, France, January 2008.

Talks

2010

1. Phase fields for network extraction from images. 24 August 2010, Tunis (Tunisia). Invited by Professor Amel Benazza at URISA (Sup'Com).
2. Phase fields for network extraction from images. 19 May 2010, Sophia Antipolis (France). SHAPE Working Group meeting at INRIA Sophia Antipolis.
3. A phase field higher-order active contour model of directed networks. 22 April 2010, Sophia Antipolis (France). ADSTIC Seminar at I3S.

2009

1. Shape modelling via phase field higher-order active contours. 29 May 2009, INRIA Rocquencourt Paris. ERCIM MUSCLE WG Meeting.
2. Shape modelling via Higher-Order Active Contours and Phase Fields: Application to hydrographic network extraction. 6 April 2009, Tunis (Tunisia). Invited by Professor Amel Benazza at URISA (SupCom).
3. Shape modelling via Higher-Order Active Contours and Phase Fields. 9 January 2009, Tunis (Tunisia). Invited by Doctor Ali Saada at LAMSIN (ENIT).

2008

1. Shape modelling via Phase Field Higher-Order Active Contours: Stability analysis for hydrographic network extraction. 15-19 December 2008, Tallahassee (Florida, USA). Invited by Professor Anuj Srivastava at FSU.
2. Shape modelling via Phase Field Higher-Order Active Contours: Stability analysis for hydrographic network extraction. 3-5 December 2008, Orlando (Florida, USA). Invited by Associate Professor Hassan Foroosh at UCF.
3. Shape modelling via Phase Field Higher-Order Active Contours: Stability analysis for hydrographic network extraction. 15-17 October 2008, Toulouse. 8th DLR-CNES Workshop on Information Extraction and Scene Understanding for Meter Resolution Images.
4. Phase diagram of a higher-order active contour energy. 11 March 2008, Sophia Antipolis (France). ADSTIC Seminar at I3S.
5. Phase Field Higher-Order Active Contours For Object Extraction from Remote Sensing Images. 4-6 March 2008, ESRI, Frascati (Rome). ESA-EUSC 2008: Image Information Mining: pursuing automation of geospatial intelligence for environment and security.
6. Tree detection and road network extraction using higher order active contours. 10-11 January 2008, CNES Paris. ORFEO Methodology Meeting.

2007

1. Phase diagram of a higher-order active contour energy. 23-30 July 2007, Beijing (China). Invited by Associate Professor Veronique Prinet, scientific director of RSIU team at LIAMA (Chinese Academy of Sciences).

Bibliography

- D. Adalsteinsson and J. A. Sethian. The fast construction of extension velocities in level set methods. *Journal of Computational Physics*, 148(1):2–22, 1999.
- L. Alvarez, F. Guichard, P.L. Lions, and J.M. Morel. Axioms and fundamental equations in image processing. *Archive for Rational Mechanics and Analysis*, 123:199–257, 1993.
- K. Appel and W. Haken. *Every planar map is four colorable*. Contemporary Math, 98, 1996.
- G. Aubert, J. F. Aujol, and L. Blanc-Féraud. Detecting codimension–two objects in an image with ginzburg-landau models. *International Journal of Computer Vision*, 65(1-2): 29–42, 2005.
- C. Bauer, H. Bischof, and Reinhard Beichel. Segmentation of airways based on gradient vector flow. In *International Workshop on Pulmonary Image Analysis, Medical Image Computing and Computer Assisted Intervention*, San Francisco, California, September 2009.
- I. Ben Ayed, A. Mitiche, and Z. Belhadj. Polarimetric image segmentation via maximum-likelihood approximation and efficient multiphases level-sets. *IEEE Transactions on Pattern Analysis and Machine Intelligence*, 28(9):1493–1500, September 2006.
- M. Beneš, V. Chalupecký, and K. Mikula. Geometrical image segmentation by the allencahn equation. *Appl. Numer. Math.*, 51(2-3):187–205, 2004.
- J. Besag. On the statistical analysis of dirty pictures. *Journal of the Royal Statistical Society*, 43(3):259–302, 1986.
- T. Blaskovics, Z. Kato, and I. H. Jermyn. Detection of circular shapes using Markov random field. In *Proceedings of the IEEE International Conference on Image Processing*, Cairo, Egypt, November 2009.
- T. Brox and D. Cremers. On local region models and a statistical interpretation of the piecewise smooth mumford-shah functional. *International Journal of Computer Vision*, 84(2):184–193, 2009.
- V. Caselles, F. Catte, T. Coll, and F. Dibos. A geometric model for active contours in image processing. *Numerische Mathematik*, 66(1):1–31, 1993.
- V. Caselles, R. Kimmel, and G. Sapiro. Geodesic active contours. *International Journal of Computer Vision*, 22(1):61–79, 1997.
- T. F. Chan and L. A. Vese. Active contours without edges. *IEEE Transactions on Image Processing*, 10(2):266–277, 2001a.
- T. F. Chan and L. A. Vese. A level set algorithm for minimizing the mumford-shah functional in image processing. In *VLSM '01: Proceedings of the IEEE Workshop on Variational and Level Set Methods (VLSM'01)*, July 2001b.

- L. Chen. Phase-field models for microstructure evolution. *Annual Review of Materials Research*, 50:113–140, 2002.
- Y. Chen, S. Thiruvenkadam, H.D. Tagare, F. Huang, D. Wilson, and E.A. Geiser. On the incorporation of shape priors into geometric active contours. In *Proceedings of the IEEE Workshop on Variational, Geometric and Level Set Methods in Computer Vision*, Vancouver, Canada, July 2001.
- Y. M. Chen, H. D. Tagare, S. R. Thiruvenkadam, F. Huang, D. Wilson, K. S. Gopinath, R. W. Briggs, and E. A. Geiser. Using prior shapes in geometric active contours in a variational framework. *International Journal of Computer Vision*, 50(3):315–328, 12 2002.
- J. Cheng and S. W. Foo. Dynamic directional gradient vector flow for snakes. *IEEE Transactions on Image Processing*, 15(6):1563–1571, 2006.
- M. Cieplak, A. Giacometti, A. Maritan, A. Rinaldo, I. Rodríguez-Iturbe, and J.R. Banavar. Models of fractal river basins. *Journal of Statistical Physics*, 91, 1998.
- I. Cohen and L. D. Cohen. A hybrid hyperquadric model for 2-D and 3-D data fitting. *Computer Vision and Image Understanding*, 63(3):527–541, May 1996.
- L. D. Cohen. On active contours and balloons. *CVGIP: Image Understanding*, 53:211–218, 1991.
- L. D. Cohen and I. Cohen. Finite-element methods for active contour models and balloons for 2-D and 3-D images. *IEEE Transactions on Pattern Analysis and Machine Intelligence*, 15(11):1131–1147, 1993.
- T. F. Cootes and C. J. Taylor. Active shape models - smart snakes. In *British Machine Vision Conference*, pages 266–275, 1992.
- E. Coppola, B. Tomassetti, L. Mariotti, M. Verdecchia, and G. Visconti. Cellular automata algorithms for drainage network extraction and rainfall data assimilation. *Hydrological sciences-journal-des sciences hydrologiques*, 52(3):579–592, June 2007.
- D. Cremers. Dynamical statistical shape priors for level set based tracking. *IEEE Transactions on Pattern Analysis and Machine Intelligence*, 28(8):1262 – 1273, 2006.
- D. Cremers. Nonlinear dynamical shape priors for level set segmentation. In *Proceedings of the IEEE International Conference on Computer Vision and Pattern Recognition*, 2007.
- D. Cremers. Nonlinear dynamical shape priors for level set segmentation. *SIAM Journal on Scientific Computing*, 35(2-3):132–143, 2008.
- D. Cremers and S. Soatto. A pseudo-distance for shape priors in level set segmentation. In *Proceedings of the IEEE Workshop on Variational, Geometric and Level Set Methods in Computer Vision*, Nice, France, October 2003.

- D. Cremers, C. Schnörr, and J. Weickert. Diffusion-snakes: combining statistical shape knowledge and image information in a variational framework. In *Proceedings of the IEEE Workshop on Variational, Geometric and Level Set Methods in Computer Vision*, Vancouver, Canada, July 2001.
- D. Cremers, F. Tischhauser, J. Weickert, and C. Schnörr. Diffusion snakes: Introducing statistical shape knowledge into the mumford-shah functional. *International Journal of Computer Vision*, 50(3):295–313, 12 2002.
- D. Cremers, T. Kohlberger, and C. Schnörr. Shape statistics in kernel space for variational image segmentation. *Pattern Recognition*, 36:1929–1943, 2003.
- D. Cremers, S. J. Osher, and S. Soatto. Kernel density estimation and intrinsic alignment for shape priors in level set segmentation. *International Journal of Computer Vision*, 69(3):335–351, 09 2006.
- D. Cremers, M. Rousson, and R. Deriche. A review of statistical approaches to level set segmentation: Integrating color, texture, motion and shape. *International Journal of Computer Vision*, 72(2):195–215, 2007.
- A. P. Dempster, N. M. Laird, and D. B. Rubin. Maximum likelihood from incomplete data via the EM algorithm. *Journal of the Royal Statistical Society. Series B (Methodological)*, 39(1):1–38, 1977. doi: <http://dx.doi.org/10.2307/2984875>.
- C. R. Dillabaugh, K. O. Niemann, and D. Richardson. Semi-automated extraction of rivers from digital imagery. *GeoInformatica*, 6(3):263–284, 2002.
- P. S. Dodds and D. H. Rothman. Geometry of river networks. i. scaling, fluctuations, and deviations. *Physical Review E*, 63(1), December 2000a.
- P. S. Dodds and D. H. Rothman. Geometry of river networks. ii. distributions of component size and number. *Physical Review E*, 63(1), December 2000b.
- P. S. Dodds and D. H. Rothman. Geometry of river networks. iii. characterization of component connectivity. *Physical Review E*, 63(1), December 2000c.
- M. A. Fischler, J. M. Tenenbaum, and H. C. Wolf. Detection of roads and linear structures in low-resolution aerial imagery using a multisource knowledge integration technique. *Computer Graphics and Image Processing*, 15:201–223, 1981.
- M. F. A. Fortier, D. Ziou, C. Armenakis, and S. Wang. Survey of work on road extraction in aerial and satellite images. Technical report, Université de Sherbrooke, Quebec, Canada, 1999.
- A. Foulonneau, P. Charbonnier, and F. Heitz. Geometric shape priors for region-based active contours. In *Proceedings of the IEEE International Conference on Image Processing*, Barcelone, Espagne, September 2003.
- M. Gstaad, M. Barlaud, and G. Aubert. Combining shape prior and statistical features for active contour segmentation. *IEEE TCSVT special session on Audio and Video Analysis for Interactive Multimedia Services*, 14(5):726–734, May 2004.

- S. Geman and D. Geman. Stochastic relaxation, gibbs distributions, and the bayesian restoration of images. *IEEE Transactions on Pattern Analysis and Machine Intelligence*, 6(6):721–741, 11 1984. 2, 9, 26
- R. Gonzalez-Cinca, R. Folch, R. Benitez, L. Ramirez-Piscina, J. Casademunt, and A. Hernandez-Machado. Phase-field models in interfacial pattern formation out of equilibrium. *ArXiv Condensed Matter e-prints*, 2003.
- M. A. Grayson. Shortening embedded curves. *Annals of Mathematics*, 129:71–111, 1989.
- U. Grenander, Y. Chow, and D. M. Keenan. *Hands: a pattern theoretic study of biological shapes*. Springer-Verlag New York, Inc., 1991. 2, 8, 27
- H. Grossauer and O. Scherzer. Using the complex Ginzburg-Landau equation for digital inpainting in 2D and 3D. In *Proceedings of Scale-Space*, pages 225–236. LNCS 2695, Springer-Verlag, 2003.
- R.E. Horton. Drainage basin characteristics. In *Trans. Am. Geophys. Union*, volume 13, pages 350–361, 1932.
- R.E. Horton. Erosional development of streams and their drainage basins: hydrophysical approach to quantitative morphology. In *Geol. Soc. Am. Bull.*, volume 56, pages 275–370, 1945.
- P. Horvath. A multispectral data model for higher-order active contours and its application to tree crown extraction. In *Advanced Concepts for Intelligent Vision Systems*, Delft, Pays-Bas, August 2007.
- P. Horvath, I.H. Jermyn, Z. Kato, and J. Zerubia. A higher-order active contour model of a ‘gas of circles’ and its application to tree crown extraction. Research Report 6026, INRIA, France, November 2006a.
- P. Horvath, I.H. Jermyn, Z. Kato, and J. Zerubia. A higher-order active contour model for tree detection. In *International Conference on Pattern Recognition*, Hong Kong, August 2006b.
- P. Horvath, I. H. Jermyn, Z. Kato, and J. Zerubia. A higher-order active contour model of a ‘gas of circles’ and its application to tree crown extraction. *Pattern Recognition*, 42(5): 699–709, 2009.
- S. Ingrassia and R. Rocci. Constrained monotone em algorithms for finite mixture of multivariate gaussians. *Comput. Stat. Data Anal.*, 51(11):5339–5351, 2007.
- E. Ising. Beitrag zur theorie des ferromagnetismus. *Zeitschrift für Physik*, 31:253–258, 1925. 3, 9, 25, 26
- S. Jehan-Besson, M. Barlaud, and G. Aubert. DREAM²S: Deformable regions driven by an Eulerian accurate minimization method for image and video segmentation. *International Journal of Computer Vision*, 53(1):45–70, 2003.

- I. H. Jermyn. *On the Use of Functionals on Boundaries in Hierarchical Models of Object Recognition*. PhD thesis, New York University, Department of Computer Science, 2000.
- M. Kass, A. Witkin, and D. Terzopoulos. Snakes: Active contour models. *International Journal of Computer Vision*, 1(4):321–331, 1988. 2, 3, 9, 18, 34
- S. Kichenassamy, A. Kumar, P. Olver, A. Tannenbaum, and A. Yezzi. Gradient flows and geometric active contour models. In *Proceedings of the IEEE International Conference on Computer Vision*, Boston, USA, June 1995.
- S. Kichenassamy, A. Kumar, P. Olver, A. Tannenbaum, and A. Yezzi. Conformal curvature flows: From phase transitions to active vision. *Archive for Rational Mechanics and Analysis*, 134(3):275–301, 1996.
- E. Klassen, A. Srivastava, W. Mio, and S. Joshi. Analysis of planar shapes using geodesic paths on shape spaces. *IEEE Transactions on Pattern Analysis and Machine Intelligence*, 26(3):372–383, 2004.
- M. S. Kulikova, I. H. Jermyn, X. Descombes, E. Zhizhina, and J. Zerubia. A marked point process model with strong prior shape information for extraction of multiple, arbitrarily-shaped objects. *International Journal of Computer Vision and Image Processing*, 2010. To appear.
- C. Lacoste, X. Descombes, J. Zerubia, and N. Baghdadi. Unsupervised line network extraction from remotely sensed images by polyline process. In *Proc. European Signal Processing Conference (EUSIPCO)*, University of Technology, Vienna, Austria, September 2004.
- C. Lacoste, X. Descombes, J. Zerubia, and N. Baghdadi. Extraction of hydrographic networks from satellite images using a hierarchical model within a stochastic geometry framework. In *Proc. European Signal Processing Conference (EUSIPCO)*, Antalya, Turkey, September 2005.
- C. Lacoste, X. Descombes, and J. Zerubia. Unsupervised line network extraction in remote sensing using a polyline process. *Pattern Recognition*, 43(4):1631 – 1641, 2010.
- I. Laptev, H. Mayer, T. Lindeberg, W. Eckstein, C. Steger, and A. Baumgartner. Automatic extraction of roads from aerial images based on scale space and snakes. *Mach. Vision Appl.*, 12(1):23–31, 2000.
- Y. G. Leclerc. Constructing simple stable descriptions for image partitioning. *International Journal of Computer Vision*, 3(1):73–102, 1989.
- W. Lenz. Beitrag zum verstandnis der magnetischen erscheinungen in festen krpern. *Physikalische Zeitschrift*, 21:613–615, 1920.
- M. E. Leventon, W. E. L. Grimson, and O. Faugeras. Statistical shape influence in geodesic active contours. In *Proceedings of the IEEE International Conference on Computer Vision and Pattern Recognition*, Hilton Head Island, USA, June 2000.

- B. Li and S. T. Acton. Automatic active model initialization via poisson inverse gradient. *IEEE Transactions on Image Processing*, 17(8):1406–1420, 2008.
- B. Lohani, D. C. Mason, T. R. Scott, and B. Sreenivas. Identification of tidal channel networks from aerial photographs alone and fused with airborne laser altimetry. *International Journal of Remote Sensing*, 27(1):5–25, 2006.
- R. Malladi, J. A. Sethian, and B. C. Vemuri. Shape modeling with front propagation: A level set approach. *IEEE Transactions on Pattern Analysis and Machine Intelligence*, 17(2):158–175, 1995.
- R. Mantilla and V. K. Gupta. A GIS numerical framework to study the process basis of scaling statistics in river networks. *IEEE Transactions on Geoscience and Remote Sensing Letters*, 2(4):404–408, October 2005.
- D. C. Mason, T. R. Scott, and H. J. Wang. Extraction of tidal channel networks from airborne scanning laser altimetry. *ISPRS Journal of Photogrammetry and Remote Sensing*, 61(2):67–83, 2006.
- H. Mayer, I. Laptev, and A. Baumgartner. Multi-scale and snakes for automatic road extraction. In *Proceedings of the European Conference on Computer Vision*, pages 720–733, June 1998.
- S.K. McFeeters. The use of the normalized difference water index (NDWI) in the delineation of open water features. *International Journal of Remote Sensing*, 17:1425–1432, 1996.
- T. McInerney and D. Terzopoulos. Topologically adaptable snakes. In *Proceedings of the IEEE International Conference on Computer Vision*, Beijing, China, 1995.
- T. McInerney and D. Terzopoulos. T-snakes: Topology adaptive snakes. *Medical Image Analysis*, 4(2):73–91, 2000.
- J. B. Mena. State of the art on automatic road extraction for GIS update: a novel classification. *Pattern Recogn. Lett.*, 24(16):3037–3058, 2003.
- T. K. Moon. The expectation-maximization algorithm. *Signal Processing Magazine, IEEE*, 13(6):47–60, Nov 1996.
- D. Mumford and J. Shah. Boundary detection by minimizing functionals. In *Proceedings of the IEEE International Conference on Computer Vision and Pattern Recognition*, June 1985.
- D. Mumford and J. Shah. Optimal approximation by piecewise smooth functions and associated variational problems. *Communications on Pure and Applied Mathematics*, 42(5):577–685, 1989.
- J. F. O’Callaghan and D. M. Mark. The extraction of drainage networks from digital elevation data. *Computer Vision, Graphics, and Image Processing*, 28(3):323–344, 1984.

- M. Ortner, X. Descombes, and J. Zerubia. Building outline extraction from digital elevation models using marked point processes. *International Journal of Computer Vision*, 72(2): 107–132, April 2007.
- S. Osher and J. A. Sethian. Fronts propagating with curvature dependent speed: Algorithms based on Hamilton-Jacobi formulations. *Journal of Computational Physics*, 79(1):12–49, 1988.
- N. Paragios and R. Deriche. Geodesic active regions: A new framework to deal with frame partition problems in computer vision. *Journal of Visual Communication and Image Representation*, 13(1-2):249–268, 2002a.
- N. Paragios and R. Deriche. Geodesic active regions and level set methods for supervised texture segmentation. *International Journal of Computer Vision*, 46(3):223–247, 2002b.
- N. Paragios, O. Mellina-Gottardo, and V. Ramesh. Gradient vector flow fast geometric active contours. *IEEE Transactions on Pattern Analysis and Machine Intelligence*, 26(3):402–407, 2004.
- T. Peng, I. H. Jermyn, V. Prinet, and J. Zerubia. Incorporating generic and specific prior knowledge in a multi-scale phase field model for road extraction from VHR images. *IEEE Transactions on Geoscience and Remote Sensing*, 1(2):139–146, June 2008a.
- T. Peng, I. H. Jermyn, V. Prinet, and J. Zerubia. An extended phase field higher-order active contour model for networks and its application to road network extraction from VHR satellite images. In *Proceedings of the European Conference on Computer Vision*, Marseille, France, 10 2008b.
- T. Peng, I. H. Jermyn, V. Prinet, and J. Zerubia. Extended phase field higher-order active contour models for networks. *International Journal of Computer Vision*, 88(1):111–128, 2010. 3, 10, 33
- G. Perrin, X. Descombes, and J. Zerubia. A marked point process model for tree crown extraction in plantations. In *Proceedings of the IEEE International Conference on Image Processing*, Genova, September 2005.
- R. Peteri, J. Celle, and T. Ranchin. Detection and extraction of road networks from high resolution satellite mages. In *Proceedings of the IEEE International Conference on Image Processing*, Barcelona, Spain, September 2003.
- N. Pinto, D. D. Cox, and J. J. DiCarlo. Why is real-world visual object recognition hard? *PLoS Comput Biol*, 4(1):e27, 2008. 1, 7
- R. Potts. Some generalized order-disorder transformations. In *Proceedings of the Cambridge Philosophical Society*, volume 48, page 106109, 1952.
- L. J. Quackenbush. A review of techniques for extracting linear features from imagery. *Photogrammetric engineering and remote sensing*, 70(12):1383–1392, November 2004.

- C. Reinbacher, T. Pock, C. Bauer, and H. Bischof. Variational segmentation of elongated volumetric structures. In *Proceedings of the IEEE International Conference on Computer Vision and Pattern Recognition*, San Francisco, California, June 2010.
- T. Riklin Raviv, N. Kiryati, and N. A. Sochen. Unlevel-sets: Geometry and prior-based segmentation. In *Proceedings of the European Conference on Computer Vision*, May 2004.
- T. Riklin Raviv, N. Kiryati, and N. A. Sochen. Prior-based segmentation and shape registration in the presence of perspective distortion. *International Journal of Computer Vision*, 72(3):309–328, 5 2007.
- M. Rochery, I. H. Jermyn, and J. Zerubia. Phase field models and higher-order active contours. In *Proceedings of the IEEE International Conference on Computer Vision*, Beijing, China, October 2005. xii, 3, 4, 5, 9, 10, 11, 31, 60, 61, 62, 66, 75, 76, 81, 83, 97, 98, 104, 105, 107, 130
- M. Rochery, I.H. Jermyn, and J. Zerubia. Higher order active contours. *International Journal of Computer Vision*, 69(1):27–42, 2006. 3, 4, 5, 6, 9, 10, 11, 12, 30, 33, 37, 38, 75, 81, 83, 130
- I. Rodríguez-Iturbe and A. Rinaldo. *Fractal River Basin: Chance and self-Organization*. Cambridge University Press, 1997.
- J.W. Rouse, R.H. Haas, J.A. Schell, and D.W. Deering. Monitoring vegetation systems in the great plains with ERTS. In *Earth Resources Technology Satellite Symposium, NASA SP-351*, pages 309–317, 1973.
- M. Rousson. *Cue integration and front evolution in image segmentation*. PhD thesis, Université de Nice-Sophia-Antipolis, 2004.
- M. Rousson and N. Paragios. Shape priors for level set representations. In *Proceedings of the European Conference on Computer Vision*, Copenhagen, Denmark, May 2002.
- M. Rousson and N. Paragios. Prior knowledge, level set representations and visual grouping. *International Journal of Computer Vision*, 76(3):231–243, 2007.
- C. Samson, L. Blanc-Féraud, G. Aubert, and J. Zerubia. A variational model for image classification and restoration. *IEEE Transactions on Pattern Analysis and Machine Intelligence*, 22(5):460–472, 2000.
- G. Sapiro. *Geometric partial differential equations and image analysis*. Cambridge University Press, 2001.
- G. Sapiro and A. Tannenbaum. Affine invariant scale-space. *International Journal of Computer Vision*, 11(1):25–44, 1993.
- J. A. Sethian. *Level Set Methods Evolving Interfaces in Geometry Fluid Mechanics, Computer Vision and Materials Science*. Cambridge University Press, 1996.

- J. A. Sethian. *Level Set Methods and Fast Marching Methods: Evolving Interfaces in Geometry Fluid Mechanics, Computer Vision and Materials Science*. Cambridge University Press, 1999.
- K. Siddiqi, Y. B. Lauzière, A. Tannenbaum, and S. W. Zucker. Area and length minimizing flows for shape segmentation. *IEEE Transactions on Image Processing*, 7(3):433–443, 1998.
- A. Srivastava, S. Joshi, W. Mio, and X. Liu. Statistical shape analysis: Clustering, learning, and testing. *IEEE Transactions on Pattern Analysis and Machine Intelligence*, 27(4):590–602, 2003.
- L. H. Staib and J. S. Duncan. Boundary finding with parametrically deformable models. *IEEE Transactions on Pattern Analysis and Machine Intelligence*, 14(11):1061–1075, 1992.
- R. Stoica, X. Descombes, and J. Zerubia. A Gibbs point process for road extraction from remotely sensed images. *International Journal of Computer Vision*, 57(2):121–136, 2004.
- G. Székely, A. Kelemen, C. Brechbühler, and G. Gerig. Segmentation of 2-D and 3-D objects from MRI volume data using constrained elastic deformations of flexible Fourier contour and surface models. *Medical Image Analysis*, 1(1):19–34, 1996.
- H. D. Tagare. Deformable 2-D template matching using orthogonal curves. *IEEE Transactions on Medical Imaging*, 16(1):108–117, 1997.
- J. Tang, S. Millington, S.T. Acton, J. Crandall, and S. Harwitz. Ankle cartilage surface segmentation using directional gradient vector flow snakes. In *Proceedings of the IEEE International Conference on Image Processing*, October 2004.
- D. G. Tarboton. Fractal river networks, Horton’s laws and Tokunaga cyclicity. *Journal of Hydrology*, pages 105–117, 1996.
- M. Taron, N. Paragios, and M.-P. Jolly. Registration with uncertainties and statistical modeling of shapes with variable metric kernels. *IEEE Transactions on Pattern Analysis and Machine Intelligence*, 31:99–113, 2009.
- K. Thornton, J. Agren, and P.W. Voorhees. Modelling the evolution of phase boundaries in solids at the meso- and nano-scales. *Acta Materialia*, 51:5675–5710, 2003.
- A. Tsai, A.J. Yezzi, and A.S. Willsky. Curve evolution implementation of the Mumford-Shah functional for image segmentation, denoising, interpolation, and magnification. *IEEE Transactions on Image Processing*, 10(8):1169–1186, 2001.
- C.J. Tucker. Red and photographic infrared linear combinations for monitoring vegetation. *Remote Sensing of Environment*, 8:127–150, 1979.
- A. M. Turing. The chemical basis of morphogenesis. *Philosophical Transactions of the Royal Society (B)*, 237:37–72, 1952.

- M. Vaillant, M. I. Miller, A. L. Younes, and A. Trouvé. Statistics on diffeomorphisms via tangent space representations. *NeuroImage*, 23:161–169, 2004.
- L. A. Vese and T. F. Chan. A multiphase level set framework for image segmentation using the Mumford and Shah model. *International Journal of Computer Vision*, 50(3):271–293, 2002.
- S. Vinson, L.D. Cohen, and F. Perlant. Extraction of rectangular buildings using DEM and orthoimage. In *Scandinavian Conference on Image Analysis (SCIA'01)*, Bergen, Norway, June 2001.
- M. Wei, Y. Zhou, and M. Wan. A fast snake model based on non-linear diffusion for medical image segmentation. *Computerized Medical Imaging and Graphics*, 28(3):109–117, 2004.
- C. Xu and J. L. Prince. Gradient vector flow: A new external force for snakes. In *Proceedings of the IEEE International Conference on Computer Vision and Pattern Recognition*, San Juan, Puerto Rico, June 1997.
- C. Xu and J. L. Prince. Generalized gradient vector flow external forces for active contours. *Signal Processing*, 71(2):131–139, 1998.
- A. Yezzi, S. Kichenassamy, A. Kumar, P. Olver, and A. Tannenbaum. A geometric snake model for segmentation of medical imagery. *IEEE Transactions on Medical Imaging*, 16(2):199–209, 1997.
- J. Youn and J. S. Bethel. Adaptive snakes for urban road extraction. In *International Archives of Photogrammetry and Remote Sensing*, pages 465–470, 2004.
- A. L. Yuille, P. W. Hallinan, and D. S. Cohen. Feature extraction from faces using deformable templates. *International Journal of Computer Vision*, 8(2):99–111, 1992.
- S. C. Zhu and A. Yuille. Region competition: Unifying snakes, region growing, and Bayes/MDL for multiband image segmentation. *IEEE Transactions on Pattern Analysis and Machine Intelligence*, 18(9):884–900, 1996.

ABSTRACT

This thesis describes the construction of an undirected network (*e.g.* road network) model, based on the recently developed higher-order active contours (HOACs) and phase fields, and introduces a new family of phase field HOACs for directed networks (*e.g.* hydrographic networks in remote sensing imagery, vascular networks in medical imagery). In the first part of this thesis, we focus on the stability analysis of a HOAC energy leading to a ‘phase diagram’. The results, which are confirmed by numerical experiments, enable the selection of parameter values for the modelling of undirected networks.

Hydrographic networks, unlike road networks, are directed, *i.e.* they carry a unidirectional flow in each branch. This leads to specific geometric properties of the branches and particularly of the junctions, that it is useful to capture in a model, for network extraction purposes. We thus develop a nonlocal phase field model of directed networks, which, in addition to a scalar field representing a region by its smoothed characteristic function, and interacting nonlocally so as to favour network configurations, contains a vector field representing the ‘flow’ through the network branches. The vector field is strongly encouraged to be zero outside, and of unit magnitude inside the network; and to have zero divergence. This prolongs network branches; controls width variation along a branch; and produces asymmetric junctions for which total incoming branch width approximately equals total outgoing branch width. In conjunction with a new interaction function for the scalar field, it also allows a broad range of stable branch widths. The new proposed model is applied to the problem of hydrographic network extraction from VHR satellite images, and it outperforms the undirected network model.

Keywords: Shape priors, higher order active contours, phase diagram, phase fields, undirected networks, directed networks, road networks, hydrographic networks, remote sensing.

RÉSUMÉ

Cette thèse décrit la construction d’un modèle de réseaux non-directionnels (*e.g.* réseaux routiers), fondé sur les contours actifs d’ordre supérieur (CAOSs) et les champs de phase développés récemment, et introduit une nouvelle famille des CAOSs des champs de phase pour des réseaux directionnels (*e.g.* réseaux hydrographiques en imagerie de télédétection, vaisseaux sanguins en imagerie médicale). Dans la première partie de cette thèse, nous nous intéressons à l’analyse de stabilité d’une énergie de type CAOSs aboutissant à un ‘diagramme de phase’. Les résultats, qui sont confirmés par des expériences numériques, permettent une bonne sélection des valeurs des paramètres pour la modélisation de réseaux non-directionnels.

Au contraire des réseaux routiers, les réseaux hydrographiques sont directionnels, *i.e.* ils contiennent un ‘flux’ monodimensionnel circulant dans chaque branche. Cela implique des propriétés géométriques spécifiques des branches et particulièrement des jonctions, propriétés qu’il est utile de traduire dans un modèle, pour l’extraction de réseaux. Nous développons donc un modèle de champ de phase non-local de réseaux directionnels, qui, en plus du champ de phase scalaire décrivant une région par une fonction caractéristique lisse et qui interagit non-localement afin que des configurations de réseaux linéiques soient favorisées, introduit un champ vectoriel représentant le ‘flux’ dans les branches du réseau. Ce champ vectoriel est contraint d’être nul à l’extérieur, et de magnitude égale à 1 à l’intérieur du réseau ; circulant dans le sens longitudinal des branches du réseau ; et de divergence très faible. Cela prolonge les branches du réseau ; contrôle la variation de largeur tout au long une branche ; et forme des jonctions non-symétriques telles que la somme des largeurs entrantes soit approximativement égale à celle des largeurs sortantes. En conjonction avec une nouvelle fonction d’interaction pour le champ de phase scalaire, le modèle assure aussi une vaste gamme de valeurs des largeurs stables des branches. Ce nouveau modèle a été appliqué au problème d’extraction de réseaux hydrographiques à partir d’images satellitaires très haute résolution.

Mots clefs: A priori de forme, contours actifs d’ordre supérieur, diagramme de phase, champs de phase, réseaux non-directionnels, réseaux directionnels, réseaux routiers, réseaux hydrographiques, télédétection.